W mass measurement and simulation of the Transition Radiation Tracker at the ATLAS experiment

Thesis submitted for the degree of
Ph.D. in Physics

by

Esben Bryndt Klinkby

April 29, 2008

Experimental High Energy Physics Group
Niels Bohr Institute
University of Copenhagen

CERN-THESIS-2008-071
02/07/2008

Abstract

At the time of writing, the final preparation toward LHC startup is ongoing. All the magnets of the machine have been installed and are currently being cooled. Most sub-detectors of the four experiments situated at the LHC ring, are installed in their final positions and are being integrated into their respective data aquisition systems.

This thesis concerns itself with the ATLAS experiment, focussing on a sub-detector named the Transition Radiation Tracker (TRT). Some attention is given to the hardware testing of the detector modules, but the main focus lies on the simulation of the detector and the comparison of the simulation with test-beam data, as well as with data collected during the commisioning phase using cosmic muons.

There is little doubt that LHC will bring insight with respect to the understanding of the universe on the fundamental level. In particular, it is anticipated that light will be shed on the origin of mass which according to our current understanding proceeds via the Higgs mechanism. Either the corresponding particle; the Higgs boson is discovered by the LHC experiments, or its existence will be strongly disfavoured. In either case, a key measurement to understand the origin of mass, is the W boson, since it is intimitely linked to the Higgs mechanism. By precise measuring the W boson mass, the allowed mass range for the Higgs boson can be constrained, both within the Standard Model and in its various extensions. Thus, regardless of the results of the Higgs search, a precise determination of the W mass is of paramount importance, and in this thesis methods are presented aiming at measurering the W mass to the highest possible precision with the ATLAS experiment.

The thesis is structured as follows. In Part I the electroweak sector of the Standard Model is reviewed and various extensions are discussed. Emphasis is put on the W mass and its relations to other observables. After a short introduction to the ATLAS experiment, the prospects for a W mass measurement are reviewed in Part II. In Part III the simulation of the Transition Radiation Tracker is discussed and results are compared to test-beam measurements. Comparison of simulation to measurements proceeds in Part IV, in which a number of somewhat practical problems faced during the commissioning period are discussed.

In loving memory of

Johanne Kirstine Klinkby

(1911 – 2007)

Contents

List of Figures

List of Tables

Part I

Introduction

Chapter 1

The Standard Model bosons

1.1 Historic review

The discovery of the W and Z bosons [UA283a, UA283b, UA183a, UA183b] at the UA1 and UA2 experiments at CERN with masses and properties as predicted by the Standard Model constitutes one of the greatest accomplishments, not only of the Standard Model, but of human intellect as such. Its significance relies on the fact the W and Z bosons in the Standard Model are the carriers of the combined electroweak force, and thus their mere existence is a direct confirmation of the unified description of the weak and electromagnetic forces.
In the more than twenty years that have passed since the discovery, the Standard Model has been tested with an ever increasing precision, but as of yet it has been able to withstand the tests (see e.g. [LEP07]). Ironically, the success of the model, by now, is one of the major problems in the efforts to understand the universe at the most fundamental level. The apparent paradox comes from the fact that despite the success of Standard Model, it is - by construction - an insufficient model. For once, the model relies on the Higgs boson to explain the masses observed for other Standard Model particles. The Higgs has yet to be discovered and the concern within the community is that the allowed parameter space is decreasing, so that even if the Higgs boson is found, it can at best only be marginally allowed as the Standard Model Higgs.

It is intriguing that one of the best ways to pose stringent tests on the Standard Model and possibly reject it, is by studying the exact same particle originally used to confirm the model: The W boson.
As will be discussed in the following, the Standard Model predicts correlations between its various parameters, in particular between the masses of the top-quark, the Higgs- and the W boson. Thus by precisely measuring the top and W masses one can constrain the mass of the Standard Model Higgs, and in fact this constrain is beginning to overlap with the lower limit Higgs mass excluded from direct searches (LEP: [The05] and Tevatron: [Bus07]).

If there is such thing as a Higgs particle, it is likely to be found it at the LHC, and by comparing with measurements of the top and W masses it should be possible to resolve the issue of mass generation once and for all.

To get to the point where the paradox arise requires some understanding of the electroweak part of the Standard Model, and this follows in the next sections.

1.2 Elements of the electroweak theory

In order to arrive at the Standard Model bosons it proves useful to begin with constructing the fermions of the theory. Consider therefore the (God given) Lagrangian density for a free massless fermion field [PS95]:

$$\mathscr{L} = \bar{\psi} i\gamma^\mu \partial_\mu \psi \tag{1.2.1}$$

To be in accordance with observations, an interaction which couples leptons to neutrinos must be introduced. Moreover, since interactions requiring right-handed neutrinos have not been observed, they are not part of the Standard Model and therefore the fields are separated into a right-handed and a left-handed component (considering only the first generation):

$$\psi_R = e_R, \quad \psi_L = \begin{pmatrix} e_L \\ \nu_e \end{pmatrix}, \tag{1.2.2}$$

where the handedness is defined by $\phi_L = \frac{1+\gamma_5}{2}\phi$ and $\phi_R = \frac{1-\gamma_5}{2}\phi$ for any given field ϕ. Introducing the $SU(2)$ quantum number T (weak isospin) and the $U(1)$ quantum number Y (weak hypercharge), the doublet is assigned $T = 1/2$ and $T = 0$ is assigned to the singlet. The upper component of the doublet has third component of the weak isospin $T_3 = 1/2$, whereas the lower component has $T_3 = -1/2$. For the singlet $Y = -2$ while the doublet has $Y = -1$. Using these assignments, the electrical charge, Q, can be related to the weak charges by: $Q = T_3 + Y/2$. The Lagrangian density decouples into a left- and a right-handed component:

$$\mathscr{L} = \bar{\psi}_L i\gamma^\mu \partial_\mu \psi_L + \bar{\psi}_R i\gamma^\mu \partial_\mu \psi_R \tag{1.2.3}$$

Since observations show, that the mass of left-handed fermions equals that of the corresponding right-handed fermions $U(1)_L \times U(1)_R$ must be restricted to the $U(1)_Y$ subgroup by which the complete group of gauge transformations for the $U(1)_Y$ part is the following:

$$\psi_L \to e^{iY\alpha}\psi_L, \quad \psi_R \to e^{iY\alpha}\psi_R, \tag{1.2.4}$$

where the phase α is an arbitrary real constant.

For the $SU(2)$ group there is only one non-trivial transformation:

$$\psi_L \to e^{i\vec{\alpha}\cdot\vec{\sigma}/2}\psi_L \tag{1.2.5}$$

where σ_j are the Pauli matrices (generators of $SU(2)$). One can now enforce that the gauge transformations not only hold globally, but also locally by substituting: $\alpha \to \alpha(x)$, where x is a space-time coordinate. In order maintain the invariance of the Lagrangian with respect the to $U(1)_Y$ symmetry, it is necessary to introduce a gauge field, B, and use this to form covariant derivatives - designed so that the extra contribution originating from the space-time dependence of the gauge is exactly canceled. Also, a kinetic energy term of the introduced fields is added in order to give physical meaning to the introduced gauge field. For the $U(1)_Y$ symmetry, the transformation results in the following Lagrangian density:

$$\mathscr{L} = \bar{\psi}_L i\gamma^\mu D_\mu \psi_L + \bar{\psi}_R i\gamma^\mu D_\mu \psi_R + \frac{1}{4}F_{\mu\nu}F^{\mu\nu} \tag{1.2.6}$$

where $D_\mu = \partial_\mu - i\frac{g'}{2}YB_\mu$ is the covariant derivative with the $U(1)_Y$ gauge coupling g' and $F_{\mu\nu} = \partial_\mu B_\nu - \partial_\nu B_\mu$ is the field tensor. The symmetries of this Lagrangian are the following:

$$\psi_L \to e^{-i\alpha}\psi_L, \quad \psi_R \to e^{-2i\alpha}\psi_R, \quad B_\mu \to B_\mu + \frac{2}{g'}\partial_\mu\alpha(x) \tag{1.2.7}$$

where the factor of 2 in the exponent is due to the assignment of $Y = -2$ for the weak hypercharge of the singlet.

For the $SU(2)_T$ symmetry the situation is similar; introducing additional three gauge vector fields, $\mathbf{W}_\mu = W_\mu^j \cdot \sigma^j/2$, the covariant derivative is modified to:

$$D_\mu = \partial_\mu - ig\frac{\sigma_j}{2}W_\mu^j - ig'\frac{Y}{2}B_\mu \tag{1.2.8}$$

by which the electroweak Lagrangian is:

$$\mathscr{L} = \bar{\psi}_L\gamma^\mu(i\partial_\mu + g\frac{\sigma_j}{2}W_\mu^j + g'\frac{Y}{2}B_\mu)\psi_L + \bar{\psi}_R\gamma^\mu(i\partial_\mu + g'\frac{Y}{2}B_\mu)\psi_R - \frac{1}{4}W_{\mu\nu}^j W_j^{\mu\nu} - \frac{1}{4}B_{\mu\nu}B^{\mu\nu} \tag{1.2.9}$$

which describes a massless fermion field ψ interacting with four massless gauge fields B and W^j.

1.3 Introducing masses: Spontaneous symmetry breaking

The observed short range of the weak interactions requires that the responsible W and Z bosons are massive. As seen in the previous section, direct mass terms are not allowed by gauge invariance. The puzzle is resolved by means of spontaneous symmetry breaking.

Consider a doublet of complex scalar so called Higgs fields, with a hypercharge of $Y = 1$:

$$\Phi = \begin{pmatrix} \phi^+ \\ \phi^0 \end{pmatrix} \tag{1.3.1}$$

This is the simplest field that can be responsible for the spontaneous symmetry breaking of the electroweak sector, and the corresponding Lagrangian is the electroweak Lagrangian of equation 1.2.9 with the additional Higgs terms:

$$\mathscr{L}_H = (D_\mu\Phi)^\dagger(D^\mu\Phi) - V(\Phi) \tag{1.3.2}$$

where the (simplest possible) potential is defined as:

$$V(\Phi) = \mu^2\Phi^\dagger\Phi + \lambda(\Phi^\dagger\Phi)^2 \quad \text{with } \lambda > 0 \tag{1.3.3}$$

For $\mu^2 < 0$ the ground state of the potential is degenerate (i.e. the phase of Φ is arbitrary) as illustrated in figure 1.3.1. The minimum is obtained when:

$$\Phi^\dagger\Phi = \frac{-\mu^2}{2\lambda} \equiv \frac{v^2}{2} \tag{1.3.4}$$

By performing a perturbative expansion around the minimum:

$$<\Phi> = <0|\Phi|0> = \begin{pmatrix} 0 \\ v/\sqrt{2} \end{pmatrix} \tag{1.3.5}$$

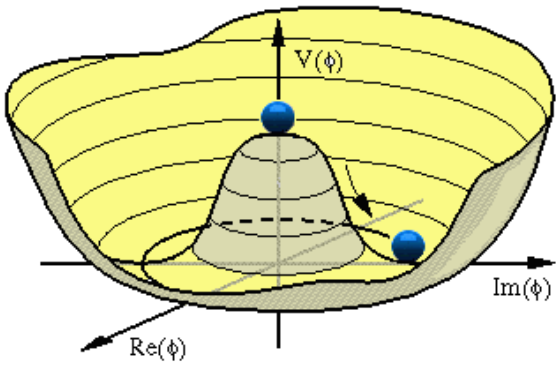

Figure 1.3.1: *Higgs potential for $\mu^2 < 0$. Source [hig08].*

the observable particles of the theory (i.e. the mass eigenstates) can be formed by the following linear combinations of the B and W fields (after going through some algebra, see [GHKD89]):

$$A_\mu = B_\mu \cos\theta_W + W_\mu^3 \sin\theta_W \tag{1.3.6}$$

$$Z_\mu = -B_\mu \sin\theta_W + W_\mu^3 \cos\theta_W \tag{1.3.7}$$

$$W_\mu^\pm = \frac{1}{\sqrt{2}}(W_\mu^1 \mp i W_\mu^2) \tag{1.3.8}$$

where θ_W is the weak mixing angle (Weinberg angle: $\tan\theta_W \equiv g'/g$).

Inserting the vacuum expectation value back into the kinetic term of the Φ field, the masses of the gauge bosons emerge as the coefficients squared of the quadratic terms:

$$(D_\mu \Phi)^\dagger (D^\mu \Phi) = \left(\frac{v^2 g^2}{4}\right) W_\mu^+ W^{\mu -} + \frac{1}{2}\left(v^2 \frac{g^2 + g'^2}{4}\right) Z_\mu Z^\mu + mixed\,terms \tag{1.3.9}$$

where $M_W = \frac{1}{2} v g$ and $M_Z = \frac{1}{2} v \sqrt{g^2 + g'^2}$ are identified. Note that only two mass terms are present in equation 1.3.9; one corresponding to the charged W fields and one for the neutral Z field. The last field, A, remains massless and is identified as the photon field. Masses for the leptons is generated similarly: I.e. by identifying terms quadratic in the fields of $(D_\mu \psi)^\dagger (D^\mu \psi)$. Note in this respect, that the three generations couple independently to the Higgs field and therefore can obtain different masses.

From the relations in equation 1.3.9 it is possible to make predictions of M_W based on measurements of α, M_Z and G_F (the Fermi coupling constant). Exploiting that θ_W is a predicted quantity through its on-shell definition $\cos\theta_W = M_W^2/M_Z^2$, the tree level prediction reads [Daw06]:

$$M_{W,tree}^2 = \pi\sqrt{2}\frac{\alpha}{G_F}\left(1 - \sqrt{1 - \frac{4\pi\alpha}{\sqrt{2} G_F M_Z^2}}\right)^{-1} \tag{1.3.10}$$

Inserting the values from [PDG06] yields: $M_{W,tree} = 80.939$ GeV to be compared to the present experimental value: $M_W^{exp} = 80.403 \pm 0.029$ GeV.

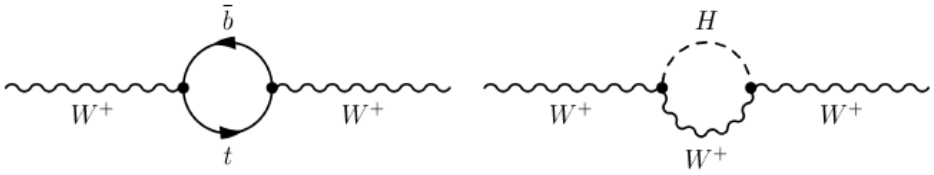

Figure 1.3.2: *Contributions to Δr. The $t-\bar{b}$ loop introduces corrections of the order: $\delta M_W \propto m_t^2 - m_b^2$ whereas for the Higgs loop diagram: $\delta M_W \propto log M_H$. Source: [Shp00].*

Some discrepancy is expected, since the above only evaluates the masses to lowest order in the coupling. Including higher order couplings and self-couplings modify the vector boson masses. The most important higher order diagrams for W^+ are shown in figure 1.3.2.

In this case, the Fermi coupling constant is modified to:

$$G_F = \frac{\pi\alpha}{\sqrt{2}M_W^2 \sin^2\theta_W} \cdot \frac{1}{1-\Delta r}, \tag{1.3.11}$$

where

$$\begin{aligned} \Delta r &= \Delta r^t + \Delta r^H \quad \text{and} \\ \Delta r^t &= \frac{3G_F m_t^2}{8\sqrt{2}\pi^2}\left(\frac{\cos^2\theta_W}{\sin^2\theta_W}\right) \\ \Delta r^H &= \frac{11G_F M_W^2}{24\sqrt{2}\pi^2}\left(\ln\frac{M_H^2}{M_W^2} - \frac{5}{6}\right) \end{aligned} \tag{1.3.12}$$

The W mass is then [Daw06]:

$$\begin{aligned} M_W/\text{GeV} = 80.939 &- 0.0579\ln\frac{M_H}{100\text{ GeV}} - 0.008\ln^2\frac{M_H}{100\text{ GeV}} - 0.5098\left(\frac{\Delta\alpha_{had}^{(5)}(M_Z)}{0.02761} - 1\right) \\ &+ 0.525\left(\left(\frac{m_t}{174.2\text{ GeV}}\right)^2 - 1\right) - 0.085\left(\frac{\alpha_s(M_Z)}{0.118} - 1\right) + \cdots \end{aligned} \tag{1.3.13}$$

The dependence on the Higgs mass and the uncertainty on m_t alone, prevents a precise evaluation of the above expression, but even if they were exactly known, the expression would still be subject to uncertainty from not going to infinite order in the couplings. This subject is revisited in section 2.2 below.

Chapter 2

Theoretical and experimental status

The Standard Model is now computed at two-loop precision [ACFW04, ACF06]. Through it is internal correlations between its parameters, the electroweak sector of the Standard Model is an extremely predictive framework, lacking only one vital ingredient yet to be discovered: The Higgs boson. As discussed in the introduction, the predictive power of the model was first demonstrated by the discovery of the vector bosons in the early eighties. A more recent example, was the discovery of the *top*-quark at a mass compatible with the Standard Model prediction [CDF94]. Presently both W's and *top*'s are subject to precision measurements. The fact that the W boson is intimately linked to the Higgs boson (as discussed in chapter 1), combined with the fact that the *top*-quark is so heavy and therefore contributes significantly to the relation between the Higgs and the W mass thorough loop corrections, imply that it is the uncertainties of the masses of the W and the *top*-quark that predominately limit the prediction of the Higgs boson mass. The status of constraining the Standard Model Higgs is summarized in figure 2.0.1(a). The direct Higgs searches performed at LEP in the late nineties [Tul02] and these which are currently ongoing at the Tevatron [Bus07], have excluded the Higgs in the range most favored by a combined Standard Model fit as is shown in figure 2.0.1(b). The large deviation from the Standard Model prediction constitutes one of the biggest problems of the model[1]. The relation between the measured and predicted values based on a combined fit to the Standard Model electroweak observables is shown in figure 2.0.2. The excellent agreement between theory and experimental results is based on a combined fit to the Standard Model parameters with a floating Higgs mass. The correspondent results for the Higgs mass is shown in figure 2.0.1(b). Restraining the Higgs to the experimentally allowed region does not severely deteriorate the combined fit due to the relatively low correlation between the Standard Model parameters and the Higgs mass.

A common approach to resolve when fitting over-constrained data is to introduce additional free parameters (or at least parameters with some degree of freedom). In a certain sense this is exactly what is proposed within the frameworks of Super Symmetry and Extra Dimensions although the parameters added, to some extent are theoretically motivated, i.e. they are "natural" extensions of the Standard Model. Before entering the discussion of these Standard Model extensions, however, the next section lists a number of additional problems faced by the Standard Model which, combined with the unresolved issues in the Higgs sector, constitute the problems that Super Symmetry and Extra Dimensional models are invented in attempts to (partially) solve.

[1] Another significant problem was reported recently: DØ and CDF showed a 3σ deviation of the phase of the B_s mixing amplitude from the Standard Model prediction. See [UT08] for details.

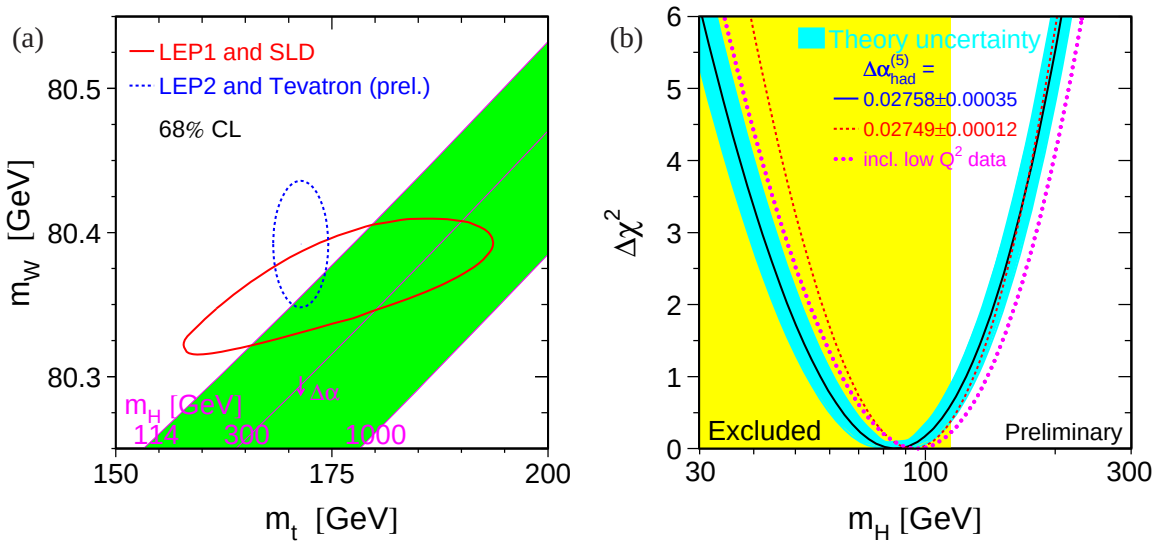

Figure 2.0.1: *(a) The correlation between M_W, m_t and the prediction of Standard Model Higgs mass, M_H. (b) Indirect result for M_H from a combined fit to the electroweak observables. The minimum is clearly excluded by direct searches. Source [The05].*

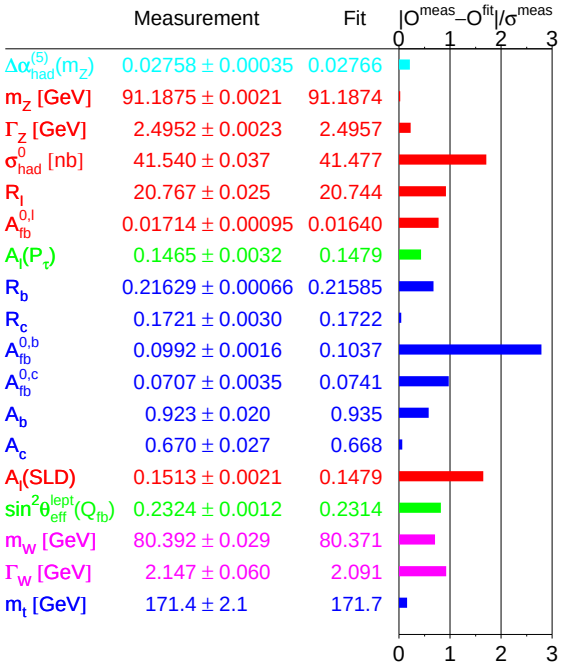

Figure 2.0.2: *Pulls of the various Standard Model electroweak observables, i.e. the deviation in units of standard deviations from a combined fit to the Standard Model. Source [The05].*

2.1 Problems of the Standard Model

One severe deficit of the Standard Model is the hierarchy problem, which concerns the value of the Higgs mass. According to figure 2.0.1(b) it must be in the range: $[115;194]$ GeV at 95% confidence level. In itself, this does not constitute a problem - the Higgs mechanism is invented to resolve the problem of the non-zero boson and fermion masses, and if incidently this requires that the Higgs mass is in the GeV range, so be it. However, due to self-couplings, the apparent mass of any particle is different at the cutoff scale, of the theory, Λ, than at the scale where the mass is probed by experiment. For fermions, the quantum corrections turn out to be of the same order as the bare fermion mass, but for the Higgs, the corrections, δM_H, are of $\mathscr{O}(\Lambda)$ [Mar97]:

$$\delta M_H^2 = \frac{|\lambda_f|}{16\pi^2}\left(-2\Lambda^2 + 6m_f^2 \ln\frac{\Lambda}{m_f}\right) \tag{2.1.1}$$

where λ_f is the Yukawa coupling and m_f is the mass of the fermion - for instance the top-quark: $m_t \approx 174.2$ GeV [PDG06]. Assuming that the Standard Model is complete (i.e. not merely a low energy approximation of some true theory), the natural choice for the cutoff scale would be the Planck scale: $\Lambda_{Planck} \sim 10^{19}$ GeV, where the Standard Model is expected to break down, since gravity at this scale can no longer be ignored. At the Planck scale, the bare Higgs mass and its corrections would then be $\mathscr{O}\left(10^{19}\text{ GeV}\right)$ and almost exactly of the same magnitude, since subtracting them must lead to a value $\mathscr{O}\left(10^{2}\text{ GeV}\right)$. Such extreme fine-tuning is unprecedented in the nature, and although possible in principle it does seem to hint some other governing mechanism - i.e. some new physics taking place at scales substantially lower than the Planck scale. In this case the cutoff scale of the Standard Model would lowered and thus the fine-tuning, at least partially, removed.

Another deficit of the model is that it fails to explain the baryon anti-baryon asymmetry observed in the universe. To account for the large asymmetry would require a *CP* violation at a level far beyond what is observed in the quark sector [KT90]. Also, the model has no dark matter candidate, and thus cannot offer an explanation as to the nature of 90% of the matter of the universe. In addition, gravity is not included in the model at all, though this is perhaps a too ambitious request at the moment.

What can perhaps better be characterized as a puzzle, rather than a problem of the Standard Model is the fact that the coupling constants of the electromagnetic, the weak and the strong parts of the Standard Model seem to nearly unify at some very large scale. Nearly, but not quite. Again, this could be purely coincidental, but could on the other hand also hint new physics, unifying the various parts of the Standard Model. Another puzzle is the origin of the generation multiplicity in the Standard Model - why is there exactly three generations? Also, the Standard Model has many free parameters (couplings, mixings etc), which could indicate the presence of a more fundamental theory limiting the phase-space. In addition, the values of some of these parameters seem to hint an underlying governing principle: Why is the mixing between quarks of different generations so small? Why is the top-quark so much heavier that than the other quarks?

2.2 Super symmetry

A theoretically appealing attempt to resolve some of the problems mentioned above is Super Symmetry (SUSY) [HLS75, HHW06]. Common features of this class of theories is that they propose a symmetry between bosons and fermions so that each of the Standard Model fermions is postulated

to have a super symmetric bosonic partner, and each Standard Model boson is postulated to have a fermionic partner. If the symmetry would be exact, the masses of the Standard Model particles and their respective partners would be the same, obviously contradicting experimental evidence. To resolve, the symmetry must be broken. Several proposals for the mechanism responsible for the SUSY breaking exists - the most popular is Minimal Super Gravity (mSugra)[2]. The name is in fact misleading - it is not a theory of super gravity. Its popularity is largely due to the fact that within mSugra the parameter-space is spanned by only five parameters (defined at a high scale $\sim 10^{16}$ GeV). SUSY must be broken at a scale above the electroweak breaking scale and the implications on the electroweak breaking are minor. The most striking difference, is that in SUSY models the Higgs sector is enlarged - the minimal content is two Higgs doublets and a singlet. All of these states acquire mass according to a procedure similar to the standard electroweak procedure described in chapter 1.

The main problem which can be resolved by the use of SUSY models is the hierarchy problem, and the reason for this is, that the additional bosonic loop diagrams contribute to the calculation of boson masses with opposite sign as their Standard Model fermionic counterparts. In the Higgs mass calculation this means that the corrections sending the bare Higgs mass to the Planck scale are canceled term by term, and thus the fine-tuning needed for the Standard Model Higgs to acquire the "observed" mass, is avoided. The fact that SUSY is broken introduces a difference between the mass of a Standard Model particle with respect to its SUSY partner. By this, the cancellation is not exact but of the order: $\delta M_H \sim \delta m_t^2 \ln \frac{\Lambda_{SUSY}}{m_t}$, where Λ_{SUSY} is the SUSY breaking scale.

Of course, the Higgs is not the only particle the additional bosons couple to - all Standard Model calculations are updated by additional diagrams. In most cases however, corrections are minor and therefore the theory as such, is not in direct conflict with the electroweak constraints, although certain regions of the SUSY phase-space are excluded from measurements of Standard Model particles. A general complication faced when working with SUSY scenarios is the enormous number of additional and largely unconstrained observables ($\mathcal{O}(100)$). Moreover, there exists a variety of different SUSY theories, which predict different relations between their parameters. One of the more popular type of models is Minimal Super Symmetry Models (MSSM). Although many other SUSY scenarios exist, focus here will lie on MSSM, the reason being that it is one of the most well established SUSY scenarios. Intense development has resulted in solid predictions in the electroweak sector, which can be confronted with measurements, and thus this particular SUSY model is of special interest for the W mass analysis presented in this thesis.
As the name suggests, MSSM is the smallest possible super symmetric extension of Standard Model. Even so, the Standard Model Higgs sector must be extended to include additional two Higgs doublets consisting of two charged and two neutral Higgs particles - one doublet is required to give mass to the up type fermions, and one to give mass to the $down$ type fermions.

Contrary to the Standard Model, the MSSM Higgs sector is largely constrained, and the masses of the additional four Higgs particles can be expressed in terms of only two parameters, conventionally chosen to be: The ratio between the vacuum expectation values of the charged and the neutral Higgs doublet: $\tan\beta = v_2/v_1$, and the mass of CP odd neutral Higgs boson A^0.

Of particular interest for the work presented here are the implications on the Higgs mass constraints given by the W and top masses, in case of MSSM.

In MSSM, the W mass calculation proceeds as described in chapter 1 for the Standard Model. The

[2] In the following, the terms 'mSugra' and 'constrained MSSM', CMSSM, are interchangeable. They denote the scenario where universality is assumed between the soft SUSY-breaking parameters m_0, $m_{1/2}$ and A_0 at the GUT scale. See [HHW06] for details.

differences are introduced through the radiative corrections Δr only, see equation 1.3.11. As in the Standard Model case, Δr depends itself on the W mass and can therefore only be solved using iterative methods. To first loop order, these has been solved, but obviously the result depend on the unknown masses of the super symmetric particles - in particular the mass of the super symmetric scalar partner of the *top*-quark: The *stop*-squark. In order not to conflict with other electroweak constraints, the approximate mass scale of MSSM SUSY particles can be established, see figure 2.2.1. Note here, the interesting observation that "light" SUSY is preferred by the electroweak constraints, which implies that SUSY, if it exists, is likely to be discovered at the LHC. Assuming that MSSM is valid and

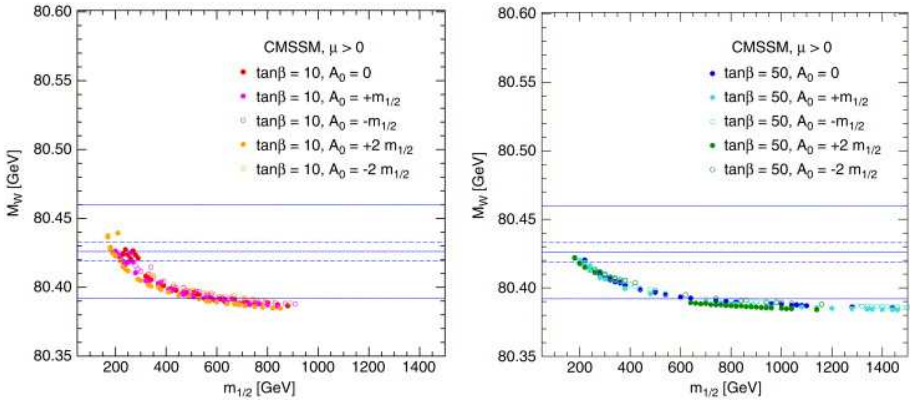

Figure 2.2.1: *M_W versus the SUSY breaking mass, $m_{1/2}$, in various CMSSM scenarios (a specific MSSM breaking scheme). The central solid lines represents the experimentally measured central value for M_W and the outer solid lines are the uncertainties ($\pm 1\sigma$) at the time of publishing the article. Since then, M_W is shifted downward (to* 80.403 ± 0.029 *GeV [PDG06]) but this thus not change the conclusion that the SUSY spectra must be "light" to avoid conflicting existing measurements. The dashed lines illustrate some supposed future experimental measurement precision. Source [HHW06].*

consequently not contradicting the electroweak measurements, it is possible to make predictions for the W mass. This important result is shown in figure 2.2.2(left). Here is shown how the region of allowed Higgs masses is shifted towards larger values in MSSM with respect to the Standard Model. The green region corresponds to the Higgs singlet, h^0, which is most natural to compare with the Standard Model Higgs (the red region). The right-hand part of the same figure illustrates the overall MSSM and mSugra performance with respect to fitting all the electroweak parameters - in general the results do not deviate significantly from the fit to the Standard Model. The theoretical uncertainties which are underlying figure 2.2.2(left) can be divided into two categories: Those which are imposed by the experimental uncertainties, and those which are inherently theoretical and stems from not calculating to infinite order in the couplings. The uncertainty resulting from the latter is not easily determined, but experience show that corrections tend to reduce in size when the order is raised, and therefore a common practice is to quote the magnitude of the highest order correction as the theoretical error. By this, the present estimates of the theoretical uncertainties are [HHW06]:

$$\delta M_W^{SM}(theory) = 4 \text{ MeV} \quad \delta M_W^{SUSY}(theory) = 10 \text{ MeV} \quad \delta M_W(exp\,intro) = 18 \text{ MeV} \qquad (2.2.1)$$

One plausible estimate of the future development is that the purely theoretical uncertainty is halved by the time of the mass measurement of the LHC. As will be shown in Part II, the prospects for reducing the experimental error are promising - perhaps a reduction factor larger than the theoretical would be possible by which the combined theoretical uncertainty could be reduced to $\sim 5-10$ MeV, both in Standard Model and MSSM.

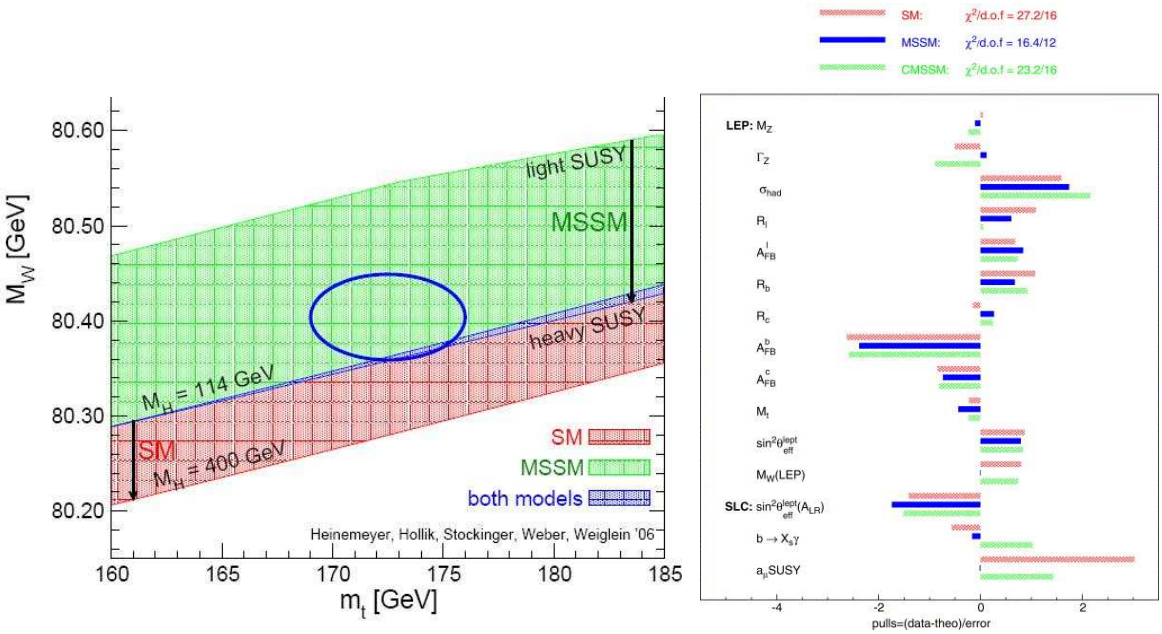

Figure 2.2.2: *Left: Correlations between the top, the W and the Higgs mass in MSSM. Right: Combined fit to all electroweak parameters within: Standard Model, MSSM and CMSSM.*

In many SUSY models, in particular in MSSM, the observed stability of the proton is not reproduced in a natural way. A popular solution is to postulate the existence of yet another symmetry called *R*-parity by which:

$$R = (-1)^{2S+3B+L} \tag{2.2.2}$$

is assumed to be a conserved quantity (S denotes the particle spin, B the baryon number and L the lepton number). Apart from solving the problem of the proton decay, this somewhat ad hoc added symmetry also has the implication that the lightest SUSY particle (which one it is differs between models) can be neutral, weakly interacting and stable and thus offers a promising dark matter candidate. Moreover, the coupling constants in MSSM and also in other SUSY models unify to exactly one, or are at least compatible with unification - see figure: 2.2.3.

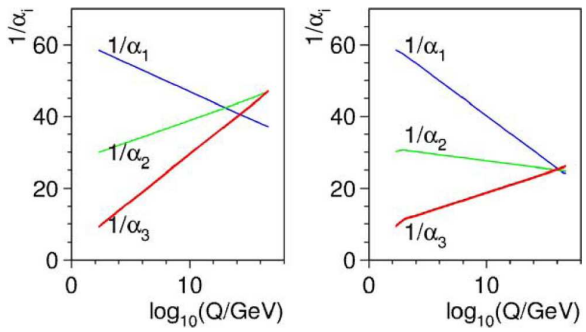

Figure 2.2.3: *Evolution of the coupling constants in Standard Model(left) and light (mass scales $\sim$ 1 TeV) MSSM SUSY (right). Source [dBS04].*

2.3 Extra Dimensions

Within the framework of extra dimensional theories, the hierarchy problem is sought resolved by the addition of extra spatial dimensions in which gravity can rule [AHDD99]. In case of d extra dimension, gravity would decrease as $1/r^{d+2}$ rather than following the usual $1/r^2$ law. Obviously, this is not correct at macroscopic scales, since gravity has been probed to $\mathcal{O}(1\text{ mm})$ [H$^+$04], but if the extra dimensions were compactified to smaller scales, R, it would escape the experimental constraints. By this, Newtons force law:

$$F_{Newton}(r) = -G_N \frac{m_1 m_2}{r^2} \propto \frac{m_1 m_2}{M_{Pl}^2 r^2}, \qquad r \gg R \tag{2.3.1}$$

is modified to

$$F_{ED}(r) \sim \frac{m_1 m_2}{M_{ED}^{d+2} r^{d+2}} \qquad R \gg r, \tag{2.3.2}$$

where M_{ED} is the effective Planck mass (or equivalently Planck scale) relevant for the quantum corrections to the Higgs mass discussed previously.

Requiring a continuous transition between the two force laws yields the following relation:

$$M_{Planck}^2 \sim M_{ED}^{d+2} R^d \tag{2.3.3}$$

By this the Planck scale is effectively lowered, and the hierarchy problem can be removed with appropriate values of R and d. A detailed calculation [AHDD99] based on the same arguments as the above, results in the following relation for the size of the extra dimensions R_d:

$$R_d = 2 \cdot 10^{\frac{31}{d}-16} \cdot \left(\frac{1\text{ TeV}}{M_{ED}}\right)^{1+\frac{2}{d}} \text{ [mm]} \tag{2.3.4}$$

In order not to reintroduce the hierarchy problem, M_{ED} should be close to the electroweak scale, for example ~ 1 TeV.
Assuming only one extra dimension, its size would have to be $R_1 \sim 10^{15}$ mm which clearly contradicting observations. However, $d = 2$ results in $R_2 \sim 1$ mm which is the approximate scale at which gravity has been tested.
Although gravitons are presumably massless particles, the fact that they can propagate in the extra dimensions implies that they appear massive when observed in four dimensions - the apparent mass, m_{app}, is given by the momentum in the extra dimensions $m_{app}^2 = p_4^2 + p_5^2 + \cdots$. Therefore the graviton is actually a dark matter candidate in some models of extra dimensions.

As for super symmetric models, a variety of extra dimensional models exist. A particular popular class of models is Universal Extra Dimensional Models in which the existence of one or more extra dimensions accessible for Standard Model fields is postulated. In order not to conflict with precision electroweak data which has been probed to length scales $\sim 10^{-15}$, the extra dimensions must be even smaller[3]. Moreover, since the additional dimensions would have to be compactified in order to escape detection, the mass eigenstates of the Standard Model particles would be discrete, and are called the Kaluza-Klein (KK) modes. By momentum conservation, the KK mode parity, $(-1)^n$ is conserved (n is the KK excitation number), and thus, for example, an excited photon cannot decay to Standard

[3] Some tricks exist to reduce this bound somewhat, see e.g. [KM07, ACD01].

Model particles. For this reason, the KK photons are in fact dark matter candidates in some models of universal extra dimensions.

The presence of extra dimensions could be difficult to distinguish from SUSY: Both frameworks predict heavier partners to Standard Model particles (and they are not mutually excluding each other). In the end, one might need to resolve by using the spin statistics where the models pose different predictions which could possibly be measured at the LHC, see e.g. [Kit07]. As for SUSY, extra dimensional models are only able to solve the hierarchy problem in case the heavier partners of the Standard Model particles are relatively light, say, in the TeV range.

2.4 Future prospects

Should a Higgs boson candidate be found at LHC, precise measurements of the W and top-quark mass will help determine whether it is a Standard Model Higgs - complementary to the direct measurements of the Higgs properties. Furthermore, different proposals of beyond Standard Model physics give different predictions on the relation between the Higgs-, the top- and the W masses, so that precise measurements of the W mass can help to distinguish between different Standard Model extensions (see e.g. figure 2.0.1(a)).

In the converse case where no Higgs and no new physics is discovered at the LHC, one would be forced to revisit the Standard Model calculations, and in this case reducing the uncertainty on its key parameters is of great importance: In particular the W mass uncertainty, since this presently accounts for the largest contribution to the mass uncertainty of the Standard Model Higgs.

At the LHC, an improvement of the W mass measurement is foreseen. Initial estimates of the expected statistics and systematics suggest that a measurement of the W mass with a precision of the order 15 MeV could be reachable [ATL99]. This would exclude large parts of the presently allowed SUSY parameters space as well as possibly the Standard Model depending on the central value (see figure 2.2.2 with a factor of roughly three reduction of the experimental bounds).

In Part II of this thesis the ATLAS detector prospects of measuring the mass are revisited, but first some aspects of the detector itself are outlined.

Chapter 3

The ATLAS experiment at the LHC

In the following, the LHC accelerator and the ATLAS experiment will be outlined. The discussion is based on [ATL08a, A$^+$07] and the reader is referred hereto for a more detailed discussion.

3.1 The Large Hadron Collider

Although protons are composite particles and therefore not optimal as beam constituents, it was decided to base LEP's successor on protons. The main reason is to limit the synchrotron radiation which ultimately made it impractical to increase beam energy at LEP. Using protons, the problems of synchrotron radiation are traded by a number of other problems; some of which are discussed below, while others will be evident during the discussion of the W reconstruction in section 5.3. Since the LHC is built in the existing LEP tunnel, the maximal collision energy is basically defined by the strength of the bending magnets. The design of the LHC magnets, however, is complicated by the fact that the equal charge of the two beams requires two separate beam lines[1]. For cost optimization, the two beam tubes share support structure and cryostat, but the coil assembled around them is different. The coils consist of a superconducting niobium-titanium alloy and are cooled by super-fluid helium. The magnets are able to provide a field of 8.33 T allowing a maximal beam energy of 7 TeV [2]. Due to quenching problems, however, it is expected to run at a reduced energy of 5 TeV per beam proton in the startup phase [Aym08].

Before entering the LHC ring, the protons are accelerated to 450 GeV by a combined effort of the existing CERN accelerators: Linac, 1 GeV booster, PS and the SPS [CER08]. Once the 450 GeV is reached at the SPS, the protons are fed to the LHC in bunches (maximally 2808), containing approximately $1.15 \cdot 10^{11}$ protons each. When all bunches are filled, the corresponding bunch-crossing time is 25 ns. Upon reaching the maximum energy of 7 TeV per beam proton, a bunch-crossing at the design luminosity, 10^{34} s^{-1}cm^{-2}, yields on average ~ 20 collisions, resulting in ~ 1000 particles emerging from the interaction region.

The bunches are brought to collision at four interaction points, around which detectors have been build:

[1] The other option: To use $p\bar{p}$ collisions was rejected due to the high costs of producing sufficient anti-protons.

[2] Only parts of the 27 km circumference can be filled with bending magnets, a certain fraction must be reserved for accelerating cavities and focusing/defocussing magnets for beam steering.

• ATLAS. Multipurpose experiment, discussed below.
• CMS[CMS06]. Multipurpose experiment using a stronger magnetic field than ATLAS, allowing for a more compact detector design.
• ALICE[AL95]. Heavy ion experiment, exploiting the fact that the LHC, apart from protons, can accelerate heavy ions such as lead to a maximum energy of 5.5 TeV per nucleon pair. Designed predominately to study the properties of the quark gluon plasma.
• LHCb [Lb03]. Motivated by the fact that at high energies, b and $b\bar{b}$ hadrons are produced in the forward cone, this single-arm spectrometer is built predominately to study b decays and CP violation in the b-quark system.

3.2 The ATLAS experiment

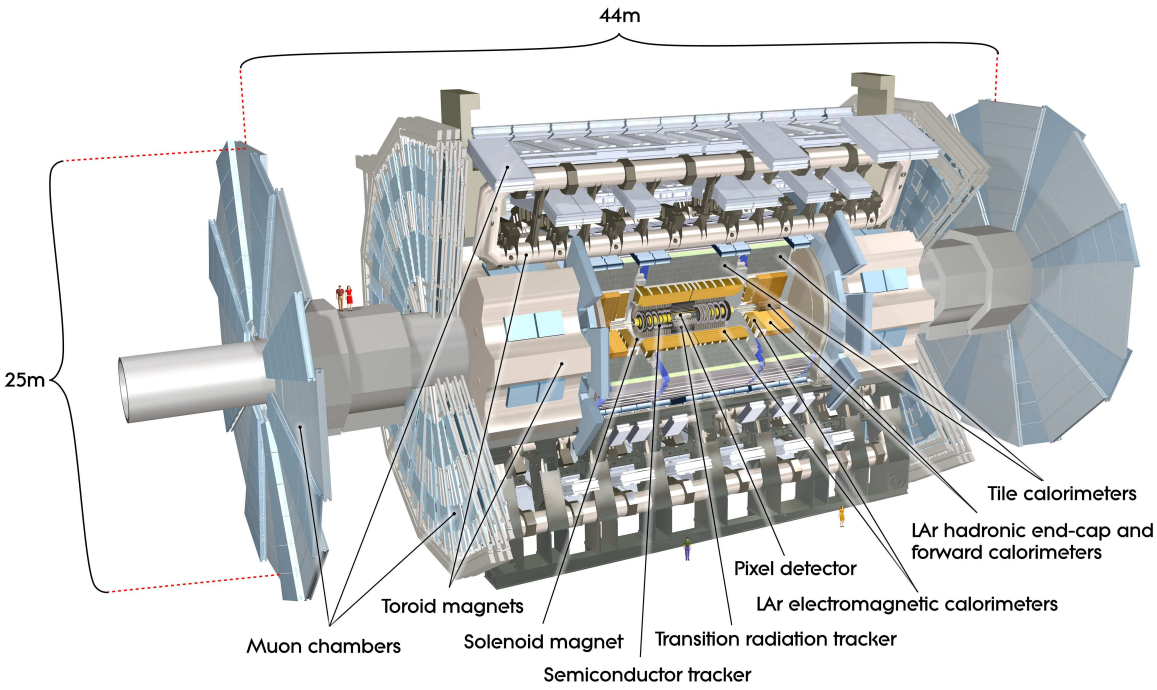

Figure 3.2.1: *Overview of the ATLAS detector. Source [ATL08a].*

Being a general purpose detector, the list of physics performance goals is, of course, extensive. However, some measurements stand out as being of particular importance. Discovering the Higgs boson is such a measurement. As discussed previously, the Higgs can, if it exists, have any mass in the $\mathcal{O}\left(10^2\ \text{GeV}\right)$ range, and it must be ensured in the detector design, that discovery is possible regardless of its mass. Since the branching ratio of the Higgs into its various decay channels differs significantly as a function of the Higgs mass, this implies that the experiment must be designed to have sufficient sensitivity in a large number of different decay channels. Another physics goal of vital importance is the possible SUSY discovery. Similar to the Higgs boson case, the masses of the SUSY

particles are largely unconstrained, and possible discovery depends on the performance of a number of sub-detector systems and their combined performance to reconstruct missing transverse energy $\not{E}_T$.

The expected cross-sections of the Higgs and SUSY processes are exceedingly small even at LHC energies: About 1 event in a billion (cross-sections of various processes at LHC are shown in figure 4.0.1). This is the reason to aim for the high interaction rate (40 MHz). Obviously the high interaction rate and the resulting large track multiplicities complicate the detector design. In order to be able to perform in the environment provided by the LHC machine, the physics performance goals can be translated into a set of detector requirements on which the ATLAS experiment has been designed:

- To cope with the interaction rate and the particle multiplicity, the electronics of all sub-detectors must be fast and radiation hard. Also, the detector granularity must be sufficiently fine so that the interesting events can be reconstructed despite the many overlapping events.
- For overall event reconstruction, and in particular to reconstruct secondary vertexes from b or τ decays, the charged particle momentum must be measured with a high resolution and efficiency: $\sigma_{p_T}/p_T = 0.05\% \cdot p_T \oplus 1\%$.
- Large acceptance in pseudorapidity and full azimuthal coverage is essential.
- To identify and precisely measure the energy of electrons and photons the electromagnetic calorimeter must perform well:
  $\sigma_E/E = 10\%/\sqrt{E} \oplus 0.7\%$.
  In addition, the hadronic calorimeter measures the energies of hadrons and jets:
  $\sigma_E/E = 50\%/\sqrt{E} \oplus 3\%$ (barrel) and
  $\sigma_E/E = 100\%/\sqrt{E} \oplus 10\%$ (end-cap).
- Muons must be accurately identified and measured:
  $\sigma_{p_T}/p_T = 10\%$ at $p_T = 1$ TeV.
- Events must be sorted on a short timescale so that uninteresting events can be rejected, hereby ensuring that the maximal output event rate is below the hardware limitation of about 200 Hz.

How these requirements are met by the ATLAS experiment is briefly discussed in the following.

3.2.1 The Inner Detector

The tracking of charged particles is performed by the Inner Detector. This detector is built utilizing a typical layered structure, consisting of three sub-detectors based on different detector technologies to best cope with the requirements. Each sub-detector consists of a barrel part and two end-caps as shown in figure 3.2.2. The resolutions quoted below represent the values of [ATL08a] which is the most recent assessment. However, as will be discussed in chapter 18, the performance of the real detector generally resembles the design well.

Pixel

Closest to the interaction point is the very radiation hard and finely segmented Pixel Detector (Pixel), whose pixels are as small as $50 \times 400\ \mu\text{m}^2$. The sensitive detectors of the Pixel barrel are placed on

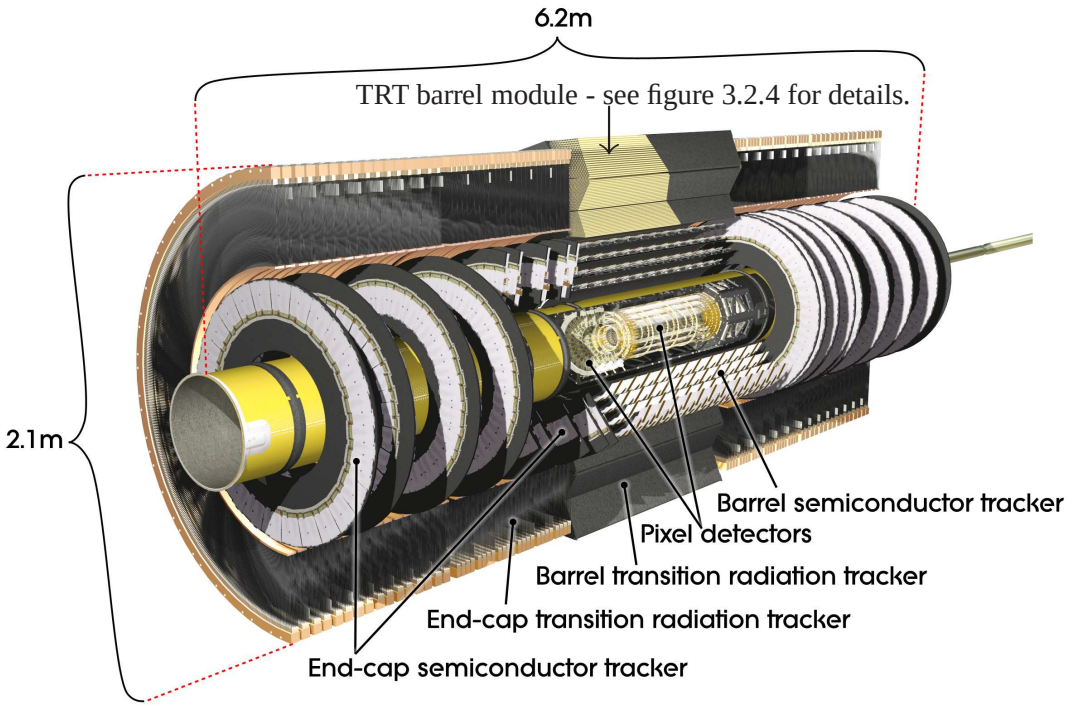

Figure 3.2.2: *The structure of the Inner Detector. Source [ATL08a].*

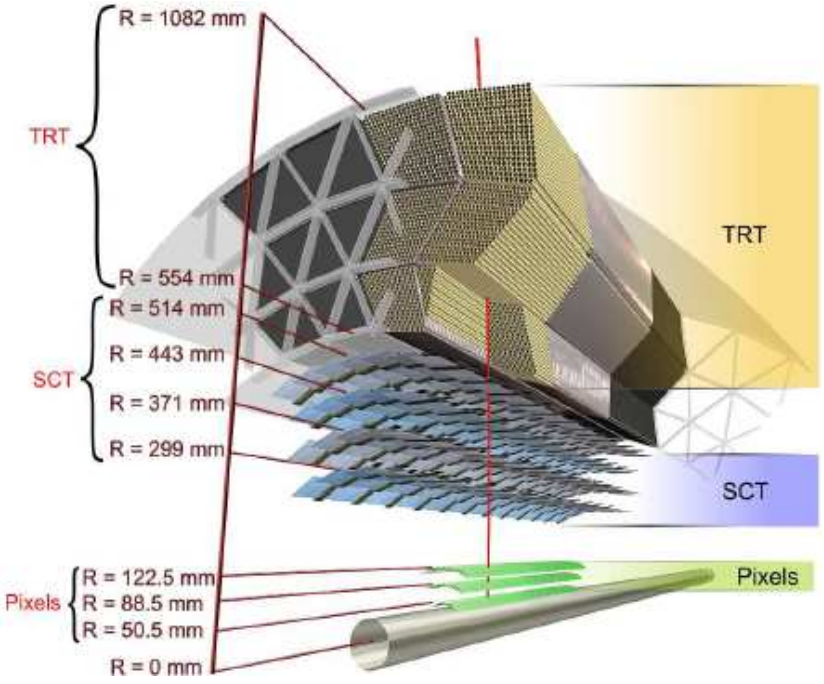

Figure 3.2.3: *The structure of the Inner Detector barrel. Source [ATL08a].*

concentric cylinders around the beam-line, whereas the end-caps consist of disks placed perpendicular to the beam axis, extending to $|z| \approx 50$ cm, as indicated in figure 3.2.3. Altogether the pixel detector counts 80.4 million read-out channels, providing three measurements for each track. In the barrel the expected intrinsic accuracy is 10 μm in $r\phi$ and 115 μm in the z plane whereas the corresponding values for the end-caps are 10 μm in $r\phi$ and 115 μm in the r direction. The innermost layer of the Pixel detector is placed merely 5.1 cm from the nominal beam position whereas layers two and three are located at 8.9 cm and 12.3 cm respectively. For this reason, the Pixel detector is subject to a significant radiation dose. Despite significant efforts to limit the effects caused by this, the harsh hadron environment in which the Pixel detector operates, causes the detector to degrade over time. It is expected that the detector will be replaced at a future detector upgrade.

SCT

The next sub-detector met by a traversing particle consists of the four double-sided silicon layers of the SemiConductor Tracker (SCT) - a silicon micro-strip detector with a read-out pitch of 80 μm. Due to a small stereo angle between the read-out strips, the SCT provides four space-points for each penetrating track. Arranged in a setup similar to the Pixel detector (see figure 3.2.2), the SCT barrel yields a binary resolution of 17 μm in $r\phi$ and 580 μm in z. In the end-caps the same $r\phi$ resolution is achieved whereas the resolution in r is 580 μm. Altogether, the SCT has 6.3 million read-out channels and occupies the region: 30 cm$< r <$ 52 cm and $|z| <$ 2.8 m.

TRT

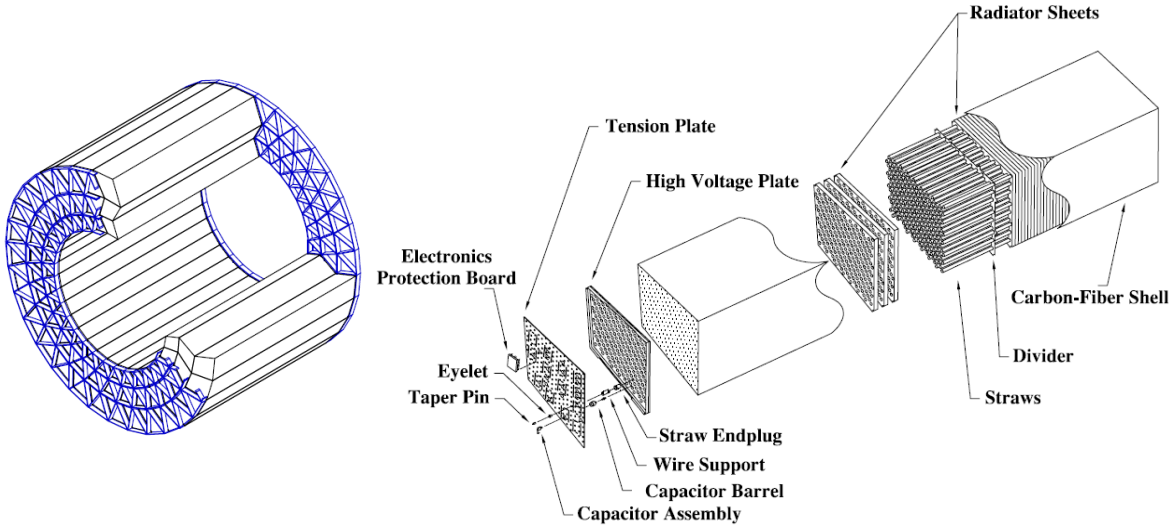

Figure 3.2.4: *Left: Layout of the 96 TRT barrel modules and support structure. Right: The structure of a TRT barrel module. Source [TRT08b].*

The cylindrical volume extending from a radius of approximately 56 cm to 108 cm is covered by the gaseous Transition Radiation Tracker (TRT).
As will be described in detail in Part III, the TRT is based partly on the principles of a normal straw based gas-detector for tracking, and partly on the principle of transition radiation for particle identification. Transition radiation arises when an ultra-relativistic charged particle traverses the boundary

between materials of different dielectric constants, as will be explained in detail in chapter 12. This effect is proportional with the γ-factor of the traversing particle and can provide particle identification capabilities from the amount of transition radiation produced by a given particle.
To exploit the transition radiation, the TRT is built from 73 layers of kapton/mylar straws containing $XeCO_2O_2$ (70:27:3) gas interleaved with radiator material. Centrally in each straw is a gold-plated tungsten wire which acts as an anode due to a voltage applied between the wire and the straw. Advantages of this design is, that the gas is relatively cheap and can be constantly exchanged, hereby diminishing effects of radiation. In the barrel region, the straws, which are 4 mm in diameter, are assembled in 96 modules of three different types (see figure 3.2.4) arranged parallel to the beam whereas the end-cap straws are arranged in 14 wheels and point radially away from the beam axis[3]. In order to reduce problems of large occupancy, the 9 innermost straw-layers in the barrel are insensitive in the central region. Also, all barrel straws are isolated centrally and read out at both ends, so that each straw provides two read-out channels. In total the TRT has 351.000 read-out channels.
In the barrel, the intrinsic measurement accuracy is expected to be 130 μm pr straw in the $r\phi$ plane. The poor single measurement resolution compared to the silicon based detectors, is largely compensated by the long lever arm and the large number of hits: A typical track leaves $\sim$ 36 hits in the TRT, by which the TRT contributes to the momentum resolution roughly as much as the combined Pixel and SCT sub-detectors during low luminosity running, L=10^{33} $s^{-1}cm^{-2}$, where the occupancy problems are not expected to dominate TRT performance.

Results from the commissioning of the Pixel, SCT and TRT sub-detectors, at the surface, as well as combined tests in the ATLAS cavern will be presented in chapter 18.

3.2.2 Calorimeters

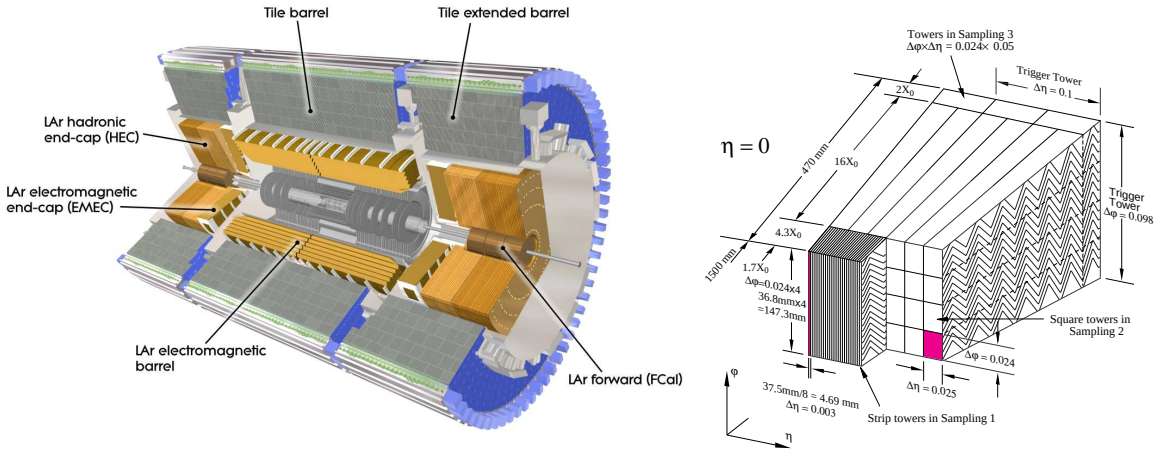

Figure 3.2.5: *Left: Overview of the calorimeter systems. Right: The structure of the LAr calorimeter. Source [ATL08a] and [ATL96a].*

The ATLAS calorimetry consists of an inner electromagnetic calorimeter supplemented by a dense hadronic calorimeter as depicted in figure 3.2.5(left). The electromagnetic calorimeter is built using

[3]The original design consisted of 18 wheels, but 4 were staged due to financial problems. It is likely that these wheels will never be installed.

an accordion structure of lead plates interleaved with liquid argon (LAr) and functions basically as a drift-chamber due to a strong electric field. This design has the advantages of complete ϕ symmetry without azimuthal cracks, and moreover the active LAr can be replaced during detector operation, hereby minimizing effects of radiation damage. The detector covers the region up to $r = 2.25$ m corresponding to >22 (>24) radiation lengths in the barrel (end-caps). The granularity shown in figure 3.2.5(right) corresponds to that of the central barrel part ($\eta = 0$). Along η, the cell size varies significantly as determined by an optimization of the energy resolution. The very fine segmented innermost sampling is designed for e/π separation, whereas most energy is deposited in the square sampling towers of the second sampling. For triggering purposes, 4 by 4 cells are combined into towers with a single output.

The hadronic calorimeter covers the region up to $r = 4.25$ m and consists of a barrel part, two extended barrels, two end-caps and two forward calorimeters. In order to reduce the effects of the radiation the latter two sub-detectors, which are subject to the largest track multiplicity, are based on LAr. The first two sub-systems are sampling calorimeters using steel absorbers and scintillating tiles of plastic. The readout proceeds via wavelength shifting fibers to photomultiplier tubes placed on the outer rim of the calorimeter. The total thickness of the tile calorimeter is 9.7 radiation lengths at $\eta = 0$. As for the electromagnetic calorimeter, the cell sizes differ significantly in η and it serves little purpose to repeat them here. Instead, the reader is referred to [ATL08a].

3.2.3 The Muon System

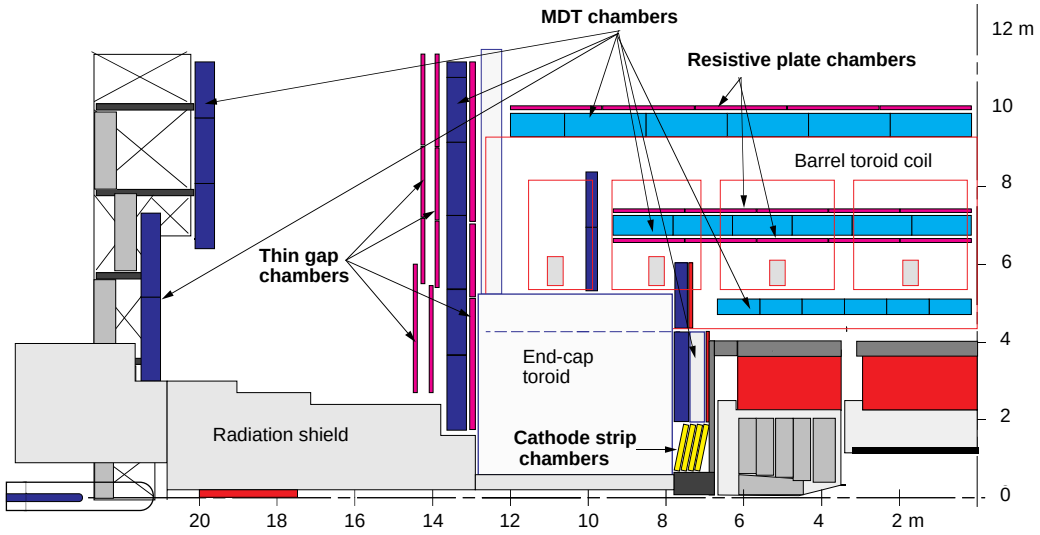

Figure 3.2.6: *Overview of the Muon System. Source [ATL08a].*

Due to the thickness of the calorimeters, the punch-through probability of hadrons into the Muon System is low, so that hits in this system can reliably be assumed to be caused by muons. However, the purpose of the Muon System is not only to identify muons, but also to provide precision measurements of muon momenta and to be used for triggering. The combination of these requirements have led to the complex design of the muon system sketched in figure 3.2.6 (and briefly explained below).

The Muon System consists of a barrel region and two end-cap regions located partially within the toroids magnets (see figure 3.2.1). In the barrel, sensitive monitoring drift tubes (MDT) are placed

on three cylindrical layers whereas the end-cap regions uses vertical concentric structures. The tubes, which are built of aluminum, have a diameter of 3 cm and are filled with a mixture of Argon (93%) and CO_2 (7%) operating under a pressure of 3 bar. Centrally in the tubes, an anode wire composed of W-Re collects the electrons freed by a passing muon. The spatial resolution which can be achieved by this design is about 80 μm per measurement.

In the regions of larger pseudo-rapidities, the requirements of segmentation and radiation hardness are more severe, and here measurements are performed by the cathode strip chambers (CSC). This multi-wire proportional chamber uses a $ArCO_2CF_4$ (30:50:20) gas-mixture, which provide a single hit resolution ~ 60 μm.

For triggering purposes, the MDTs and CSCs are not useful due to the long drift times involved (up to 700 ns) and therefore two separate sub-systems have been built: Resistive plate chambers (RPC) in the barrel region and thin gas chambers (TGC). The main reason to base the trigger chamber on different technologies is the difference in occupancy between the barrel and the end-cap. Both sub-detectors are based on small gas volumes and provide drift-times of typically 10 ns.

As opposed to other sub-systems, the space limitations faced by the Muon System are not severe, and thus the advantages of long lever arms can be afforded. For example, are the MDTs of the barrel layers placed at radii of 4.93 m, 7.12 m and 9.48 m respectively.

3.2.4 The magnet system

For the Inner Detector, a magnetic field of approximately 2 T is provided by the central solenoid (CS), situated at $1.22 \text{ m} < r < 1.31$ m. In order to prevent heating problems induced on the surrounding sub-detectors, the central solenoid is based on a superconducting mixture of NbTi, Cu and Al cooled by liquid helium. The fact that the magnet is placed in front of the calorimeters allows its size to be small, but also implies that electromagnetic showers tend to start in the magnet rather than in the calorimeter. In order to diminish this effect and prevent unnecessary degrading of the calorimeter performance, the magnet is constructed using a minimum of material. In addition, the magnet is located inside a vacuum vessel shared by the electromagnetic calorimeter hereby eliminating two vacuum walls.

Muons are bend by the barrel- and end-cap air-core toroids, which are based on the same superconducting alloy as the central solenoid. The huge toroid system encapsulates the experiment, except for parts of the muon layers, as can be seen in figure 3.2.1. Needless to say, the fields provided varies significantly in the volume of the ATLAS experiment, peaking at approximately 4 T.

3.2.5 Triggering

Since the type of events that the LHC is primarily built to search for (i.e. Higgs and SUSY) are expected to be extraordinarily rare, the interaction rate must be enormous. At the design luminosity, bunch-crossings take place every 25 ns yielding about 20 collisions on average. Even utilizing zero suppression and packing, the raw data rate from the ATLAS experiment would be ~ 80 TB/s [4] - which is clearly beyond present day capabilities of data handling and storage. To bring this rate to an acceptable level, a three level trigger filtering system has been implemented, each level refining the decision of the previous level, based on an increasing amount of data. A schematic view of the trigger system is provided in figure 3.2.7. At the level one trigger (L1), the decision on whether or not to keep

[4] Assuming 2 MB/event, i.e. 2 MB·40 MHz=80 TB/s.

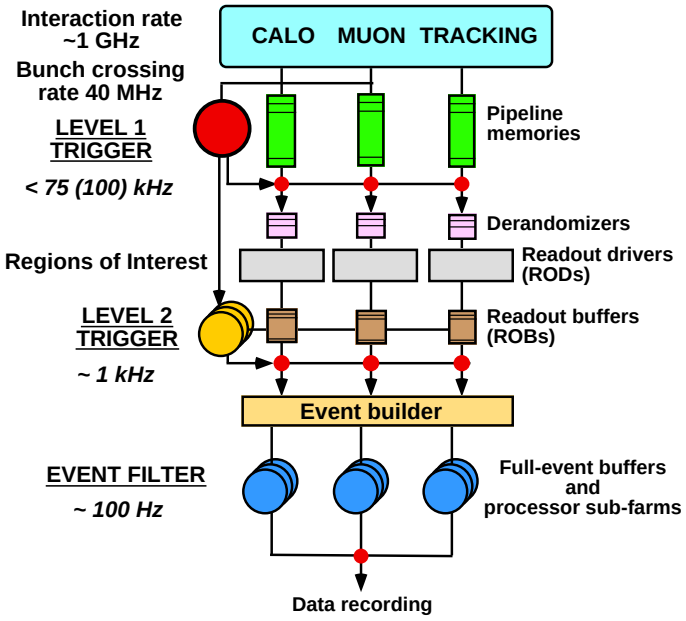

Figure 3.2.7: *Overview of the ATLAS triggering scheme. Source [ATL99].*

an event is based on the trigger chambers of the muon spectrometer, as well as reduced-granularity cells of the electromagnetic- and hadronic calorimeters. Thus, anything with sufficiently high p_T, whether it be muons, electrons, photons, jets, hadrons or even $\not{E}_T$ causes a positive trigger decision. While awaiting the L1 decision (maximally 2.5 μs) subsequent events are stored in pipelines, and upon completion, the initial 40 MHz event rate is reduced to 75 kHz.
The level two trigger (L2) is based upon the Regions of Interest (RoI) defined by the L1 trigger, but refines the reconstruction by reading the full granularity of all available detector data within the RoIs. Within typically 40 ms the event rate is hereby reduced to about 3.5 kHz.
This rate is sufficiently low that the events can be fully reconstructed at the event filtering (EF), which uses optimized versions of the standard offline ATLAS reconstruction software as well as various conditions data[5]. After Event Filtering, the event rate is reduced to roughly 200 Hz. Although this rate can be handled offline, limitations of bandwidth and CPU resources for the event analysis imply, that offline analysis cannot be performed centrally by all users. Instead, the data is distributed to a number of computer facilities around the world, directly from the ATLAS pit.

In modern particle physics, of course, it is not sufficient to perform collisions and measure the outcomes in the detector. The experiment must also be simulated in order to reliably extract signatures of new (or known) physics phenomena. The complexity of the ATLAS experiment as briefly summarized above is reflected in the software which simulates ATLAS events. An introduction to the software developed and used in the ATLAS experiment is given in chapter 9. Before entering the details of the simulation, however, the next part of the this thesis is devoted to a study of the capabilities of the ATLAS experiment to measure the mass of the W boson.

[5]Data from the experiment describing the instantaneous condition of the detector, i.e. threshold settings, voltages, temperatures etc.

Part II

W mass analysis

Chapter 4

Introduction to the W mass analysis

Integral parts of the analysis and writeup is adopted and expanded from two papers: [ATL08b] and [ATL08c] which are in the publishing process at the time of writing. The first paper is written in collaboration with S. Mehlhase, T. Petersen, M. Boonekamp and N. Besson whereas co-authors of the latter are: T. Petersen, M. Boonekamp, and N. Besson. For completeness and readability the content (and parts of the writeup) of the two papers has been merged and expanded, and constitutes this Part of the thesis. With respect to the papers, additional focus is here put on the work done by the author, however, it is emphasized that not all results are due to author. In particular, the results presented in chapter 7 is based on studies done by the other authors.

In the previous chapters, the importance of the M_W measurement was argued. In this Part of the thesis, the ATLAS experiment prospects for the W mass measurement are discussed. Compared to the Tevatron measurements [CDF07a, CDF07b, DØ98, DØ96, DØ00b], which currently dominates the world average [PDG06], the increase in energy and luminosity imply an increase in statistics, so that the ATLAS M_W measurement, is expected not to be statistically dominated as has been the case for the Tevatron measurements. Consequently, understanding and minimizing systematic errors become of paramount importance for the M_W measurement, and this is the topic of the present analysis.

The expected W cross-section at the LHC is about 20 nb [H$^+$03]. In 10 fb^{-1} of data, a benchmark for one year of integrated luminosity during the first years of stable running, more than 100 million W- and nearly 10 million Z events will be collected in the exploitable decay channels ($W \to e\nu, \mu\nu$ and $Z \to ee, \mu\mu$), providing a combined statistical sensitivity of about 2 MeV for the W mass measurement. The total expected production cross-section for W's at the LHC is shown in figure 4.0.1.

Especially the large Z sample is of importance since this precisely measured resonance, due to the large overlap in kinetics, can be used to constrain and evaluate the W systematics.

Earlier estimates [ATL99, H$^+$03, B$^+$07a] of the systematic uncertainties affecting the M_W measurement amount to $\delta M_W \sim 20$ MeV for the ATLAS experiment. The main sources are the imperfect determination of the absolute energy scale, and the uncertainties in the W boson kinematic distributions (rapidity, transverse momentum), which in turn stem from proton structure functions uncertainties and higher orders QCD effects. As discussed in the following chapters, the uncertainties can be significantly reduced using Z boson measurements.

The analysis is structured as follows: After introducing the W production and reconstruction, the signal selection and fitting procedure are discussed in section 5.3. Also listed here are the ingredients

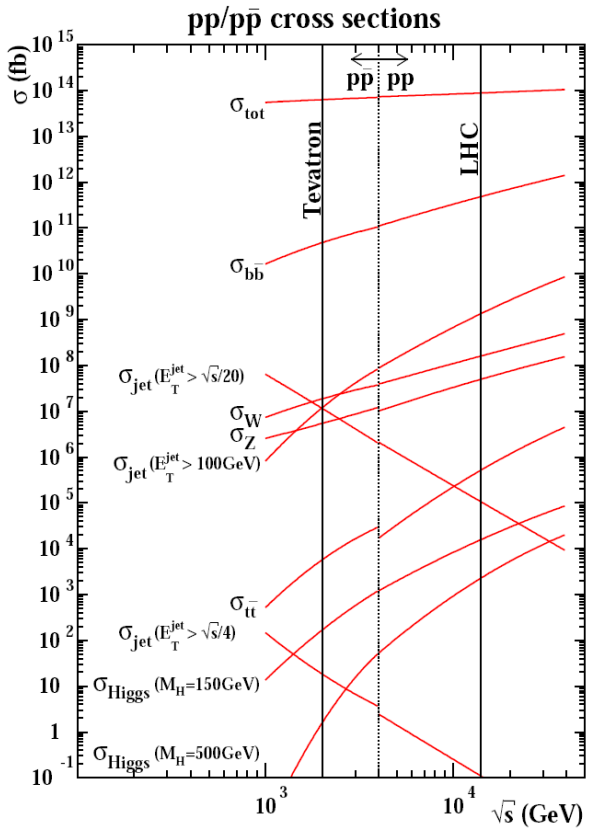

Figure 4.0.1: *Expected production cross-sections at the LHC. Source: [LHC06].*

needed to describe the W distributions used in the fit, and a general description on how these ingredients can be determined. The sources of uncertainty are then treated in turn, in chapter 6 (experimental uncertainties), chapter 7 (theoretical uncertainties), and chapter 8 (backgrounds, underlying event, and effects related to the machine operation). Correlations between these effects are discussed in section 8.4, and the results are summarized in section 8.5 and discussed in section 8.6, which concludes the analysis.

Chapter 5

W mass measurement

5.1 *W* Production

At the LHC, the dominant production mechanism for *W* and *Z* bosons is the Drell-Yan process of quark-antiquark annihilation - see figure 5.1.1. Being a proton-proton collider, the anti-quarks would have to be sea quarks whereas the quarks can be either valence or sea quarks. The enhanced availability of *u* quarks with respect to *d* quarks from the proton substructure (uud), implies that the cross-section for W^+ production is larger than that of W^- and have slightly different kinetics as will be discussed in section 7.3.1. In hadron machines, even when produced in the Drell-Yan process,

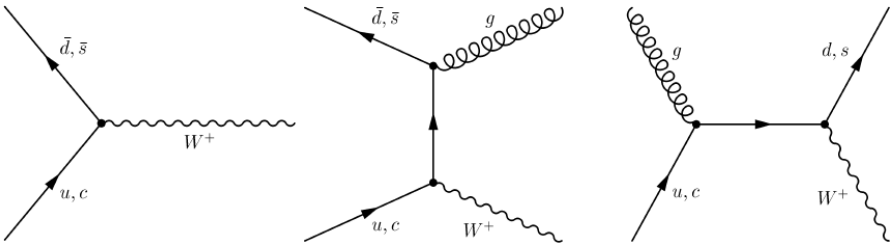

Figure 5.1.1: *Diagrams for W^+ production. Left: Leading order Drell-Yan production. Middle and right: Diagrams to first order in α_s. Source [Shp00].*

W's will acquire some transverse momentum due to the Fermi motion of the quarks in the hadron. However, a much larger source of transverse momentum is contributions to the *W* production from higher order diagrams which include gluon- or quark radiation, as shown in figure 5.1.1. As a result, the *W* can obtain a significant momentum in the plane transverse to the beam, p_T, as shown in figure 5.1.2(left). The momentum is balanced by quark/gluon radiation, experientially seen as a spray of hadrons bouncing the boson: Hadronic jet(s) - see figure 5.1.2(right).

5.2 *W* reconstruction

Since a *W* boson decays within $\sim 10^{-25}$ s it must be reconstructed from its decay products. The decay can proceed either leptonically or hadronically - the branching fractions of the available decay modes are given in table 5.2.1. Since the di-jet cross-section at hadron colliders is many orders of magnitude

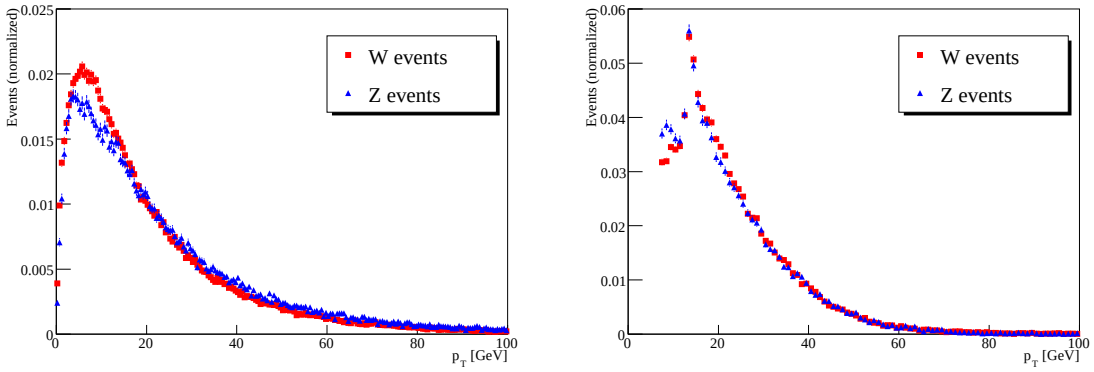

Figure 5.1.2: *Left: Reconstructed transverse momentum of W and Z bosons in the muon decay channel. The larger resolution in the W events causes the wider peak at low p_T, while at higher p_T the Z spectrum slightly dominates. Right: Jet p_T in $W \to \mu\nu$ and $Z \to \mu\mu$ events. The structure at low p_T is due to the jet reconstruction algorithm.*

Decay mode	*Branching fraction*
$e^+\nu_e$	$10.75 \pm 0.13\%$
$\mu^+\nu_\mu$	$10.57 \pm 0.15\%$
$\tau^+\nu_\tau$	$11.25 \pm 0.20\%$
$q\bar{q}'$	$67.60 \pm 0.27\%$

Table 5.2.1: *Branching ratios for W^+. Source [PDG06].*

larger than the W boson cross-section, the hadronic decay modes of W and Z bosons are not usable (see figure 4.0.1 $\sigma_{tot} \approx \sigma_{di-jet}$). The τ mostly decays hadronically, and even when it does decay leptonically, the two additional neutrinos created with respect to the electron and muon channel make this mode unsuitable for precision mass measurements. Therefore, only the leptonic decay modes $W \to \ell\nu$ and $Z \to \ell\ell$ where $\ell = e, \mu$ are considered for the W and Z reconstruction.

In an LHC collision, the remnants of the interacting protons proceed undetected along the beam line. Moreover, the momentum fractions of the interacting quarks are unknown, by which full event reconstruction is possible only in the transverse plane (but of course parts of the event such as Z decays can be fully reconstructed). In case of W production and decay, the event reconstruction is further complicated by the presence of a neutrino, which escapes the experiment undetected. To reconstruct the W despite the difficulties one must take advantage of the facts that the ATLAS experiment offers close to 4π coverage in solid angle, and that only very rarely additional neutrinos are produced in a W event ($< 1\%$). By this, one can assume that everything, with significant transverse momentum, except for the neutrino from the W decay, is reconstructed. The transverse momentum of the neutrino is then simply given as the energy imbalance of the event, evaluated by vectorially summing all energy deposits in the detector. Rewriting the invariant mass equation for the W in terms of measurable quantities yield:

$$
\begin{aligned}
M_{inv}^2 &= (E^l + E^\nu)^2 - (\vec{p}_T^{\,l} + \vec{p}_T^{\,\nu})^2 - (p_z^l + p_z^\nu)^2 \\
&\Downarrow \\
M_T^2 &\equiv (E_T^l + E_T^\nu)^2 - (\vec{p}_T^{\,l} + \vec{p}_T^{\,\nu})^2 \\
&\approx 2\vec{p}_T^{\,l} \cdot \vec{p}_T^{\,\nu} = 2p_T^l p_T^\nu (1 - \cos(\Delta\phi_{l\nu}))
\end{aligned}
\tag{5.2.1}
$$

where $\Delta\phi_{l\nu}$ is the angle between the decay products as illustrated in figure 5.2.1 and it has been used that $E_l \gg m_l c^2$. The right hand side of this figure illustrates a typical Z decay and the difficulties faced when reconstructing. As indicated by the sizes of the uncertainty ellipses, these decays are fully reconstructed to a high level of precision. Nonetheless, the $W \to l\nu$ and $Z \to ll$ events are very similar both from a physics- and a detector point of view. By this, the precisely reconstructed Z events, inferring the constraints given from the LEP measurements of the Z properties, constitute an excellent sample for calibration and for the study of systematics in W events as will be discussed later.

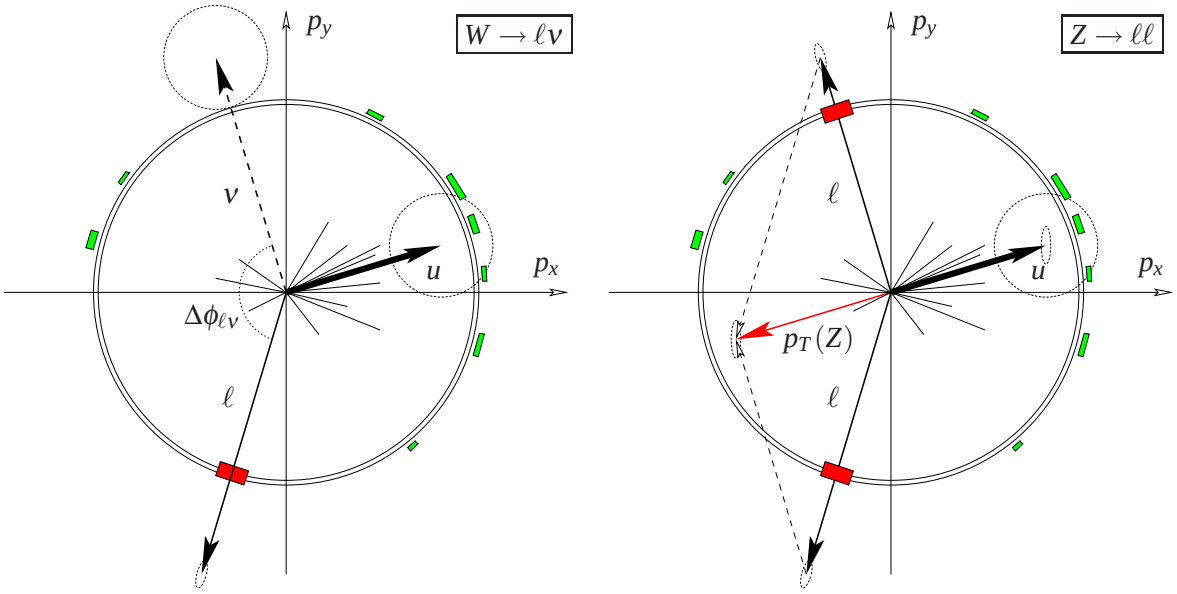

Figure 5.2.1: *Transverse view of a $W \to \ell\nu$ (left) and a $Z \to \ell\ell$ (right) event. The combined transverse momentum of the recoil u, which should match that of the boson, is used to estimate the momentum of the undetected neutrino in the $W \to \ell\nu$ decay. The dotted ellipses represent the uncertainties.*

5.3 Outline and strategy of the analysis

5.3.1 Simulation and data sets

The simulated W and Z samples on which this study is based are generated using the `PYTHIA` event generator [SMS06]. Photon radiation is carried out by `PHOTOS` [BW94], and τ-decays are handled by `TAUOLA` [JWDK93]. Simulation of particles passing through the detector is done using `GEANT4` [G403] based on the implementation of the ATLAS geometry in the so called GeoModel (explained in chapter 9). Events are reconstructed using the ATLAS software. The simulated data is partly used as real data ("pseudo-data"), and partly to produce the templates, exploiting the generator-level

Channel	Statistics [events]	Cross-section [pb]	Corresponding $\mathscr{L}$ [pb^{-1}]
$W \to e\nu$	170143	20510	13.3
$W \to \mu\nu$	189903	20510	13.5
$Z \to ee$	377745	2015	218.7
$Z \to \mu\mu$	150650	2015	83.4

Table 5.3.1: *Number of events, cross-sections, and corresponding luminosity of the simulated W and Z signal samples used in this chapter.*

distributions together with estimated detector smearing corrections. The samples used in this chapter are due to the Computer Systems Commissioning (CSC) production [AFGS$^+$07] and the simulated statistics of the main signal samples are shown in table 5.3.1. As can be seen from this table, the W signal samples correspond to about 13 pb^{-1} but for transparency, all results presented in this chapter are scaled to 15 pb^{-1} in order for the reader to be able to assess what can be done which this limited amount of data. In the section concluding the chapter all results obtained are summarized and scaled to 10 fb^{-1}, which is the luminosity expected for the competitive W mass measurement of ATLAS [ATL08b, ATL97a]. In chapter 7 special customized simulations of larger data samples are defined and used.

5.3.2 Event selection

W events are required to have one isolated lepton[1] with p_T above 20 GeV and missing transverse energy ($\not{E}_T$) in excess of 20 GeV. Z events are required to have two isolated and oppositely charged leptons with p_T above 20 GeV. The triggers providing these events are an isolated 15 GeV electron trigger and a 20 GeV muon trigger. The electrons are required to pass tight identification criteria[2], and only muons which are reconstructed from track-segments in both the Inner Detector and the Muon Spectrometer are used [CSC08a]. Both electrons and muons are required to lie within the tracking region $|\eta| < 2.5$ (see figure 5.3.1). In addition, the calorimeter barrel - end-cap transition region $1.3 < |\eta| < 1.6$ is excluded for electrons due to poorer resolution, lack of uniformity and most importantly significant bias on the lepton momentum.

Apart from this basic selection, some other requirements apply. To reject backgrounds from $t\bar{t}$ and QCD di-jet events, the signal events are required not to have large hadronic activity. A summary of the requirements can be found in table 5.3.2. The reason for the somewhat arbitrary cut values is, that the cuts should be optimized with respect to the final systematic error, and therefore a cut optimization at the present stage of the analysis (i.e. before data is available) would be premature[3].

The expected numbers of events in 15 pb^{-1} from the above mentioned event selection are summarized in table 5.3.3. Though the expected number of reconstructed Z events is an order of magnitude smaller than that of W events, the fact that Z events are fully reconstructed and thus have much better mass resolution compensates for this deficit.

[1] The ratio between the energy in a cluster of size $\Delta R \equiv \sqrt{\Delta\eta^2 + \Delta\phi^2} \leq 0.2$ and the full energy in the cells of a 3x7 sliding windows is required to have some minimum value. The exact value depends E_T and η. For details see [ATL08e].

[2] Based on hadronic leakage, isolation and electromagnetic samplings. For details see [ATL08e].

[3] It is not as in many other analyzes useful to optimize with respect to signal significance. Instead, a cut that make the W and Z look alike is preferable.

Requirement	$W \to e\nu$	$W \to \mu\nu$
Reconstructed lepton	$p_T > 20$ GeV, $\lvert\eta\rvert < 2.5$	$p_T > 20$ GeV, $\lvert\eta\rvert < 2.5$
Isolation	$E_T^{\text{cone}}/E_T < 0.2$	
Missing energy	$\not\!\!E_T > 20$ GeV	$\not\!\!E_T > 20$ GeV
Crack region	Remove $1.30 < \lvert\eta\rvert < 1.60$	
Recoil momentum	$p_T < 50$ GeV	
Requirement	$Z \to ee$	$Z \to \mu\mu$
Reconstructed leptons	$p_T > 20$ GeV, $\lvert\eta\rvert < 2.5$	$p_T > 20$ GeV, $\lvert\eta\rvert < 2.5$
Isolation	$E_T^{\text{cone}}/E_T < 0.2$	
Crack region	Remove $1.30 < \lvert\eta\rvert < 1.60$	
Recoil momentum	$p_T < 50$ GeV	

Table 5.3.2: *Selection criteria for the W and Z decays. See text for details.*

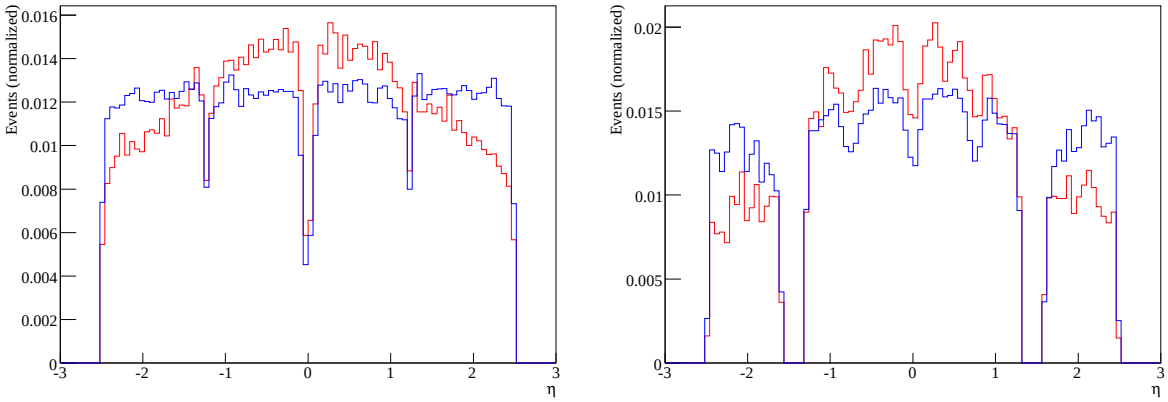

Figure 5.3.1: *Distribution in η of reconstructed muons (left) and electrons (right) from W events (blue) and Z events (red).*

Channel	$W \to e\nu$	$W \to \mu\nu$	$Z \to ee$	$Z \to \mu\mu$
Acceptance [%]	44.3	45.4	42.4	39.9
Reconstruction eff. [%]	21.7	39.1	10.4	33.4
Statistics for 15 pb^{-1} [10^3]	66.7	120.2	3.2	10.1

Table 5.3.3: *Acceptances, total reconstruction efficiencies, and resulting statistics for 15 fb^{-1} of data. The W cross-sections are inclusive, while the Z cross-sections are for invariant masses above 60 GeV. Both contain the relevant branching fractions. The acceptance is the fraction of events which lies within the detector acceptance, while the reconstruction efficiency is the overall efficiency for an event to pass all selection criteria.*

5.3.3 Input to *W* mass fit

The fact that the invariant mass of the W cannot be reconstructed forces the use of variables sensitive to the W mass for the measurement. As explained in the introduction of this chapter, one such variable is the transverse mass, defined as:

• $M_T^W \equiv \sqrt{2p_T^l p_T^\nu (1-\cos(\Delta\phi_{l\nu}))}$.

But there are also others:

• The lepton transverse momentum, p_T^l.

• The missing transverse momentum, $p_T^\nu \equiv \not{E}_T$.

The lepton transverse momentum is measured with an accuracy of about 2% for electrons and muons in the momentum range of interest (cf. sections 5.4.2 and 5.5.1). This is an order of magnitude better compared to the accuracy of the missing transverse energy determination, which has a resolution of about 20-30% (section 5.5.2). Finally, the W transverse mass combines the two along with the angle between them in the transverse plane.

All of the above distributions have a Jacobian edge either at $M_W/2$ (p_T^l and p_T^ν) or M_W (M_T^W), which is sensitive to the W mass - see figure 5.3.2. The sharpness of the edge is affected both by the resolution and the boson p_T.

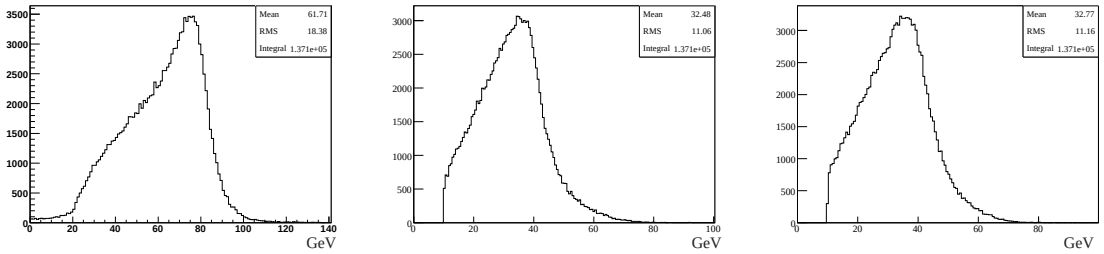

Figure 5.3.2: *Distributions sensitive to M_W based on quantities of reconstructed $W \to \mu\nu$ events. M_T (left), transverse muon momentum (middle) and $\not{E}_T$ (right).*

While the lepton p_T has a very good resolution, the p_T of the boson smears this Jacobian edge. On the contrary, M_T^W is to first order insensitive to the p_T of the boson, but here the edge is smeared by the poor resolution of the missing transverse energy (see figure 5.3.3). Finally, p_T^ν suffers from both effects, and is therefore the poorest candidate for a fitting variable.

Since M_T^W is formed from p_T^l and p_T^ν, it is of course correlated with p_T^l. However, the correlation is only about 30%, and since they have different systematic errors, combining the measurements could improve the sensitivity.

5.3.4 Fitting the *W* mass with templates

The lepton transverse momentum and W transverse mass distributions, p_T^l and M_T^W, shown in figure 5.3.3, are the result of several non-trivial effects. For this reason no analytical expression describes the distributions in detail, and one is forced to use numerical methods to describe and compare distributions. One method of comparing two such distributions is template fitting. Templates of the p_T^l and M_T^W distributions produced with varying M_W values, are compared bin by bin to the corresponding distribution observed in data (see figure 5.4.4). The comparison is based on a binned χ^2 method.

To estimate the impact of a given systematic effect on the W mass determination, templates unaware

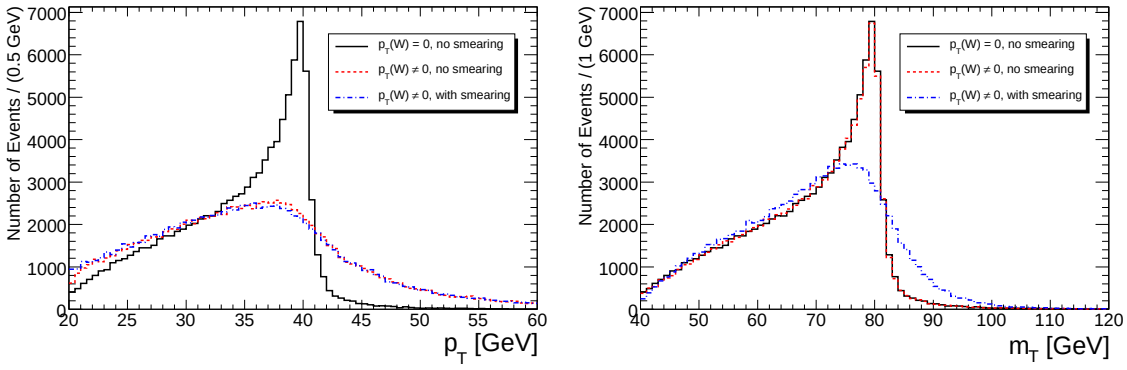

Figure 5.3.3: *Distributions of p_T^l (left) and M_T^W (right), showing the Jacobian edge, and the effects of resolution and recoil (i.e. p_T of the W). While p_T^l is more sensitive to the recoil than the resolution, the converse is true for the M_T^W distribution.*

of the effect under consideration are produced and subsequently fitted to data, which includes the effect. Assuming an unbiased fit, in the absence of systematic effects (cf. sections 5.4 and 5.5), the resulting shift in fit value measures the systematic error on the W mass from not including the effect. By gradually changing the size of an effect, the systematic error on the W mass as a function of the effect can be determined. As most effects are small, the dependencies are approximately linear. In general different systematic effects have different influence for the p_T^l and M_T^W fits. If an effect can be characterized by one parameter (α), the systematic errors (δM_W) can be calculated from the derivative $\partial M_W/\partial\alpha$ times the size of the uncertainty $\delta\alpha$. If more parameters are required, the systematic uncertainty is calculated from all parameters α_i and their covariances $\mathrm{Cov}_{i,j}$ [Cow].

$$\delta M_W = \frac{\partial M_W}{\partial \alpha}\delta\alpha \quad \text{(Single parameter)} \qquad \delta {M_W}^2 = \sum_{i,j}\frac{\partial M_W}{\partial \alpha_i}\frac{\partial M_W}{\partial \alpha_j}\mathrm{Cov}_{i,j} \quad \text{(Multi parameter)}$$

Thus, the evaluation of systematic effects used throughout the analysis proceeds in two steps: First the dependence of M_W on the systematic effect is mapped with respect to a characterizing parameter ($\frac{\partial M_W}{\partial \alpha}$). The next step is to estimate the expected uncertainty on α, $\delta\alpha$, by which the impact on the W mass measurement is found as the product of the two quantities.

5.3.5 Required inputs

For the above procedure to work in practice, one must predict the p_T^l and M_T^W distributions as a function of the W mass. These distributions however result from many effects, which need to be included correctly in order to avoid biases in the mass fit. The inputs needed are listed below.

• **Experimental inputs**: The energy scale and resolution need to be known in order to describe the Jacobian edge correctly (position and spread). Electron and muon reconstruction efficiency effects also distort the spectra, if this efficiency is p_T dependent (and for electrons it is - cf. section 5.4.3).

• **Theoretical inputs**: The W rapidity distribution, y^W, affects the M_T^W and p_T^l distributions through acceptance effects. The transverse momentum of the W, p_T^W, directly affects the p_T^l spectrum, whereas

its impact on the M_T^W spectrum is weaker. The shape of the y^W and p_T^W distributions result from the proton structure functions and from higher-order QCD effects. The lepton angular distribution in the W rest frame is of importance for both p_T^l and M_T^W and changes with the W polarization [MO94]. Finally, QED effects (photon radiation in the W decay) shifts the lepton p_T downward. Since the radiated photons are mostly collinear to the charged decay lepton, the impact on electrons and muons is different: The measured muon momentum entirely reflects the momentum loss by radiation, whereas the electron energy, measured essentially in the electromagnetic calorimeter, includes most of the radiated energy.

• **Environmental inputs**: These include, among others, backgrounds surviving the W selection, underlying event, pile-up effects on reconstructed energies and momenta, random neutron hits in the muon spectrometer ("cavern background"), and the impact of a non-zero beam crossing angle. In all cases, imperfect modeling of these inputs biases the event reconstruction, lead to distorted p_T^l and M_T^W distributions.

After presenting the fitting procedure below, the systematics originating from these inputs are discussed separately.

5.4 Fitting the W mass with templates - electron channel

5.4.1 Modeling templates for W mass fit

Two assumptions have to be validated before one can start the studying systematics using the template approach. The *unbiasedness* of the fit in itself and the *portability* of the calibration from the Z to the W. The unbiasedness is tested by assuming perfectly known physics and detector response. In practice, the detector response is determined at this stage from direct comparisons of the lepton reconstruction to the generator-level kinematics, using events from the W sample. The fit is then repeated using templates with the detector response estimated from the Z sample, still comparing reconstruction to generator-level truth. An unbiased result validates the portability, i.e. that detector parameters can indeed be ported from Z to W events, justifying an *in situ* determination of these parameters using Z events.
In addition it has to be verified that the template components can be included without biasing the fit, and thus that a subsequent calibration, which matches the truth, will yield unbiased templates. This is tested in the following.
Note that *per event* truth information is used only in the first step, to obtain E_{rec}/E_{truth} - the distribution which is fitted. In the following steps only distributions of the same quantity are used, by which the exercise can be performed in real data, with Z events playing the role as truth. The procedure is depicted in figure 5.4.1. The statistical sensitivity of the $W \to e\nu$ sample, corresponding to 13.3 pb^{-1} of data, is about 120 MeV, and an estimate of the required precision on the detector response parameters to keep the systematic uncertainty within this limit is provided.

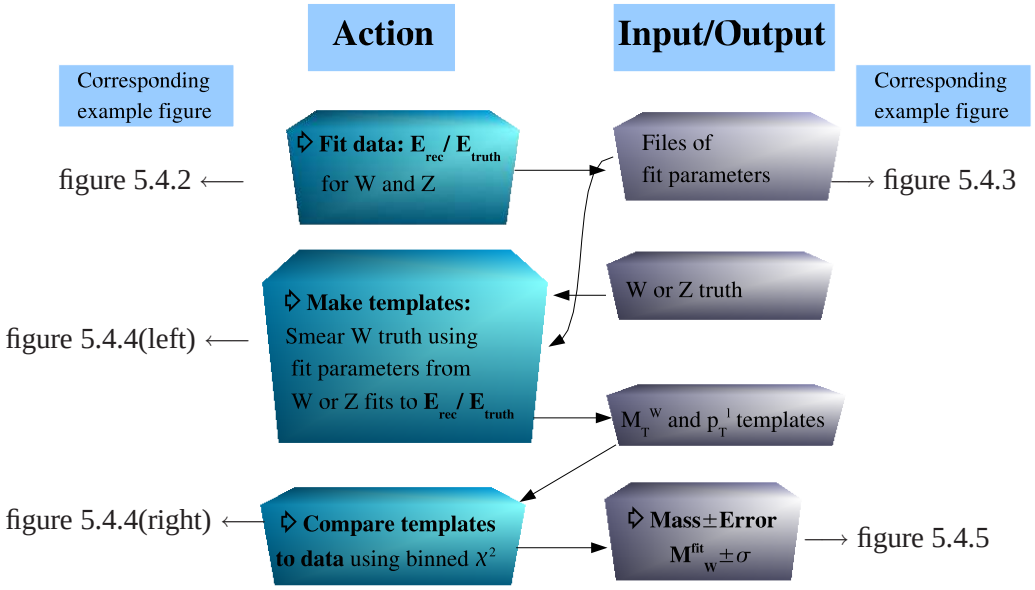

Figure 5.4.1: *Outline of the template fitting procedure.*

5.4.2 Fits to M_W using templates: Validation of the method - electron channel

In this section the electron channel is studied, the detector parameters being determined from fits to E_{rec}/E_{true}, the ratio of reconstructed to true energy of the decay electrons. The fits are performed using the so-called "Crystal Ball" probability density function [Gai82], which aims at describing the result of calorimetric resolution together with upstream energy loss in a single function. It has four parameters and consists of a Gaussian core, and a power-law tail at low energy. Its expression is, up to normalization factors:

$$CB(x) \quad = \quad \begin{cases} e^{-(\frac{x-\alpha}{\sigma})^2}, & x > \alpha - n\sigma \\ (\beta/n - |n| - x)^{-\beta}, & x < \alpha - n\sigma \end{cases} \tag{5.4.1}$$

where $x = E_{rec}/E_{true}$, α is the position of the peak, σ the Gaussian width; n gives, in units of σ, the point of transition between the Gaussian and power-law descriptions, and β is the exponent controlling the tails. The relative normalization of the two components preserves continuity at $\alpha - n\sigma$, up to the first derivative. While not fully satisfactory from a theoretical point of view (the combination of resolution effects and radiation should in principle be given by a proper convolution), it is very effective in describing the observed electron response.
The fits are performed in bins of η and p_T. The angular range $0 < |\eta| < 2.5$ is divided in intervals of size $\Delta\eta = 0.1$. In each interval, fits are done for 10 GeV$< p_T <$ 70 GeV, in intervals $\Delta p_T = 10$ GeV. Figure 5.4.2 shows a number of example fits, at different values of η and p_T. The η dependence of the fit parameters, for 30 GeV$< p_T <$ 40 GeV, is displayed in figure 5.4.3. In the fits, the β parameter was constrained to the range $0 < \beta < 5$. As the examples in figure 5.4.2 illustrate, the β parameter appears to systematically choose values close to its upper bound, while satisfactory fits are still obtained. The main reason for this is the strong correlation between β and n, and the fits indicate that in practice, only one of the two can be fitted.

Therefore, the remaining of the analysis uses a fixed $\beta = 5$, and treat the response functions in terms of α, σ and n only.

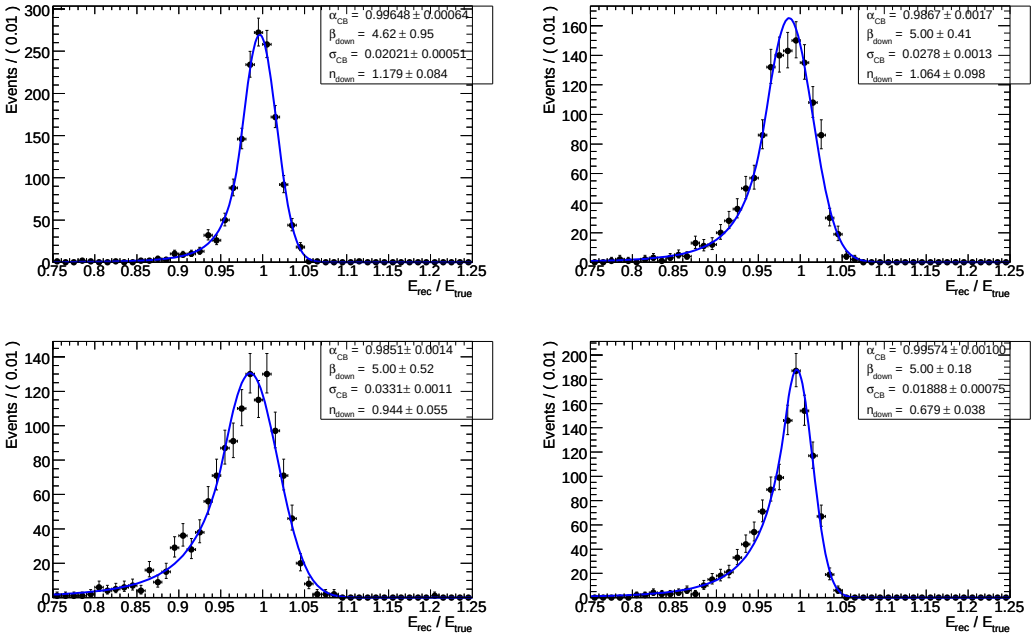

Figure 5.4.2: *Example of detector response functions fitted to* E_{rec}/E_{true}*, for* 30 GeV $< p_T^e <$ 40 GeV*. From upper left to lower right:* $0.4 < |\eta| < 0.5$*,* $0.8 < |\eta| < 0.9$*,* $1.3 < |\eta| < 1.4$*, and* $1.9 < |\eta| < 2.0$*.*

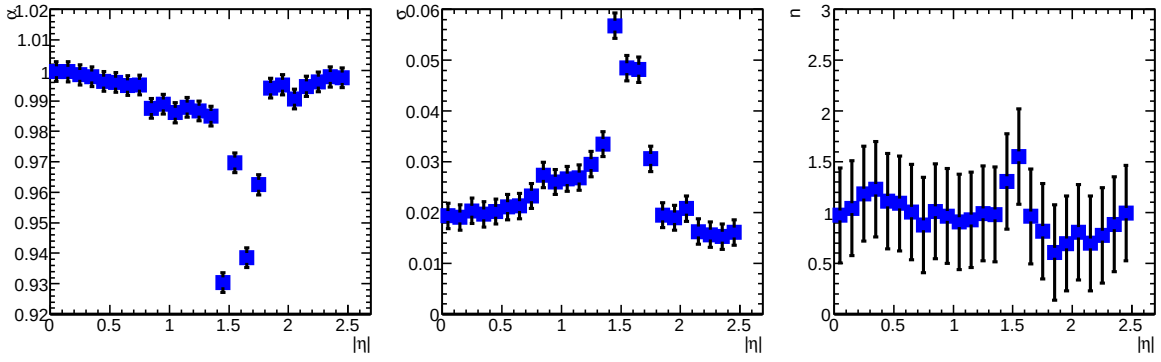

Figure 5.4.3: η *dependence of* α*,* σ *and n, for* 30 GeV $< p_T^e <$ 40 GeV*.*

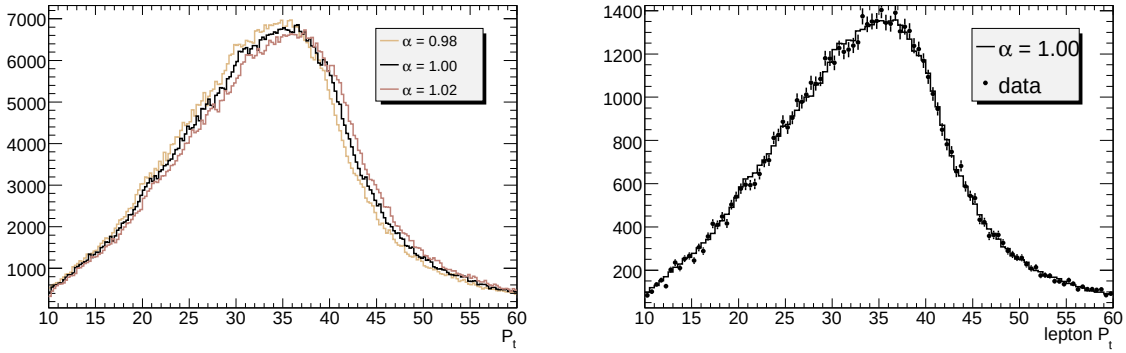

Figure 5.4.4: *Left: Templates obtained at three example mass points, namely* $\alpha = M_W/M_W^{true} = 0.98, 1, 1.02$. *Right: Template for* $\alpha = 1$ *(histogram), compared to the pseudo-data (points).*

The p_T-spectrum templates are produced from generator-level $W \to e\nu$ events, where the electrons are smeared using the above function and parameters according to their kinematic variables. Three example template distributions are shown in figure 5.4.4(left), corresponding to three values of M_W. The number of events used to produce the templates is ten times larger that the fully simulated sample size. Although this limits the impact of statistical fluctuations in the templates on the result, template fluctuations are still visible.

The mass fit is performed using binned χ^2 comparisons between the pseudo-data and the template histograms. Given that all p_T bins contain at least several hundred events, the χ^2 of a given comparison can be defined as:

$$\chi^2 = \sum_{i=1}^{N} \frac{(n_{i,data} - n_{i,template})^2}{\sigma_{i,data}^2 + \sigma_{i,template}^2}, \tag{5.4.2}$$

where the sum is over the histogram bins, and n and σ are the bin contents and their errors, respectively ($\sigma = \sqrt{n}$). Computed as a function of M_W used in the templates, the χ^2 follows the parabola illustrated in figure 5.4.5, which can be used to determine the M_W^{fit} as the vertex and its error, σ, is the interval from the vertex to the point where the parabola is increased by one unit. In practice, this is computed as $1/\sqrt{par(2)}$, where $par(2)$ is the constant of the second degree term in the polynomial. The result obtained is: $M_W^{fit} = 80.468 \pm 0.117$ GeV, to be compared to the input value $M_W^{true} = 80.405$ GeV. The stability of this result is verified by repeating the exercise a number of times, with the detector smearing applied independently in each exercise (i.e., producing independent sets of templates). The distribution of M_W^{fit} has a spread well compatible with the estimated fit uncertainty.

Thus it is concluded that within the statistical sensitivity of the $W \to e\nu$ sample, the current procedure provides an unbiased estimate of M_W.

5.4.3 Sensitivity of M_W^{fit} to the template components

This section quantifies the stability of M_W^{fit} under variations of the assumptions used to produce the templates.

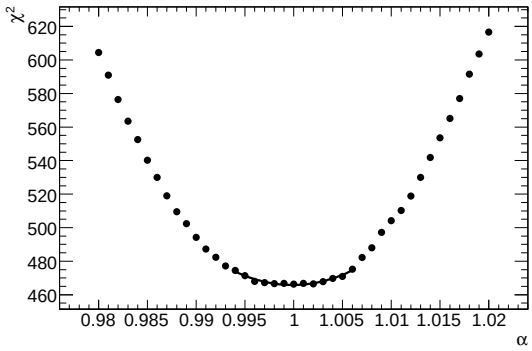

Figure 5.4.5: χ^2 *vs.* $\alpha = M_W/M_W^{true}$*, for the comparisons of pseudo-data and templates described in the text.*

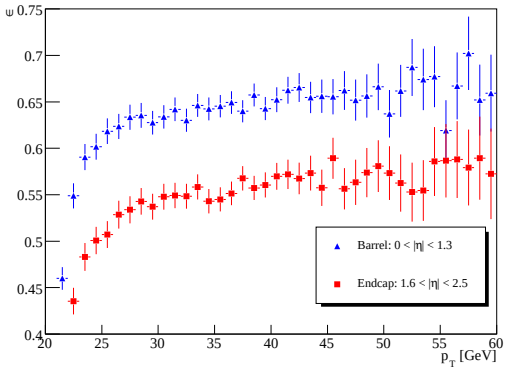

Figure 5.4.6: *Electron reconstruction efficiency as a function of* p_T*, for different regions in* η*. Measured using electrons from* W *decay.*

Efficiency

Distortions in the p_T distribution can be caused by the lepton reconstruction efficiency, in the case where it has a non-trivial p_T-dependence, i.e. $\varepsilon_l = \varepsilon_l(p_T)$. This is the case in the electron channel, as illustrated in figure 5.4.6.

The impact of this p_T-dependence is quantified by taking the pseudo-data as it is, but assuming a flat efficiency in the templates. Since $\varepsilon_l(p_T)$ is an increasing function of p_T, one can expect that the templates will be biased toward lower p_T-values, inducing a positive shift in M_W^{fit}. Performing the mass fit indeed yields $\delta M_W = 360$ MeV (this bias corresponds to a perfectly flat efficiency assumption). Thus the estimated relative bias per percent due to the p_T-dependence of ε_l is:

$$\partial M_W/\partial \varepsilon_l = 3.6 \text{ MeV}/\%. \tag{5.4.3}$$

Note that the analysis only relies on the p_T-dependence of ε_l and not on its absolute value.

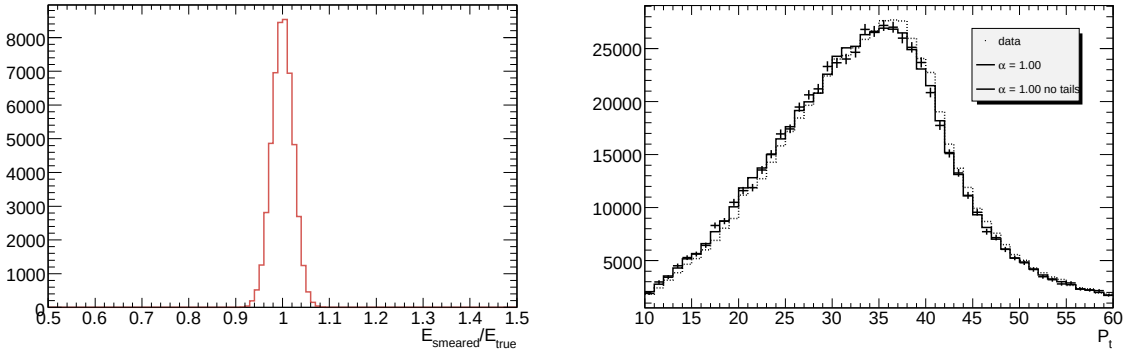

Figure 5.4.7: *Left: Response function at* $0.2 < \eta < 0.3$, $20\ \text{GeV} < p_T < 30\ \text{GeV}$*, removing the non-Gaussian part of the distribution. Right: Pseudo-data (points), compared to templates produced assuming* $M_W = M_W^{true}$*, with non-Gaussian tails included (full line) or not (dashed line).*

Non-Gaussian tails

The impact of non-Gaussian tails is studied as follows. Starting from the detector response parametrization described in section 5.4.2, the tails of the distribution are suppressed by assuming a pure Gaussian response. The parameters describing scale and resolution are kept to their previous value and templates are produced and fitted to data as above.
The procedure is illustrated in figure 5.4.7. The response distribution can be compared to figure 5.4.2 to assess the impact of neglecting the non-Gaussian part of the distribution. As can be seen, the corresponding templates are biased toward higher p_T; thus it is expected, that an underestimation of the tails should imply a negative δM_W.

The resulting bias is $\delta M_W = -555$ MeV, corresponding to an underestimation of the non-Gaussian tails by 100%. By denoting τ the non-Gaussian fraction of the response function and assuming a linear dependence, the bias as a function of the relative error on the tails can be estimated as:

$$\partial M_W / \partial \tau = -5.5\ \text{MeV}/\%. \tag{5.4.4}$$

5.4.4 Comparison of *W* and *Z* events

Before explicitly calibrating detector parameters from Z events and applying them in the M_W fit, it must be verified that this procedure is indeed justified - i.e. the portability must be verified. To this end, the detector response fits as described in section 5.4.2 are performed on the $Z \to ee$ sample, obtaining a map of the response parameters α, σ and n as a function of η and p_T of the electrons.
A first check is to compare the obtained values of the fit parameters to those extracted from the W sample. This is illustrated in figure 5.4.8. Agreement is found within the statistical sensitivity throughout the analyzed electron phase space, for all parameters. Thus it is expected that templates produced using detector response to Z events will provide an adequate description of W events.

A M_W fit is performed next. Templates are produced from generator-level $W \to e\nu$ events, smeared according to detector performance based on Z events. The resulting distributions are shown in figure 5.4.9; good agreement is observed. The result of the fit is $M_W^{fit} = 80.567 \pm 0.118$ GeV, compatible

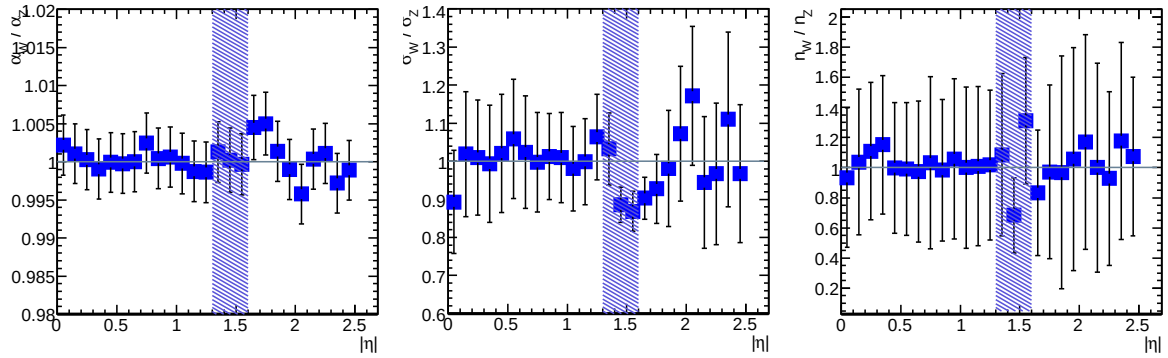

Figure 5.4.8: *Ratio of the fitted values of α (left), σ (middle) and n (right), between W and Z events. Each histogram represents the η dependence of the parameter, for* 30 GeV $< p_T^e <$ 40 GeV.

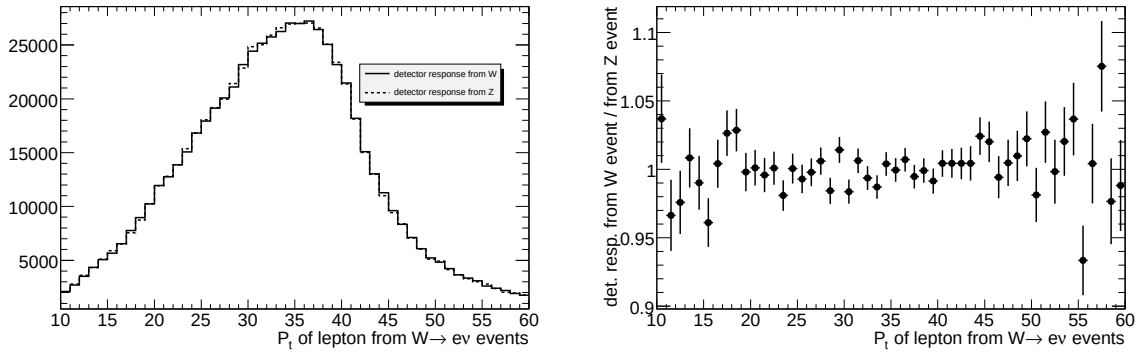

Figure 5.4.9: *Left: Templates obtained for $\alpha = M_W / M_W^{true} = 1$, with detector performance obtained from W events (full line) and from Z events (dashes). Right: Ratio of the left-hand side histograms.*

with the input value $M_W^{true} = 80.405$ GeV.

5.5 Fitting the *W* mass with templates - muon channel

5.5.1 *W* decays in the muon channel

In many respects, the muon channel yields similar results as those shown for the electron channel and focus in this section lies primarily on the differences. In addition, a template fit of the M_T^W distribution is described.

The functional dependence of scale and resolution for the M_W fit is the same in the muon channel as for the electron channel. The muon momentum resolution is generally slightly worse, and whereas the electron resolution improves with p_T, the converse is true for the muon resolution. Figure 5.5.1 shows four examples of the momentum ratio distributions p_T^{rec}/p_T^{true} for muons - two from W events and two from Z events. As can be seen, the shapes can be modeled well with a core bifurcated Gaus-

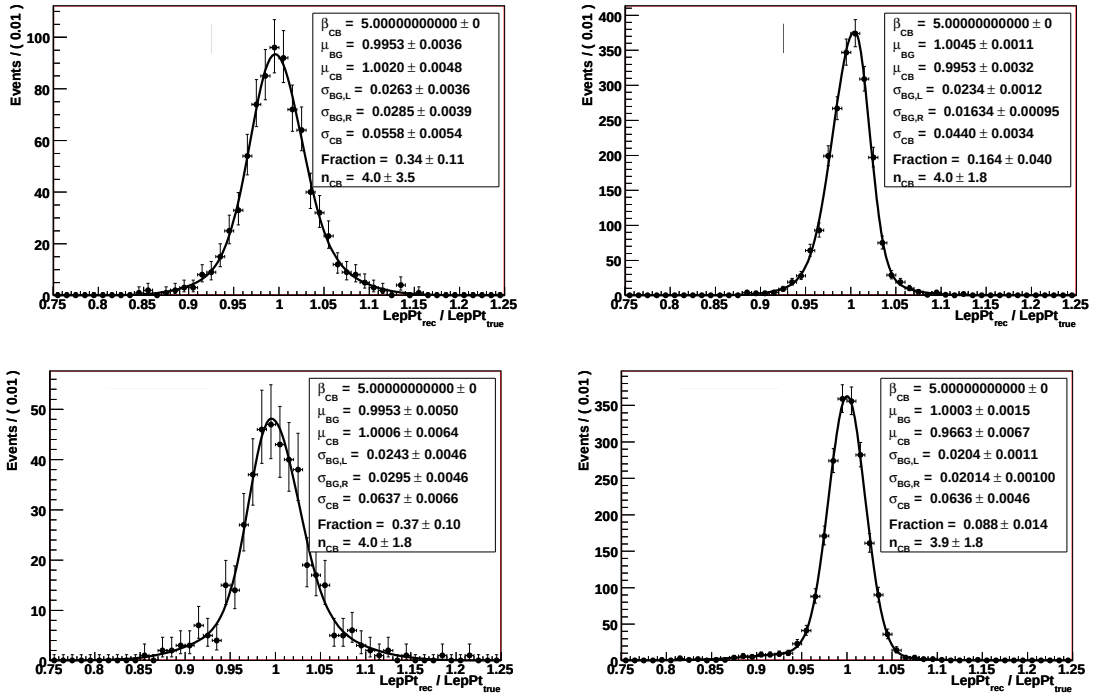

Figure 5.5.1: *Distributions of transverse momentum ratios p_T^{rec}/p_T^{true} for muons from W (top) and Z (bottom) decays at* $1.5 < |\eta| < 1.6$ *(left) and* $0.5 < |\eta| < 0.6$ *(right) in the momentum range 10-20* GeV *(left) and 30-40* GeV *(right). Abbreviations: CB: Crystal Ball (equation 5.4.1), BF: Bifurcated Gaussian, L: Left, R: Right.*

sian[4] distribution (BF), describing the general muon bias and resolution, complemented by an out-lier Crystal Ball function (CB) accounting for the muons, which encounter parts of the detector with poor muon spectrometer coverage and increased material, resulting in a slightly degraded resolution.

To check the portability, the fitted constants are again compared between *W* and the *Z* events, as can be seen in figure 5.5.2. In general, the resemblance is satisfactory although some degree of discrepancy is observed. A number of crosschecks are performed to validate the fitting- and smearing procedure:
- p_T and η binning effects.
- Increased template statistics.
- Taking into account uncertainty on fit-parameters when defining smearing functions.
- Fit smearing distributions and compare with original fit.

Some results from these exercises are shown in Appendix A. Here it suffices to state that the studies did not reveal significant problems in the method used.

Figure 5.5.3 shows the results of the template fitting and verifies the unbiasedness of the fitting procedure. The results are 80.400 ± 0.106 GeV when smearing using the detector response from *W* and 80.541 ± 0.105 GeV when using the *Z* detector response function. Both are in compatible the input value of 80.405 GeV.

Unlike the electron case, the muon reconstruction efficiency does not vary significantly over the mo-

[4] An asymmetric Gaussian with two widths: One accounting for events on the right-hand side of the peak, and one accounting for events on the left-hand side.

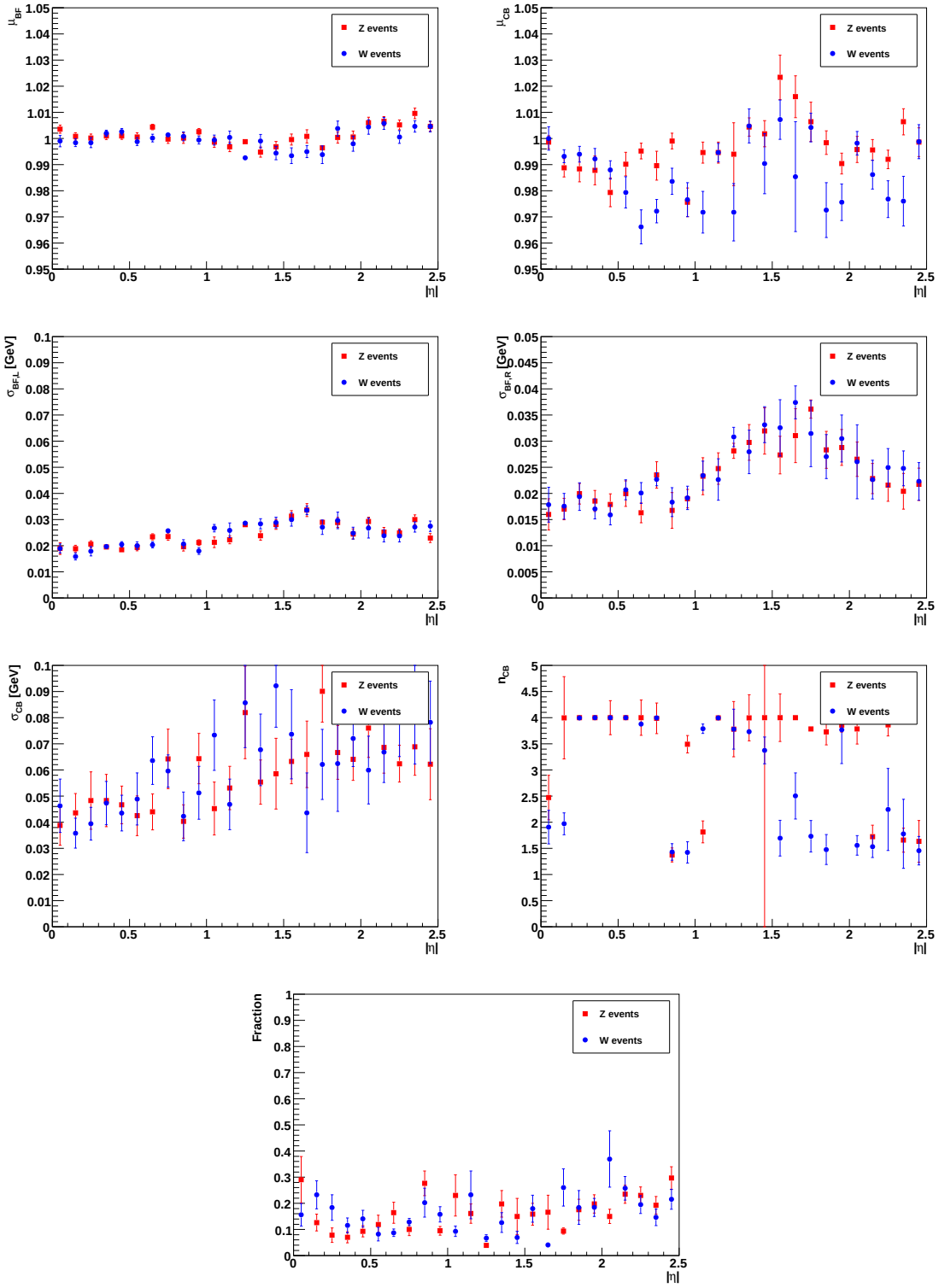

Figure 5.5.2: *Comparison of fit parameters between W (blue) and Z (red) events for muons in the momentum range* 30 GeV $< p_T <$ 40 GeV *in 25 bins of* $|\eta|$.

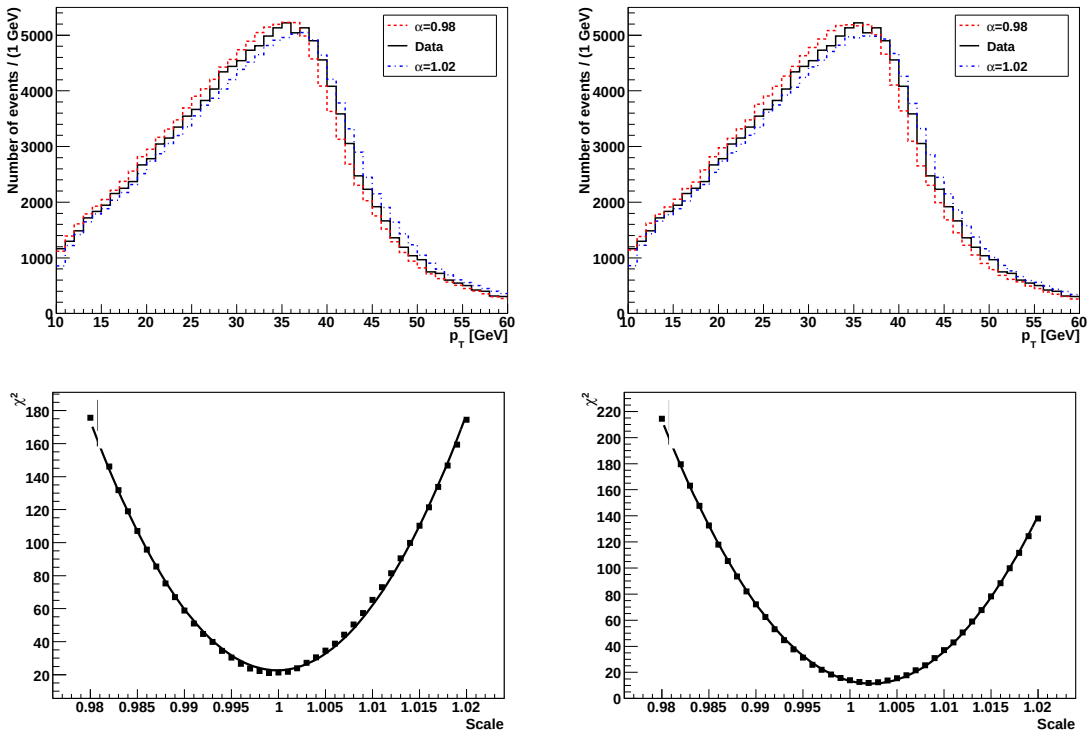

Figure 5.5.3: *Top: Reconstructed p_T^l distributions for data (black) along with templates produced with the W mass hypothesis* 78.792 GeV *(red) and* 82.008 GeV *(blue). The templates have been smeared using the detector response from W (left) and Z (right). Bottom: χ^2 value of fitting templates to the reconstructed distribution as a function of the template's W mass hypothesis (compared to the nominal mass). Left plot is smeared using the W smearing functions and right plot is smeared using those from Z events.*

mentum range of interest. As can be seen from figure 5.5.4, the efficiency is approximately constant above 10 GeV, varying only slightly between the barrel ($\varepsilon = 95.8\%$) and end-cap ($\varepsilon = 94.3\%$) region, due to increase of material. As the reconstructed muons are required to have a momentum above 20 GeV, the efficiency is essentially constant.

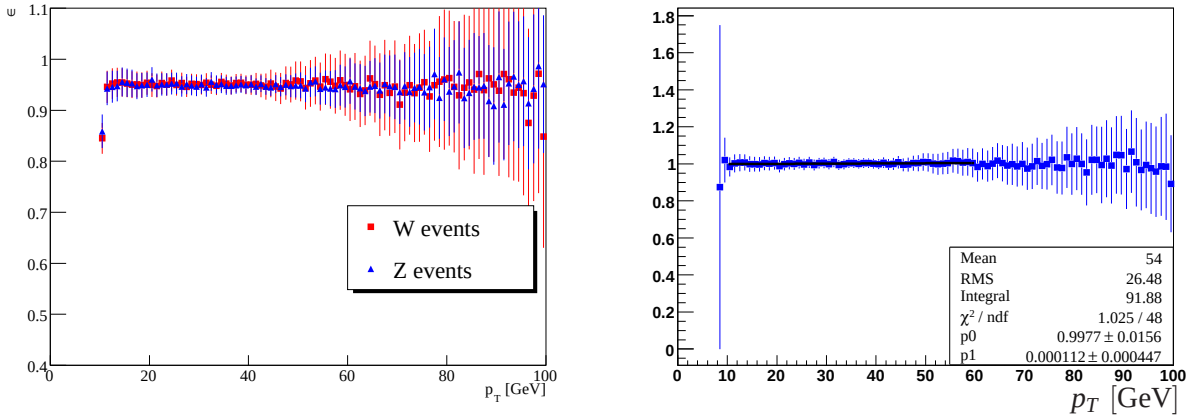

Figure 5.5.4: *Left: Muon efficiency as a function of p_T for W (red) and Z (blue) events. The hypothesis of a flat probability in the range* $10-60$ GeV *has been tested to be valid. Right: Muon efficiency ratio between W and Z events. No p_T dependence is seen, and a linear fit yields a slope of* (0.00011 ± 0.00045)*, consistent with zero.*

The flatness of the efficiency is expected to be retained up to several hundred GeV, where radiative losses grow larger than those due to ionization. Using the "tag-and-probe" method [DØ00a], the hypothesis of a flat muon efficiency is tested. The uncertainty in the linear fit translates for 15 pb^{-1} into a systematic error of: $0.00045\ \text{GeV}^{-1} \cdot 50\ \text{GeV} \cdot 100\% \cdot 3.6\ \text{MeV}/\% = 8\ \text{MeV}$, which is much less than in the electron channel, as expected.

By comparing figures 5.4.2 and 5.5.1 it is clear that the muon p_T^{rec}/p_T^{true} ratios have less events in the tail as compared to the corresponding electron distributions E_{rec}/E_{true}. Thus the non-Gaussian tail is smaller in the muon case, and to estimate the impact of non-perfect modeling, the electron result, $\partial M_W/\partial\tau = -5.5\ \text{MeV}/\%$, can be used as an upper limit of the effect.

5.5.2 Fitting the transverse *W* mass

Having tested the template fitting of the p_T^l distribution, this section concerns to the M_T^W distribution. In addition to the lepton transverse momentum residuals, this fit requires residuals for the missing momentum. In terms of $\not{E}_T$ the detector response is expected to depend on the total transverse hadronic activity, $\sum E_T(\text{hadrons})$, (i.e. total and not vectorial sum) and the recoil momentum perpendicular to the direction of the leptons (cf. figure 5.2.1).
Dividing the hadronic activity into 10 bins in the range [0;200] GeV and the perpendicular recoil momentum into 10 bins in the range [0;40] GeV, each with an additional overflow bin, yields a satisfactory description of the missing momentum response. An example of the residual distributions can be found in figure 5.5.5. The distributions are well described by two Gaussian distributions with a common mean, and unlike the lepton momentum ratios, the missing momentum residuals are not expected nor observed to have asymmetric tails.

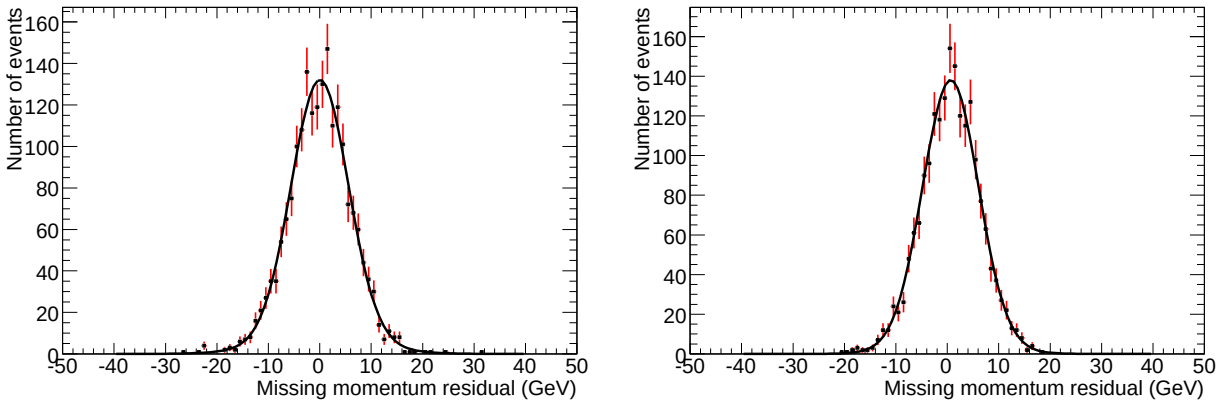

Figure 5.5.5: *Distribution of* $\not\!\!E_T$ *residuals,* $\not\!\!E_T{}^{rec} - \not\!\!E_T{}^{true}$*, for* W *decays with a recoil momentum parallel (left) and perpendicular (right) to the lepton axis in the range [8;12]* GeV *and a hadronic activity in the range [20;30]* GeV*. The fitting function describes the distributions well* (χ^2/ndf *in all* ($\sum E_T(hadrons)$, p_T^l) *bins is below 2.*

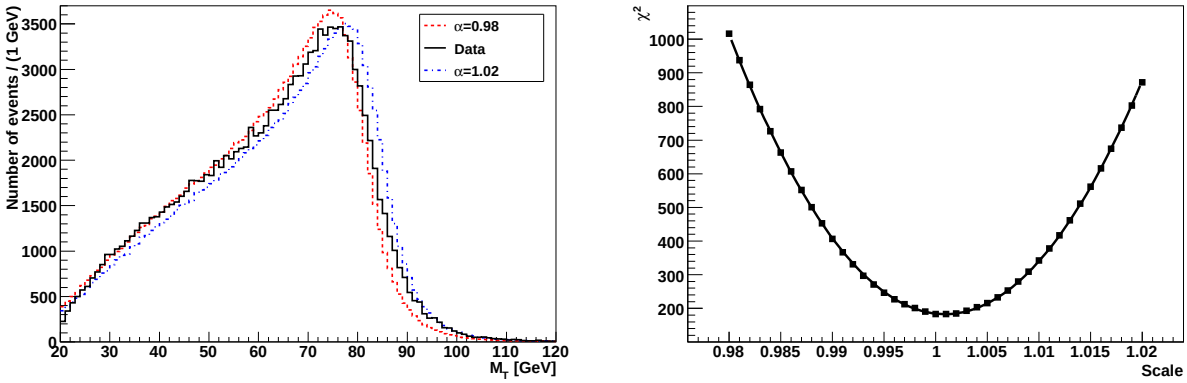

Figure 5.5.6: *Left: Reconstructed* M_T^W *distribution (black) along with templates produced with the* W *mass hypothesis* 78.792 GeV *(red) and* 82.008 GeV *(blue). Right:* χ^2 *value of fitting templates to the reconstructed distribution as a function of the template's* W *mass hypothesis (compared to the nominal mass). The fit yields* 80.421 ± 0.059 GeV *in agreement with the input value of* 80.405 GeV*.*

Using the above modeling of the missing momentum response, M_T^W templates are produced and the unbiasedness of the fit is tested. Unlike the lepton case, no additional efficiency curve has to be included, as the missing momentum is calculated for every event. As can be seen from figure 5.5.6, the M_T^W templates match the reconstructed distribution, and the fit is unbiased, giving a fitted value of $M_W^{fit} = 80.421 \pm 0.059$ GeV compared to an input value of $M_W^{true} = 80.405$ GeV.

5.5.3 Fitting the transverse *W* mass using the *Z* events for calibration

In the case of transverse mass fitting, the detector response is not exactly the same for W and Z events. The discrepancy is in the missing momentum perpendicular to the lepton direction, where the residual for Z events is slightly biased toward negative values in most configurations (see figure 5.5.7).

While the missing momentum residual yields the same result for Z and W in the direction parallel to

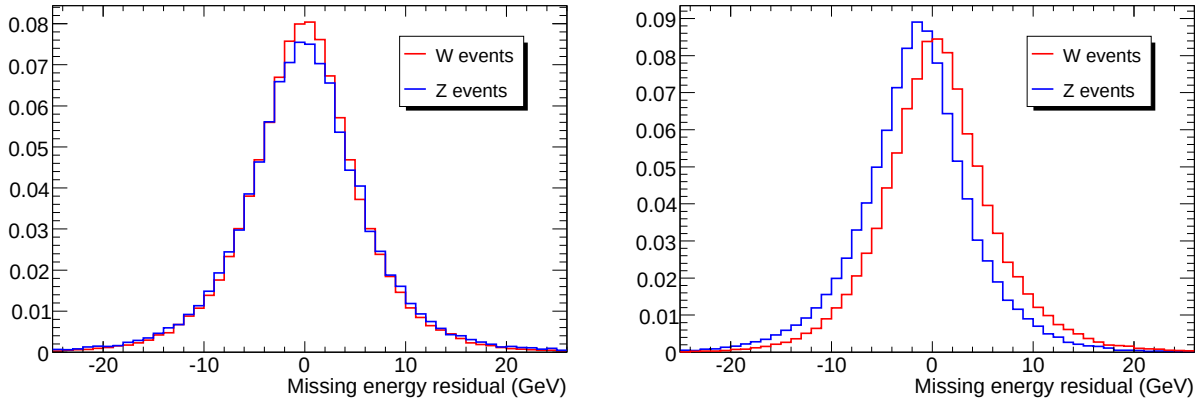

Figure 5.5.7: *Distribution of $\not\!\!E_T$ residuals, $\not\!\!E_T{}^{rec} - \not\!\!E_T{}^{true}$, parallel (left) and perpendicular (right) to the lepton axis for W and Z decays.*

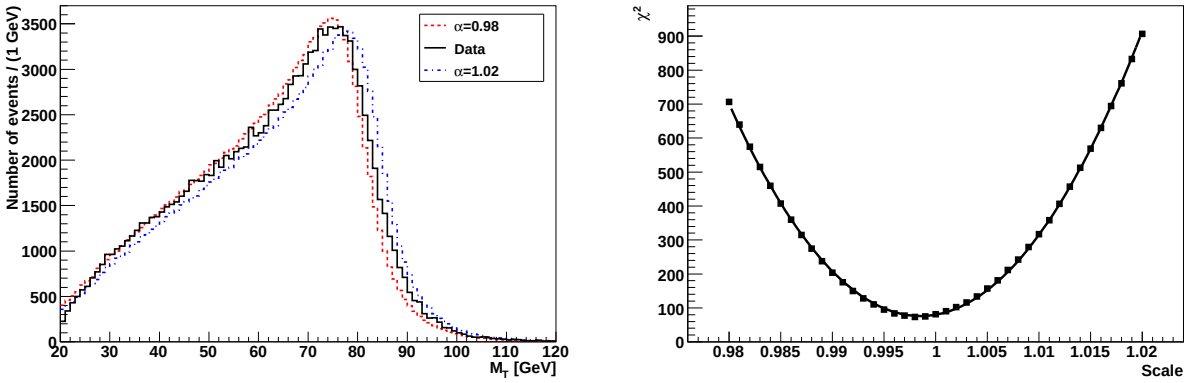

Figure 5.5.8: *Left: Reconstructed M_T^W distribution (black) along with templates produced with the W mass hypothesis* 78.792 GeV *(red) and* 82.008 GeV *(blue). Right: χ^2 value of fitting templates to the reconstructed distribution as a function of the W mass hypothesis. The fit yields* 80.347 ± 0.060 GeV*, which is one standard deviation from input value of* 80.405 GeV*.*

the muon, this is not the case in the perpendicular direction. Though the shape of the two residuals are compatible, their means are shifted. The shift is thought to be caused by the missing momentum algorithm, which is not capable of separating the leptons from the hadronic recoil to the required level of precision. This results in a difference between the asymmetric W events and the more symmetric Z events. Since the resolution is dominated by the hadronic recoil, this does not change between the W and the Z distributions. The parallel direction is unaffected, as the lepton momentum does not affect this direction.

This important issue is the topic section 6.3. Here a procedure is presented to assess and quantify the bias, allowing the $\not\!\!E_T$ scale and resolution in Z and W to be compared despite the significant bias.

Postponing the dealing of the problematic issues and proceeding as normal yields the result shown in figure 5.5.8, which is based on the Z response functions. The fit yields 80.347 ± 0.060 GeV compared to an input value of 80.405 GeV. Incidentally, no significant bias is observed. However, a better calibration of the missing momentum scale is needed.

5.6 Statistical uncertainty as a function of fitting range

As previously stated, the sensitivity to the W mass comes from the Jacobian edge in the fitting distribution. Generally the Jacobian edge is slightly sharper for the M_T^W distribution (see figure 5.3.3), yielding a smaller statistical uncertainty. To test the influence of the fitting range, three different fitting ranges have been tested for the p_T^l and M_T^W distributions in the $W \to \mu\nu$ sample. Since the typical M_T^W values are double that of the p_T^l values, the size of the fitting range is chosen to be double. The result is shown in table 5.6.1. As can be seen this table, the p_T^l statistical uncertainty changes of about 30%

Transverse lepton momentum, p_T^l		Transverse W mass, M_T^W	
Fitting range [GeV]	$\sigma_{\text{stat.}}$ [MeV]	Fitting range [GeV]	$\sigma_{\text{stat.}}$ [MeV]
10-70	95.5	20-140	58.7
20-60	106.2	40-120	59.1
30-50	131.0	60-100	61.5

Table 5.6.1: *Statistical uncertainty as a function of fitting range for p_T^l and M_T^W fits. The uncertainties are the result of the sharpness of the Jacobian edge (see figure 6.4.3).*

with fitting range, while the M_T^W statistical uncertainty is essentially insensitive to the range, and generally somewhat lower as expected. Considering that most systematic effects (such as backgrounds, electron calibration and efficiency, etc.) are largest at low momenta, a sacrifice in p_T^l statistical uncertainty will be countered by a gain in systematic uncertainty. Expanding the fitting range to higher momenta, e.g. 30-100 GeV yields a statistical uncertainty of 107 MeV, which means that some of the statistical sensitivity can be regained. For the M_T^W fit a narrow range is surely preferable. However, it is not possible to quantify the gain, and optimize the fitting range, until all systematic uncertainties have been calculated.

Chapter 6

Calibration using Z events

6.1 Lepton scale and resolution

The Z boson resonance has been measured very precisely at the LEP during the 90's [ADL$^+$06]. The Z boson mass and width can be exploited as an absolute reference to determine as precisely as possible the detector energy scale, its linearity and resolution.

The basic method is rather simple, and consists in comparing the position and width of the observed mass peak in reconstructed di-lepton events with the Z boson parameters. A shift of the observed position of the mass peak, with respect to the nominal Z peak position, is corrected for by scaling the detector response, hence determining the detector absolute scale; the additional spread of the mass distribution, as compared to the natural Z boson width, is used to estimate the resolution.

The high statistics expected at the LHC however impose a number of refinements. First, the scale obtained as above is averaged over the lepton kinematic spectrum, whereas an energy-dependent scale is needed for a correct description of the Jacobian distributions in W events. Secondly, lepton energy resolution effects induce a small but non-negligible shift in the di-lepton invariant mass distribution. This shift needs to be subtracted before converting the scale measured from the Z invariant mass distribution into the scale used to describe the Jacobian distributions in W events. The resulting method has been described in detail in [BB06], and is summarized below.

Impact on M_W from the lepton scale, α_l and resolution, σ_l

Using the electron transverse momentum as observable, templates with varying scale and resolution are produced. For each choice of the lepton scale α_l, the χ^2 parabola is fitted using the fixed set of templates. By this, the relation between the fit result, expressed as $\delta M_W \equiv M_W^{fit} - M_W^{true}$ and the relative scale $\delta_{rel}\alpha_l \equiv \frac{\alpha_l^{fit} - \alpha_l^{true}}{\alpha_l^{true}}$ is determined, as illustrated in figure 6.1.1(left).

As expected for small systematic effects, the relation between the size of the systematic effect and its impact on the W mass measurement can be satisfactorily described by a linear fit. Not surprisingly, a strong dependence is found as the slope of the fit:

$$\frac{\partial M_W}{\partial_{rel}\alpha_l} \sim 800 \text{ MeV}/\%, \tag{6.1.1}$$

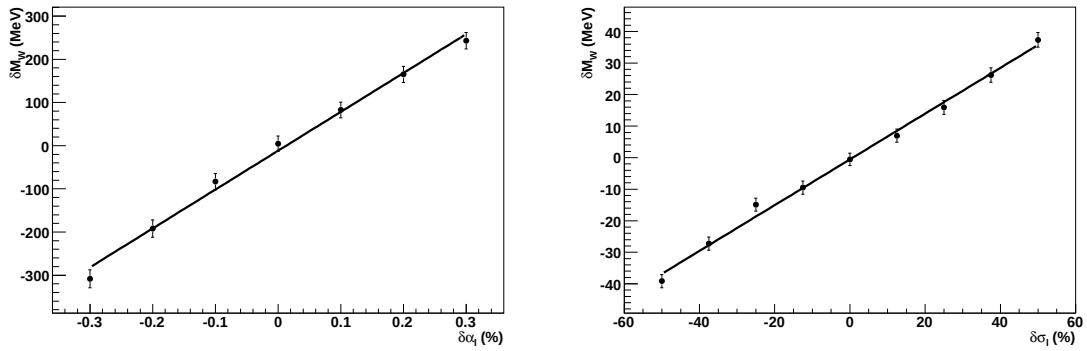

Figure 6.1.1: *Left: Bias on M_W, $\delta M_W = M_W^{fit} - M_W^{true}$, as a function of the relative bias on α_l, $\delta\alpha_l = (\alpha_l^{fit} - \alpha_l^{true})/\alpha_l^{true}$. Right: bias on M_W as function of the resolution bias, $\delta\sigma_l = (\sigma_l^{fit} - \sigma_l^{true})/\sigma_l^{true}$. A linear dependence is observed in each case, with $\partial M_W/\partial_{rel}\alpha_l = 800$ MeV/% and $\partial M_W/\partial_{rel}\sigma_l = 0.8$ MeV/% respectively.*

Note that this result means that the error inflicted on the W mass is directly proportional to the average lepton scale error (800 MeV/% $\approx M_W/100\%$). The effect of the resolution is studied by varying the resolution parameter in the pseudo-data while fitting to templates with fixed resolution and collecting the corresponding values of M_W^{fit}. This provides the relation between the resolution bias and the resulting bias on M_W:

$$\frac{\partial M_W}{\partial_{rel}\sigma_l} = 0.8 \text{ MeV}/\% \tag{6.1.2}$$

as illustrated in figure 6.1.1(right).

6.2 Lepton performance determination *in situ*

In this section the algorithms to calibrate the lepton response using Z events are reviewed, and the results are fed back to the M_W fit.

The calibration of the absolute energy/momentum[1] lepton scale plays a central role, as it is the largest systematic uncertainty and the starting point of all other calibrations.

To first order, a single average lepton scale factor, defined as $\alpha = E_{\text{Reco}}/E_{\text{Truth}}$, independently of η and p_T, can be obtained by demanding that the reconstructed Z peak matches its known mass.

6.2.1 Average scale and resolution

First a global scale analysis is performed to verify whether neglecting possible non-linearities in the response can be expected to induce a significant bias. In the following, only to the electron channel is considered. Fixing the non-Gaussian tail parameters to $n = 0.8$ and $\beta = 5$, as expected from the studies performed in section 5.4.3, templates of the Z resonance are produced by varying the electron scale and resolution. These response parameters are applied to generator-level electrons as before. The templates are then fitted to the fully simulated Z peak. A very good fit is obtained, as shown in

[1] These two terms cover the same aspect, but will generally be used about electrons and muons, respectively.

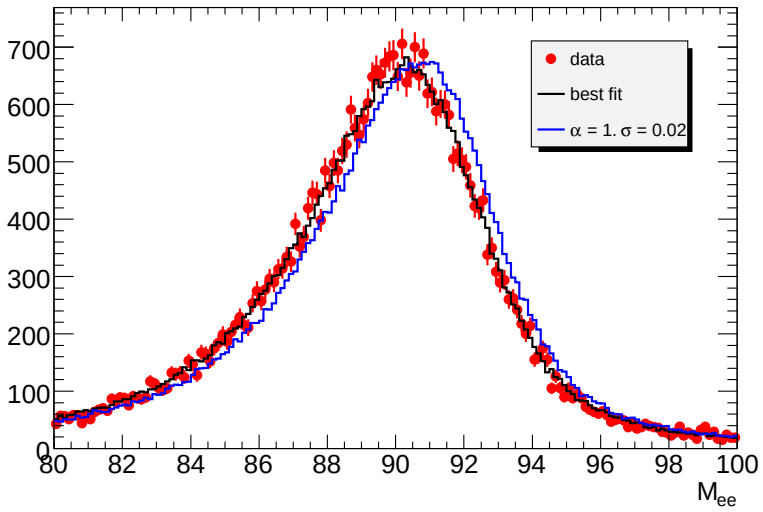

Figure 6.2.1: *Fully simulated data (dots with error bars), compared to an example resonance template with* $\alpha = 1$, $\sigma = 0.02$, *and to the best fit.*

figure 6.2.1. An average scaling factor of $\alpha = 0.9958 \pm 0.0003$, and an average relative resolution of $\sigma = 0.0207 \pm 0.0003$ provide a satisfactory description of the resonance.

The precision of the fit corresponds to $\mathscr{L} = 200$ pb^{-1}.

While this assures the correct lepton scale and resolution for Z events, the energy scale obtained in this way might not apply to W events. Because of non-linearities and non-uniformities, the different p_T and η distributions in W and Z events can possibly introduce significant bias.

6.2.2 Differential calibration

If needed, an upgrade to a differential calibration can be performed, which contrary to the average calibration includes variations in energy/momentum, η, and/or ϕ. The key ingredients to such a calibration are:

- The precise knowledge of the Z mass, width, and decay kinematics.
- The overlap in p_T and η of the decay leptons (cf. figure 6.2.3).
- The very large sample of Z bosons that will be produced at the LHC.

The calibration uses a large sample of reconstructed $Z \to \ell\ell$ events along with a corresponding simulated sample (representing the knowledge of the Z line-shape). Through a comparison of the two in bins of the variables of interest (p_T, η, and ϕ) one can extract the scale and resolution in each of these bins.
By considering the scale and resolution variations in p_T, one can obtain the correct parameters for the (largely overlapping) W region from the Z region of p_T, hence securing linearity of the lepton scale.

For each event the two leptons are assigned to bins i and j (choosing $i \geq j$) according to energy / momentum, η, and/or ϕ. Based on the lepton bins, events are divided into categories (i, j). For each category (i, j), the reconstructed sample is compared to the known Z line-shape (obtained from the corresponding simulated sample), and a Z mass resolution function R_{ij} is obtained from requiring that its convolution with the theoretical line-shape matches the reconstructed distribution (see equation 6.2.1). Each of these Z mass resolutions R_{ij} are the direct result of combining two lepton momentum resolutions R_i and R_j:

$$f(M_Z)_{ij}^{\text{Reco}} \;=\; f(M_Z)_{ij}^{\text{Truth}} \otimes R_{ij}, \qquad R_{ij} \;=\; R_i \otimes R_j \tag{6.2.1}$$

The complicated lepton scale and resolution calibration can thus be split into two parts, which both saves computing time and allows for intermediate checks and changes. Given N lepton bins and thus lepton resolution functions to determine, there are $N \times (N+1)/2$ Z mass resolution functions, and thus the over-constrained system can be solved by a global χ^2 fit. This calibration procedure is illustrated in figure 6.2.2. Because of the non-zero p_T of the W and Z bosons (and to a certain extent

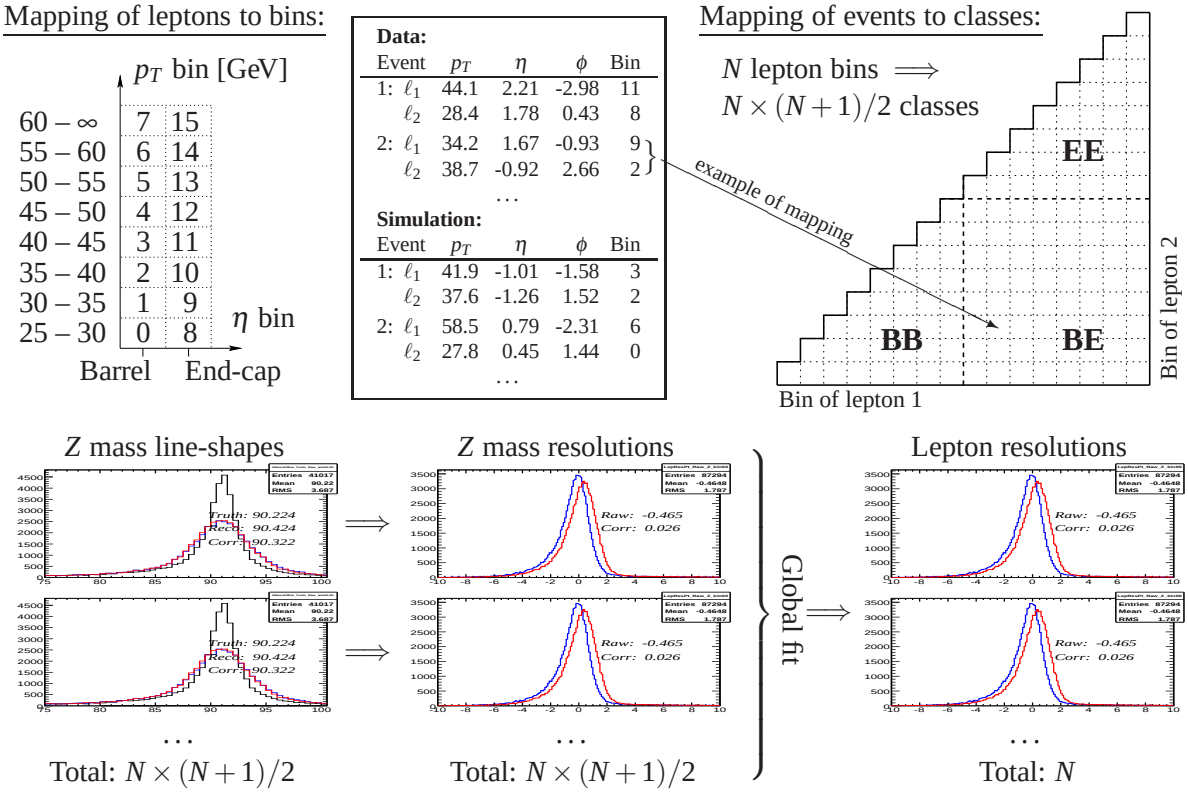

Figure 6.2.2: *Illustration of the lepton detector response calibration. Events from data/simulation (box) are divided into categories (squares top right) according to the reconstructed/truth p_T and η of the two leptons, here eight p_T bins and two η bins (barrel (**B**) and end-cap (**E**)), as demonstrated (top left). For each category a Z mass resolution function (bottom middle) is determined from folding it with the simulated distribution to match the reconstructed one (bottom left). Finally, lepton bias and resolution parameters are determined for each of the $8 \times 2 = 16$ lepton bins, by fitting the $16 \times 17/2 = 136$ Z mass resolutions, which each is a result of the individual lepton resolutions (bottom right).*

also their widths), the correlation between p_T and η is diluted. This allows for a determination of the detector response for all combinations of p_T and η, and a large overlap between the high statistics

calibration constants determined with Z bosons and used for W bosons. The overlap in p_T and η is shown in figure 6.2.3.

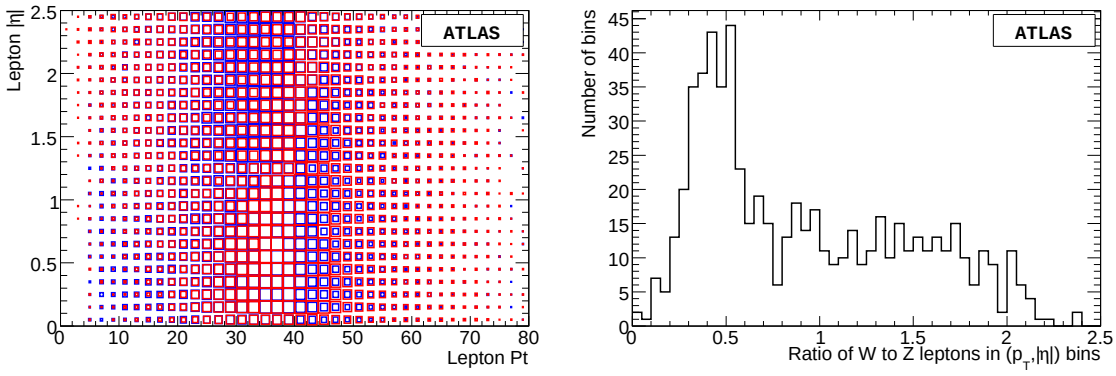

Figure 6.2.3: *Left: η versus p_T for muons of W (blue) and Z (red) decays (normalized to the same number of events). Right: The ratio between the content of the (η, p_T) cells of the W and Z histogram on the left-hand side. Note that there is no region in phase space where the leptons of the W and Z events are disjunct - i.e. the Z events can be used for calibration in the full phase space, but of course the statistics relative to the W statistics differs depending on η and p_T.*

A simplified version of the above analysis has been performed, with the aim of obtaining not the full resolution functions, but simply their means, which corresponds to the scale (i.e. possible biases). This means that the resolution functions R in equation 6.2.1 reduces to calibration constants. The result of the calibration is shown for both electrons and muons in figure 6.2.4, along with the scales obtained from the truth information.
As can be seen from the figure, the simplified calibration yields the correct scales in general. Some fluctuations around the expected values is seen, but this is possibly the result of not conducting the full calibration, which includes the full shapes of the distributions, and not just their means. Curiously, the electrons and muons in both barrel and end-cap seem to have the same scale offset and structure as a function of p_T.

For the present analysis, the outlined procedure for differential in situ calibration has not been attempted, it is presented as a possible extension needed for the actual M_W measurement in ATLAS.

6.3 Recoil scale and resolution

The W and Z bosons are produced similarly and thus one expects the main features of remaining part of the event (i.e. the underlying event) to be alike on a statistical basis[2]. For this reason one can study the recoil scale and resolution in fully reconstructed Z events, and apply the results to W events after performing the relevant verification. QCD events (minimum bias and di-jet) will on average have vanishing $\not{E}_T$, which can also be used as a cross check of the hadronic detector response.

[2]One obvious difference is, the different phase space available, ultimately caused by the difference in the W and Z boson masses.

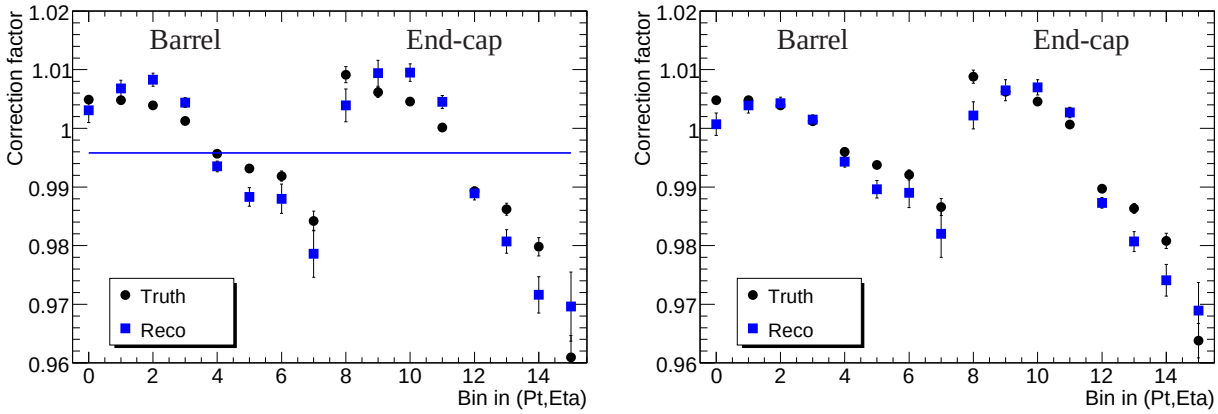

Figure 6.2.4: *Lepton scale constants for electrons (left) and muons (right) as obtained from simplified calibration to the Z peak (blue circles) and from truth (black squares). The first eight bins are scale constants for leptons of increasing p_T reconstructed in the barrel, while the last eight are for those in the end-cap (see text). The result is in good agreement with average scale of* 0.9958 ± 0.0003 *(indicated by blue line in left plot) found in section 6.2.1.*

The main conceptual difference with respect to the lepton scale calibration is, that for $\not{E}_T$ there is no immediate overlap between the W and Z case, whereas for the transverse lepton momentum the overlap is significant.

To enforce an overlap between $\not{E}_T$ in W and Z events and thus give a "handle" to the calibration, $Z \rightarrow ee$ events are considered, artificially removing a lepton, here an electron.

As a first naive attempt the electron removal is performed offline - simply by removing the four vector of an electron at the analysis level (i.e. after the event reconstruction). The procedure is depicted in figure 6.3.1. As expected the result of the removal shows the appearance of a significant $\not{E}_T$ in the "$Z \rightarrow e\nu$" event. The small and more or less randomly oriented existing $\not{E}_T$ vector has been added to the p_T of the removed electron and the result is labeled as: *EtMiss_mod* in figure 6.3.1.
Assuming that the $\not{E}_T$ calculation is indeed unbiased, one can in a straightforward way predict the impacts of the $\not{E}_T$ scale and resolution on the W mass measurement. In this simplified situation, the systematic effects are given by the uncertainty of the mean and width of *EtMiss_mod* residual which in turn are determined solely by the Z statistics.

Repeating the procedure pictured in figure 6.3.1 for various fractions of the full Z sample statistics gives the uncertainties of the peak position and resolution depending on the Z statistics. The points scales as $1/\sqrt{\#Z}$ as expected and are shown in figure 6.3.2 along with a fit.

Assuming an unbiased $\not{E}_T$ calculation, the expected error on the W mass introduced by the imperfect (but unbiased) $\not{E}_T$ calculation is obtained by scaling figure 6.3.2 to 10 fb^{-1} which yield a relative precision of: $\delta_{rel}\alpha_{\not{E}_T} = 5 \cdot 10^{-5}$ and $\delta_{rel}\sigma_{\not{E}_T} = 6 \cdot 10^{-4}$ respectively.

The next step is to map the uncertainties of the $\not{E}_T$ mean and resolution into derivatives, which can be used to estimate the impact on the W mass due to $\not{E}_T$ scale and resolution. This is done by the template fitting based on templates of various scales: $\delta\alpha_{\not{E}_T}$ and resolutions: $\delta\sigma_{\not{E}_T}$ respectively. The result is shown in figure 6.3.3.

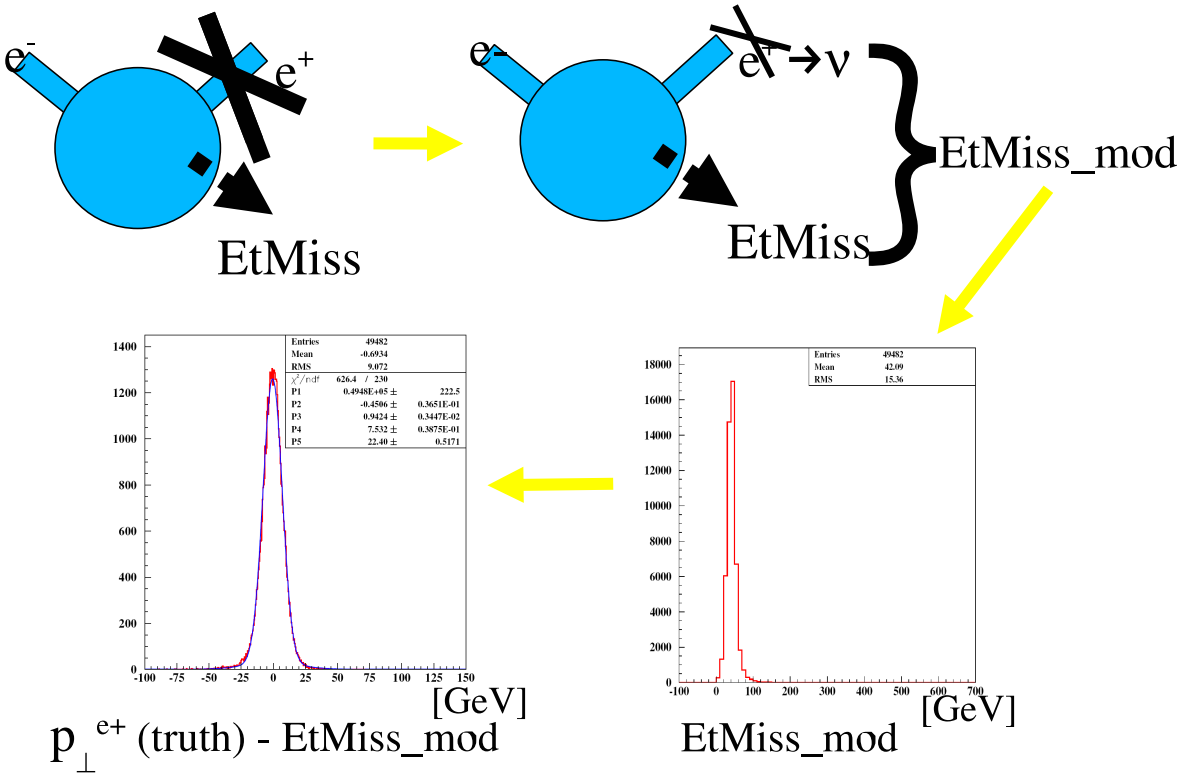

Figure 6.3.1: *An electron of a $Z \rightarrow ee$ event is removed and the corresponding transverse momentum is added to the missing energy.*

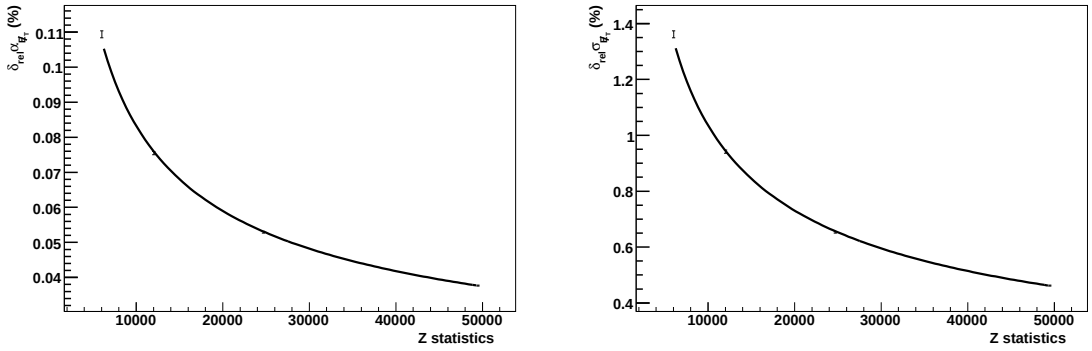

Figure 6.3.2: *Left: statistical sensitivity to $\alpha_{\not{E}_T}$, as a function of the accumulated Z statistics. Right: statistical sensitivity to $\sigma_{\not{E}_T}$.*

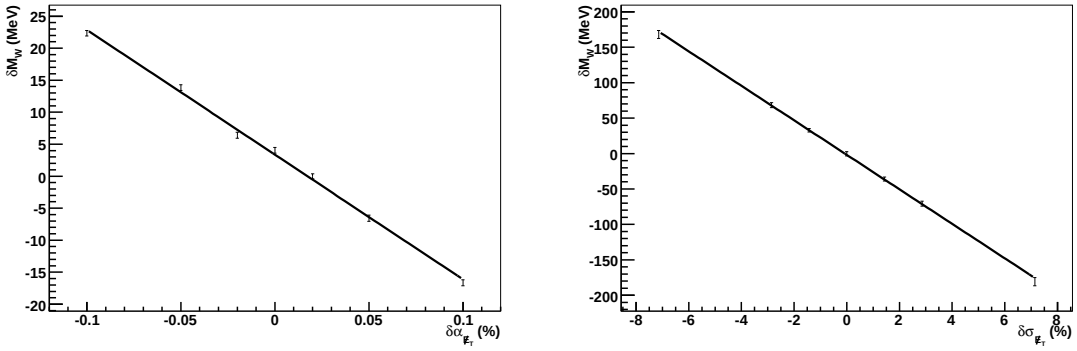

Figure 6.3.3: *Left: Bias on M_W, $\delta M_W = M_W^{fit} - M_W^{true}$, as a function of the bias on the recoil scale, $\delta\alpha_{\not\!\!E_T}$. Right: δM_W as function of the resolution bias, $\delta\sigma_{\not\!\!E_T}$. A linear dependence is observed in each case, with $\partial M_W/\partial_{rel}\alpha_{\not\!\!E_T} = -200$ MeV/% and $\partial M_W/\partial_{rel}\sigma_{\not\!\!E_T} = -25$ MeV/%.*

Impact of $\not\!\!E_T$ scale, $\alpha_{\not\!\!E_T}$, and resolution, $\sigma_{\not\!\!E_T}$, on the M_W measurement

The bias on M_W is evaluated by systematically varying the recoil scale, producing corresponding pseudo-data samples as discussed in the previous sections, and fitting each sample to perfectly calibrated templates. In the form of a derivative, the following dependency of the M_W bias on the recoil scale and resolution is obtained:

$$\frac{\partial M_W}{\partial_{rel}\alpha_{\not\!\!E_T}} = -200 \text{ MeV}/\% \qquad \frac{\partial M_W}{\partial_{rel}\sigma_{\not\!\!E_T}} = -25 \text{ MeV}/\% \tag{6.3.1}$$

as illustrated in figure 6.3.3.

6.4 Refined estimates: Neutrinofication

In the previous section the lepton was naively removed offline, implicitly assuming perfect separation between leptonic and hadronic signals in the $\not\!\!E_T$ calculation. I.e. it is assumed that the $\not\!\!E_T$ algorithm must perform equally well regardless of whether the $\not\!\!E_T$ is low as in *Z* events of significant as in *W* events. The fact that the peak in figure 6.3.1 is off-centered reveals that this assumption, in general, is not justified. To assess the bias a lepton of a *Z* event is removed prior to reconstruction: The lepton is *neutrinoficated*. This method avoids mixing the lepton and hadron signals, which is a problem of the current $\not\!\!E_T$ algorithm.

To accomplish, a software package is written, entering the reconstruction chain before the $\not\!\!E_T$ calculation and already at this stage removes the calorimeter cells corresponding to a $Z \to ee$ electron. The outline is as follows:

- Reconstruct $Z \to ee$ events using the event selection criteria explained in section 5.3.2.
- When a electromagnetic cluster of a $Z \to ee$ electron is identified, the energy content of its cells is replaced by noise as shown in figures 6.4.1 and 6.4.2.

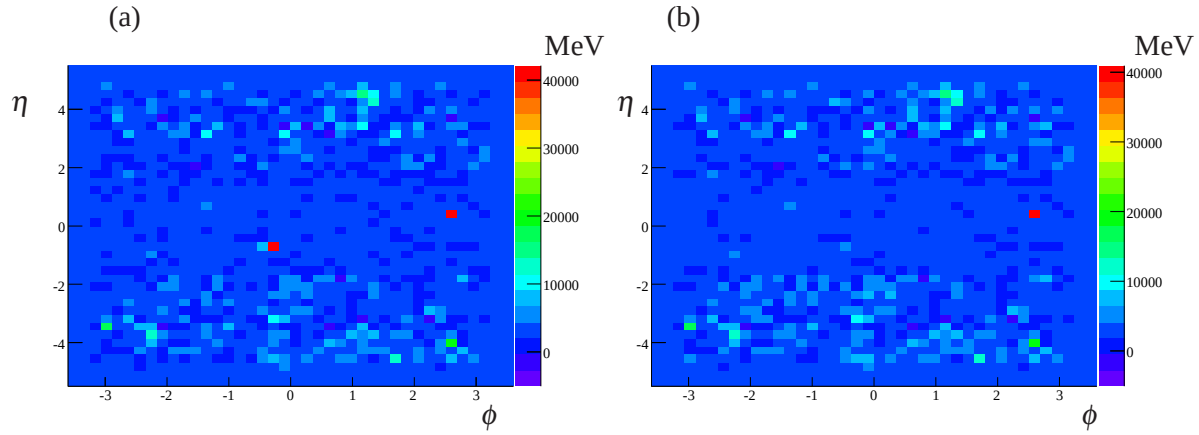

Figure 6.4.1: *Electron cluster removal. The projection of all calorimeter cell energies onto a plane (i.e. all layers summed) before (a) and after the modification (b).*

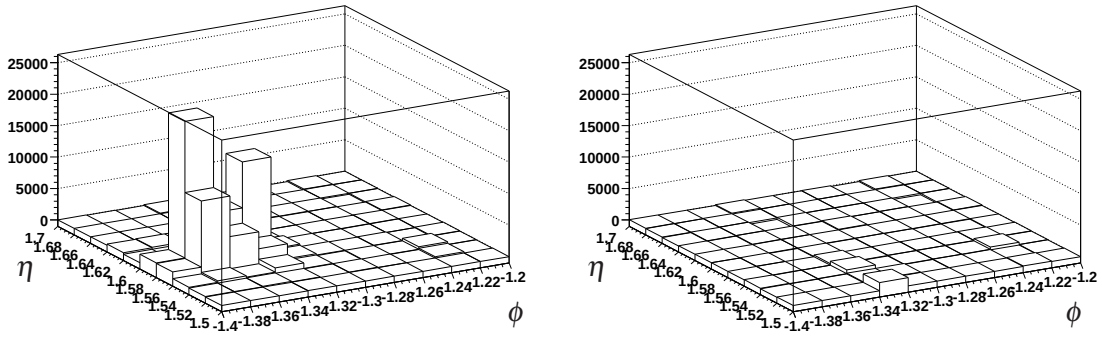

Figure 6.4.2: *Left: electron cluster in a $Z \rightarrow ee$ event. Right: the same calorimeter region, after the cluster has been removed. The energy in each cell belonging to the electron cluster is replaced by a number drawn from a Gaussian with mean and RMS corresponding to detector noise in cells of the same type.*

The cluster corresponding to a $Z \rightarrow ee$ electron is now removed, and the reconstruction algorithm sequence proceeds; in particular the clustering- and $\not\!\!E_T$ calculation.
When completed the $\not\!\!E_T$ of the event and truth electron transverse momentum of the electron can be compared - examples of this are shown in the next section.

Note that although the present approach makes use of the MC truth, the constraint on the Z mass combined with excellent tracking makes a real $Z \rightarrow ee$ event essentially as good as MC truth and thus the method is useful in real data as well.

6.4.1 Neutrinofication performance

The lepton removal requires that one can identify and remove the electron signal from the struck calorimeter cells, and substitute by a *realistic* contribution from noise and hadronic background. Several approaches have been tested, such as replacing the contents of the electron cluster cells by energy measured away from any high-p_T object in the event (e.g. at 90° in azimuth), or by the average expected electronic and hadronic noise. Some results obtained using different noise algorithms can be found in Appendix A.3.

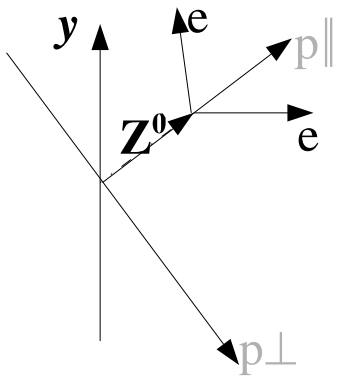

Figure 6.4.3: *Take into account the natural topology of the event: The (transverse) Z direction of flight. Obviously, one cannot define this system in data for W events as easily due to the undetected neutrino. However, the bias introduced by using instead the $\not\!\!E_T$ vector is considered to be insignificant.*

To assist the $\not\!\!E_T$ performance group in locating the origin of the bias, as well as to validate the Neutrinofication tool, some additional tests are made. Among these tests are:

- Dependence on choice of $\not\!\!E_T$ calculation algorithm.
- Dependence on the number of neighboring cells removed.
- Dependence on the ΣE_T of the event and the transverse lepton momentum.

The reader is refereed to Appendix A.3 for details on the Neutrinofication performance. In summary, the results show that the *object based* $\not\!\!E_T$ algorithm [ATL08d] (on which figure 6.4.4 is based) has the smallest bias, and that the number of neighbors removed and choice of noise algorithm has little or no influence on the bias. Also, as expected there are clear correlations between the magnitude of the bias and ΣE_T on one side and the transverse lepton momentum on the other.

6.4.2 Results

To determine the $\not\!\!E_T$ resolution and possibly correct for the bias in its measurement, the difference between reconstructed $\not\!\!E_T$ of $Z \rightarrow ee$ events before and after the removal of one electron is compared to the to the transverse momentum of the removed electron. A non-zero average value of this distribution points to a bias in the $\not\!\!E_T$ reconstruction.

As was concluded in section 5.5, the conventional coordinate system tends to conceal the effects of the event to event bias. Instead the natural frame of the event, with axes parallel ($\parallel$) and perpendicular ($\perp$) to the Z boson transverse momentum, is used as coordinate system, see figure 6.4.3. Imperfect calibration of $\not\!\!E_T$ will show up as biases in these distributions, which can then subsequently be corrected for within the statistics available. Projecting the missing energy onto the coordinate system defined in figure 6.4.3 reveals a significant bias as shown in figure 6.4.4(bottom left).
As can be seen in this example, a bias is observed in the $\not\!\!E_T$ reconstruction along the Z line of flight. No bias is observed along the other axis. In this example, the calibration thus appears correct on average in the conventional coordinate system, but the $\not\!\!E_T$ reconstruction does not respond correctly to the event-by-event topology.

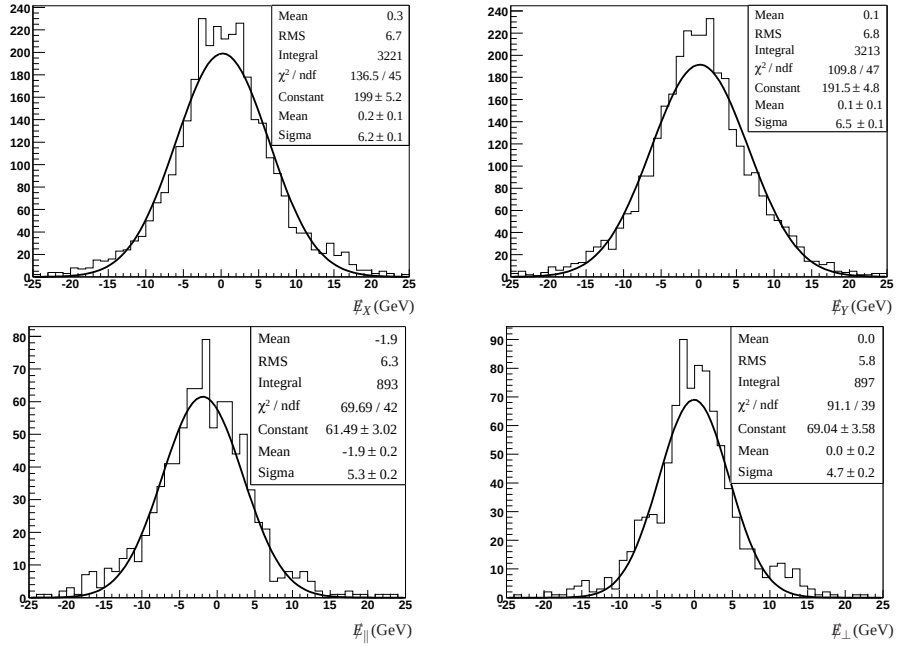

Figure 6.4.4: *Top: resolution of $\vec{\not\!\!E}_T$, projected onto the (x,y) coordinate system, for unmodified, fully simulated $Z \rightarrow ee$ events. Bottom: $\vec{\not\!\!E}_T$ resolution in the $(\parallel, \perp)$ coordinate system. The absence of bias along the x and y axes show that the overall calibration is correct on average, but the observed bias along the $\parallel$-axis, corresponding to the Z line of flight, indicates imperfect calibration of the response to the event-by-event topology.*

Obviously, the correct procedure to resolve, would be to track down and correct the bias in the $\not\!\!E_T$ algorithm. This, however, is beyond the scope of the present analysis. Instead it is assumed that in time of the actual W mass measurement using the transverse mass, this will be corrected[3]. Even in this case, it must be verified that the Neutrinofication approach is a valid procedure to obtain the $\not\!\!E_T$ bias and resolution, i.e. it must be proved that no bias is added by the Neutrinofication approach (but also no bias is removed, that remains up to the $\not\!\!E_T$ community). To this end, one approach to quantify the possible added bias, is to consider the quantity $\not\!\!E_{T\,before}$-$\not\!\!E_{T\,after} + p_T(truth)$ in the two coordinate projections (where 'before' and 'after' refers to before and after Neutrinofication). In case bias is added, this distribution should be off centered, otherwise not. The results is shown in figure 6.4.5.
From this figure it is concluded that neutrinofication does not add significant bias, and can thus be assumed to be a valid method to obtain the $\not\!\!E_T$ resolution and scale. Since the $\not\!\!E_T$ resolution and scale break down into the parallel and perpendicular direction, derivatives plots corresponding to figure 6.3.3 must be replaced by two dimensional distributions, as shown in figure 6.4.6.

As can be concluded from the present discussion, $\not\!\!E_T$ reconstruction is a very difficult experimental algorithm to control, especially to the level of precision desired for the W mass measurement. Therefore, the estimated impact on the W mass measurements, obtainable either from figure 6.4.6 or the correspondent one dimensional one (figure 6.3.3) should be seen as a final aim. Instead, lacking proof that the sensitivity enhancement provided by increasing the statistics to 10 fb^{-1}can be fully exploited, it is assumed that and overall uncertainty of $\delta M_W(\sigma_{\not\!\!E_T}, \alpha_{\not\!\!E_T}) = 5$ MeV can be reached.

[3]Already at the time of writing, part of the bias have been corrected with respect to the presented results. Further improvements are expected in a near future (ATLAS offline software release 14).

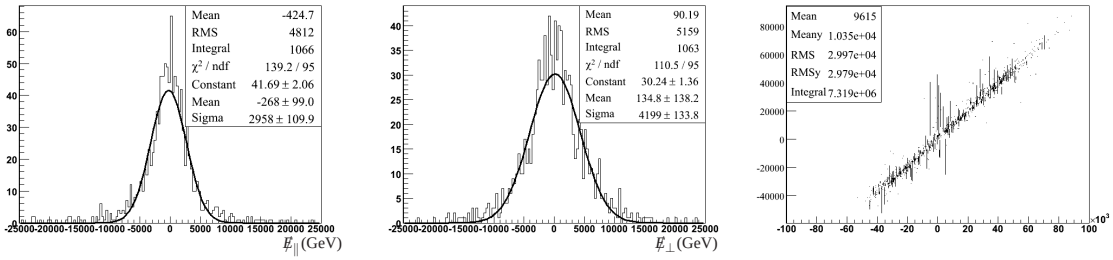

Figure 6.4.5: $\not{E}_{T\,before} - \not{E}_{T\,after} + p_T(truth)$ *in the parallel (left), and perpendicular (middle) directions. Also shown(right) is* $\not{E}_{T\,before} - \not{E}_{T\,after}$ *versus* $p_T(truth)$ *in the parallel direction.*

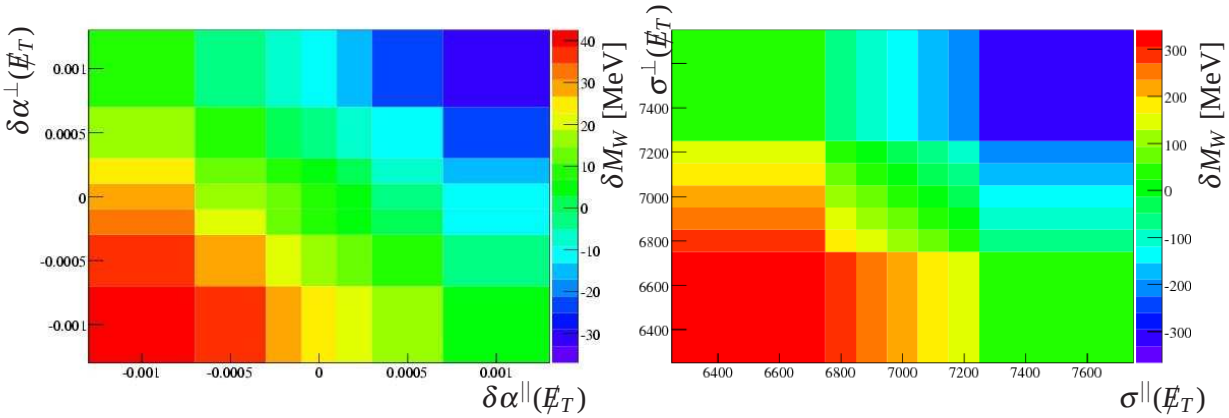

Figure 6.4.6: *Relation between the uncertainties of the* $\not{E}_T$ *scale and resolution and the corresponding error introduced on the* W *mass measurement. Data has not been scaled and has a resolution 7000 MeV.*

This is a factor of three higher than the purely statistical sensitivity, and a factor of three smaller than the systematic uncertainty obtained in recent CDF measurements [CDF07a] based on an integrated luminosity of 200 pb^{-1}and about 8000 Z events for calibration of the hadronic recoil.

6.5 Summary of experimental uncertainties at $\mathscr{L}$ = 10 fb^{-1}

The response parameters determined in situ using Z events (cf. section 6.2) are used to produce templates of the p_T^l-spectrum in W events, as shown in figure 6.5.1. The resulting fit yields $M_W = 80.466 \pm 0.110$ GeV, with no bias with respect to the true value. This result shows that for $\mathscr{L} = 15$ pb^{-1}, propagating a global scale determined on Z events does not induce a significant bias in the analysis. Given this result one can estimate the impact of the scale and resolution uncertainties on the W mass measurement using the results presented in section 6.2 and equations 6.1.1 and 6.1.2:

$$\delta M(\alpha) = \frac{\delta\alpha}{\alpha} \cdot \frac{\partial M}{\partial \alpha_{rel}} \sqrt{\frac{\mathscr{L}_{sample}}{\mathscr{L}_{final}}} = \frac{0.0003}{0.9952} \cdot 800\ \text{MeV}/\% \cdot \sqrt{\frac{200\ \text{fb}^{-1}}{10\ \text{fb}^{-1}}} \approx 4\ \text{MeV and correspondingly}$$

$$\delta M(\sigma) = \frac{\delta\sigma}{\sigma} \cdot \frac{\partial M}{\partial \sigma_{rel}} \sqrt{\frac{\mathscr{L}_{sample}}{\mathscr{L}_{final}}} = \frac{0.0003}{0.0207} \cdot 0.8\ \text{MeV}/\% \cdot \sqrt{\frac{200\ \text{pb}^{-1}}{10\ \text{fb}^{-1}}} \approx 1\ \text{MeV}.$$

From the fits presented in figures 5.4.2 and 5.5.1 a conservative estimate of the uncertainty on the fraction of events in the non-Gaussian tails is given by the uncertainty on the fraction between the two fit function components (Crystal Ball and Bifurcated Gauss). Typically the relative error is $\sim 5\%$ by

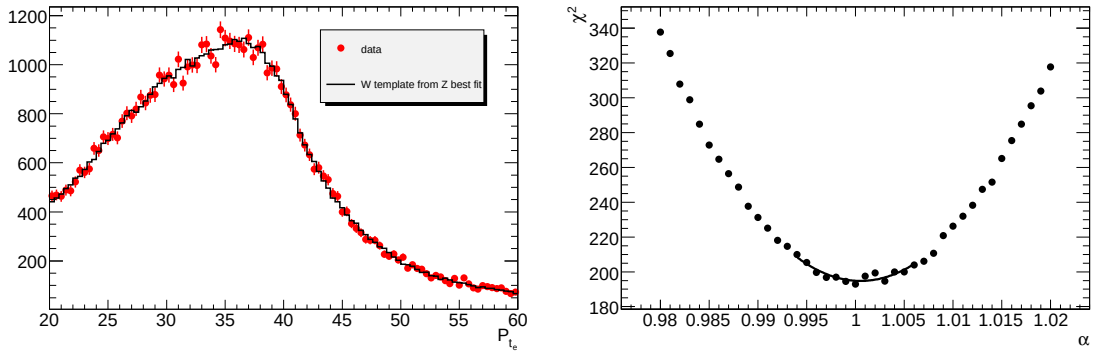

Figure 6.5.1: *Left: p_T^l-spectrum from fully simulated W decays (dots with error bars), and p_T^l-template obtained assuming the Z-based scale and resolution and the true value of M_W. Right: Template fit to M_W.*

Method	$p_T(e)$	$p_T(\mu)$	$M_T(e)$	$M_T(\mu)$
$\delta M_W(\alpha)$	4	4	4	4
$\delta M_W(\sigma)$	1	1	1	1
$\delta M_W(tails)$	1	0.5	1	0.5
$\delta M_W(\varepsilon)$	0.5	0.3	0.5	0.3
$\delta M_W(\sigma_{\not{E}_T}, \alpha_{\not{E}_T})$	–	–	5	–

Table 6.5.1: *Summary of experimental systematic uncertainties at 10 fb^{-1} in* MeV.

which an estimate of the precision of which the non Gaussian event fraction will be know at 10 fb^{-1} is $\approx 0.2\%$. The estimated impact on the W mass measurement is then given by equation 5.4.3, the result is: 0.5 MeV. For electrons, the tails and hence the uncertainty in their determination are some larger. In table 6.5.1 this is taking into account by doubling the error based on the muon result. The expected precision of the in situ efficiency measurement (section 5.5) and equation 5.4.3 imply a systematic uncertainty on the fit result of about $\delta M_W = 8$ MeV in the muon case. For electrons, [CSC08b] shows that the electron efficiency can be determined to within 1.5% using 100 pb^{-1}, yielding a corresponding error of: $1.5\% \cdot 3.6$ MeV$/\% = 5$ MeV. Assuming pure statistical nature, the expected uncertainty at 10 fb^{-1} is ≈ 0.3 MeV for muons and ≈ 0.5 MeV for electrons. It was not attempted to determine the recoil calibration in situ. However, a method was presented to assess and evaluate the $\not{E}_T$ algorithm to the required level of detail needed for the measurement of M_W in this channel. Presently, it is unknown to which level the ATLAS $\not{E}_T$ will be unbiased at the time of the M_W measurement. Reckoning that a total absence bias is unlikely, the Tevatron experience is taking into account, allowing an estimate of the systematic error due to the combined $\not{E}_T$ scale and resolution of 5 MeV.

Chapter 7

Theoretical uncertainties

Below the uncertainties related to imperfect physics modeling of W production are discussed. The correlation of the mass measurement with the W width, the impact of final state radiation, and biases in the p_T^l and M_T^W distributions induced by p_T^W and y^W distortions are discussed in turn.

7.1 W boson width: $\delta M_W(\Gamma_W)$

A change in the W width, Γ_W, affects the Jacobian edge, and can cause a bias in the W mass measurement. To assert the size of this effect, samples with the same W mass, but W widths varying in the range $1.7-2.5$ GeV were produced and subsequently fitted. The relation between Γ_W and its effect on the M_W fit result is linear, with a slope depending on the distribution used in the mass fit. Using W transverse mass gives:

$$\frac{\partial M_W}{\partial_{rel}\Gamma_W} = 3.2 \text{ MeV}/\%$$

whereas the corresponding result when fitting the lepton transverse momentum is:

$$\frac{\partial M_W}{\partial_{rel}\Gamma_W} = 1.2 \text{ MeV}/\%$$

The intrinsic width of the W resonance Γ_W has been measured to be 2.141 ± 0.041 GeV, while the Standard Model prediction is 2.0910 ± 0.0015 GeV [PDG06]. It should be taken into account that the LHC data is expected to improve the precision on the W width significantly. Considering previous measurements, an improvement by roughly a factor five should be achievable, leaving the uncertainty $\delta M_W(\Gamma_W) =$1.3 MeV and 0.5 MeV for the M_T^W and p_T^l fit, respectively.

Of course, inclusion of Γ_W as a systematic uncertainty in the W mass measurement is unambitious: Γ_W is worthwhile to be measured, providing a test of the standard model in itself. In practice, M_W and Γ_W will likely be extracted simultaneously, from two-parameter fits to the usual distributions.

7.2 QED final state radiation: $\delta M_W(QED)$

Final state radiation (FSR) causes significant distortions of the naive, lowest order p_T spectrum of the W decay leptons. The stability of the theoretical calculation below is estimated, using the PHOTOS

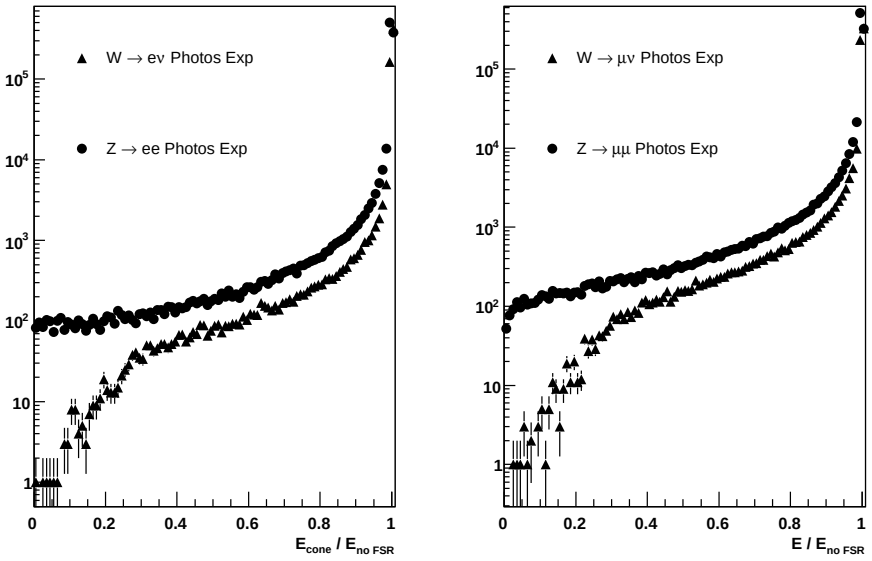

Figure 7.2.1: *Distribution of the fraction of measured lepton energy relative to the energy in absence of FSR for* PHOTOS *in exponentiated mode. All photon energy radiated within a cone of radius* $\Delta R = \sqrt{\Delta\eta^2 + \Delta\phi^2} = 0.1$*, corresponding to the size of reconstructed electromagnetic clusters is added to the energy of electrons. Muon momentum is measured bare, after FSR.*

program [GW06] as a benchmark.

The numerical importance of final state radiation is illustrated in figure 7.2.1, which displays the distribution of the measured lepton energy fraction relative to their energy in the absence of FSR. For electrons, measured via calorimetric clusters, most of the (collinearly radiated) photon energy is collected in the cluster. The momentum of muons tracks, on the contrary, is measured independently of any photon radiation. The average muon energy is shifted 1% with respect to the initial value, meaning that ignoring the effect entirely would cause a bias on the W mass of about 800 MeV. The theoretical stability of the calculation is thus of critical importance.

In recent versions of PHOTOS, it is possible to switch between several degrees of precision, i.e. number of orders in α. In particular, W and Z boson decays can be simulated with photon emission up to O(α), O(α^2), O(α^4), or with photon emission exponentiation - a scheme for reshuffling the dominant terms between orders of expansion [YFS61]. To study the model differences, about 10^6 events have been generated for each setting, and for each production and decay channel ($W \to l\nu$, $Z \to ll$, for $l = e, \mu$).

Figure 7.2.2 shows the evolution of the average energy fractions, $R_{FSR} = < E_{cone}/E_{noFSR} >$, for successive theoretical refinements. The different results obtained for electrons and muons reflect the different methods by which their energy or momentum is measured. The calculation appears stable to within $\sim$1-2$\cdot 10^{-4}$, the residual differences being compatible with statistical fluctuations.

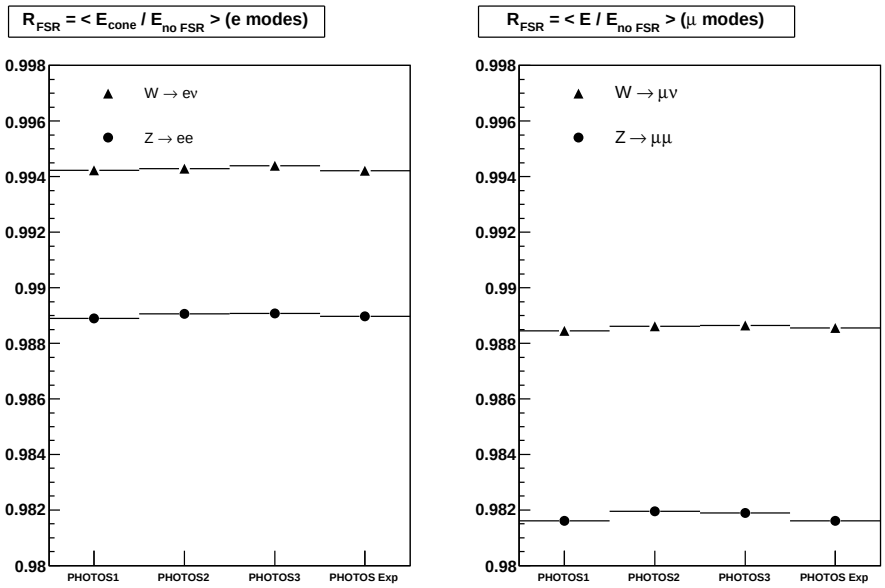

Figure 7.2.2: *Development of* $R_{FSR} =< E_{cone}/E_{noFSR} >$ *(i.e. average of the distributions of figure 7.2.1), for various* PHOTOS *settings.*

To support the above argument, consider the Z boson mass measurement at LEP1 [ADL$^+$06]. Similarly to the case for ATLAS, QED corrections, in the form of initial state radiation off the electron beams, have a large impact on the Z line-shape, inducing a decrease of the cross-section of about 30%, and a shift of the peak position of about 100 MeV. Nevertheless, the theoretical uncertainty on these effects are estimated to 0.3 MeV, compared to a total measurement uncertainty of 2.1 MeV. The theory of QED radiation thus carries negligible uncertainty.

For the QED induced M_W uncertainty to be as small, the event generators used to produce the templates thus need to have similar theoretical accuracy, with the additional complication that the present analysis requires an exclusive description of the final state (i.e., a complete description of the photon distributions), whereas the Z line-shape analysis only relies on the effective energy of the beams after radiation. In [NW06], the accuracy of the PHOTOS algorithm is upgraded to NLO accuracy. Similarly, the HORACE event generator [CMNT04] contains QED and weak corrections to NLO accuracy. Both programs implement photon emission exponentiation.

It is therefore assumed that ultimately $\delta M_W(QED) \leq 1$ MeV can be reached. This assumption is conditioned by the availability of the necessary tools in time for the measurement.

Finally note that W and Z events behave differently under QED radiation, as illustrated in figure 7.2.3. The average energy fraction in Z events is 5-7$\cdot 10^{-3}$ smaller than in W events, depending on the final state. The energy scale measurement (cf. chapter 6) and the W mass measurement should properly account for the difference in the respective QED radiation patterns. This will be discussed further in section 8.4.

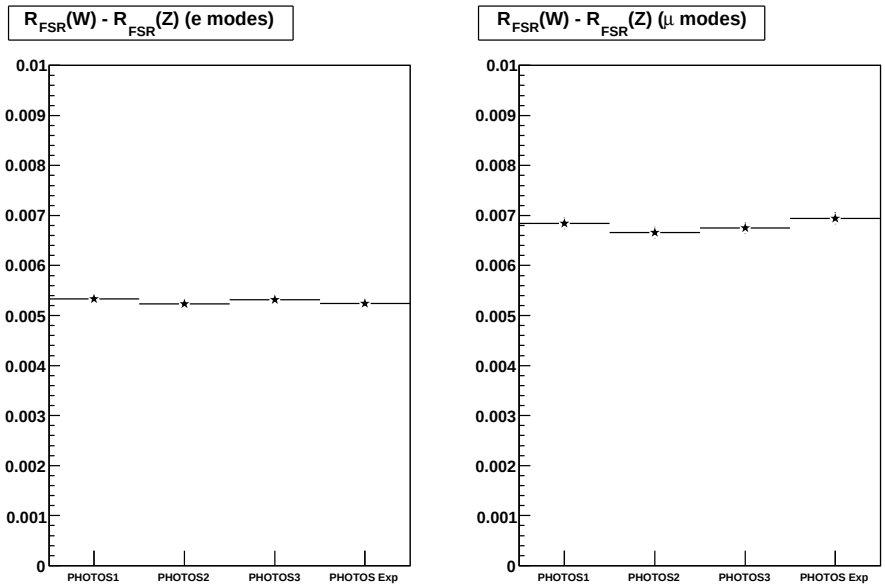

Figure 7.2.3: *Difference between W and Z events of the averages of figure 7.2.2, for various* PHOTOS *settings (see text).*

7.3 *W* distributions

The *W* rapidity and transverse momentum distributions result from the interplay of the proton structure functions, and strong interaction effects at the *W* production vertex. To simplify the discussion, the longitudinal and transverse distributions are considered independently, as respective results of parton distributions and QCD higher orders.

7.3.1 Rapidity distribution: $\delta M_W(y^W)$

The *W* rapidity distribution is essentially driven by the proton parton density functions (PDFs). The study is based on the CTEQ6.1 structure functions sets [P$^+$02], which provide, in addition to the global best fit, PDFs corresponding to the variation of each diagonal parameter (i.e., the linear combination of input parameters that diagonalize the covariance matrix) by ± 1 standard deviation. The PDF-induced uncertainty for an observable is obtained by computing its value with all sets, taking the central value as given by the best fit, and quadratically summing the biases (with respect to the best fit value) obtained from the uncertainty sets.

As illustrated in figure 7.3.1 (see also [B$^+$07a]), the current PDF uncertainties induce an uncertainty in the *W* rapidity distributions which, through acceptance effects, propagates a systematic uncertainty on the *W* mass determination of $\sim$25 MeV. Below an attempt to estimate how this will improve with the LHC data is presented.

At the LHC, *W* and *Z* particles are essentially produced through sea quark interactions; the influence of valence quarks is small. Low-x, high-Q^2 sea quarks mainly evolve from higher x, lower Q^2 gluons, and a consequence from perturbative QCD flavor symmetry is that up to initial asymmetries and heavy-

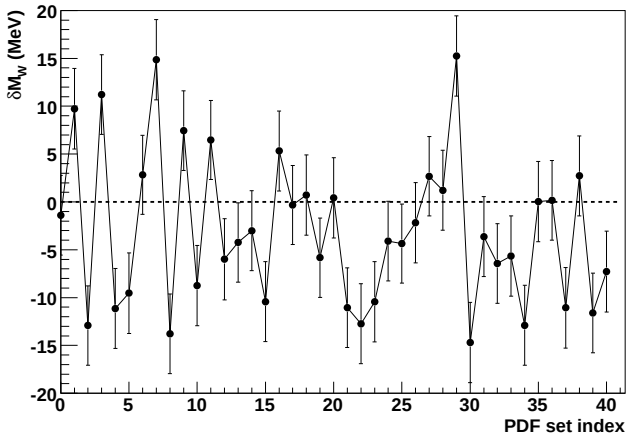

Figure 7.3.1: *Bias on M_W obtained when varying the proton PDFs within their uncertainties. Each point on the abscissa corresponds to a given PDF set: Set 0 is the best fit, and gives 0 bias by definition; sets 1-40 are the uncertainty sets, each inducing a given bias on M_W. The total uncertainty on M_W is given by the quadratic sum of the biases, giving $\delta M_W \sim 25$ MeV.*

quark mass effects, the different quark flavors should be represented democratically. This then implies, that the impact of sea quark PDF uncertainties on W and Z production should be very similar. In other words, when varying PDFs within their uncertainties, one expects a strong correlation between the induced variations of the W and Z distributions.

This is confirmed by figure 7.3.2(left)[1], which shows the correlation between the widths of the W and Z boson rapidity distributions. It is chosen to use the distributions RMS, denoted σ_y^W and σ_y^Z, to quantify their width. The spread of the points represents the current uncertainty on the W and Z rapidity distributions, and the error bars on each point represent the expected precision of a measurement exploiting 10 fb^{-1} of LHC data. The current CTEQ6.1 prediction, $\sigma_y^Z = 2.16 \pm 0.03$, will be refined to a precision of $\delta\sigma_y^Z = 0.001$. Exploiting figure 7.3.2 (right), which quantifies the correlation between σ_y^W and σ_y^Z, this can be translated into a prediction of the W boson rapidity distribution, $\delta\sigma_y^W = 0.0013$, to be compared to the current prediction $\sigma_y^W = 2.24 \pm 0.03$.

From the above arguments it seems reasonable to expect an improvement on the Z rapidity distribution by a factor $\sim$30. This is also illustrated in figure 7.3.3, where two extreme predictions (with current knowledge) of the Z rapidity distribution are compared with an example distribution representing the same measurement. Given the residual decorrelation between the W and Z distributions, this translates into an improvement on the W rapidity distribution by a factor ~ 23.

Starting with $\delta M_W(y_W) \sim$25 MeV, putting in a precise measurement of the Z rapidity distribution at the LHC, and exploiting the strong correlation between the W and Z production mechanisms, the final uncertainty from the description of the W rapidity distribution is thus anticipated to be: $\delta M_W(y_W) \sim$1 MeV.

In practice, the analysis will of course proceed via a formal QCD analysis to the LHC data: The

[1]This plot is reminiscent from figure 2 in [Nad05], displaying similar correlations in the production rates. Note that for the present purpose, normalizations are irrelevant and interest is only in the distributions.

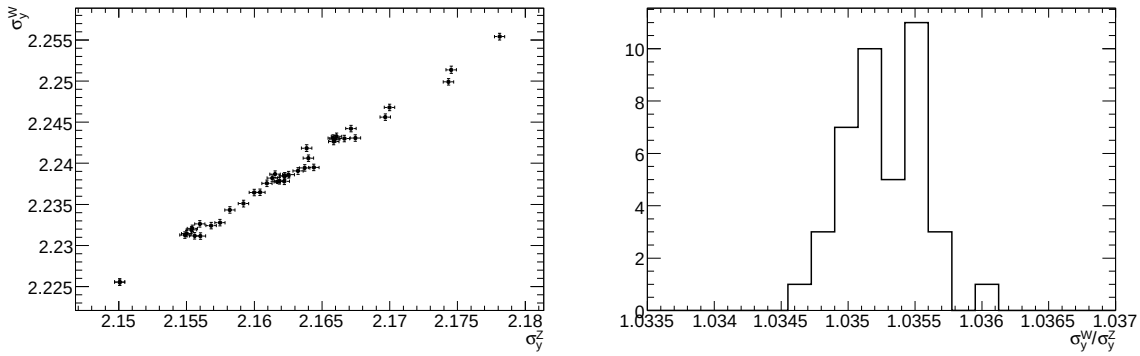

Figure 7.3.2: *Left: Correlation between the W and Z rapidity distributions, estimated via their spreads in rapidity σ_y^W and σ_y^Z, when varying the CTEQ6.1 PDFs within their uncertainties. The fitted pseudo-data is scaled to an integrated luminosity of 10 fb^{-1}. Right: Distribution of the ratio σ_y^W/σ_y^Z, again varying the PDFs within their uncertainties. The spread of the ratio distribution is $4 \cdot 10^{-4}$.*

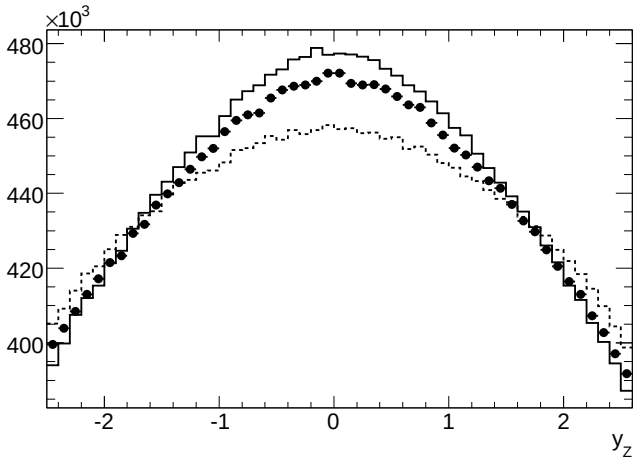

Figure 7.3.3: *The line histograms represent two extreme predictions for the Z rapidity distribution, as given by the CTEQ6.1 PDF sets. The points are pseudo-data, obtained with the central set, and scaled to an integrated luminosity of 10 fb^{-1}.*

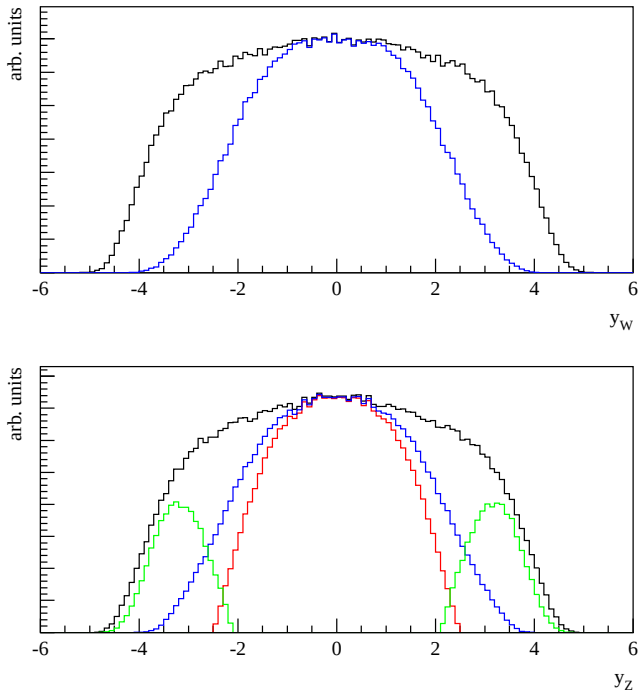

Figure 7.3.4: *Upper plot: The outer histogram represents the complete rapidity distribution for W production at the LHC; the inner histogram represents the range selected by the condition $|\eta_l| < 2.5$. Lower plot: The outer histogram represents the complete rapidity distribution for Z events. The innermost histogram is obtained requiring two decay leptons within $|\eta_l| < 2.5$; the intermediate histogram is obtained when allowing one electron within $|\eta_l| < 4.9$. The two symmetric histograms at high rapidity correspond to the LHCb muon acceptance.*

measured Z differential cross-section $\mathrm{d}\sigma/\mathrm{d}y$, together with other measurements, will be fed to parton distribution fits, and the systematic $\delta M_W(y^W)$ from the improved PDF sets will be evaluated as above. The present discussion however allows to estimate the expected improvement while avoiding these complications.

Note also that Z rapidity distribution can be analyzed over a domain that fully includes the range relevant for W production. The usual Z acceptance, given by $|\eta_l| < 2.5$ for both decay leptons, can be extended in the electron channel by allowing one of the electrons to be detected within $|\eta_e| \lesssim 4.9$. In addition, high-rapidity Z events will be produced and detected at LHCb [Lb03] (for example, the geometric acceptance of the muon detector is approximately $2.1 < |\eta_\mu| < 4.8$). Accounting for this, and as illustrated in figure 7.3.4, the W rapidity range selected for the M_W measurement is entirely included in the Z. This remains true in terms of the parton momentum fractions.

The above results are partly consequences of the assumed flavor and charge symmetry in the low-x proton; notably, the parton parameterizations used in the fits used above assume that $d(x) = \bar{d}(x) = u(x) = \bar{u}(x)$ at low-x, and $s = \bar{s}$ at all x. This implies the strong correlation discussed above, since the Z production rate is proportional to $u\bar{u} + d\bar{d} + \ldots$, and the W rate is proportional to $u\bar{d} + d\bar{u} + \ldots$. It is thus important to quantify the dependence of the result on these hypotheses.

The anti-quark flavor asymmetry $\bar{u} - \bar{d}$ was measured to be non-zero in the region $0.015 < x < 0.35$, and $Q^2 \sim 50\ \mathrm{GeV}^2$ [NA5194, NS01], in contradiction with the flavor symmetry assumption. The

relative asymmetry, $(\bar{u}-\bar{d})/(\bar{u}+\bar{d})$, is however of the order $\sim 10^{-2}$, decreasing towards higher Q^2. Starting from $\bar{u}=\bar{d}$ and full correlation between W and Z production (i.e. W and Z distributions have the same rate of change under PDF variations), $\bar{u}\neq\bar{d}$ induces a decorrelation of order $(\bar{u}-\bar{d})/(\bar{u}+\bar{d})\times(u-d)/(u+d)$, where both factors are of order 10^{-2} (see for example figure 1 in [P$^+$02]). Hence, even in the presence of non-vanishing $\bar{u}-\bar{d}$, the freedom of the W distributions is very limited once Z ones have been precisely measured. Thus it is assumed that the estimates remain correct; nevertheless, measurements of the W charge asymmetry, sensitive to $\bar{u}-\bar{d}$, will allow to verify this hypothesis. Additional information will be provided by measuring M_W in W^+ and W^- events separately.

7.3.2 Transverse momentum distribution: $\delta M_W(p_T^W)$

The prediction of vector boson p_T distributions at hadron colliders has long been an active subject [CSS85, MS99, BNOY05]. It is also a crucial input for the W mass analysis, especially when using the p_T^l observable. Below the impact of p_T^W uncertainties on the W mass determination is discussed.

The measurable p_T^W and p_T^Z distributions are the result of several effects, most notably the repeated, partly non-perturbative parton radiation occurring in the transition from the low-Q^2 proton towards the hard process (commonly referred to as parton showers, or QCD resummation). Another source is the transverse momentum intrinsic to the partons in the proton. Rather, reckoning that although W and Z production differ in several respects (the coupling to initial partons is different in both phase space and flavor), the non-perturbative mechanisms are universal, it is evaluated how precisely their combined effect can be measured in neutral current events, and how this improves the W predictions. Notice that heavy flavor PDFs have caused only a small decorrelation between W and Z events in the previous section; this is assumed to remain true in this discussion.

The relation between the biases in the modeling of p_T^W and the measurement of M_W is investigated by applying scaling factors to the p_T^W distributions in the pseudo-data, deducing the corresponding p_T^l distributions, and fitting M_W against un-distorted templates. The bias in M_W appears to be a linear function of the p_T^W mis-modeling, with a slope of order 0.3, meaning a 3 MeV bias on p_T^W results in a 1 MeV bias on M_W, when exploiting the p_T^l distribution for the W mass measurement (when M_T^W is used, the effect is negligible).

Neutral current di-lepton events allow to measure the p_T^{ll} distribution, as a function of mass, over a large mass range. Assuming usual selections, p_T^{ll} will be measured precisely for 30 GeV $< M_{ll} \lesssim$ 200 GeV. This large lever arm, in addition to the very precise determination of p_T^{ll} on the Z peak, provides a precise control of p_T^{ll} when $M_{ll}\sim M_W$. This is illustrated in figure 7.3.5, which displays the di-lepton mass dependence of its average transverse momentum, $< p_T^{ll} >$.

On the Z peak, p_T^{ll} will be known to about 7 MeV with an integrated luminosity of 10 fb^{-1}. Thanks to the Drell-Yan continuum, the accuracy in the region of M_W is still $\sim$8 MeV. This leads to an uncertainty on M_W of about 3 MeV.

Arguably, the p_T^W distribution can not be summarized by its mean value. However, in the low p_T^W region, it can be empirically described by a two-parameter function. As an exercise, the mass-dependence of the parameters were determined on Drell-Yan events, their values and uncertainties in the M_W region were used to produce p_T^l pseudo-data as above, and corresponding fits to M_W were performed. The spread in M_W resulting from the uncertainty in the empirical parameters was found compatible with the above estimate.

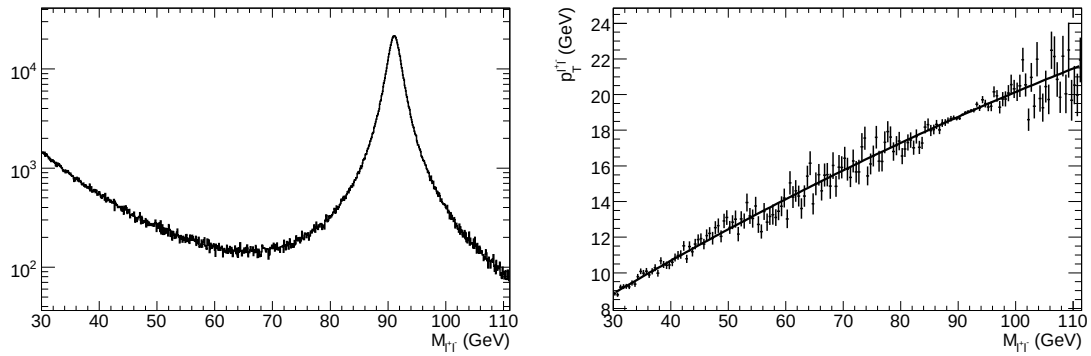

Figure 7.3.5: *Left: Di-lepton invariant mass spectrum, from inclusive neutral current events (γ and Z exchange are included). Right: Di-lepton average p_T as a function of the di-lepton invariant mass. The W-mass region is strongly constrained by the lever arm provided by the Z peak and the Drell-Yan rise at low mass (note the improved precision in these regions). The points correspond to a measurement with 10 fb^{-1}.*

Chapter 8

Environmental uncertainties

8.1 Backgrounds

The leptonic W final states benefit from low backgrounds. The dominant contributions come from similar vector boson decays; $W \to \tau(\to l\nu\nu)\nu$, $Z \to ll$ (where one lepton is not reconstructed), and $Z \to \tau(\to l\nu\nu)\tau$. QCD di-jet events will, despite their large cross-section, not be dominant due to the good particle identification capability of the ATLAS detector[ATL97a]. The backgrounds from $t\bar{t}$ and W^+W^- events are negligible.
If the size and shape of the backgrounds would be perfectly known, they would not affect the W mass measurement, as they could be included in the templates. The systematic error on M_W arises from uncertainties on the background shape and normalization in the fitting range of the p_T^l and M_T^W spectra.

Uncertainties on the W and Z background size, relative to the signal size, depend on cross-sections, branching fractions and acceptances. These are obtained from [PDG06] and take into account the studies described in sections 5.4.3 and 7.3. Note that in contrast to the studies presented until now, the background uncertainty does not scale with statistics.

The background shapes are determined from simulation, and are essentially unaffected by variations in the production, decay, and resolution model. For QCD background, as a separate study, both normalization and shape will have to be measured directly from the data. The p_T^l distributions, including signal and backgrounds, are illustrated in figure 8.1.1.

$W \to \tau\nu$ events: The largest background is from $W \to \tau\nu$ events, where the τ decays leptonically. This background is irreducible, as the final state is identical to the signal; however, due to the additional neutrinos, its p_T^l and M_T^W are on average lower, leaving only a tail into the fitting range. Despite being the main background, its uncertainty is small, as only τ decay parameters and the acceptance enter, with respective uncertainties of 1.0% and 2.5%.

$Z \to ll$ events: The second largest background is from $Z \to ll$ events, where one lepton is either undetected or not identified. The latter background can be reduced using a Z veto rejecting events, where the lepton and a second isolated object (track and/or cluster) forms an object with an invariant mass between 80 and 100 GeV (see figure 8.1.2). Due to the high mass of the Z boson, the p_T^l

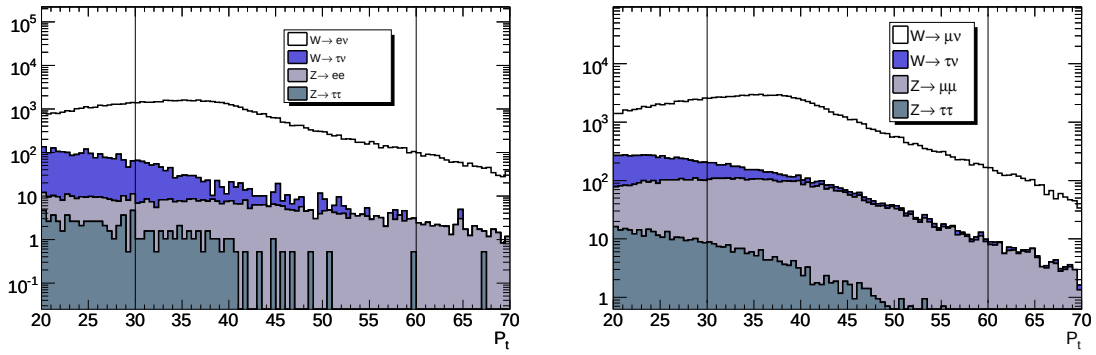

Figure 8.1.1: *Signal and background in the p_T^l distributions, for $W \to e\nu$ (left) and $W \to \mu\nu$ (right). The upper histogram is the signal; the lower histograms correspond, from bottom to top, to $Z \to \tau\tau$, $Z \to ll$, $W \to \tau\nu$.*

distribution extends well into the fitting range. The M_T^W distribution is less affected due to the low of missing momentum in these events.

The size of this background has uncertainties from the W to Z cross-section ratio R_{WZ} (1.8%), Z veto efficiency uncertainty (2.0%) and the acceptance uncertainty (2.5%). It is expected to be larger for muons than for electrons, as the former cannot be vetoed for $|\eta| > 2.7$ and thus contribute significantly to $\not\!\!E_T$.

$Z \to \tau\tau$ events: A small background originates from the $Z \to \tau\tau$ process, where one τ decays leptonically, while the other is not identified. While the cross-section for such a process is small, it can contain significant $\not\!\!E_T$ and is thus likely to pass the W selection criteria. The largest uncertainty in the size of this background comes from the τ detector response (5.0%), along with cross-section ratio R_{WZ} (1.8%), and acceptance (2.5%) uncertainties.

The expected background from boson events is summarized in table 8.1.1.

Electron channel		Muon channel	
Process	Fraction [%]	Process	Fraction [%]
$W \to e\nu$	97.8	$W \to \mu\nu$	93.9
$W \to \tau\nu$	1.4	$W \to \tau\nu$	1.4
$Z \to ee$	0.7	$Z \to \mu\mu$	3.9
$Z \to \tau\tau$	0.1	$Z \to \tau\tau$	0.2

Table 8.1.1: *Signal and expected bosonic backgrounds fractions after the event selection described in section 5.3.2 and in the p_T^l range [30;60] GeV.*

QCD events: Due to theoretical difficulties, the QCD background can not be obtained reliably from simulation. It will thus have to be measured directly from data. For the Run I W mass measurement at CDF, this background was estimated to a precision of $\sim 50\%$ [Gor98], limited by lepton identification

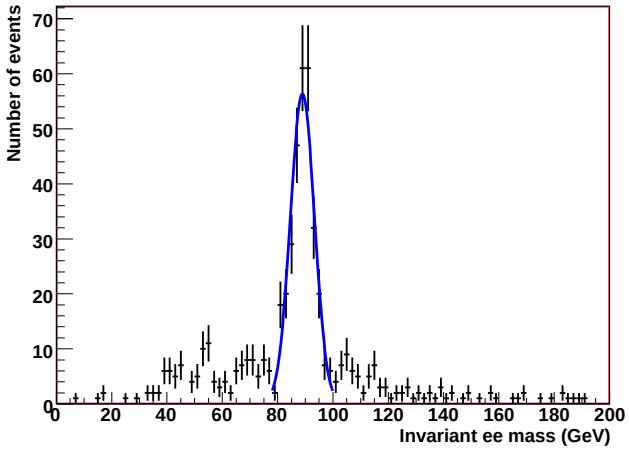

Figure 8.1.2: *Distribution of invariant mass between lepton and a second isolated object (track and/or cluster) in $Z \to ll$ events. Events in the range 80-100 GeV are rejected.*

performances and statistics. At ATLAS, a precision of $\sim 10\%$ is assumed in the electron channel, where this background is expected to be significant. The assumed improvement is justified by the superior granularity and better electron identification resulting from the good resolution of the electromagnetic calorimeter [ATL97a]. The muon final state is less contaminated by jet events, muons being measured behind all calorimetry. A specific background is however constituted by muons from hadron decays in flight. As there is presently no reliable measure of the uncertainty on this background, the results implicitly assume it is small. It should be stressed that these estimates are essentially qualitative. A realistic estimate of their impact on the measurement will only be possible with data.

Overall impact: As mentioned, the background shapes are determined from simulation. They are essentially unaffected by variations in the production, decay and resolution model. For QCD background, as a separate study, both normalization and shape will have to be measured directly from the data. First the overall impact of the backgrounds is assessed. The backgrounds remaining after the selection described in section 5.3.2 are given in table 8.1.1, and the p_T spectrum of each process is shown in figure 8.1.1.

Ignoring the background altogether in the templates leads to a bias $\delta M_W = -10$ MeV. This is however the result of a conspiracy: The $W \to \tau\nu$ background alone gives a bias of -80 MeV, while the $Z \to \ell\ell$ background gives a bias of $+70$ MeV; both sources of background can vary independently within the uncertainties given above. The other backgrounds have negligible impact. Thus, the estimated bias per percent relative error on the background normalization (checked to scale linearly with the size of the background) is:

$$\partial M_W / \partial N_{\tau\nu-\mathrm{bkg}} = -0.8 \text{ MeV}/\%, \quad (8.1.1)$$

$$\partial M_W / \partial N_{\ell\ell-\mathrm{bkg}} = 0.7 \text{ MeV}/\%. \quad (8.1.2)$$

For completeness and in spite of the mentioned difficulties, the impact on the M_W measurement from

the QCD background is taken from [ATL08b] to be:

$$\partial M_W / \partial N_{QCD-\mathrm{bkg}} \quad = \quad 0.05 \text{ MeV}/\%. \tag{8.1.3}$$

Note that the backgrounds are evaluated by fitting the transverse lepton p_T distribution and assumed to be valid also in the transverse mass fit. This of course need not to be the case, but there is little reason to suspect that the transverse mass distribution should suffer significantly more from backgrounds than the p_T^l distribution.

8.2 Pileup and underlying event

The soft hadronic activity accompanying the hard process (underlying event), and the overlap with soft events produced in the same bunch crossing (pile-up) generate additional particles that contribute to the detector occupancy. In particular, the additional calorimetric energy overlaps with the electron signal and distorts the scale measurement.

Typically, a soft event produces about 10 particles per unit rapidity (integrated over ϕ), with average transverse momentum $p_T \sim 500$ MeV [M$^+$05a, M$^+$05b]. An electron cluster of typical size $\Delta\eta \times \Delta\phi \sim 0.1 \times 0.1$ is expected to contain about 40 MeV of hadronic background, to be subtracted from the electron signal.

In particular, the hadronic background may have a non-negligible Q^2-dependence, generating a non-universality between W and Z events. These effects are small, but need to be properly accounted for when aiming at a precision on the absolute scale of $\delta\alpha/\alpha \sim 2 \cdot 10^{-5}$.

This aspect was not studied here, but the argument of [ATL97a] is followed. By measuring the energy flow away from any high-p_T objects, as a function of η, independently in W and Z events, a 2% precision on the hadronic energy flow looks achievable. Such a result would bring down the size of the effect from 40 MeV to about 1 MeV.

Thus, it is concluded that although soft hadronic interactions generate shifts in the energy measurements which are large compared to the statistical sensitivity to M_W, these shifts can be measured in the data with sufficient accuracy. The final contribution to δM_W is small. This source affects the electron scale and the recoil measurement; the muon scale is not affected.

8.3 Beam crossing angle

According to the specifications of the LHC accelerator, the proton beams are brought to collision at an crossing angle of 142.5 μrad [BHO99]. In terms of momentum, this translates into a 7000 GeV/c $\cdot$ $142.5 \cdot 10^{-6} \approx$ 1 GeV/c boost in the horizontal plane, per beam proton. In the simulation however, protons collide head-on, giving rise to a systematic shift in p_x^W of all particles produced. In addition, the simulation fails to take into account the momentum-spread of the beam particles - an effect which might increase the smearing of the quantities used for the W mass determination. In order to study the bias introduced to the W mass measurement from these sources, software was developed allowing to boost and smear the four vectors of the particles produced in a collision [Kli08]. The modification takes place at the generation level - i.e. before passing the generated particles through the detector. Since any realistic boost or smearing is merely a perturbation of the usual event record, the detector in

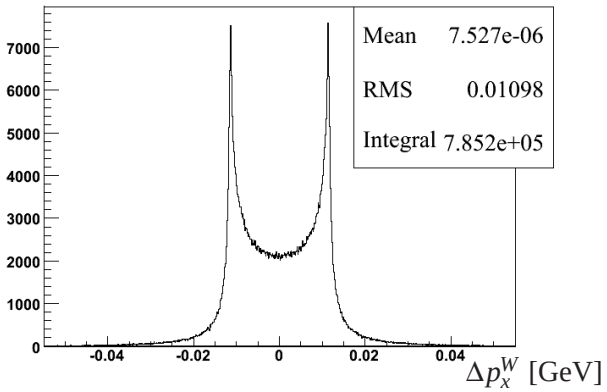

Figure 8.3.1: *Distribution of difference in the transverse W momentum resulting from the boost,* $\Delta p_x^W = p_x^W - p_x^{boost}$.

assumed to respond similarly in the two cases. For this reason a study was performed using Resbos Z, and W samples, where larger statistics can be afforded [BY97]. In figure 8.3.1 is shown the difference in the transverse W momentum resulting from the boost. Obviously the boost causes a shift in p_x^W and therefore $p_\perp$ in the individual event, but what is important for the present analysis is, that on the average, $p_\perp^W$ is approximately unaffected by the boost, as it should be as most of the effect is averaged out by the rotational symmetry. By this, as many W's increase- as decrease their $p_\perp^W$, and by the same amount (in average). Note that the magnitude of the spread is as one would expect from x_W which has central value around $x_W = M_W / p_{beam} \approx 0.006$, by which the expected central $p_\perp$ difference is: $x_W \cdot 2$ GeV$/c \approx 11$ MeV/c - coinciding with the peaks observed in figure 8.3.1.

The size of the effect is estimated as usual, by including the p_x^{boost} in the pseudo-data and letting the templates unchanged. The effect is found to be smaller than 0.1 MeV.

The beam spread has an influence on W events similar to that of the beam crossing angle: The individual events may be shifted in $p_\perp$, whereas $< p_\perp >$ is unchanged. Since the magnitude of the shift is expected to be smaller yet than in the case of beam crossing angle, it is concluded that also this contribution to the systematic error is insignificant.

During the study of the influence of the beam crossing angle on the W mass measurement a software package was developed. Since, the beam crossing angle and spread, despite its little influence on the W mass measurement, in principle affects all ATLAS analyzes, the code has been made public and is part of the standard ATLAS offline software repository. The connection of the tool to the remaining ATLAS reconstruction chain is depicted in figure 8.3.2. The tool can be steered, so that not only can

Figure 8.3.2: *The EventBoost algorithm. See [Kli08] for details.*

the events be boosted according to the LHC machine specifications, also the bunches can be smeared either as Gaussian ellipsoids or boxes. It is yet unknown which of the two (if any) is the more realistic, and of course other bunch shapes are easily implemented.

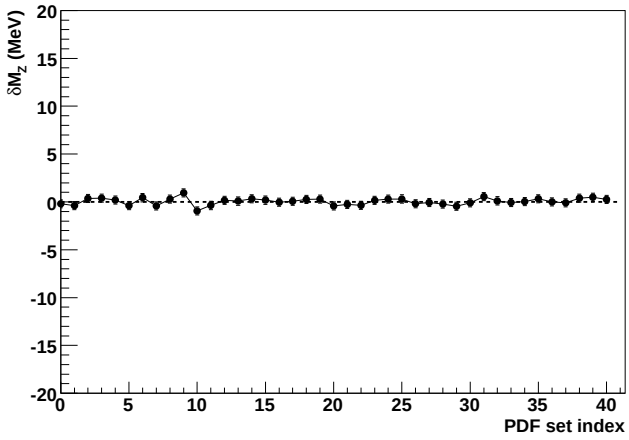

Figure 8.4.1: *Bias on M_Z obtained when varying the proton PDFs within their uncertainties. Each point on the abscissa corresponds to a given PDF set: Set 0 is the best fit, and gives 0 bias by definition; sets 1-40 are the uncertainty sets, each inducing a given bias on M_Z. The total uncertainty is given by the quadratic sum of the biases. The result is: $\delta M_Z \sim 2.5$ MeV.*

8.4 Correlations

So far, all main sources of systematic uncertainties have been investigated independently. Before moving to the combination of the results, it needs to be addressed whether important correlations are to be expected between the sources. It is however beyond the scope of this work to discuss this issue extensively, and this section concerns only the most important examples.

The uncertainty related to the absolute scale has the strongest lever arm on the determination of M_W ($\delta M_W/\delta\alpha = 1$). Therefore, it is investigated below whether uncertainties which affect the W mass measurement can also bias the absolute scale.

8.4.1 Absolute scale vs. PDFs

Z boson mass templates are produced with the CTEQ6.1 central set and compared to pseudo-data produced with the 40 uncertainty sets. The results of the 40 fits are displayed in figure 8.4.1, in the form of biases with respect to position of the mass peak obtained in the templates. The CTEQ6.1 uncertainty sets induce typical biases of $\sim$0.5 MeV with respect to the central value. Summing over all uncertainty sets gives a total scale uncertainty of about 2.5 MeV. This translates into $\delta M_W \sim 2.2$ MeV.

In other words, with current knowledge, the PDF uncertainties induce a direct systematic uncertainty of about 25 MeV via distortions of the W distributions (cf. section 7.3.1), and an indirect uncertainty of 2.2 MeV via distortions of the Z line-shape, propagating to the absolute scale determination.

Hence, the conclusions of section 7.3.1 are essentially unchanged. Using measurements of the Z boson distributions, the PDF induced systematic uncertainty should drop to about 1 MeV.

8.4.2 Absolute scale vs. QED corrections

QED corrections affect the determination of the absolute scale in two ways.

First, as was mentioned in section 7.2, the observed W and Z decay lepton spectra are strongly affected by photon emission. This effect needs to be taken into account properly when producing the Z mass templates. In muon final states, the theoretical distributions are based on the final muons, after simulation of the QED photon emissions. Final state electrons can not be separated experimentally from the mostly collinear photons. Hence, the simulation needs to reproduce this recombination precisely. This demands precise theoretical control of the photon distributions, an aspect which seems under sufficient control (cf. section 7.2). Likewise, a precise description of the detector geometry and electromagnetic calorimeter (EMC) shower development in the simulation are needed to properly simulate the fraction of photon energy recombined in a given electron cluster.

Secondly, as a consequence of the above, the absolute scale extracted from Z events actually corresponds to a mixture of photons and electrons. In ATLAS, the EMC response to electrons and photons is different by about 1%, an effect coming from calorimeter geometry (because their showers develop differently, electrons and photons of a given energy do not "feel" the same sampling fraction) and from the passive material in front of the EMC, which causes early showers or conversions, with different probabilities for both particle types [ATL96b]. It is thus important to know whether W and Z behave similarly in this respect, and if any difference is well understood theoretically.

As is shown in figure 8.4.2, the electron energy fraction in electromagnetic clusters differs by about 0.6% between W and Z events, meaning that the energy scale measured in Z events needs to be corrected by a factor $1\% \cdot 0.6\% = 6 \cdot 10^{-5}$.

Failing to take this factor into account would induce a bias of ~ 5 MeV on the M_W fit. However, figure 8.4.2 also shows a good stability of the theoretical prediction. Hence, although this correction is not negligible, it does not carry a significant uncertainty.

8.5 Impact on the W mass measurement

Below the main results are summarized. Table 8.5.1 recalls the main systematic contributions to the p_T^l- and M_T^W-based M_W measurement, with 10 fb^{-1} of data. In both tables, numbers are given for the electron and muon channels separately when applicable.

The major difficulty is, as expected, the determination of the absolute energy scale of the experiment. The analysis of the Z peak however allows to strongly constrain this uncertainty. The analysis is non trivial, because in addition to the Z mass parameters, many other effects enter the theoretical description of the line-shape; most notably, QED radiation. Although the effect is large, the theoretical understanding is adequate, as the LEP1 Z mass measurement indicates. The Z mass relies on an analytical formulation of the QED corrections; the W mass measurement at the LHC however requires a complete MC implementation at the same level of precision.

The electron channel appears somewhat more difficult than the muon channel. The first reason is the p_T-dependent electron identification efficiency, which distorts the Jacobian distributions. This effect is essentially absent in the muon channel. The second reason is again related to QED radiation: Since the muons do not recombine with the emitted photons, the description of the effect is purely theoretical. In the case of electrons, a large fraction of the radiated energy is included in the electron

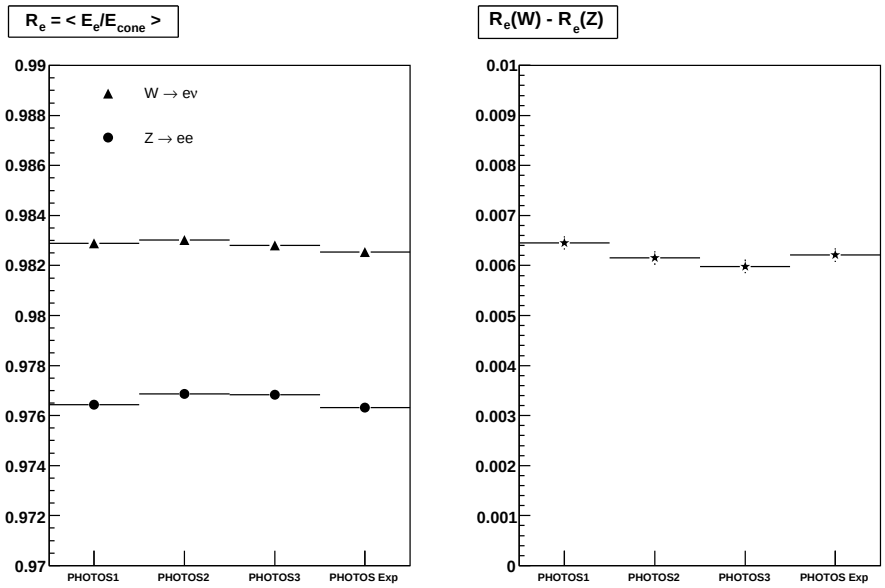

Figure 8.4.2: *For electron final states in W and Z events, the energy fraction R_e deposited by electrons in reconstructed electromagnetic clusters (1-R_e is photon energy), for various* `PHOTOS` *settings (see section 7.2).*

cluster. Determining this fraction requires a precise description of the detector geometry, and reliable simulation of electromagnetic showers.

The uncertainties related to the description of the y^W and p_T^W distributions are estimated to be small once the Z differential cross-section has been measured. The largest remaining systematic comes from the modeling of p_T^W, in the p_T^l-based measurement, contributing a 3 MeV uncertainty. The M_T^W measurement is more stable in this respect. This advantage, however, is compensated by additional experimental complications related to the experimental control of the $\not\!\!E_T$ reconstruction. As discussed in section 7.3, this result relies on the assumption of light quark flavor and charge symmetry in the low-x, high-Q^2 proton. Relaxing these hypotheses within bounds allowed by the existing data is presumably unlikely to invalidate the result.

Backgrounds contribute an uncertainty $\delta M_W \sim 2$ MeV. Of all components, the background from jet production is the least well known, but its contribution is expected to be small. The possible impact of cosmic rays and hadron decays in flight, which occur in the muon channels, is not investigated, but Tevatron experience indicates the impact is small [CDF07a].

The most questionable uncertainties are the recoil scale and resolution. The estimates presented are based on the assumption of a totally unbiased $\not\!\!E_T$ evaluation. A method has been presented to evaluate the possible bias of $\not\!\!E_T$ in data, and it is likely that this will indicate that a significant systematic uncertainty must be added in the M_T^W measurement. However, at the present time, it is not possible to estimate this systematic error with any certainty, and therefore the number quoted in table 8.5.1 is based on the Tevatron experience.

All in all, a total uncertainty of $6-7$ MeV can be achieved, in each channel, using either the p_T^l of the M_T^W method, with the equivalent of 10 fb^{-1} of data. Most sources of systematic uncertainty are expected (and assumed) to scale with the accumulated Z statistics; notable exceptions are backgrounds,

QED radiative corrections and the underlying event. Their contribution to δM_W is however subdominant. Combining channels, and allowing for more data, one can therefore expect further improvement.

8.6 Conclusions and perspectives

The most important systematic uncertainties affecting the W mass determination at the ATLAS experiment have been investigated. It is found that the analysis of Z production constrains most of the systematic uncertainties to a total of $6-7$ MeV per channel, exploiting 10 fb^{-1} of data. Increasing statistics may allow to move towards $\delta M_W \sim \delta M_Z$, an absolute lower bound on the LHC timescale.

Among all investigated sources of systematic uncertainty, two items in particular rely on assumptions. The first one concerns the treatment of QED radiation. It is argued that the theory is under very good control, having notably allowed a very precise Z mass measurement at LEP1, where QED effects are large, but the uncertainties finally have an almost negligible contribution. To preserve this situation at the LHC, the M_W measurement requires QED simulation tools providing the same level of accuracy.

The second assumption concerns the effect of the light sea asymmetry in the proton. Relaxing the symmetry assumption in use in the current global QCD fits will cause some decorrelation between W and Z production at the LHC. This decorrelation is expected to be small, but will have to be measured using the LHC experiments, notably using the rapidity-dependent W charge asymmetry, $(\sigma_{W^+} - \sigma_{W^-})/(\sigma_{W^+} + \sigma_{W^-})$, and the study of associated W + charm production.

A number of obvious sources have not been studied explicitly, notably the underlying event (affecting the electron energy scale) and W polarization effects (affecting the leptonic angular distributions). It is believed these mechanisms can be brought under sufficient control, on the time scale of the LHC measurement of M_W.

The results presented here have only exploited Z boson measurements. Many other robust calibration processes exist, that give additional constraints on the detector performance and on the physics mechanisms influencing W production. While first providing a way to verify the robustness of the Z-based calibrations, these processes can help to reduce the uncertainties further in the case of consistent results. These refinements are reserved to the analysis of the forthcoming ATLAS data.

Note that CMS is expected to achieve similar sensitivity as ATLAS with mostly uncorrelated systematics (since the lepton scale determination causes the largest error) [B$^+$07b].

Source	Effect	$\partial M_W/\partial_{rel}\alpha$ [MeV/%]	$\delta_{rel}\alpha$ [%]	δM_W [MeV]
Prod. Model	W width	1.2	0.4	0.5
	y^W distribution	–	–	1
	p_T^W distribution	–	–	3
	QED radiation	–	–	<1
Lepton measurement	Scale & lin.	800	0.005	4
	Resolution	1	1.0	1
	Efficiency	3.6	0.15 (e)	0.5 (e); 0.3 (μ)
	Tails	–	–	1 (e); 0.5 (μ)
Recoil measurement	Scale	–	–	–
	Resolution	–	–	–
Backgrounds	$\tau\nu$	-0.8	2	1.6
	ll	0.7	2	1.4
	QCD events	0.05	10	0.5
Pile-up and U.E				<1 (e); $\sim 0(\mu)$
Beam crossing angle				<0.1
Total (p_T^l)				$\sim$6

Source	Effect	$\partial M_W/\partial_{rel}\alpha$ [MeV/%]	$\delta_{rel}\alpha$ [%]	δM_W [MeV]
Prod. Model	W width	3.2	0.4	1.3
	y^W distribution	–	–	1
	p_T^W distribution	–	–	1
	QED radiation	–	–	<1
Lepton measurement	Scale & lin.	800	0.005	4
	Resolution	1	1.0	1
	Efficiency	3.6	0.15 (e)	0.5 (e); 0.3 (μ)
	Tails	–	–	1 (e); 0.5 (μ)
Recoil measurement	Scale	-200	–	–
	Resolution	-25	–	–
	Combined	–	–	5
Backgrounds	$\tau\nu$	-0.8	2	1.6
	ll	0.7	2	1.4
	QCD events	0.05	10	0.5
Pile-up and U.E				<1 (e); $\sim 0(\mu)$
Beam crossing angle				<0.1
Total (M_T^W)				$\sim$7

Table 8.5.1: *Breakdown of systematic uncertainties affecting the M_W measurement, when using the p_T^l distribution (top) and the M_T^W distribution (bottom). The projected values of $\delta_{rel}\alpha$ are given for a single channel and assume an integrated luminosity of 10 fb^{-1}.*

Part III

Simulation of the Transition Radiation Tracker

Introduction to Part III

The precision measurement of the W mass discussed in the previous chapters relies on the performance of all sub-detector systems and their description in the software. This part of the thesis concerns itself with the simulation of the ATLAS experiment - in particular the TRT sub-detector. Since this sub-detector contributes to the momentum resolution about as much as the Pixel and SCT combined, the TRT, including accurate simulations of its performance, is of integral importance for the W mass measurement, as well as for many other ATLAS analyzes. As discussed in section 8.4, accurate knowledge of the detector geometry with respect to both active and non-active material is important when estimating the systematic error on M_W arising from QED corrections.
In chapter 9, the implementation of the detector geometry in the simulation is introduced. Summarized in this chapter is also the software implementation of the TRT geometry as it appears after an update based on survey data from the TRT assembly. In chapter 10, the digitization scheme used in the TRT is discussed, focusing on a number of updates in the underlying model, which have been implemented. The results of these updates are in chapter 11 compared with corresponding results obtained in test-beam data. The transition radiation model, and a tune to the same is presented in chapter 12, whereas an example of the usage of the TRT for reconstruction of photon conversions is presented in chapter 13. One expected application of this is in situ updates of the detector geometry, but before entering this discussion, the next chapter describes how the initial geometry is determined, and how it is described in the software.

Chapter 9

Simulation and detector description

In order for the ATLAS experiment to be a useful tool to gain knowledge of the physics taking place during and after the collision of two proton beams, the simulation of the detector response is of utmost importance. The complexity of not only the final states but also the detector itself calls for precision simulation allowing for detailed comparisons with data.

The simulation of events proceeds in several steps: First event generators simulate the primary hard physics process. The output in terms of particle types and their four vectors is subsequently passed to the detector simulation which propagates the particles through the detector while simulating its interactions with the traversed material. For interactions with active material - i.e. some sub-detector volume, the position, time and energy deposit is recorded as a "simulation hit" (*simhit*). Based on collections of *simhits* the task for the digitization is to simulate the detector response as it would appear in the real detector. Finally tracks, clusters etc. are found by the reconstruction algorithms regardless of whether the input is that coming from the digitization software or from the real detector.

Event generation: In the ATLAS experiment a number of specialized event generators are used, each favored for some special application. However, most physics groups have some usage of multi-purpose event generators such as `Pythia` [SLMS03] and `Herwig` [C$^+$02] - at least to generate QCD background samples. Quite often the specialized event generators are linked to general purpose toolkits, which then take care of the hadronization of the underlying soft event.

Detector simulation: As opposed to event generators, the detector description and detector simulation takes place centrally using respectively the GeoModel [BT04, Bou03] and `GEANT4` frameworks [G403]. Apart from propagating tracks through the detector, the detector simulation also takes care of decaying any long lived particles on the way. For the propagation, detailed magnetic field- and detector geometry maps are utilized, so that the direction of each particle in a given step is calculated based on the initial particle momentum and the local fields (electrical or magnetic). Depending on the material and particle, the cross-section for all possible interactions with the material are calculated, and based on random draws, it is decided whether or not some given interaction takes place in the given step.

Although in many respects successful, the so-called *full simulation* as described above only have a somewhat limited usage. The reason is, that with $\sim$200 tracks in an average interesting physics event, the time spent for simulating the detector response exceeds 30 minutes per event on a standard computer (1 GHz). In the ideal world, e.g. the W mass analysis, would require $\mathcal{O}(10)$ times the number of simulated events compared to real data events. However, with $\mathcal{O}(100\ \mathrm{M})$ expected events,

this is simply not feasible. What is done throughout the physics groups is therefore to rely on different fast simulation schemes[1] as much as possible, and only use full simulation when it is absolutely required (and even in this case often with questionable statistics).

Digitization: Regardless of the level of precision of the simulation, the simulated events need to be digitized before comparison with detector output is possible. Whereas the simulation of particles passing through the detector is performed centrally regardless of sub-system, the digitization is carried out in custom software packages, as required due to the technological differences between the sub-detectors.

The approach used for the TRT is described in detail in chapter 10, but common for all sub-detectors is, that the task consists of transforming a list of *simhits* as supplied from the simulation, to a realistic digitized output as it would appear coming directly from the detector hardware.
For the TRT this requires that the energy deposit is translated to an amount of ionization, which is then drifted to some anode, where it gives rise to a signal. As is the case in the real detector, the signal is shaped and finally discriminated against some threshold in appropriate time-bins. Depending on whether the signal is above threshold, the output of the digitization (as from the real detector) is a stream of digits.

Reconstruction: Using calibration and alignment data, the complex task for the reconstruction algorithms is, by the use of numerous pattern recognition methods, to combine the various digits coming from the different detector parts into tracks and clusters. Due to the detector complexity, some effort has been invested in order to slim the output to ease practical aspects of the offline physics analysis. Also, to support the many different types of physics analysis expected, the output of the reconstruction algorithms comes in multiple formats with various amount of information and event sizes.

9.1 Detector description

The description of the ATLAS detector, and in particular the Inner Detector, is performed centrally within the GeoModel framework as outlined in figure 9.1.1. Sub-detectors are described in the software by separate software modules, called GeoModels, which along with the service structures such as cables and pipes, are built from primary numbers stored in a versioned database called the Detector Description Database. The simulation geometry needed by `GEANT4` is automatically generated from the GeoModel description using the Geo2G4 package. Similarly, the geometries necessary for the digitization and reconstruction are interfaced by the InDetReadoutGeometry package. Note that this approach, where all geometry information is stored centrally, ensures synchronization between reconstruction and simulation geometries.

Inside the different GeoModels, the sub-detectors are build from a hierarchical structure, each having a set of translational and rotational transformations related to it. One advantage of this is that effects such as misalignments, which may well concern different groupings of sensitive detector elements such as a TRT barrel module, can be handled easily. For example, aligning a TRT module can be done by a simple translation, based on a single vector, rather than moving the individual shells, radiators, straws etc. An example of this is shown in figure 9.1.2, where arrows indicate the individual movement of the TRT barrel modules (only arrows corresponding to the intermediate module layer are shown). This illustration is based on large scale test of the full simulation framework of ATLAS; the CSC

[1] Ranging from the most crude: A simple smearing of the generator level kinematics, to more advantaged approaches where the traversed detector parts are taking into account [S+06].

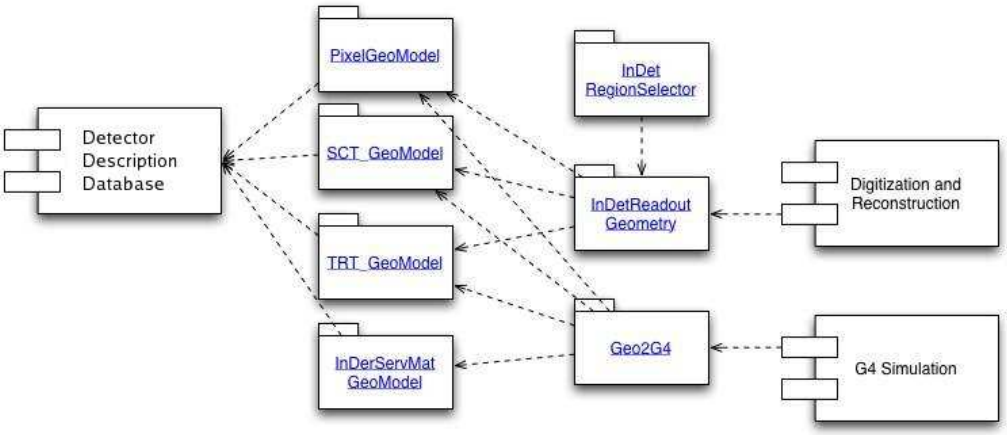

Figure 9.1.1: *Overall architecture of the Inner Detector GeoModel. On the left-hand side is the Detector Description Database. The middle boxes (with blue writing) refer to various geometry related C++ packages. The right-hand boxes indicate their connection with the remaining software (also C++ structures). Source [Gor08].*

production [AFGS+07] which, among other things, consisted of a test of the misalignability of the detector, and to what extent the reconstruction and calibration is able to correct for the misalignment. Other tests are related to the material density of the detector which is scaled in some regions.

When making misalignments or performing general development on the detector description, the complexity of the detector geometry requires continuous validation with specialized tools. One of the most common problems arising when performing such work is geometry clashes, i.e. volumes belonging to the same level in the hierarchical structure, which by mistake overlap each other (or they extent outside their "mother" layer). In the obvious cases, such overlaps may be so large that they can be spotted easily using detector visualization tools such as HEPVis [S+08] or the VP1 tool [K+08]. For illustration purposes, figure 9.1.3 shows an example from VP1 where a cooling tube is misplaced so that it accidentally overlaps with a TRT straw.

In less severe cases, overlapping volumes can be difficult to locate by visual inspection, and a commonly used method in such situations, is to simulate the response of non-physical particles called Geantinos. These particles do not have interactions but can report which detector elements they traverse and how much material they encounter. In a region of geometry overlap they will report their position as well as the names of the two volumes simultaneously encountered, hereby easing the bug finding for the developer. Even if there are no overlaps, Geantinos are useful to test the alignment of the various sub-detector volumes with respect to each-other (according to read-out geometry), since one can visualize the coordinates of the various sub-detectors hit, and compare with the expected straight line of the Geantinos (no interactions imply straight tracks).
An example of the usage of Geantinos is given in figure 9.1.4, where it is exploited that Geantinos apart from supplying the names of the encountered volumes, also can measure the amount of material traversed in terms of radiation lengths, λ.

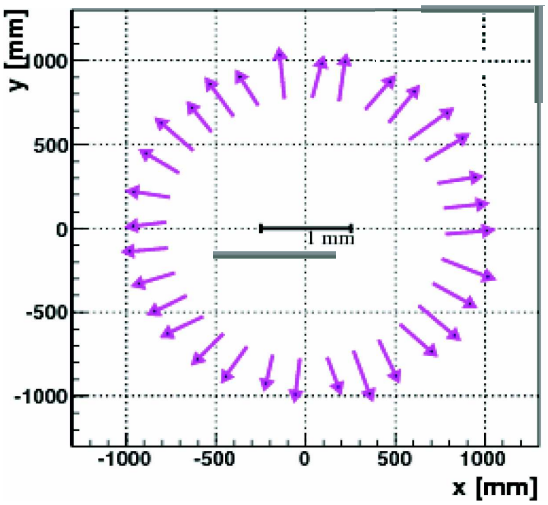

Figure 9.1.2: *Example from the CSC misaligned production. The individual TRT barrel layer 1 modules have been misplaced, and the task of the TRT calibration is to find and correct for the misplacements. Figure is provided by A. Bocci.*

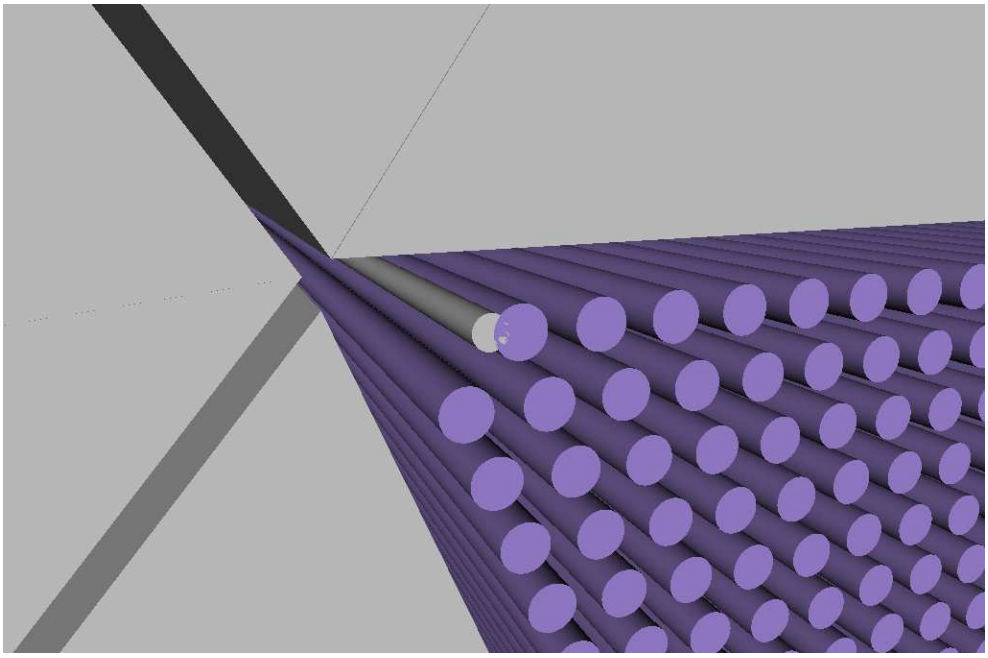

Figure 9.1.3: *Clash between a cooling tube and a straw in a TRT barrel module. Visualized using the VP1 tool.*

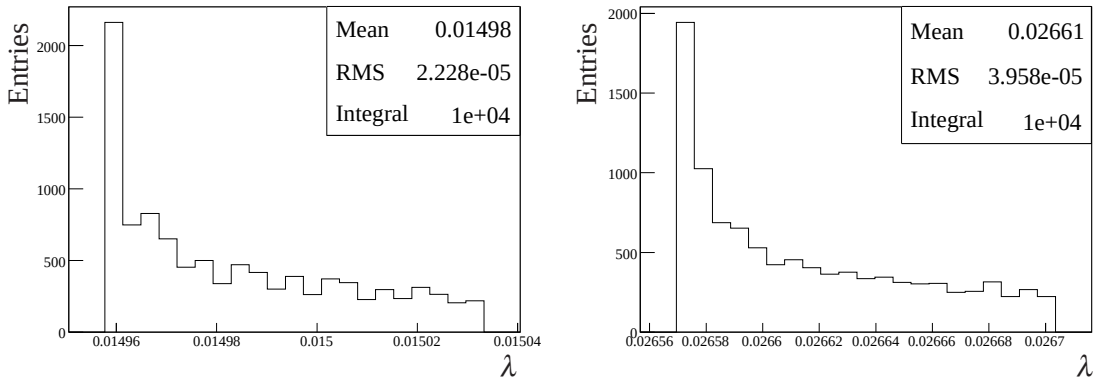

Figure 9.1.4: *Radiation lengths, λ, encountered by 10 K Geantinos fired in the region $|\eta| < 0.1$ before (left) and after (right) an update of a volume called TRT Barrel Outer Support (as the name suggests the volume describes support structures, see figure 9.1.7). Note that the distributions have the same shape, but the scale on the x axis differs, showing that the geometry was unaltered, only the density was increased.*

9.1.1 As built detector geometry

The ATLAS detector description consists not only of a description of the active volumes, but also accounts for non-active (dead) material such as support structure, wires, etc. For the TRT, the latter has recently been subject to a major revision, since the "as built" geometry and weight deviated significantly from what was outlined in the original design report [ATL97a]. The latter basically defined the TRT GeoModel until measurements of the assembled detector parts allowed for an update.

As described in [Gou06] the completed TRT detector was subject to detailed measurements of dimensions and weight in the assembly hall, and a significant effort was invested in blue print studies as well as discussion with constructors. Following this, the total barrel weight was observed to have increased by $\sim$10% with respect to the original design, mainly due to changes in the dimensions of the support structure volumes and material composition. Figure 9.1.5 shows the increase of material in the service region following the software implementation of the revised geometry.

Based on measurements for the end-caps [Gou07], a similar increase of weight was implemented in the software[2], with the addition, that survey data showed that the $\pm z$ symmetry previously assumed in the TRT GeoModel software could not be retained. When subsequently implementing these updates in the software a number of technical problems had to be resolved, such as frequent geometry clashes due to overlapping volumes - often between volumes belonging to different sub-detectors. To solve the puzzle, the whole hierarchical structure was revisited - a visualization of the resulting GeoModel structure is provided in figure 9.1.6.

A weight comparison between survey data and the updated GeoModel for both barrel and end-cap is given in table 9.1.1, whereas illustrations of the volume described in this table can be found in figures 9.1.7 and 9.1.6. Also, a visualization of the material increase is provided in figure 9.1.8. As can be seen in this figure, the increase of material especially pronounced in the transition region between the TRT barrel and end-cap, and consequently the negative impact on the physics performance is larger in this region.

In the software, the virtual detector is built to resemble the real detector geometry. However, this is

[2]The implementation was a joined effort between T. Shin and the author.

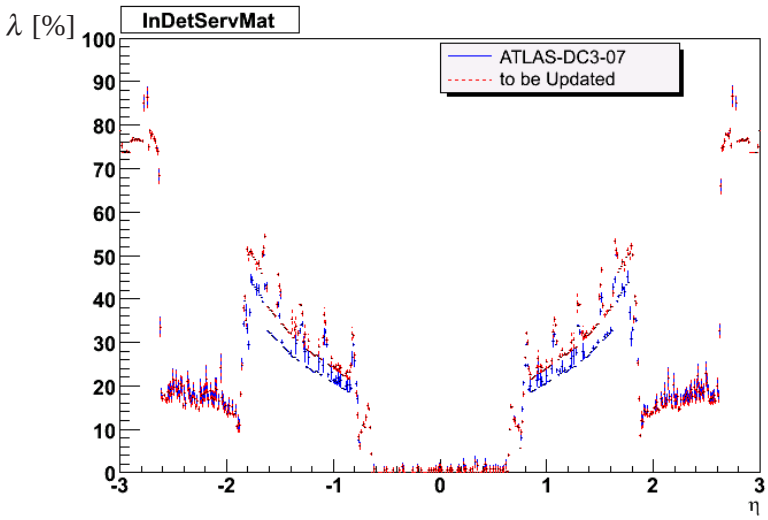

Figure 9.1.5: *TRT barrel material in terms of radiation lengths, λ, before (blue) and after (red) the major update discussed in the text. "ATLAS-DC3-07" is an example of a Geometry tag, which specifies a particular version of the Detector Description Database.*

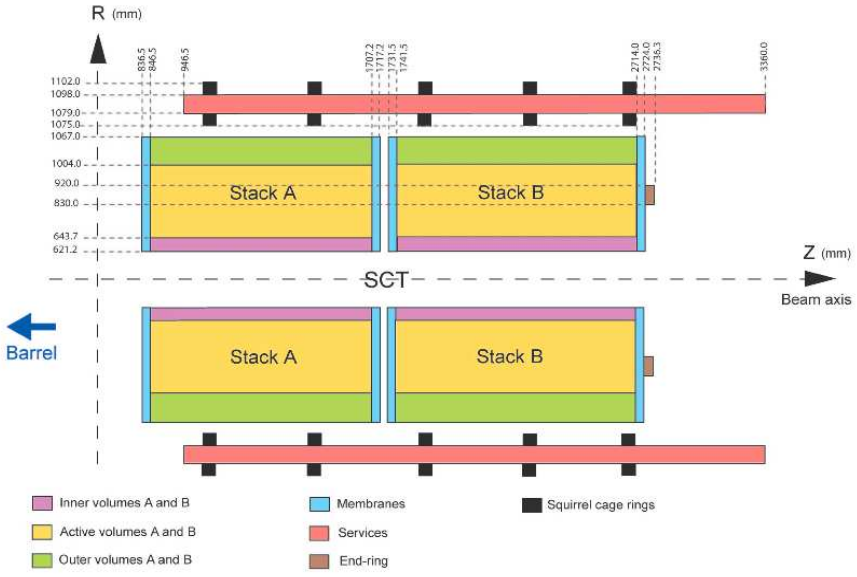

Figure 9.1.6: *Overview of volumes describing the TRT end-cap in the TRT GeoModel. The term "stack" denotes a collection of end-cap wheels.*

	Volume	Measured [kg]	GeoModel [kg]
Barrel	Active region	361.8	359.4
	End-Flange	226.4	226.4
	Services	25.4	25.4
	InnerSupport	23.7	23.7
	OuterSupport	65.6	65.6
End-cap	Inner Volume A	37.6	37.5
	Inner Volume B	33.5	33.5
	Active region A	92.1	97.5
	Active region B	104.0	100.7
	Outer Volume A	269.8	269.8
	Outer Volume B	276.3	276.4
	Membranes	48.4	48.3
	Services	219.0	218.9
	End-ring	11.9	11.6
	Squirrel Cages	36.1	36.7

Table 9.1.1: *Weight comparison between survey data and the updated GeoModel of the various TRT sub-detector parts.*

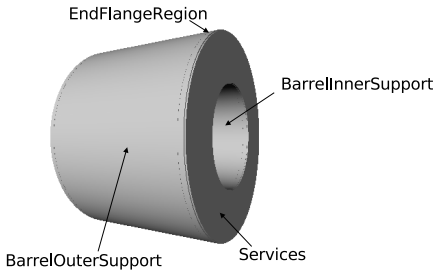

Figure 9.1.7: *The TRT barrel and services. Plot is provided by T. Shin.*

feasible only to a certain level of detail. In some cases, for example when describing airy volumes with a large number of cables from the detector read-out, it is not possible to exactly reproduce the real detector. What is done in this case is to determine the nuclear composition of the material (e.g. a cable) and describe the enclosing volume as consisting of homogeneously averaged material with the correct nuclear content but with a density scaled so that the overall weight corresponds to the measured. An example of this is shown in figure 9.1.4, where the density of a volume called BarrelOuterSupport (see figure 9.1.7) is scaled to match measurements of the detector, as determined in the assembly hall.

When adding new volumes to the GeoModel, corresponding new nodes (sets of primary numbers) are added in the Detector Description Database, and updates generally consists of updating a number of database entries while adding a few new ones. Subsequently, the software needs to be updated in order to be able make use of the new database entries to build the additional volumes. However, an issue of integral importance is backward compatibility; i.e. the fact that it must be possible, with the latest version of the software, to reproduce results computed with older versions of the software and older versions of the Detector Description Database. Also, this ensures that data, once stored, can always be reconstructed at a later point using an appropriate geometry. Due to this, the developer must constantly ensure that updated software, when presented with an older version of the Detector Description Database (communicated through a geometry tag), resembles the corresponding older version of the software. Some effort is invested to ensure backward compatibility without complicating the overall software structure or the readability of the code too much.

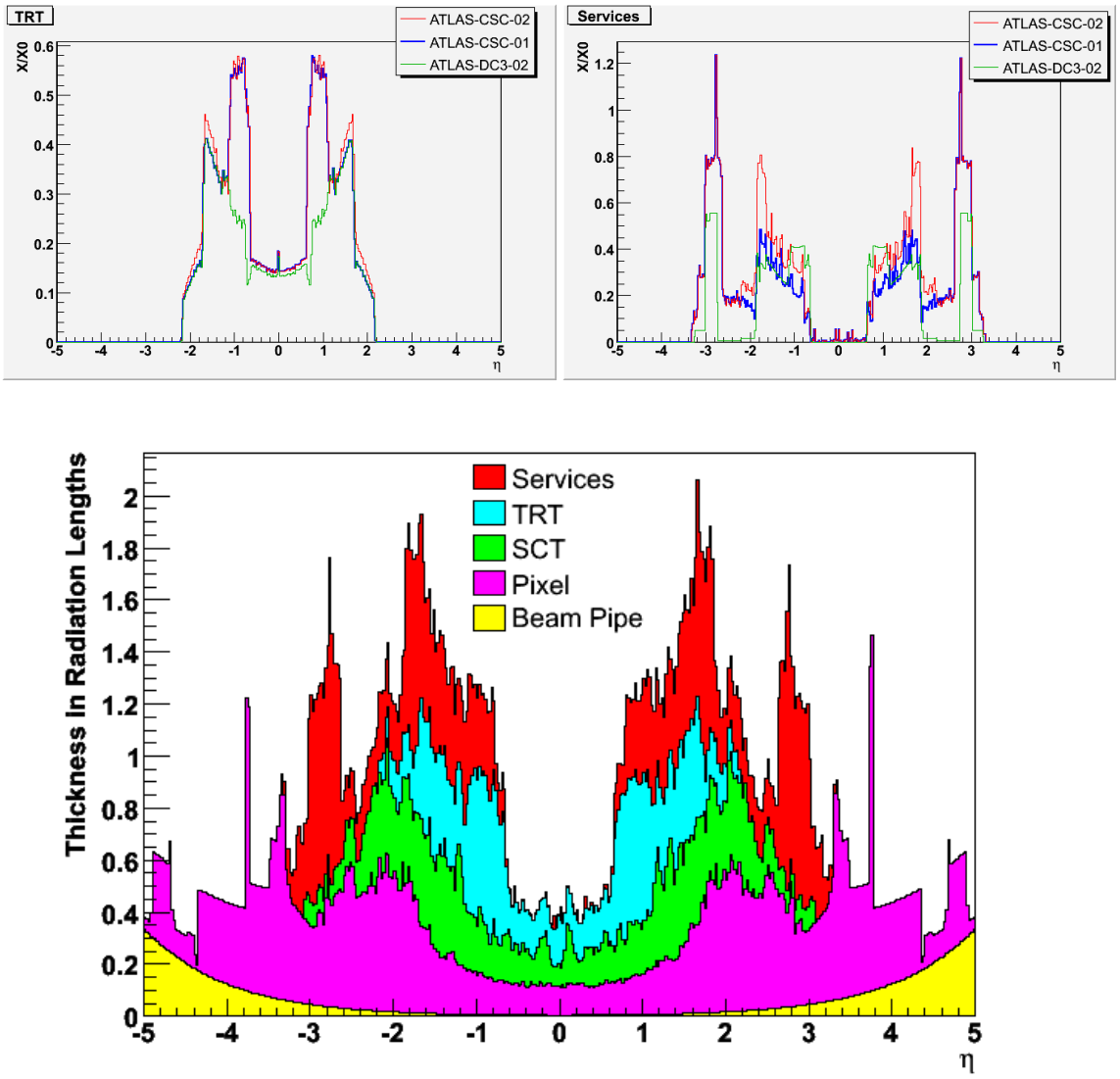

Figure 9.1.8: *Up: Updates in the TRT (left) and Services (right). The different histograms represent different geometry tags - the red histograms correspond to the most recent tag including the updates discussed in the text. Below: Present material budget of the Inner Detector [Gor07] (geometry tag: ATLAS-CSC-02).*

Chapter 10

TRT digitization

10.1 TRT thresholds and digitization scheme

The time-structure and amount of the energy deposited in a TRT straw when crossed by a particle, in principle holds a great deal of information, usable both for tracking and particle identification. For practical reasons, the analog signal in the wire is digitized in the front-end electronics before it, given a level 1 trigger, is read out by the higher level triggers and possibly stored offline. More specifically, the analog signal treatment (amplification and shaping) as well as the analog to digital conversion step is performed in the ASDBLR chips[1] while the links to the timing, trigger and read-out systems are handled by DTMROC's[2].

The analog to digital conversion proceeds via discrimination against two thresholds:

- LT: Low threshold used for tracking. Approximately corresponding to the signal height produced by a single electron cluster with a deposit of 300 eV.
- HT: High threshold used for detecting the absorption of energetic photons emitted by electrons (mostly) through transition radiation. The high threshold is usually set in the range 5-7 keV. Chapter 12 discusses transition radiation and explains why a HT setting in this range is optimal.

With respect to the LT, the 25 ns period corresponding to one bunch crossing, is divided into 8 bins of approximately 3.125 ns (giving a resolution of $3.125\ \text{ns}/\sqrt{12} \approx 0.9$ ns), and in each bin a single bit is stored, indicating whether the LT was exceeded (1) or not (0). Regarding HT, only one single bit is stored, representing the whole 25 ns period. Data is then read out in 75 ns segments, requiring a total of 27 bits per read out straw.

The terminology used in the following will be, that a digit has a HT if at least one of the three possible HT bits is set, and the term *bit pattern* refers to the pattern of the 24 LT bits. A few examples of typical bit patterns are shown in table 10.1.1.

Since the energy loss of particles passing through matter (i.e. dE/dx loss as described by the Bethe-Bloch equation [PDG06]) depends on the γ-factor, the probability of a given LT bit being set depends on the γ-factor of the penetrating particle. Due to the large mass difference between the most abundant

[1] Abbreviation for Amplifier/Shaper/Discriminator with Baseline Restoration, see [BNVBW96] for details.
[2] Abbreviation for Drift Time Measuring Read Out Chip, see [A$^+$01] for details.

Bit Pattern	HT	LT Bit Pattern	Typical cause
0 00000000 0 00001111 0 11111000	off	000000000000111111111000	Passing π
0 00000000 1 11111110 0 00000000	on	000000001111111000000000	Passing e
0 00111110 1 00000011 1 11111110	on	001111100000001111111110	π followed by e

Table 10.1.1: *Three examples of TRT digits and their typical physics causes.*

particles: π, p, e and μ, their γ-factors generally differ significantly for comparable momenta, and thus the bit pattern contains particle identification information simply from the number of LT bits being set. To make use of this, a parameter called time-over-threshold, ToT, is defined. ToT represents the number of set LT bits between the leading edge (the first set bit encountered from the left-hand side) and the trailing edge (the last set bit). In case the last bit set coincides with the last bit in the string, the ToT is set to zero. Note that this definition is somewhat ambiguous: For example one could count as well unset bits in between the leading- and trailing edge, and in fact this was done in earlier versions of the software[3]. A study of the energy loss in the TRT and its usability for particle identification purposes is given in [Ric08].

10.2 General digitization outline

The task of the TRT digitization software is, based on *simhits*, to generate a list of digits for each straw simulating the output of the read-out electronics of the real detector. The TRT digitization package is based on the energy deposits supplied by the simulation. For the TRT, however, the default `GEANT4` simulation approach turns out to be inaccurate to simulate the physics of a charged particle passing through the very thin gas layers. Customized packages called the Transition Radiation model (TR) [Dam04] and Photon Absorption and Ionization model (PAI) [AC80] perform the creation transition radiation, and the energy loss of charged particles due to ionization respectively. The results, in terms of a timed list of energy deposits, are propagated to the TRT digitization where they constitute the primary input. Using the known ionization potential, the content of the list is interpreted as clusters corresponding to a number of initial electrons at a given point in space and at a given time. The primary task of the digitization is to simulate the drift of these electrons to the anode wire, and to model the response of the front-end electronics to the signal thereby created.
The TRT digitization software has a long list of contributers[4] The present structure is mainly due to T. Kittelmann [Kit07]. Below, a number of updates in the model are discussed, but it is emphasized, that the overall framework is not due to the author.

10.3 The physics of electron drift - A simplified model

In order to understand and improve the simulation of electron drift toward the anode, it is beneficial to develop a simplified model. The predictions of this model can then be compared to a very detailed gas simulation performed by a program called Garfield [Vee93], which in itself is much too detailed and computational heavy to be used in any large scale simulation of detector response. The simplified model is not intended nor able to provide precise drift times or spread, but by comparing the results

[3] ATLAS offline software release 12 and older [OAC+06].
[4] Some of whom are: P. Nevski, F Luehring, D. Barberis. and K. Assamagan

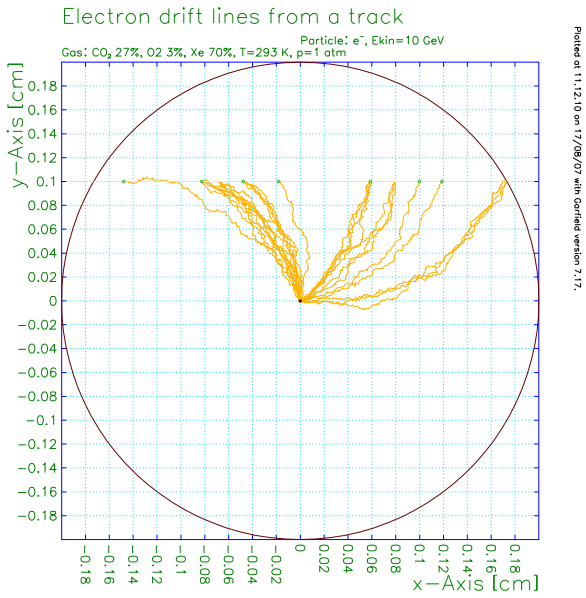

Figure 10.3.1: *Snapshot of electron drift according to Garfield simulation with a 2 T magnetic field perpendicular to the plane of the paper.*

with the Garfield simulation, it helps understanding the dependence of the various parameters, and can thus pinpoint where the TRT digitization can be improved. In the following, a simple model is built which describes the drift of an electron to the anode wire.
In general, the time, t, spent for an electron to drift from its initial position to the anode wire can be expressed as the following integral along the electron path:

$$t = \int_{path} \frac{1}{v(s)} ds \tag{10.3.1}$$

Since the electrons undergo scattering while drifting toward the anode, one might expect that the effective drift distance is prolonged with respect to the direct path. One way to parametrize this is to rewrite the length of the electron trajectory to an effective length given by:

$$s \mapsto \sqrt{r \cdot (r+d)} \tag{10.3.2}$$

where r represents the length of the direct path, and d is a diffusion parameter. Apart from the electric field responsible for the overall drift, there is also a magnetic field, which over the volume occupied by a given straw can be assumed constant. To the extent that the field has a component perpendicular to the direction of drift (so that $\vec{E} \times \vec{B}$ is non vanishing) this tends to increase the drift distance as illustrated in figure 10.3.1. A simple parametrization of this is illustrated in figure 10.3.2, which also explains the parameters used below (note that in the following, only half the electron path is considered for simplicity). Assuming small deviations from the direction path, the figure gives:

$$r = \rho \sin\phi \rightarrow \phi = \arcsin(r/\rho) \approx r/\rho + \frac{1}{6}(r/\rho)^3 \tag{10.3.3}$$

The increase of the trajectory, Δ, thus becomes:

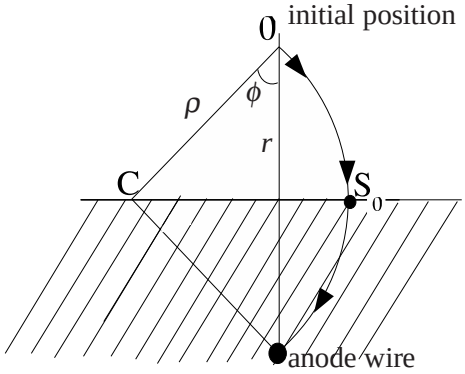

Figure 10.3.2: *Simplified electron drift under influence of a magnetic field. The electron path is assumed to be part of a large circle centered at C and with radius ρ. The hatched area is not considered for the development of the model - the factor of two from the increased path length is anyway absorbed in a constant.*

$$\Delta \propto \rho \cdot \phi - r \approx \rho \left(r/\rho + \frac{1}{6}(r/\rho)^3 \right) - r = \frac{1}{6} r^3/\rho^2 \tag{10.3.4}$$

In addition, since $p_\perp \approx 0.3\rho B$ by which $\rho \propto 1/B$, the following hold for the deviation, Δ: $\Delta \propto r^3 B^2$, where it is assumed that the mean transverse momentum is similar for all electrons.

So in the presence of a magnetic field component along the wire and therefore perpendicular to the electron drift, one expects, apart from the terms discussed above, an additional r^3 term which is proportional to B^2.

Taking into account that the expression for s already contains one factor of r, the revisited expression containing effects due to the deviation caused be the magnetic field reads:

$$s \mapsto \sqrt{r \cdot (r+d)} \cdot (1 + r(r+d))\, kB^2 \tag{10.3.5}$$

for some constant k.

In order to evaluate the integral of equation 10.3.1 a few approximations are needed; the first of which is to expand v as a power series:

$$v(s) \approx v_0 + v's + \frac{1}{2} v''s^2 + \cdots \tag{10.3.6}$$

by which the integral reads:

$$t = \frac{1}{v_0} \int_0^{S_0} \frac{ds}{1 + \frac{v'}{v_0}s + \frac{1}{2}\frac{v''}{v_0}s^2} \tag{10.3.7}$$

Keeping terms of the order s^2, the integral can be solved by a Taylor expansion:

$$t = \frac{1}{v_0} \int_0^{S_0} \left(1 - \frac{v'}{v_0}s - \frac{1}{2}\frac{v''}{v_0}s^2 + \frac{v'^2}{v_0^2}s^2 \right) ds = \frac{1}{v_0} \left(S_0 - \frac{1}{2}\frac{v'}{v_0}S_0^2 - \frac{1}{6}\frac{v''}{v_0}S_0^3 + \frac{1}{3}\frac{v'^2}{v_0^2}S_0^3 \right) \tag{10.3.8}$$

Inserting the expression for s (equation 10.3.5) and keeping terms of order r^3 leads to the following

expression:

$$\begin{aligned} t = & \frac{1}{v_0}\sqrt{r(r+d)}\left(1+kB^2r(r+d)\right) \\ & -\frac{1}{2}\frac{v'}{v_0^2}\sqrt{r(r+d)}\left(1+2kB^2r(r+d)+k^2B^4d^2r^2\right) \\ & +\frac{1}{v_0^3}\left(\frac{1}{3}v'^2-\frac{1}{6}v_0v''\right)\left(r(r+d)\right)^{3/2}\left(1+3kB^2dr\right) \end{aligned} \tag{10.3.9}$$

Obviously the above argument is crude, omitting a number of subtle effects. However it does qualitatively explain the behavior observed in figure 10.3.3, where the derived expression (equation 10.3.9), is tested against detailed Garfield simulations in the two cases: With and without magnetic field. The fits are performed in two steps. First the *magnet off* results are fitted and the parameters accessible: d, v_0, v' and v'' are then fixed before fitting the *magnet on* results. The results are the following:

$$\begin{aligned} d &= (0.0\pm1.6)\ \mu\text{m} \\ v_0 &= (62.6\pm1.1)\ \mu\text{m/ns} \\ v' &= (-1.7\pm0.5)\ \text{ns}^{-1} \\ v'' &= (-2.0\pm0.2)\ \mu\text{m}^{-1}\text{ns}^{-1} \\ k &= (1.22\pm0.02)\cdot10^{-8}\ \text{T}^{-2} \end{aligned} \tag{10.3.10}$$

Note that the negative sign of v' is expected since the electric field decreases as a function of radius, and that the magnitude of v_0 is reasonable compared to the expected 50 μm/ns [TRT08a]. The negligible value of d indicates that this parameter is inaccessible due to the approximations, i.e. the diffusion which must be present is absorbed in the other parameters. That diffusion indeed exists is obvious from the snapshot of a simulated event shown in figure 10.3.1.

In figure 10.3.4, the drift time is shown as a function of magnetic field magnitude in various configurations. The data is fitted using equation 10.3.9. The good description illustrates that only the field along the wire is relevant, and that the dependence on the drift time (for a constant drift distance) is quadratic as expected. Apart from showing the validity of the physics model, the fact that the two sets of measurements are described by the same fit illustrates that the constants multiplying the magnetic field term are the same in barrel- and end-cap-like geometry: Only the $\vec{B}$ field perpendicular to the drift influences the drift time. In the simulation, the drift time dependence on the magnetic field is implemented by using two sets of (r,t) measurements: One without field and one with $B = 2$ T (perpendicular). For each cluster, the components of the magnetic field are retrieved from the magnetic field map using the precise cluster position, and the drift time is computed from the parabola with vertex in the $t = (B = 0, r_{cluster})$ and intersecting the point $t = (B = 2\ \text{T}, r_{cluster})$. By this approach, the drift in any configuration of local (x,y) in the straw and with any $\vec{B}$ field is accurately described and simulated.

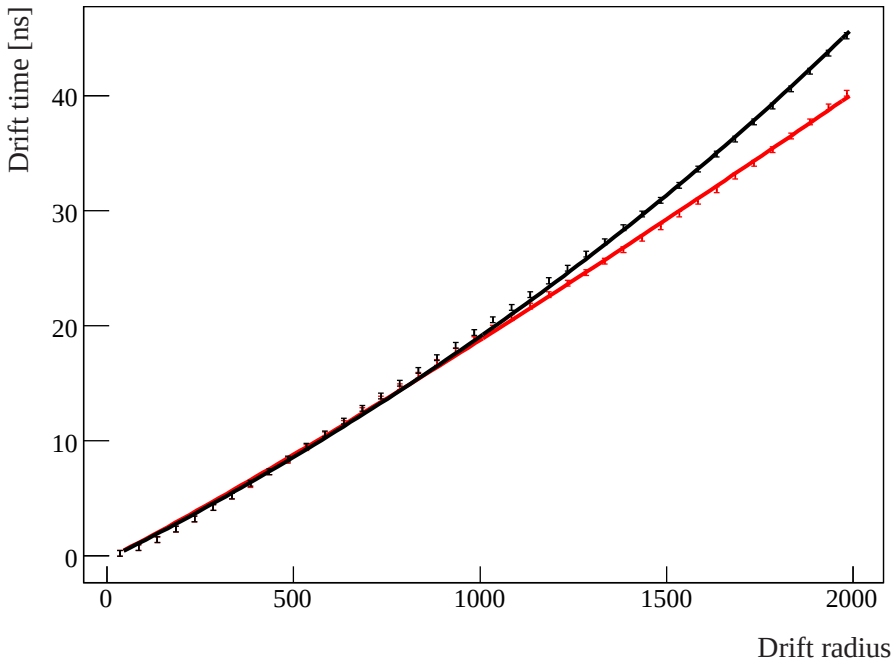

Figure 10.3.3: *Drift time as a function of drift distance without magnetic field (red) and with a 2 T field perpendicular to the direction of drift (black). The simulated data is fitted using the expression in equation 10.3.9.*

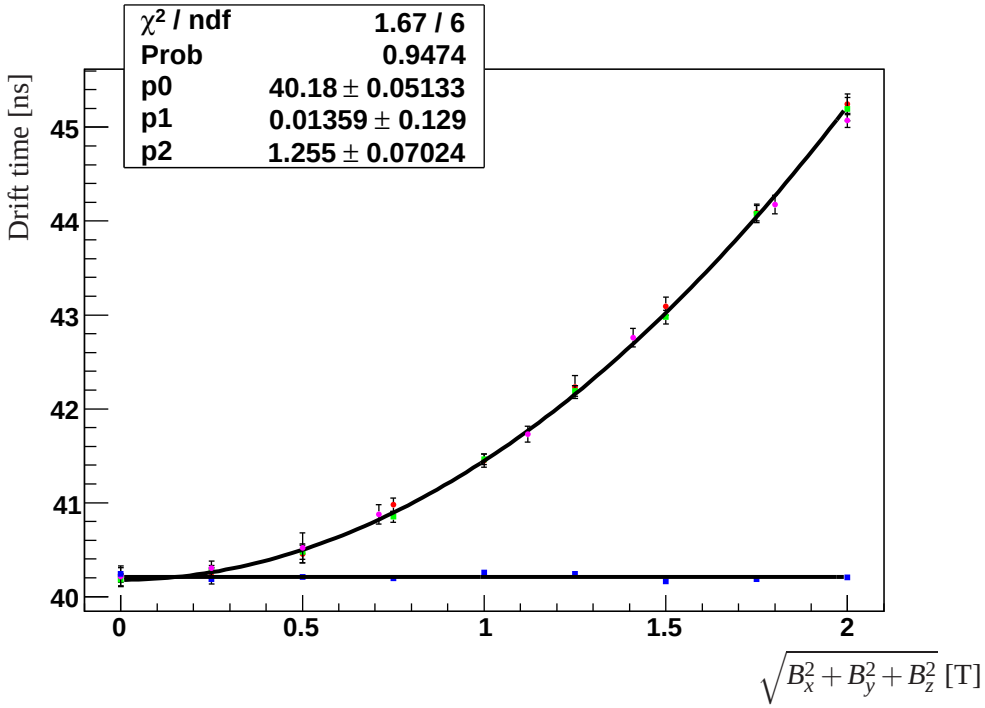

Figure 10.3.4: *Drift time as a function of magnetic field for straws (placed along the z direction, centered at $(x,y)=(0,0)$) based on simulations using electrons placed at $(x,y)=(0,2)$ mm (i.e. at the straw wall). Red and green correspond to $(0,0,B_z)$ and $(B_x,0,0)$ respectively. Purple is $(B_x,0,B_z)$ for various combinations, whereas the blue points are $(0,B_y,0)$. The latter fit is consistent with a constant.*

As briefly accounted for in the simplified model, the following effects are important in order to arrive at a precise simulation:

- **Input**: From the PAI model simulation a timed list of energy deposits and corresponding positions is retrieved.
- After correcting for the flight time, i.e. the time spent for a particle with light velocity to reach the straw volume, the overall drift due to the presence of the electric field is simulated.
- Once electrons start drifting, the presence of the magnetic field becomes important (depending on whether or not the electron drift has a component perpendicular to the field).
- Stochastic recapturing of drift electrons in the drift gas.
- Drift time spread.
- Gain amplification.
- Signal propagation time along the (direct and reflected).
- Discriminating the signal against threshold.

Apart from the effects of overall drift under the influence of the magnetic field, which has already been described above, these effects are treated separately below.

10.4 Determining the initial number of electrons in a cluster

Although the ionization energy for Xenon is only about 12 eV, measurements have shown that on average 25.3 eV is used per ionization [Cwe06]. The explanation lies in the fact that the ion gains energy by the ionization in terms of vibrations and excitation of gas molecules [Cwe06]. In the default simulation, no spread in the number of primary electrons was accounted for in the TRT digitization, but a detailed study reveals that this number, N, should fluctuate as a Gaussian with width; $\sigma = 0.19N$ [Cwe06]. In the present version, this has been implemented with the cut off, that no more electrons than $E_{cluster}[\text{eV}]/12$ eV can be produced (and no less than zero).

10.5 Recapture

When electrons drift toward the anode, there is some probability of them being recaptured by the electronegative oxygen in the gas. The details of the process are complicated due to the presence of the magnetic field which tends to stretch the energy levels of oxygen, hereby increasing the $O_2 + e^- \rightarrow O + O^-$ and $O_2 + e^- \rightarrow O_2^-$ cross-sections. The effect, however, is implemented in the Garfield simulation package allowing for detailed study.

In the previous versions of the TRT digitization software, electrons were subject to a constant recapture probability of 60%. In figure 10.5.1(a-c) is shown the effect on the time-over-threshold distribution from changing this number. The distributions have the expected behavior: Reducing the number of electrons arriving at the wire reduces the time over threshold. Also shown is the effect on time over threshold for hits belonging to tracks depending on the distance of closest approach of the track to the

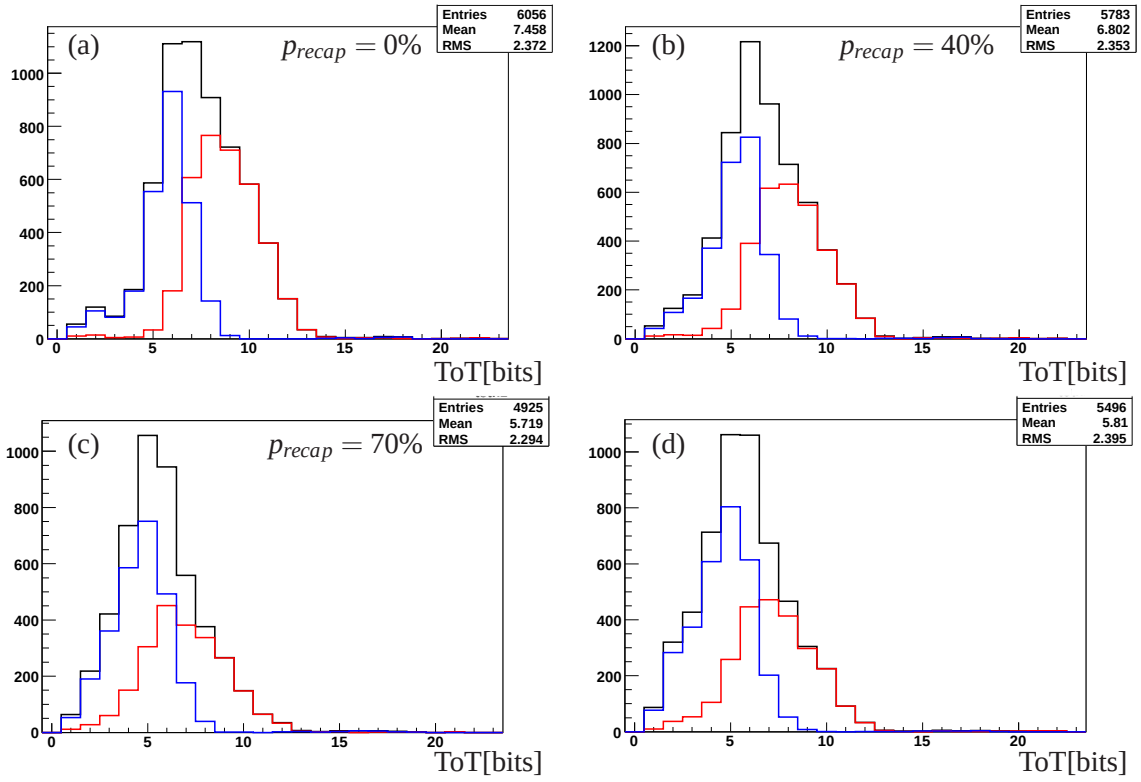

Figure 10.5.1: *Effect on time-over-threshold of the recapture probability: p_{recap}. Black curves are for all tracks, while, blue and red curves are for tracks with distance of closest approach to the anode wire less than- and greater than 1 mm respectively. (d) represents the recent implementation utilizing the reattachment curve of figure 10.5.2 rather than merely a constant reattachment probability as is the case in (a-c).*

wire, illustrating that time over threshold is influenced differently depending on the track orientation in the straw.

Inaccurately simulated time over threshold could influence the physics performance, since many analyzes require the time over threshold to exceed a minimum value to reject noise or select electrons, whose larger signal tends to cause a larger value of the time over threshold variable.

Figure 10.5.2 shows the results of a Garfield simulation of the recapturing probability in the gas used in the TRT. Not surprisingly there is a strong dependence on r. A satisfactory description is obtained by fitting the data using a fourth order polynomial as shown in the figure.

In the digitization, the fit curve is implemented in such a way that for each primary freed electron, a flat random number is discriminated against the curve and the electron is ignored in the digitization if this number is above the curve (i.e. using the 'hit and miss' technique [P^{+}95, PDG06]). This implementation gives rise to the time-over-threshold distribution shown in figure 10.5.1(d). A comparison of this figure to the corresponding distribution of the previous approach shown in figure 10.5.1(a-c) shows that the resemblance is largest for recapture probability; $p_{recap} = 70\%$, but in the present implementation the RMS is somewhat increased.

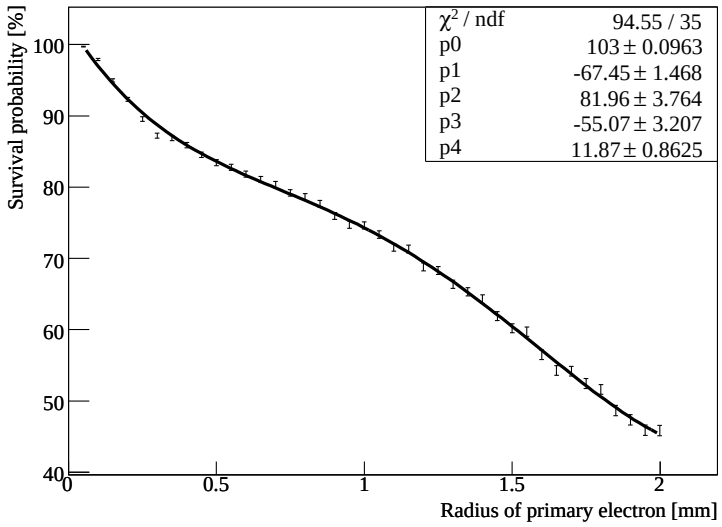

Figure 10.5.2: *Survival probability of individual electrons as a function of cluster radius with respect to the wire.*

10.6 Gain amplification and drift time spread

Closely related to the issue of recapture is the amplification of electrons during drift and the corresponding spread in the final number of electrons arriving at the anode wire.

Figure 10.6.1(left) shows the gain of single non-recaptured electrons as a function of the production radius r.

From studying the details of this figure, one can realize that not only does the gain depend on r, so does the spread of the gain. I.e. in order to get the distributions of gain correct for all values of r, it is necessary to fit the gain as a function of r and for each drifting electron choose a gain from one such distribution by using the *rejection principle* (also know as the "hit and miss" method [P$^+$95, PDG06]).

In figure 10.6.2 is shown two examples of fits to gain at different distances from the electron to the

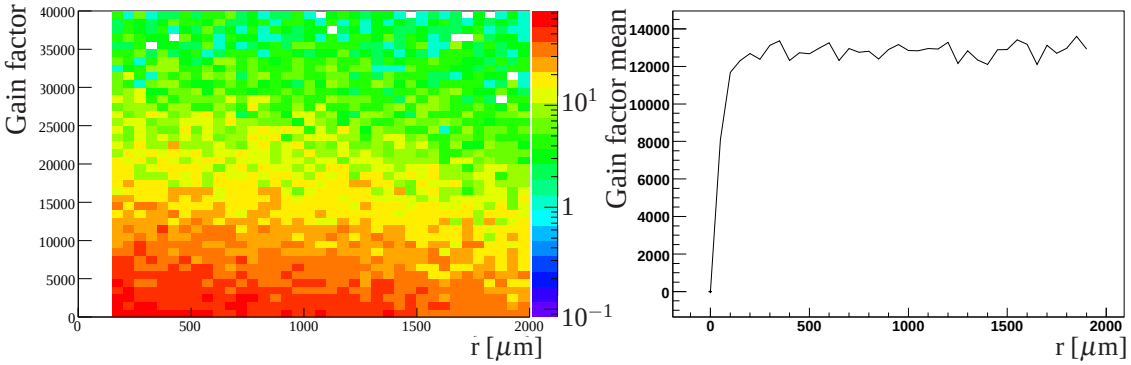

Figure 10.6.1: *Left: Distribution of gain for single (surviving) electrons as a function of their distance to the wire. Right: Mean values of the left-hand distribution connected by piecewise linear functions as implemented in the software (note that the left-hand distribution extents outside the plotted range).*

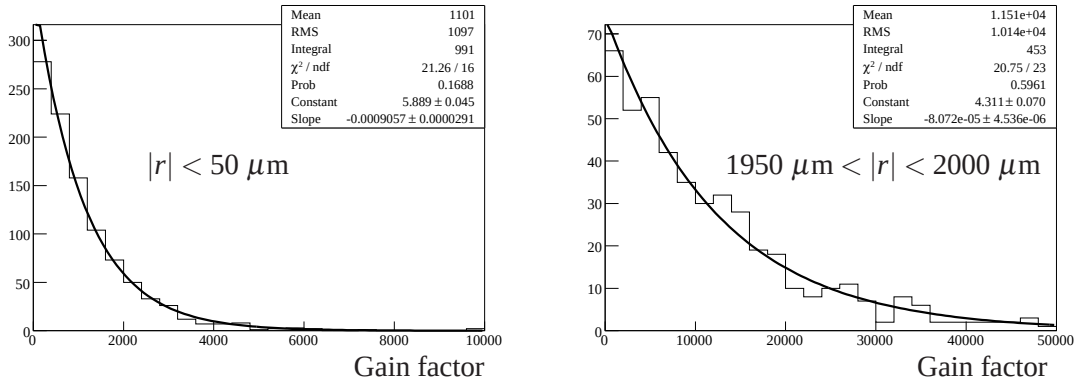

Figure 10.6.2: *Exponential fits to gain in two different bins of r. Notice the difference in plot range.*

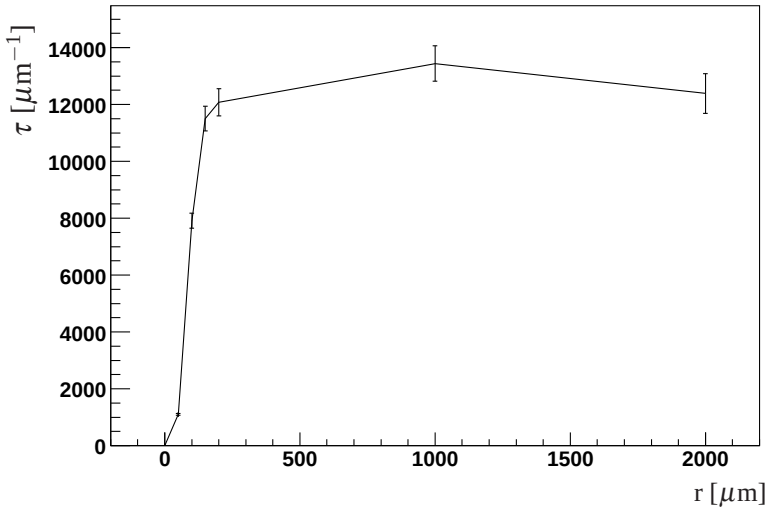

Figure 10.6.3: *Parametrization of rate parameters from fits to gains at various values of drift distances.*

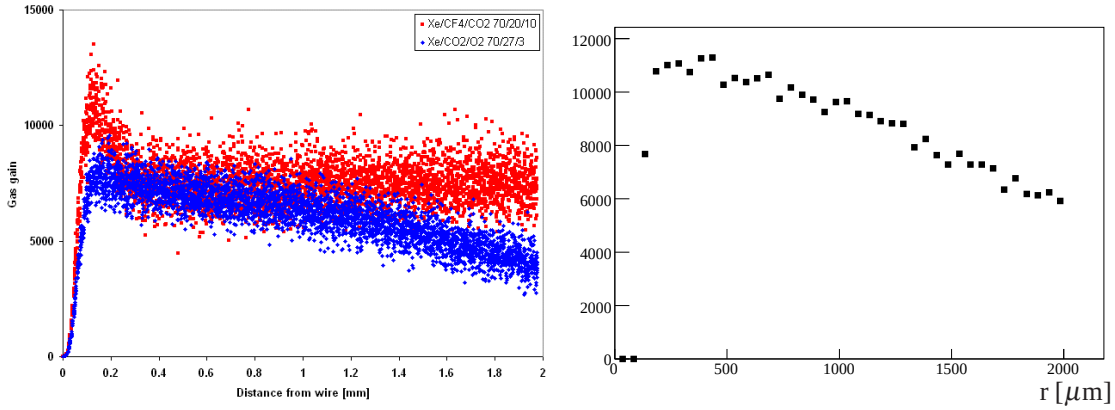

Figure 10.6.4: *Comparison between previous (left, blue points) and present (right) gain modeling as explained in the text. Left-hand plot is due to P. Cwetanski.*

anode. The exponential fits satisfactorily describe the distributions allowing the rate parameter of the exponentials (i.e. the "decay constant") to be parametrized as shown in figure 10.6.3. This is what has been implemented in the software, which therefore proceeds as follows: Given a distance from the initial (surviving) primary electron, a rate parameter is retrieved from the piecewise linear parametrization of the rate parameter distribution (figure 10.6.3). Since the naive reject method, would be very CPU demanding due to the tail of the exponential function, a refined approach is utilized by exploiting that numbers, t, generated according to an exponential distribution of rate parameter τ can be generated simply by:

$$t = \frac{-1}{\tau} ln(f) \tag{10.6.1}$$

for a flat random number $f \in [0;1]$ [PDG06].

In figure 10.6.1 is shown the results of single electron gains. In the previous implementation no corresponding plot is available, but only the combined effect of gain and recapture evaluated by simulating clusters of 250 primary electrons and calculating the average number of electrons reaching the wire per initial electron, see figure 10.6.4(left). In order to compare the two approaches, the recapture probability plot shown in figure 10.5.2 is multiplied by the gain distribution (figure 10.6.1(right)) and the result is shown in figure 10.6.4 (right).

Apart from an overall scale difference explained by updates in the Garfield simulations [Cwe07], the distributions share most features. Since in the end, only the low threshold is tuned, the actual scale of the distributions is not important, and in the digitization software, both figures 10.5.2 and 10.6.1(right) are normalized (whereas figure 10.6.4 is not used at all).

10.7 Signal shaping

Once the electrons arrive at the wire, the response of the front-end electronics is modeled:

- Energy deposits are filled (as delta functions) into a vector in the appropriate time bins.
- This vector is convoluted with the signal shaping functions.

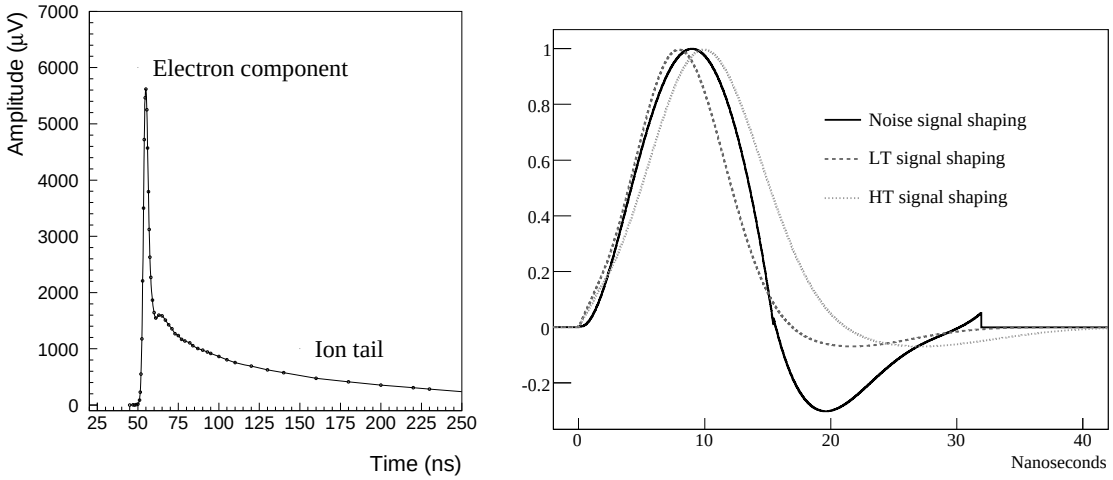

Figure 10.7.1: *On the left-hand plot is shown the a signal from a cascade in a straw. The ion tail is compensated by active baseline restoration by the front-end electronics. The right-hand plot shows the shaping functions implemented in the digitization package to model the effect of the ASDBLR chips. Note that the curves are normalized to a maximum height of 1. Source [ATL97b, Kit07].*

- The signals are then discriminated against low and high thresholds in appropriate time slices and the output digit constructed.

In figure 10.7.1 is shown the implemented signal shaping functions. No updates have been performed with respect to this particular part of the TRT digitization package, and the reader is referred to [Kit07] for details.

In order to complete the digitization overview, two additional actions were taking:

- Noise is added based on a test-beam study.
- Mis-functioning straws are removed.

Since these issues are largely decoupled from the remainder of the TRT digitization, they will be discussed (in chapters 15 and 16) after a comparison between the digitization model outlined above and test-beam results .

The digitization model described in this chapter, has been implemented in the TRT digitization package. Backwards compatibility is ensured by the use of a so-called digitization version, which is a flag stored in the Detector Description Database. The above model corresponds to TRT digitization version 11.

Chapter 11

Comparison with data

In the previous chapter, the model for simulating the TRT detector response was presented. In this chapter, simulated data based on this model is compared with data from test-beam studies. Before presenting the actual results, the first short section is devoted to describing the experimental facilities from which the data originate: The 2004 Combined Test Beam setup (CTB) [DGDG$^+$05, ATL07].

11.1 The 2004 Combined Test Beam

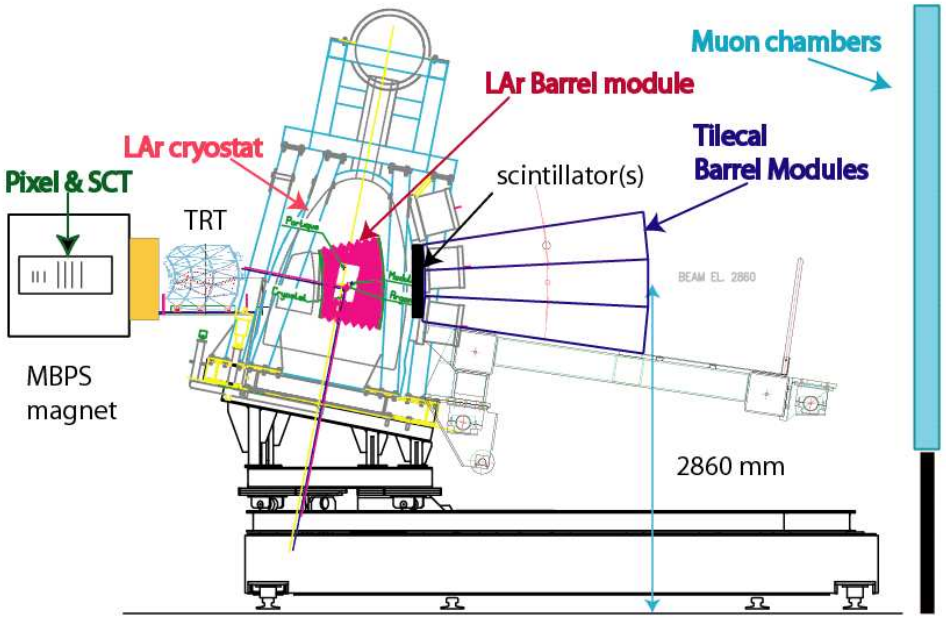

Figure 11.1.1: *Basic setup of the 2004 Combined Test Beam. Source [DGDG$^+$05].*

In July 2004 a fully functional slice of the ATLAS detector was placed at the CERN Prévessin site at the end of a test-beam delivered by the SPS [CER08]. Using various targets and magnet field selectors, beams of either pions, electrons or muons were delivered at the detector setup.
In figure 11.1.1 this setup is shown, with the beam entering from the left. Before and after passing the TRT barrel, the beam passes through various detectors providing particle identification, tracking and shower vetoing. The dipole magnet encapsulating the Pixel and SCT provides a maximal field of 1.4 T.

The setup thus provides events where the identity of the passing particle is well known and with good external knowledge of the parameters of the passing track, making them suitable for detailed studies of detector performance. Details of the CTB setup and its performance are described in [DGDG$^+$05, ATL07].

Regarding the TRT, this was the first test-beam with the front-end electronics (including the ASDBLR chips) essentially of the final design, while the read-out chain and data acquisition system were final prototypes, very similar to those used in ATLAS.

11.2 $r-t$ relationship

Regardless whether one is discussing data or MC, what is obtained from the front-end electronics (or the corresponding part of the simulation) are streams of bits, with each bit corresponding to a time slot of 3.125 ns, and the bit value specifying whether or not the signal exceeded the threshold in the given time slot. However, in terms of tracking particles, what is more relevant than the time, is the corresponding radius at which a particle crossed the straw. The process of interpreting the measured time as a radius, is itself an involved process known as "the $r-t$ calibration". The ambiguity of determining the side of the anode at which a given particle passed, must be resolved by the tracking algorithm. Assuming that the drift velocity of the freed electrons is approximately constant (independent of radius in the straw), one would expect that a plot of r versus t for multiple passing particles would exhibit a V-like structure, which is the reason that this particular distribution is often referred to as a V-plot. I.e.

$$r \approx v_{drift} \cdot (t_{bin} \cdot 3.125 \text{ ns} - t_0) \tag{11.2.1}$$

An example of such a plot is shown in figure 11.2.1. Note that apart from the V-like structure there is a certain offset, denoted t_0, which varies from straw to straw and depends in a complicated way on the length of read-out wires, synchronization of the front-end electronics etc. t_0 is extracted from the data itself and subtracted before further processing of the data. The $r-t$ calibration is performed separately for data and MC.

The comparison between data and MC falls naturally in two categories: Those which depend strongly on the $r-t$ relation, and those which do not. To the first category belong resolution studies, whereas efficiency and to some extent time-over-threshold studies, fall in the latter.
The reason for this distinction is that once the TRT digitization is changed according to prescription described in the previous chapter, the $r-t$ should be re-calibrated in order for the tracking to work optimally. This will be postponed to the resolution study, performed on a toy MC which is presented in section 11.6. As will be discussed in section 11.6, the comparison of resolution between data and simulation is not entirely straightforward, and certain assumptions must be made. However, as discussed below, the comparison of efficiency and time-over-threshold is indeed feasible without introducing questionable assumptions. Since the time-over-threshold distribution has some dependence

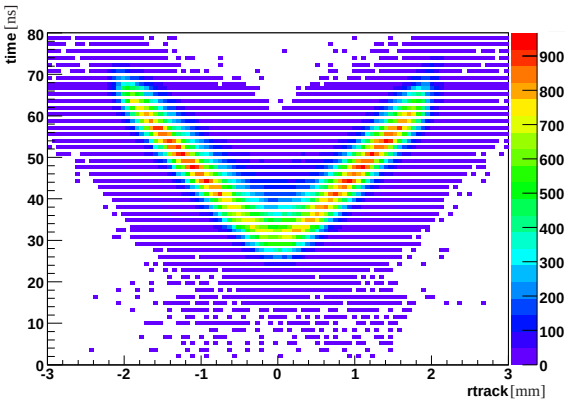

Figure 11.2.1: *The so-called V-plot, showing the relation between drift radius and the measured time.*

on the $r-t$ relationship, this study is repeated in the next section where the $r-t$ is re-calibrated.

11.3 Efficiency and Time over Threshold comparison between data and MC

11.3.1 Data selection and analysis cuts

The Combined Test Beam data was collected using a large number of different configuration setups, some of which are useful for the present study and some not.
The detector setup differed mainly by the magnetic field strength, whereas the applied beams differs in energy, particle composition and position (i.e. vertical elevation with respect to the sub-detector modules). In table 11.3.1 the main features of the runs used in the present analysis are summarized. Data taken from runs with magnetic field is preferred since the field tends to sweep away the low energy electrons which are otherwise present in the beam and which could potentially interfere with the results. Note that the field is applied only in the Pixel/SCT region, and the wake field is negligible, so that particle tracks in the TRT (called TRT segments) can be assumed straight apart from multiple scattering in the material.

run number	E [GeV/c]	B [T]	N_e	N_π
2118	2	0.33	41877	8336
2106	5	0.82	36865	38322
2107	9	1.4	11094	35046

Table 11.3.1: *Run selection and size according to the selection in [MP07].*

In order to bypass effects of imperfect tracking algorithms, it is necessary to perform a number of quality cuts to ensure that only events with properly reconstructed tracks are considered. The requirements are:

- Precisely one global track per event, defined as a track consisting of both Pixel, SCT and TRT hits.

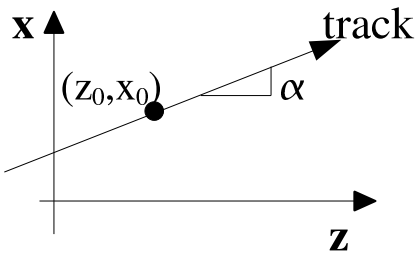

Figure 11.3.1: *Coordinate system for the track fitting. The z axis is defined by the beam and x is the vertical direction.*

- Precisely one TRT segment built from at least 9 TRT hits.
- Precisely one LAr calorimeter cluster.
- Well defined particle identification (PID) from Čerenkov detectors using the method presented in [MP07].

Based on a global track passing the above requirements, a linear refit is made using the TRT straws belonging to the track. The straw positions entering in the fit are determined by a calibration using selected test-beam data, see [MP07] for details. Assuming straight tracks in the $zx-$plane, the χ^2 of a track fit to the N measurements defining the TRT segment can be expressed as:

$$\begin{aligned}\chi^2 &= \sum_{i=1}^{N} \frac{(x_i - x_{track})^2}{\sigma_i^2} \\ &= \sum_{i=1}^{N} \frac{(x_i - (x_0 + \alpha(z_i - z_0)))^2}{\sigma_i^2}\end{aligned} \tag{11.3.1}$$

where i runs over the N measurements defining the TRT segment of the track and σ_i represents the measurement error. The coordinate system is explained in figure 11.3.1. As can be seen in this figure, a track is defined from one set of coordinates: (z_0, x_0) and a slope α. Assuming equal errors for all measurements, the χ^2 minimum conditions read:

$$\begin{aligned}&\frac{\partial \chi^2}{\partial x_0} = 0 \implies \sum_{i=1}^{N}(x_i - (x_0 + \alpha(z_i - z_0))) = 0 \implies \\ &x_0 = \frac{1}{N}\sum_{i=1}^{N}(x_i - \alpha(z_i - z_0))\end{aligned} \tag{11.3.2}$$

$$\begin{aligned}&\frac{\partial \chi^2}{\partial \alpha} = 0 \implies \sum_{i=1}^{N}(x_i - (x_0 + \alpha(z_i - z_0)))(z_i - z_0) = 0 \implies \\ &\sum_{i=1}^{N}(z_i - z_0) = \sum_{i=1}^{N} x_0(z_i - z_0) + \alpha\sum_{i=1}^{N}(z_i - z_0)^2\end{aligned} \tag{11.3.3}$$

Combining equations 11.3.2 and 11.3.3 leads to the following closed expression for α:

$$\alpha = \frac{\sum_{i=1}^{N} x_i(z_i - z_0) - \frac{1}{N}\left(\sum_{i=1}^{N} x_i\right)\left(\sum_{i=1}^{N}(z_i - z_0)\right)}{\sum_{i=1}^{N}(z_i - z_0)^2 - \frac{1}{N}\left(\sum_{i=1}^{N}(z_i - z_0)\right)^2} \tag{11.3.4}$$

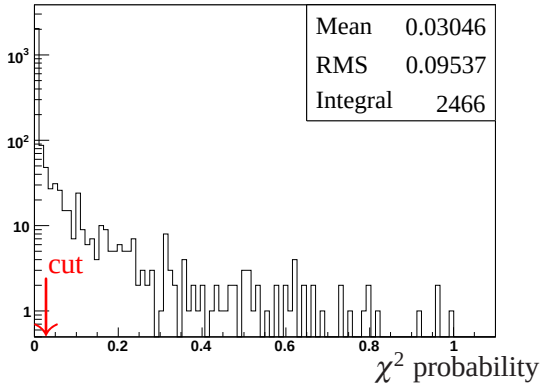

Figure 11.3.2: *Distribution of χ^2 probabilities.*

From the track defined by α, a new track is formed using the nominal straw positions plus or minus the drift radius depending on which gives the lesser contribution to the χ^2 sum. In case the track has a kink, or has outliers (hits which by mistake are assigned to the track), it could dilute the efficiency analysis, and to reject such tracks, an effective χ^2 is formed:

$$\chi^2 = \frac{1}{N}\sum_{i=1}^{N}\frac{\left(x_{hit}-x_{track}\right)^2}{1000\ \mu m^2} \tag{11.3.5}$$

where the denominator is chosen arbitrarily for normalization only.

Problematic tracks are identified by their large χ^2 with respect to straight tracks or conversely a low χ^2 probability - see figure 11.3.2. As indicated, tracks with a χ^2 probability less than 0.025 are omitted from the following analysis.

11.3.2 Efficiency in data

The straw positions are evaluated using all useful CTB data (as described in [MP07]) and are thus known with high precision (uncertainty is negligible). Having also firm tracks, the hit efficiency can be investigated. In order to make detailed comparison with simulations, the efficiency dependence on the impact parameter of the track to the anode wire is of special interest, since this distribution allows one to indirectly test the validity of the Garfield simulations of gain and reattachment probability, presented in the previous chapter, on which the TRT digitization software is based. The efficiency as a function of the impact parameter of the track to the anode, r, is calculated by forming the distance ratio, between distributions of *distance from anode wires corresponding to track-hits to the track* and *distance from all anode wires to the track.*

$$\varepsilon(r) = \frac{\Sigma_{hitsontrack}\, dist(wire,track)}{\Sigma_{allstraws}\, dist(wire,track)}, \tag{11.3.6}$$

where the Σ's indicate the fact that the efficiency is formed by a ratio of *distributions* of distances (i.e. they do not represent actual summations). As illustrated in figure 11.3.3, the numerator of equation 11.3.6 is formed from all the shaded straws, meaning that it includes hits which do not belong to the original track but are within the nominal straw radius of it. The reason for including these hits, is to try, as much as possible, to reduce effects of ineffective tracking (i.e. to be, as much as

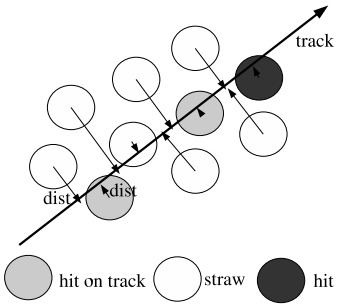

Figure 11.3.3: *Efficiency is calculated by forming the ratio of distances, dist, from anode wires corresponding to hits on the track, to distance to the track for all anode wires. Only the shaded straws enter in the numerator of equation 11.3.6 whereas all straws enter in the denominator (note that the inclusion of additional straws missed by the track in the denominator has no effect - cf. equation 11.3.6 with zero numerator).*

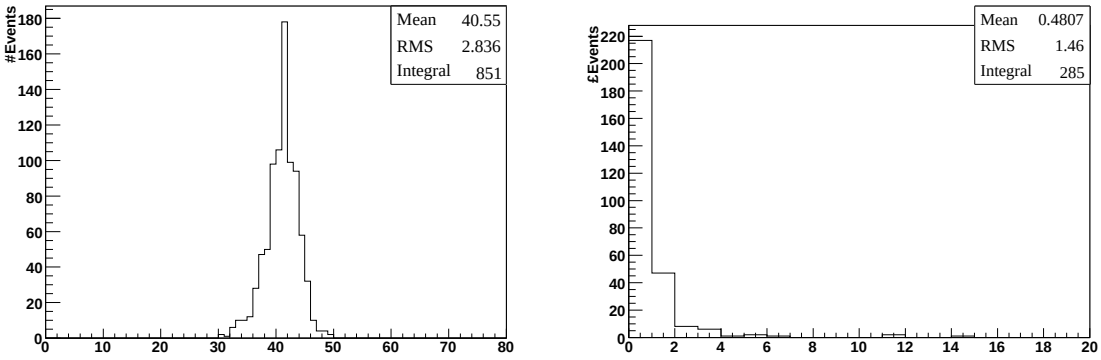

Figure 11.3.4: *Left: Number of TRT hits on 100 GeV pion tracks. Right: Number of hits added to the track - based on interception between track and straw volume.*

possible, tracking independent). In principle this approach introduces a bias to the track parameters (which are determined by the hits defining the original global track), but given the large average number of TRT hits on each track (≈ 40), combined with the fact that only on average 1.5 hits are added by this procedure, the modification of the track-parameters from a including the additional hits is insignificant - see figure 11.3.4.

In addition, an unavoidable bias is introduced by the tracking algorithm defining the input track, since it is required that tracks have at least 9 TRT hits. As the beam enters the TRT modules approximately along the straw layers, the impact parameters, of a track to the anodes it passes can be significantly correlated, as can be realized considering the beam profile shown in figure 11.3.5. Thus the requirement of a minimum number of TRT hits per track, can influence the individual tracks differently. However, taking into account figure 11.3.4(left), the tail of rejected tracks with less than 9 TRT hits is expected to be negligible, and thus this bias insignificant.
By the above approach, the track-parameters are determined more or less independent of the $r-t$ relationship on which normal tracks depend and the straw positions are precisely known, so resolution effects only play a minor role. Before the summations are performed, all non-functioning straws are removed. Although this is trivially done in the simulation, it is not always the case for data due to possible non-constant detector performance (i.e. the situation where a given channel changes its properties over time). Potentially this means, that occasionally some straws are included in the de-

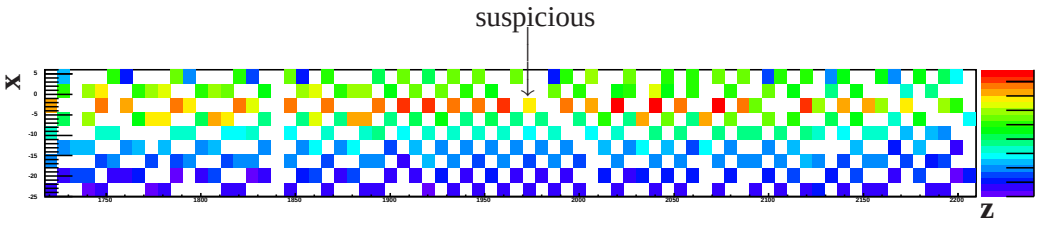

Figure 11.3.5: *Occupancy map (i.e. occupancy as a function of (z,x) position) for the 2 GeV pion run.*

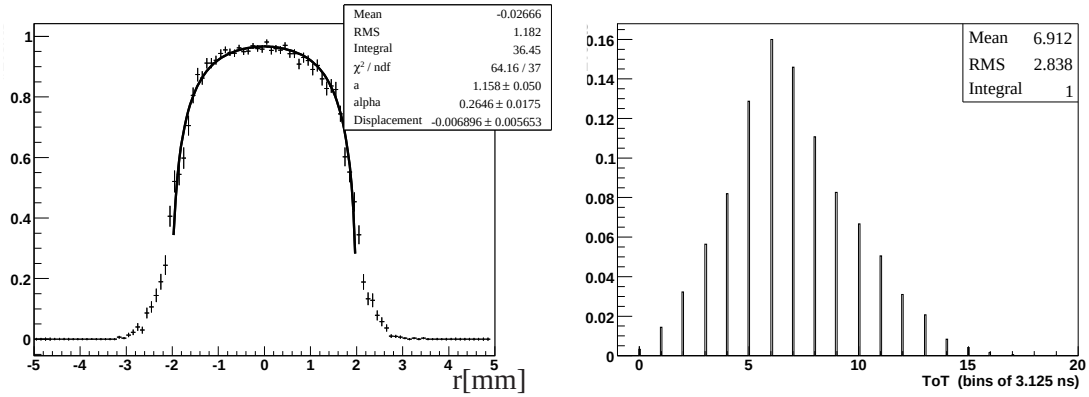

Figure 11.3.6: *Left: Efficiency as a function of the impact parameter of the track to the anode wire (2 GeV run). Care is taken in order to get the bin error correct when dividing the two statistically dependent histograms on which the plot is based. Right: Time-over-threshold for the same data sample.*

nominator sum, although they were temporarily non-functioning. Consider the occupancy map shown in figure 11.3.5. The beam profile is clearly seen, but a few straws in the beam region exhibit suspiciously low efficiency which could indicate non-constant running conditions, but could also simply mean that some straws have a constantly low efficiency (an example is indicated by an arrow). To make firm conclusions, however, requires a detailed investigation of the running conditions of the individual straws over time.
Moreover, as will be discussed in chapters 15 and 16, the TRT modules chosen for the test-beam setup were known to have stability problems. Due to time constraints, it was decided not to pursue this issue and instead cope with the fact that the normalization used for the efficiency could be slightly off. This implies, that the apparent derived efficiency is reduced with respect to a realistic ATLAS efficiency. When running the full experiment, all straws will be monitored constantly and the instantaneous efficiency will be accessible, hereby eliminating the problem. From figure 11.3.5 one could also gain knowledge of the detector noise, however this issue is postponed till chapters 16 and 17 where separate noise studies are presented.

In figure 11.3.6 the efficiency of all particles of a 2 GeV run is plotted as a function of the impact parameter (i.e. no PID requirements). At the straw edge, $r = 2$ mm, the efficiency falls off. Also shown is the corresponding time-over-threshold distribution. The left-hand plot in this figure is the basis of the discussion which follows below.

11.3.3 Features of a simple efficiency parametrization

It is difficult to construct a well defined and unambiguous measure for the efficiency, and the present approach does not claim to results in such a measure. Since resolution effects are not considered in

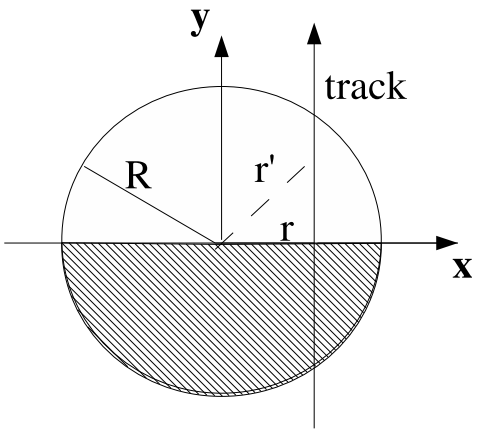

Figure 11.3.7: *Notation used in equation 11.3.7. Note that this expression concerns integration in half a straw only (disregarding the shaded region) which explains the factor of 2 in the exponent.*

the below parametrization, it can, however, serve as an upper limit of the efficiency which can be expected.

The fit shown in figure 11.3.6(left), is based on the following expression:

$$\varepsilon(r) = 1 - e^{-2a\sqrt{R^2-r^2}\cdot\frac{\int_0^{\sqrt{R^2-r^2}}(1-\alpha\sqrt{r^2-y^2})dy}{\int_0^{\sqrt{R^2-r^2}}dy}} = 1 - e^{-2a\left(\sqrt{R^2-r^2}-\frac{\alpha}{2}[ln(\frac{R+\sqrt{R^2-r^2}}{|r|})r^2+R\sqrt{R^2-r^2}]\right)} \quad (11.3.7)$$

I.e. the efficiency is approximated by a Poisson distribution of electron clusters along the track, times a constant reattachment probability per unit length of the electron drift. The various parameters of equation 11.3.7 are explained in figure 11.3.7.

By this, the fit parameters can be interpreted as:

- α: Reattachment probability per unit length.
- a: The number of produced electrons per unit length, that would give rise to a signal if $\alpha = 0$.

In the full MC model, the reattachment probability is described by the polynomial shown in figure 10.5.2, whereas in the present simple model it is approximated simply by a straight line. However, from figure 10.5.2 it is realized that the deviations from a straight line are not too significant, and if the measurements are approximated by a straight line the corresponding slope would be $0.3\ \text{mm}^{-1}$ which is roughly the size of α in the above fit (see figure 11.3.6(left)).

The value of the fit parameter a suggests that only: $1.2\ \text{mm}^{-1} \cdot 4\ \text{mm} \approx 5$ surviving electron clusters are created along a track passing through the center of a straw. This number seems rather low, especially when comparing to the number of created electron clusters for such a track - see figure 11.3.8. However, there is no saying that one electron cluster reaching the anode wire is actually sufficient to produce a signal; one can beforehand not know whether a better fit is obtainable by including more terms from the Poisson expansion: $P(x) = e^{-<x>} \cdot (1 + c_1 < x > + \frac{1}{2}c_2 < x >^2 + \cdots)$. Including one or two terms improves the fit quality somewhat (see Appendix B.2, figure B.2.2) without major changes in the fit-parameters. However the price to pay by this, is that the model gains complexity by the

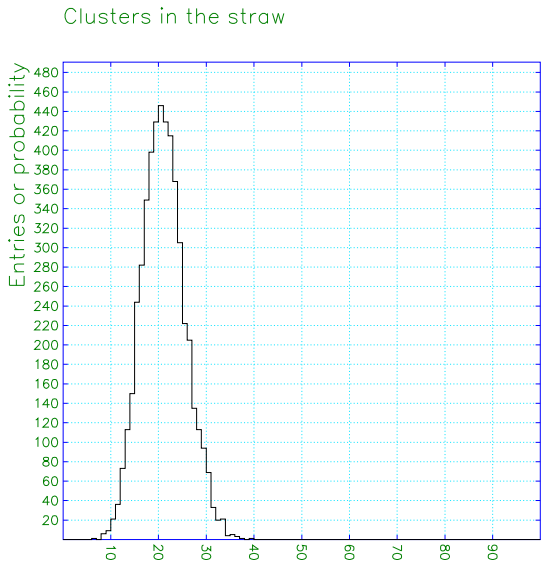

Figure 11.3.8: *Number of electron clusters produced by a track passing a wire with vanishing impact parameter according to Garfield simulations. Additional plots showing various distributions of electric charge can be found in Appendix B.1.*

additional constants and it implies that the interpretation of the parameter a must be revised. For this reason, only the simplest model is considered below - i.e. equation 11.3.7. The mere fact that the observed efficiency in data can be described using a very simple model based on the same ideas as the MC model is reassuring for its further development and illustrates that the simple model seems to catch the main features of the data.
Note that the good agreement is obtained despite the fact that the expression in equation 11.3.6 does not have terms describing the spread caused by the varying avalanche effects nor does it take into account the finite resolution introduced by the track resolution.

The fit-function does not attempt to describe the tails (i.e. events at $|r| > 2$ mm) which, apart from a (small) contribution induced by the finite resolution, are thought to be due to δ-rays. The latter should of course not enter into efficiency calculation, but to some extent it inevitably will. Also, the presence of δ-rays implies that the integrated efficiency depends on the limits to which the fit is performed. The dependence is shown in figure 11.3.9. Due to the presence of δ-rays, combined with the non-constant detector performance, is not trivial to obtain a single unambiguous value for the efficiency. However for the given 2 GeV run, one can with some certainty claim that the observed efficiency is above 92% which is the value obtained from integrating figure 11.3.6(left) in the range $|r| < 2$ mm. Note that the presence of δ-rays lower the value with respect to the true efficiency, which could be significantly higher.

Efficiency dependence on particle type and energy

In order to investigate a possible dependence of the efficiency on the particle type, efficiency distributions for electrons and pions are compared for run 2118 and the resulting distributions are shown in figure 11.3.10. The PID requirement reduces significantly the statistics, but no differences can be found. Since the fits of figure 11.3.10 are compatible, not only with each-other, but also with the

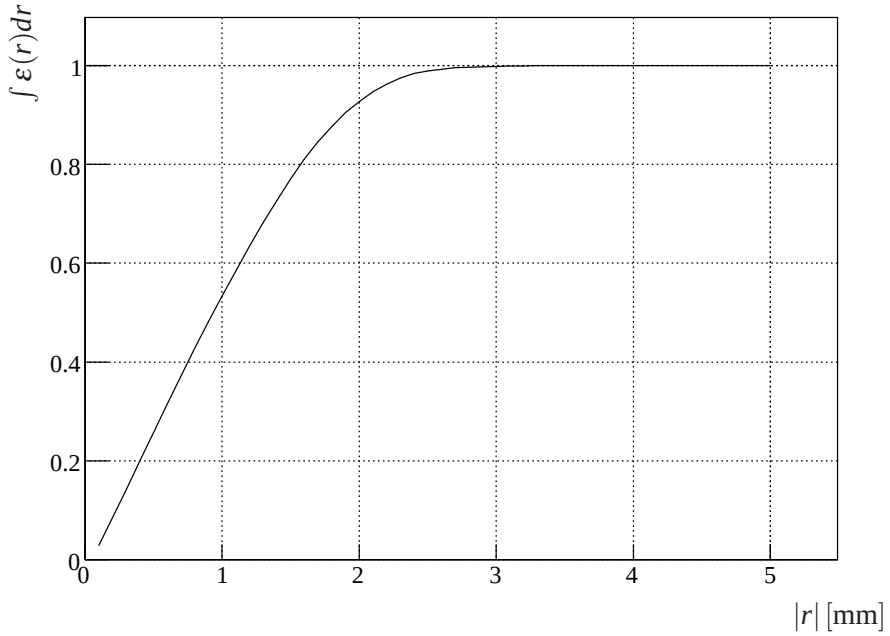

Figure 11.3.9: *Integrated efficiency for the 2 GeV pion run of figure 11.3.6. For $r = 2$ mm the efficiency is 92%.*

corresponding fit when no PID requirement is implemented (figure 11.3.6), the latter approach will be utilized in the following due to the higher statistics.

Figure 11.3.11 shows the efficiency ratio between the selected runs as a function of impact parameter. Despite the apparent structure, the ratios are compatible with a constant fit. Again, the questionable statistics makes is difficult to make firm conclusions. Also, the beams differ in composition, and although it was argued above, that possible efficiency differences between particle types are small, they still can influence this study, since the statistics is improved compared to figure 11.3.10.

Based on figures 11.3.10 and 11.3.11 it seems plausible that efficiency could differ somewhat according to particle type and energy. To quantify would require a more detailed study and increased data samples. Although interesting in its own right, such study lies outside the realm of the TRT simulation

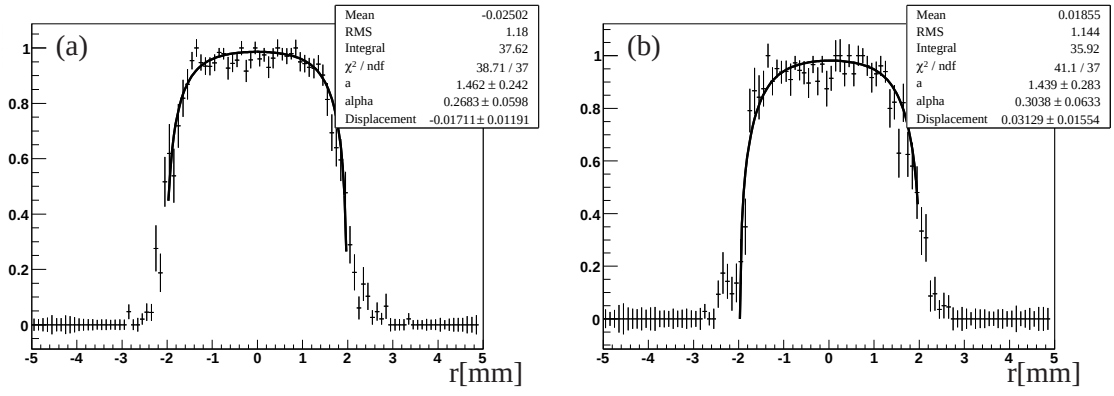

Figure 11.3.10: *Efficiency as a function of r for electrons (a) and pions (b) for run 2118. Corresponding figures without PID requirement for runs 2106 and 2118 can be found in Appendix B.2.*

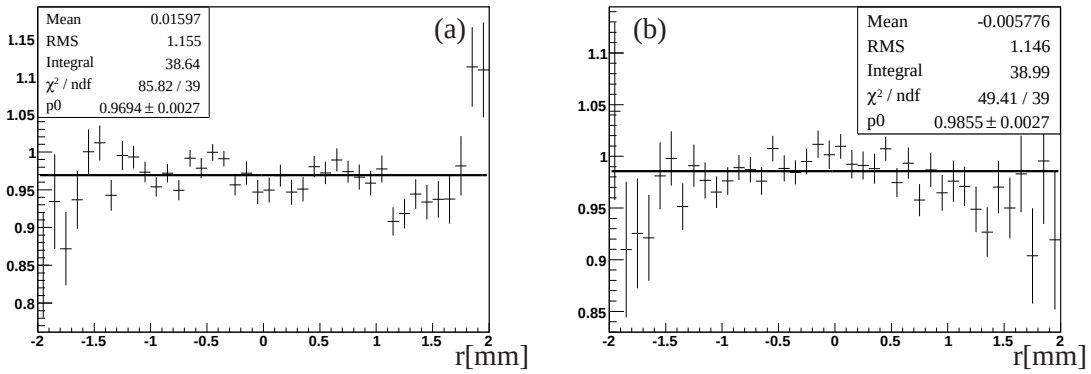

Figure 11.3.11: *Ratios between efficiency as a function of r for runs: 2106/2107 (a) and runs: 2106/2118 (b) without PID requirement.*

validation and will therefore not be performed here.

It has been shown that the difference in efficiency due to particle type or energy can only be minor, and it will not be taken into consideration in the following comparison between data and MC which is based solely on run 2118, without PID requirements.

11.4 Efficiency and time-over-threshold distributions in MC

The above discussion concerned the test-beam data only, but of course the method is usable for simulated data as well and this section provides corresponding fits to the MC efficiency in order to tune the simulation to resemble data.
Since the only free parameter in the simulation is the low threshold setting, LT, the task of tuning the MC reduces to comparing efficiency fits produced with various LT settings, to the corresponding distribution in data (i.e. figure 11.3.6).

Note that this approach simultaneously tests all aspects of the full digitization model, including all the updates. The main results are shown in figures 11.4.1 and 11.4.2 containing efficiency- and time-over-threshold distributions for various LT settings, superimposed with the corresponding distributions for data. A Kolmogorov test of the efficiency distributions reveals that the best match is found for the MC with a low threshold value of 300 eV. Incidentally, this value is the same as the hardware setting used for the data taking. It should be emphasized that the tuning parameter of the MC and the hardware setting have somewhat different meanings and therefore could have different values: The hardware setting is actually an “electron count”, which is interpreted as a signal height, whereas in MC, LT is a tuning parameter, influenced in essence by all aspects of the underlying simulation.

No fine-tuning of the MC efficiency distribution is performed due to the fact, that the time-over-threshold or resolution distribution could equally well be chosen as tuning distribution. For this reason, it is sufficient to state with respect to efficiency, LT=300 eV matches data well, and LT=250 and LT=350 are clearly excluded. For time over threshold, the situation is less clear, but figure 11.4.2 suggests that LT=250 eV is preferred.

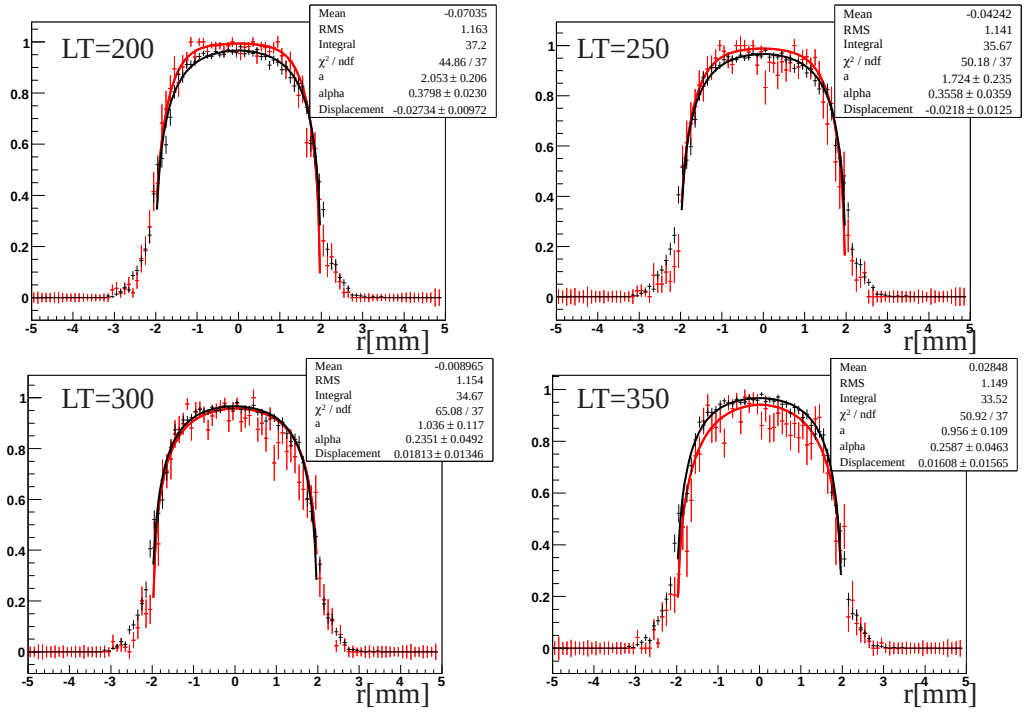

Figure 11.4.1: *Efficiency for various LT settings for a 2 GeV pion run (run 2118). Data is black and MC red.*

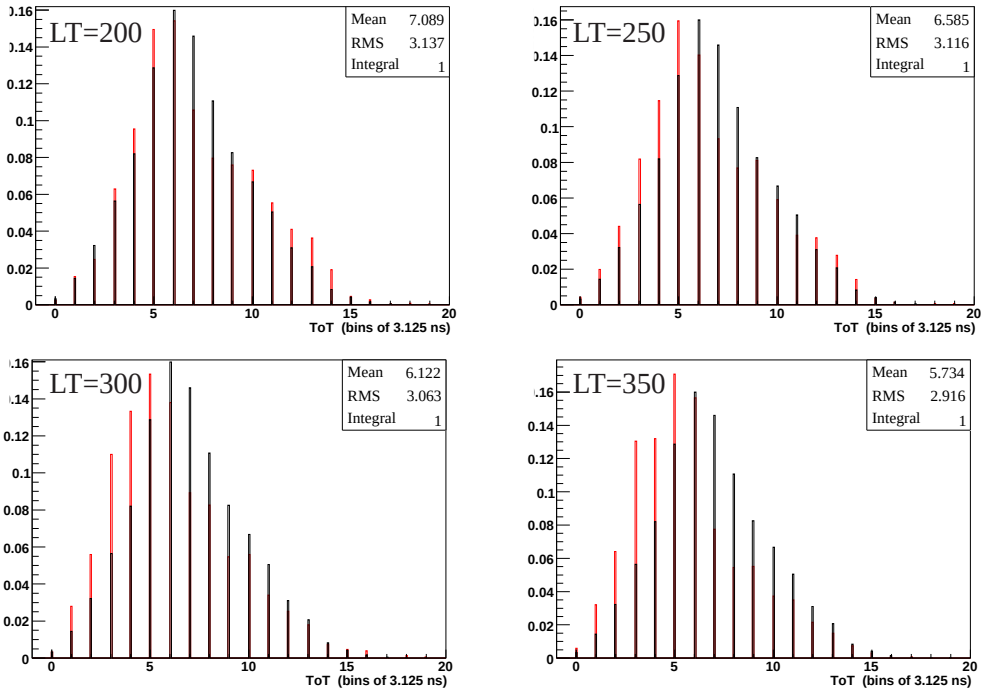

Figure 11.4.2: *Time-over-threshold for various LT settings for a 2 GeV pion run (run 2118). Data is black and MC red.*

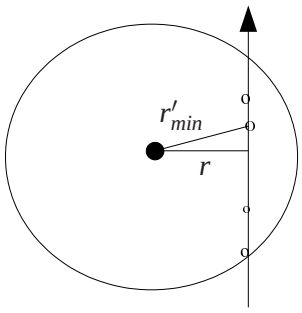

Figure 11.5.1: *Event showing a typical number and distribution of electron clusters (4 clusters) which survive the drift and result in a signal large enough to exceed the threshold.*

11.5 Comparison between simple physics model and $r-t$ relationship

Since the measured average $r-t$ relation (e.g. figure 11.2.1) concerns the distance of closest approach from the track to the anode wire (corresponding to r in figure 11.3.7), while the drift time versus drift distance distribution of figure 10.3.3 shows the drift time of single electrons along their trajectories (corresponding to r' in figure 11.5.1) comparison is not straight-forward. The reason is mainly that the parameter a is small. Since a is interpreted as the mean number of electrons produced per millimeter, its small value implies that the probability that an electron is produced close to the minimum distance from a track to the wire is low - see figure 11.5.1. Another reason is, that a typical cluster does not contain a sufficient number of electrons to give rise to a signal on its own[1].

As a consequence, the electron drift distance, r', generally differs quite significantly from the distance of closest approach form the track to the wire: r. In an attempt to understand the observed $r-t$ relations, a small toy MC routine was developed from the following principle:

- Assume that the number of electron clusters produced along a track of impact parameter r is Poisson distributed with a mean of: $2a\sqrt{R^2-r^2}$, where R refers to the straw radius.
- Since some electrons do not reach the wire, the relevant Poisson mean must be scaled by the inverse of the mean fraction of recaptured electrons at $r=0$: $\frac{\int_0^R(1-\alpha r')dr'}{\int_0^R 1dr'} = 1-\alpha$[mm] since $R = 2$ mm. By this, the mean of the Poisson distribution becomes: $\frac{2a\sqrt{4\text{ mm}^2-r^2}}{1-\alpha}$.
- Once the number of electron clusters has been determined, they are distributed randomly and independently along the trajectory. Hereby the r' distribution is obtained.
- For each electron, compare a random number to $1-\alpha r'$ (actually compared to the full fit function of figure 10.5.2) and reject if the number falls above the curve.
- In the list of surviving electrons, store the one with the smallest value of r': This electron is the one which gives rise to the signal in this simplified model (i.e. LT$\rightarrow$ 0).
- For each r', calculate the corresponding drift time, t, using equation 10.3.9, thus ignoring diffusion and spread. By this, histograms of r can be filled for each time interval of 3.125 ns corresponding to the time bins of the read-out electronics.

[1]This can be the case despite the fact, that the more complicated fits discussed in section 11.3.3 were not able to quantify this issue.

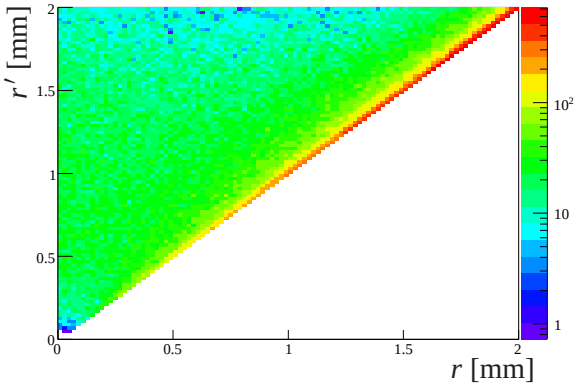

Figure 11.5.2: *Relation between r and r'.*

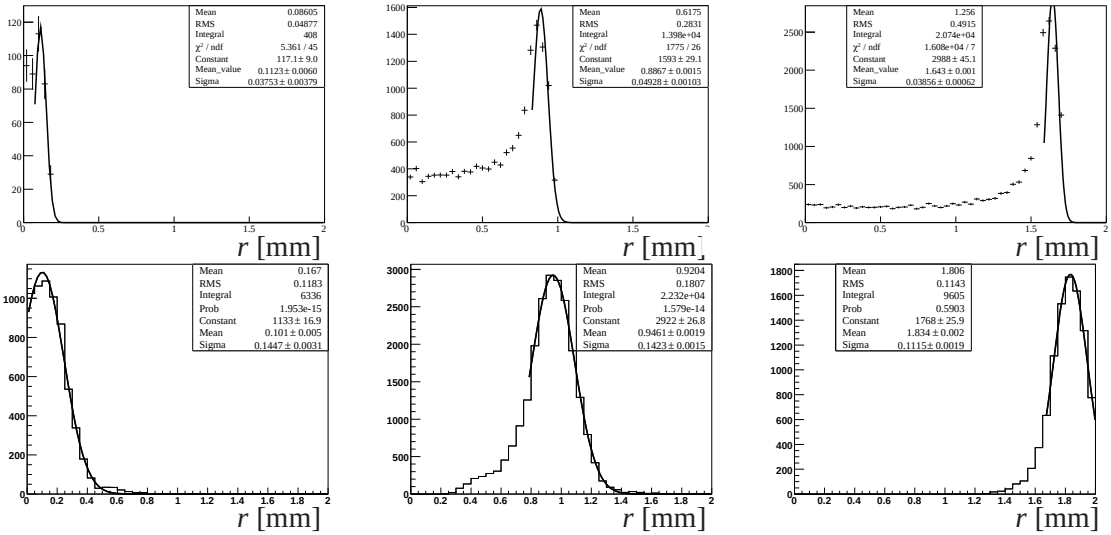

Figure 11.5.3: *Fits to r in three different bins of t. The upper figures are the results of the simplified model, whereas the lower ones are default results from the Combined Test-Beam, where the tails have been cut away.*

In figure 11.5.2 the relation between r and r' is shown, and the spread is clearly seen to be significant. In order to make a reasonable comparison with the 'default' $r-t$ relation used for tracking (i.e. the relation found using the standard procedures of the ATLAS offline software), the central part of the peak in histograms of r for the various t bins, is fitted with a Gaussian. The fit limits are defined to resemble the default fits as used in the standard ATLAS offline software. A few examples of the fits are presented in figure 11.5.3 where also the corresponding default examples are found. Corresponding histograms for all time bins are found in Appendix B.2.

Obviously the model above underestimates the width of the distributions. This is perhaps not so surprising given the simplicity of the model - it only attempts to account for effects caused by the low average number of electron clusters produced along a track, and the spread due to e.g. avalanche, cluster energy spread, diffusion and LT fluctuations is not included. For this reason the error calculated from the spread in r' is expected to be considerably less than the error in the $r-t$ relation. Overall, however, the model does seem to describe the main features as shown in figure 11.5.4.

Although it remains to be seen whether the full MC simulation (i.e. the TRT digitization in the offline

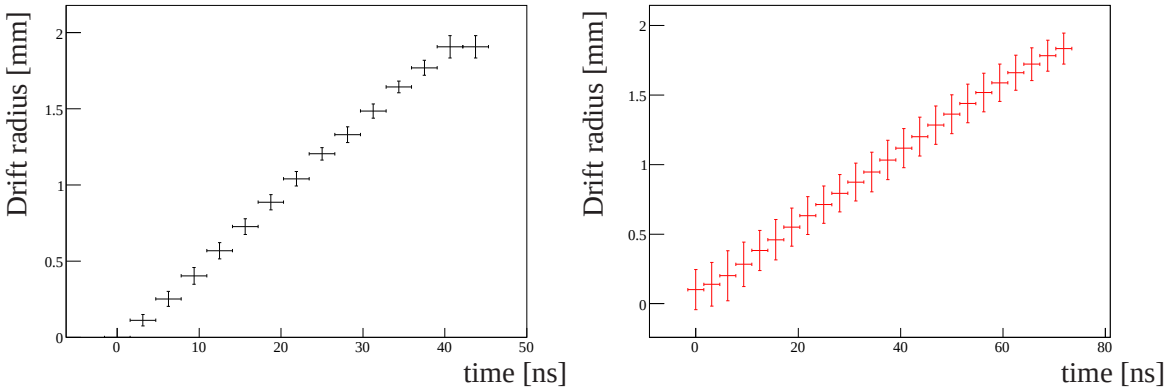

Figure 11.5.4: *Distribution of mean and errors for toy MC (left) and default $r-t$ relations (right).*

software) succeeds in describing the data resolution, the good resemblance between the simple model and the $r-t$ relation combined with the fact that the toy MC is built on the same principle as the TRT digitization package suggests, that the physics model underlying the TRT digitization is indeed valid and indicates that most important physics features are captured in the simulation.

11.6 Resolution in data and MC

The outline and methods used in this section are based on [Kit07], where the reader is referred for an in depth discussion of the TRT resolution[2].
To check the resemblance between the data and MC tracking resolution, a study is performed based on a 100 GeV pion sample. Using the full simulation scheme described in chapter 10, the passage of 2M particles through a TRT straw is simulated with a flat distribution of the impact parameter and using the optimal low threshold setting found in the previous section (LT=300 eV). For each simulation, the impact parameter, r, and the output digit is stored, so that in the following data analysis, r is fitted in bins corresponding to which time bit contains the leading edge - i.e. the first "1" when reading the digit from left to right (i.e. from smaller to larger times). The central part of the distributions obtained in this way are fitted with Gaussians as in the case for the toy MC study of the previous section. Some results are shown in figure 11.6.1, whereas the remaining are found in Appendix B.2. From

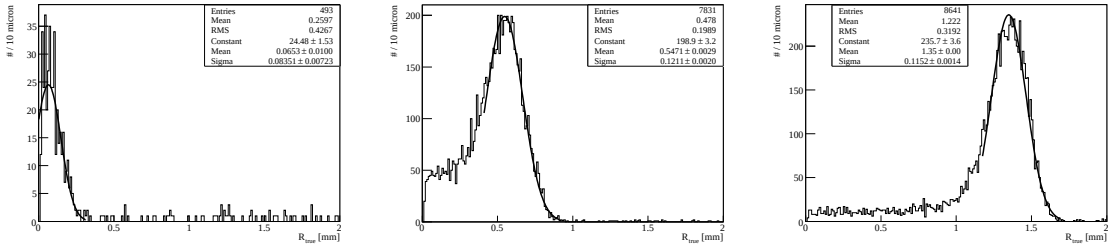

Figure 11.6.1: *r in three bins t for the full digitization model.*

[2]Note, that the work presented in [Kit07] is prior to the presented updates in the TRT digitization software, hereby complicating a direct comparison between these results, and the results presented in this thesis.

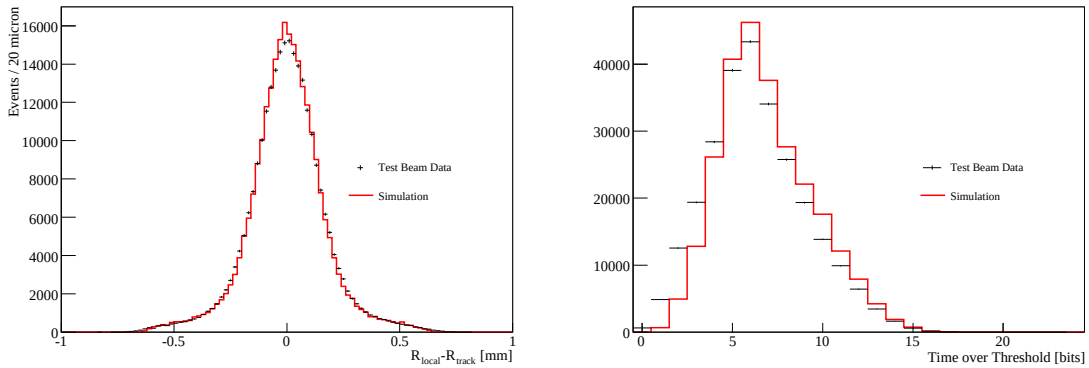

Figure 11.6.2: *Track residuals (left) and time-over-threshold (right) distributions for data and simulation using 100 GeV pions.*

these distributions the effect discussed in section 11.5 of the low number of initial clusters causing the tail on the left-hand side of the peak is clearly observed. In order to make a reasonable comparison of resolution with the test-beam data, $r-t$ relations are formed based on the fits of figure 11.6.1. Since the data, as opposed to the simulation used here, suffers slightly from the fact that neither the track nor the straw positions are known precisely, the corresponding uncertainty contributions need to be added to the simulation results before making any comparison. The estimated uncertainty of the individual wire positions is: 33 μm as determined from track residuals between SCT- and TRT segments [Han08]. The uncertainty introduced by the tracking is $\sim 130\ \mu\text{m}/\sqrt{33.5-2}$, since the average number of TRT hits per track in the used data is 33.5 and the track resolution is 130 μm. Assuming that the effects are of Gaussian nature, these two contributions are added randomly to the residual. Finally a 4σ cut is performed on both data and MC, by which the resolution and time-over-threshold distributions of figure 11.6.2 are obtained.

The resemblance between data and MC is very good - a Kolmogorov test reveals a probability of 6% for the two residual histograms to follow the same distribution. Repeating the above exercise for different LT settings yields the distributions found in Appendix B.2. The optimal LT value as determined from Kolmogorov tests to the residual plots is 338 eV with a corresponding probability of 52%. Recalling that LT=300 eV is optimal according to the efficiency study presented in section 11.4, and that the time-over-threshold distribution suggests a value ~ 250 eV (in both studies) it is concluded that all three methods of optimization results in compatible LT settings. Given that different aspects of the TRT digitization model are probed using the three methods some inconsistency between the results are expected and the fact that they all arrive at similar values is a significant accomplishment. The default software setting is LT=300 eV, which can therefore be retained; with the present knowledge and simulation model there is no strong argument for changing this value. When the LHC goes into operation, a much more detailed optimization is possible and it is likely that this statement will be revisited.

Chapter 12

Transition radiation

The previous chapter focused on the TRT abilities as a tracking detector. In this chapter emphasis will be put its the particle identification capabilities.

12.1 Theory of transition radiation

Transition radiation (TR) arises when ultra-relativistic charged particles cross a boundary between media with different dielectric constants, i.e. a charged particle in a non-uniform electric field. This process is analogous to bremsstrahlung, which arises due to a particle moving in a electromagnetic field.

As shown below, the probability of a given particle to emit transition radiation is determined solely by the γ-factor (apart from material properties). The TRT is build to exploit this for particle identification purposes - in particular to distinguish electrons from pions. Electrons tend to have large γ-factors and thus are likely to emit TR photons which makes them separable from the abundant low energy background of mainly pions. The theory of transition radiation is treated in detail in [Dol86, Ege98] and the references therein. Only a few results important for the TRT will be summarized here.

In the case of a single regular foil, the total energy radiated by a charged particle when passing from vacuum to the foil is:

$$E_{rad} = \frac{1}{3}\alpha\gamma\hbar\omega_p \tag{12.1.1}$$

where ω_p is plasma frequency of the foil and is given by:

$$\hbar\omega_p = \frac{\sqrt{4\pi N_e r_e^3} m_e c^2}{\alpha} \tag{12.1.2}$$

where N_e is the electron density, r_e is the classical electron radius, m_e is the electron mass and α is the fine-structure constant.

Strictly speaking, this result is only valid in case the plasma frequency of the surrounding medium, ω_{gas}, is zero, which is the case for a transition from vacuum. However, the result holds approximately in the limit: $\omega_{foil} \gg \omega_{gas}$ as is the case for the relevant materials of the TRT: $\hbar\omega_{polypropylene} \approx 20$ eV and $\hbar\omega_{air} = 0.70$ eV. For practical usage, not all transition radiation photons are useful, since some minimum energy, E_{cutoff} must be required for detection (due to the absorption spectrum in the detection gas). The number of photons created at a single boundary fulfilling this requirement is Poisson

distributed with a mean of:

$$N_\gamma = \frac{\alpha}{\pi}\left(\ln\frac{\omega\gamma}{E_{cutoff}}(\ln\frac{\omega\gamma}{E_{cutoff}}-2)+\frac{\pi^2}{12}+1\right) \tag{12.1.3}$$

Assuming a detector sensitive to photons with energies above 1 keV thus implies that an electron of 100 GeV on the average produces ≈ 0.12 photons with sufficient energy. For detector usage the low single-foil emission probability is compensated by using many foil layers. In the TRT end-cap each straw-layer is interleaved with about 15 uniform regular 15 μm thick polyethylene foils separated by 200 μm gas gaps (300 μm in some regions). Studies show (see figure 12.1.1(left)) that this composition is optimal (due to constructive interference of the radiation, regular foils are better than non-regular foils, foam and fibers). The thickness and number of foil layers are optimized with respect to PID performance, subject to constraints from the material budget and space limitations. The geometry and modular design of the TRT barrel prevents usage of regular foil radiators and an assessment shows that fibers oriented perpendicular to the expected particle trajectory is the best practical option given these constraints - see figure 12.1.1(left). At nominal threshold (5-7 keV), the probability for exceeding threshold is here about 15% below that of a regular foil.

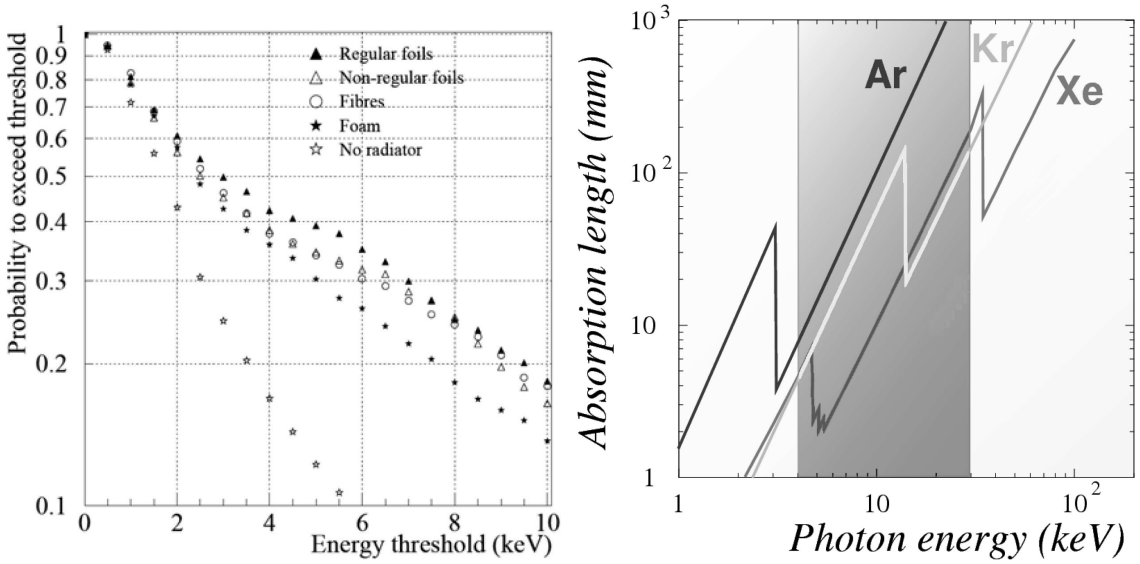

Figure 12.1.1: *Left: HT probabilities as a function of threshold for different radiator types. Right: Photon absorption length in high Z noble gases. Source [Cwe06].*

Upon creation, the TR photons, which are not reabsorbed in the foils or in the intermediate gas, enter the straws of the TRT and are subsequently absorbed in the Xenon gas flushed through the straws of the TRT detector. Xenon is chosen based on its low photon absorption length at the relevant photon energies (see figure 12.1.1 (right)) while other gases are added for stability, drift velocity and detector safety reasons. The final composition is $XeCO_2O_2$ (70:27:3).
The TR photons are emitted highly collinear to the particle trajectory (opening angle $\theta \approx 1/\gamma$) preventing ambiguities when assigning HT hits to tracks in the offline reconstruction. By this, the fraction of hits along the trajectory of a given particle which contain HT can be easily interpreted as a HT probability and be used in a straight-forward manner for particle identification.

Figure 12.1.2 shows the TR spectrum from a polyethylene surface. This plot, along with the ones shown in figure 12.1.1 suggest that the HT value giving the optimal electron identification is of the in

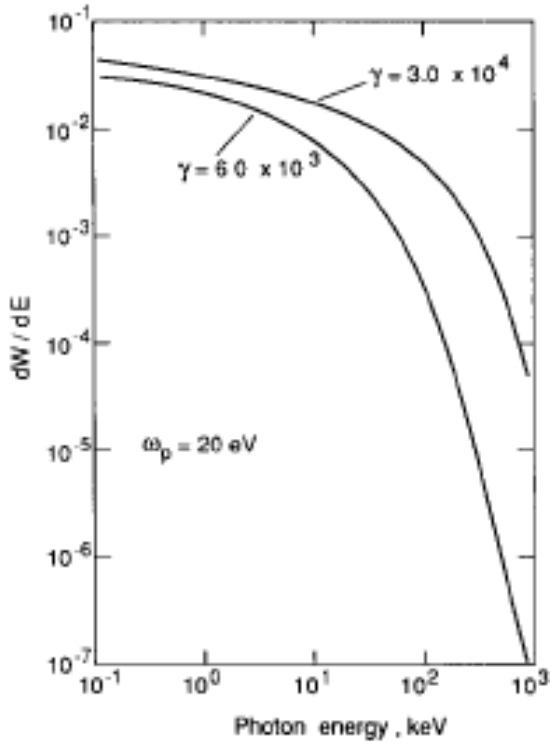

Figure 12.1.2: *The radiated TR spectrum from a polyethylene surface. Source [Dol86].*

the neighborhood of 6 keV - the 'final' tuning of the hardware setting of course awaits LHC collisions.

12.2 Simulating transition radiation

The simulation of transition radiation is based on the model presented in the previous section and the references therein. In this section the tuning of the TR model to match CTB data is discussed.

Figure 12.2.1 shows the HT probability from a study of the CTB, as a function of γ-factor [MP07]. The plot is the result of a careful track selection and strict requirements ensuring reliable and high separation between the particle species. The contamination is estimated to be below 1‰ in all configurations, and in most samples considerably lower than that. As would be expected from the above considerations, the HT probability curve resulting from the selection (figure 12.2.1) shows no dependence on the particle species, only on the γ-factor - i.e. there is no discontinuity in the curve in the regions between different particle species. The function used for the fit (as well as for the corresponding fits to simulations discussed in the following sections) is a generic onset function:

$$p_{HT}(\gamma) = p_0 + p_1 \log_{10}(\gamma) + \frac{p_2}{1+\exp(-(\log_{10}(\gamma) - p_3)/p_4)} \tag{12.2.1}$$

The various components of this function are discussed in the next sections.

To reduce ambiguities in track-selection from e.g.: $e^- \to e^-\gamma \to e^-e^+e^-$ or pion decays, the MC study is based entirely on muons. The muon energies are selected in such a way that their γ-factors

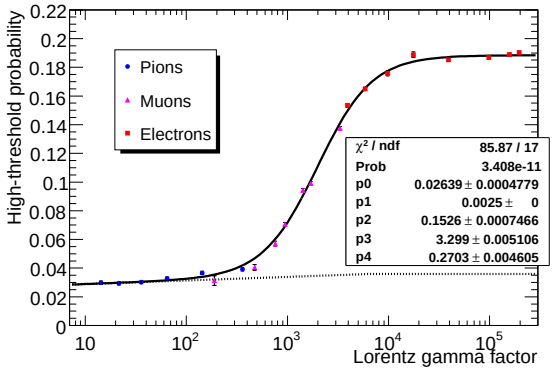

Figure 12.2.1: *HT probabilities for different particles as a function of γ-factor from test-beam.*

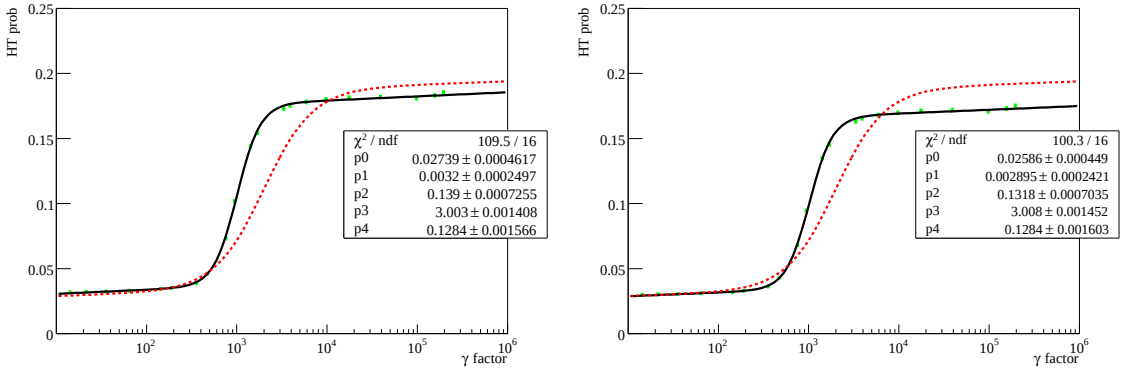

Figure 12.2.2: *MC HT probabilities as a function of γ-factor (full curves). Each point represents an average of 10000 tracks. On the left is shown the result obtained using the default setting: HT=6 keV whereas the right-hand figure shows the result after tunning the low energy plateau to data: HT=6.25 keV. Note that in both plots, the TR efficiency is set to the somewhat arbitrary default setting: 0.8. The dotted curves shown in both plots is the data fit as described by the parameters in figure 12.2.1.*

match those of the Combined Test Beam - i.e. a muon run corresponding to each point in figure 12.2.1.

The tuning of the transition radiation model proceeds in three steps: First the low energy dE/dx tail is tuned, then the TR onset part is tuned and finally the high energy plateau.

12.2.1 Step 1: Tuning the *dE/dx* tail

Figure 12.2.2(left) shows the default MC HT probability corresponding to the test-beam data of figure 12.2.1. Low energy ionization has been subject to intense study during a period of many years. Most of the important results are implemented in the PAI model which in this domain is very trustworthy. It is therefore considered safe, to tune the low γ tail of figure 12.2.2(left) to data using as tuning parameter the HT setting. Switching off the TR model in the simulation gives the pure dE/dx curve shown in figure 12.2.3(left).

In the combined test-beam study, a dependence of the specific module on the HT probability was found, but never fully understood [Pet07]. Due to this, the curve in figure 12.2.1 can be fitted only by

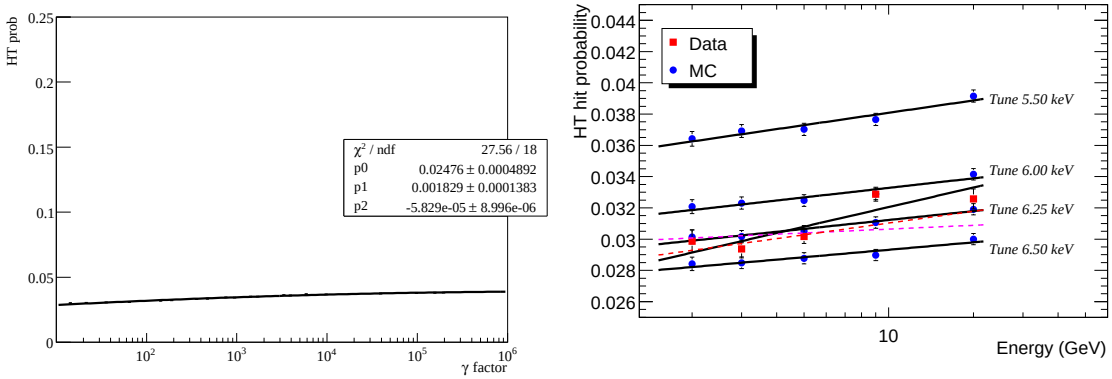

Figure 12.2.3: *Left: MC dE/dx curve in the full range after tuning the low energy tail to data. Obtained by switching off the TR creation. Right: dE/dx of MC with different settings, and various fits to data as explained in the text.*

artificially scaling the low- and high-energy plateau. Obviously, this causes some uncertainty in the fit, since the scaling to a large extent is arbitrary. In figure 12.2.3(right) the purple lines show the result of different fit approaches, and due to their spread a precise fine-tuning of the high threshold setting is premature, and 6.25 keV is chosen since it is sufficiently close to all data fits. Incidentally, this HT setting is not to deviant from the nominal value of HT$=$ 7.0 keV which is the CTB hardware setting. Note, that corresponding to the case of the LT setting, the meaning of the software and hardware definitions differ, and some discrepancy can be expected. The resulting TR onset curve is shown in figure 12.2.2(right).

When compared to the corresponding distribution measured in the test-beam (the dotted curve in the same figure) it is clear that there are differences which cannot be explained by an inaccurate HT setting - instead it seems that the transition radiation model as implemented in the software is inaccurate.

12.2.2 Step 2: The transition radiation onset

As mentioned earlier, the transition radiation simulation in the ATLAS experiment is based on a custom implementation of the model presented above, and not the `GEANT4` default which was poorly suited for the transition radiation simulation needed by in the TRT software, since it does not take into account interference between radiation produced at different gas-foil transitions.

A study of the details of the transition radiation model implementation in the ATLAS software, reveals a potential problem for the barrels modules. The foam responsible for creating the TR photons is in lack of a better model approximated by the same foil as for the end-cap. Differences in the transition radiation production are introduced only via a constant factor whose effect is to disregard a certain fraction of the created TR photons in the barrel with respect to the end-caps (named TR efficiency in the following). Taking figure 12.1.1 into consideration it seems plausible that this could not only result in a wrong overall high threshold probability in the $\gamma \rightarrow \infty$ limit, but also the details of the TR onset curve could be inaccurate.

In order to force the onset curve of the MC to match that of data, the number of created MC transition radiation photons is modified according to the ratio between the fits to the HT probability curves for data and MC after subtracting the dE/dx curve shown in figure 12.2.3(left). The ratio of the fits of

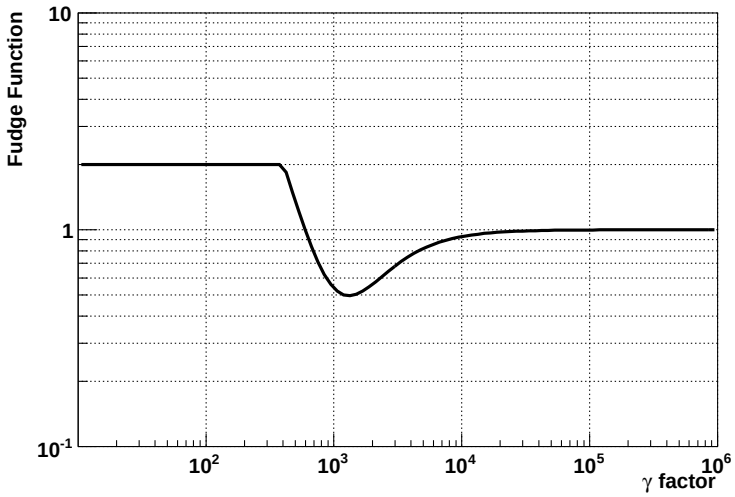

Figure 12.2.4: *Fudge function scaling the number of photons in MC to give the TR onset curve of data. The maximal allowed value of the fudge function is 2.*

figures 12.2.1 and 12.2.2 has the functional form:

$$N_\gamma \rightarrow N_\gamma \cdot \frac{1+e^{-(\log\gamma-3.008)/0.1284}}{1+e^{-(\log\gamma-3.299)/0.2703}} \tag{12.2.2}$$

where N_γ is a Poisson number with mean as given by equation 12.1.3. The function is shown in figure 12.2.4 - including a cutoff, implemented so that the correction do not exceed a factor of 2. The cutoff is needed in order not to wrongly interpret, and artificially scale, small differences between the low energy tails of the data and MC curves, as being due to transition radiation. The reason to subtract the dE/dx curve is that only the TR model is to be modified - not the dE/dx part underneath which is assumed valid.

The resulting HT probability curve is shown in figure 12.2.5(left) along with the CTB curve. Clearly, the main features of the TR onset is now effectively reproduced in the simulation, the only remaining issue is to tune the high energy plateau which is done below.

12.2.3 Step 3: The saturation level

Since the number of transitions between gas and fibers is finite and since some fraction of the TR photons are reabsorbed in the foam, the HT probability saturates at a certain γ-factor. The final tuning concerns the simple matching of the saturation plateau in data and MC. In the simulation (actually in the digitization) this is done by tuning the overall TR efficiency. The final result of the tuning is shown in figure 12.2.5(right). The corresponding TR efficiency is 95%.

12.3 Conclusion

The method and results described in this chapter are implemented in the ATLAS simulation software and used per default. In the present situation, where the HT probability curve of MC matches data

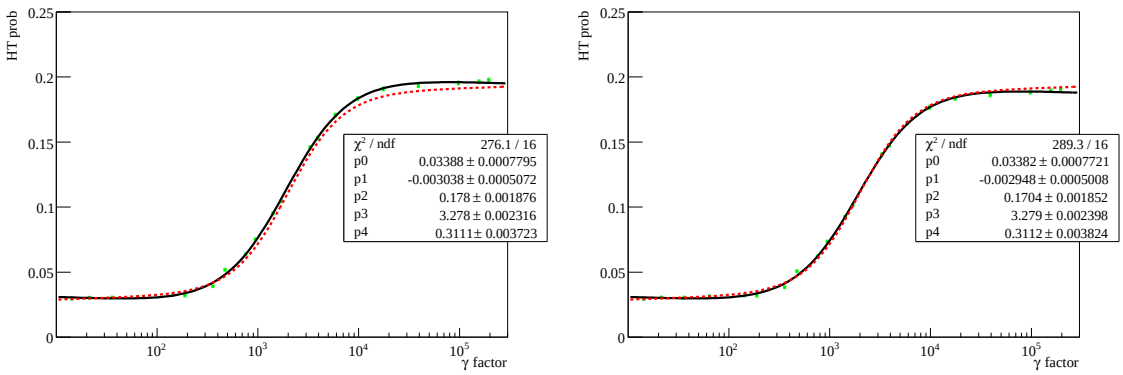

Figure 12.2.5: *Modified MC (full curves) and data (dotted curves). Left: TR efficiency 100%, Right: TR efficiency 95%.*

well, it is clear that PID information can be extracted in data as well as in reconstructed MC solely based on the HT probability curve. An advantaged approach is being developed, where not only HT probability, but also time-over-threshold and single track χ^2 are combined to a common PID probability.

Note that the present analysis concerns barrel tuning only, since no recent test-beam data exist for the end-caps. In principle future cosmics data, using a Xenon based active gas rather than the Argon based which has been used so far, could be used at least for a rough tuning. However, the η dependence of the HT probability which is expected for collision data, cannot be probed using cosmics. For this reason the corresponding tuning of the end-caps will await ATLAS collision data.

Chapter 13

Late conversions

Having now described both hardware and software aspects of the TRT, this chapter presents an example of the usage of the detector; namely to reconstruct photon conversions taking place in the detector. As will be argued below, such reconstruction has multiple applications ranging from material mapping capabilities to reconstruction of Higgs events in the $\gamma\gamma$ channel.

13.1 Introduction

In chapter 9, the material budget of the TRT is discussed. Table 9.1.1 summarizes the most precise knowledge presently available as obtained from surveys, as well as the corresponding values from the TRT GeoModel. From the discrepancy between the values of the survey and the GeoModel one can estimate the uncertainty to be at the level of a few percent and the geometry is presumably known to similar precision. When the experiment goes into operation it is anticipated that the uncertainty on the position of the active detector elements, will be highly improved due to the individual sub-system alignment as well as the global alignment. For the TRT, it is planned to use large pion samples to continuously monitor the position of each straw. Preliminary analysis [Boc08, BH07] suggests, that the individual straw positions in the barrel can be determined to within $\sim 0.3\ \mu$m in ϕ and $\sim 0.3\ \mu$m in the radial direction. However, the alignment is not able to directly measure the location of non-active material, and for certain precision measurements this distribution is of importance. An example is the W mass measurement in the $W \to e\nu$ channel, where the relative precision is aimed at less than half a permille. As discussed in Part II, the dependence on the simulation with respect to the momentum scale determination, and thus the detector material, is avoided by in situ calibration using the Z events, differentially in η and p_T. However, other systematic errors, like the systematic error introduced by final state radiation, do depend on the ability of the simulation to accurately resemble data, and in general, of course, it is desirable to have accurate simulations. In order for this to be possible, all parts of the ATLAS detector must be minutely accounted for in the detector description of the simulation, both with respect to position, shape and nuclear composition. Unless special techniques are employed, table 9.1.1 (or more precisely the full underlying GeoModel) represents the most exact knowledge of the non-active material at the present stage, and is not expected to be significantly improved during the detector operation.
However once data taking starts, photons will be among the produced particles. In figure 13.1.1, the expected photon statistics after triggering is shown as a function of E_T corresponding to one year of

low luminosity running. Clealy, the sample size is large enough to allow for a detailed mapping of the detector from the reconstruction of the conversion vertexes as will be explained below.

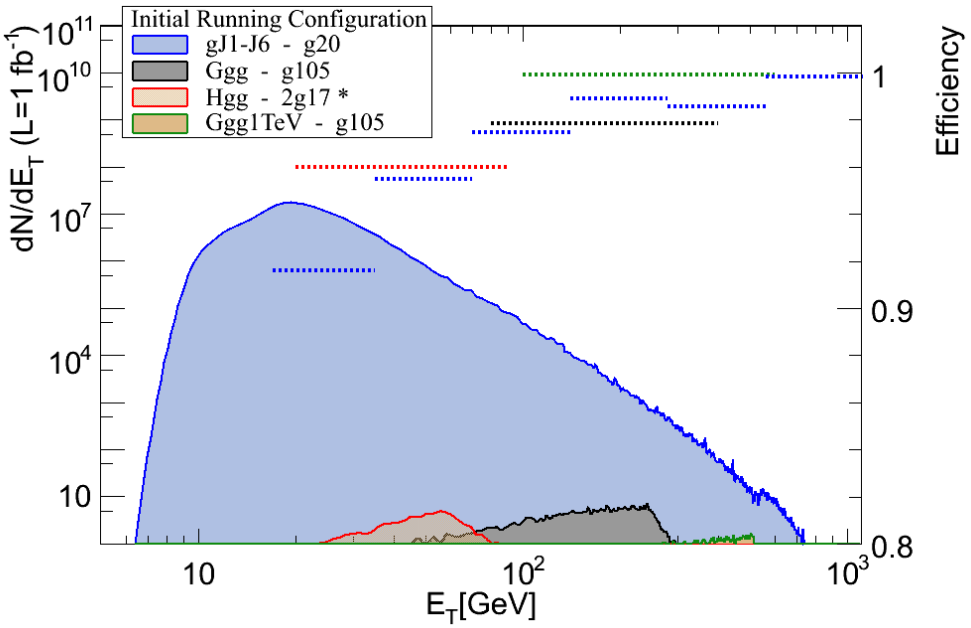

Figure 13.1.1: *Photon p_T spectra after triggering corresponding to one year of running with low luminosity. Only selected channels are shown - note that the photons from π^0's are not included. The main contribution is due to photon-jet events (labelled gJ1-J6), whereas the signal events studied: Gravition to photon-photon (two different samples labelled Ggg) and Higgs to two photons (Hgg) constitute small pertubations on this 'background'. The trigger efficiencies (according to various trigger menus referred to in the legend) are shown on the right-hand scale, and indicated in the figure using the color-coded dotted lines. Source: [And07].*

13.2 Theory of photon conversions

As explained in chapter 3, one of the important design parameters of the LAr calorimeter, is its ability to distinguish photons from electrons. In order for the calorimeter to find a photon produced in the interaction region, the photon must pass through the entire Inner Detector. In vacuum, of course, the photon range is infinite, but in presence of matter, a photon can scatter on free electrons or atoms in the material and more importantly: A photon can undergo pair production, since momentum can be transfered from a close-by nucleus to a passing photon, hereby satisfying energy/momentum conservation in the conversion vertex (which is impossible in vacuum). The leading order diagrams for this process are shown in figure 13.2.1(left).

Other processes like Compton scattering of a photon on a free electron, and Raleigh scattering of a photon on an atom are strongly suppressed with cross-sections orders of magnitudes below the pair production cross-section [Leo87].

Within the energy reach of LHC, the cross-section for photon conversion is approximately constant:

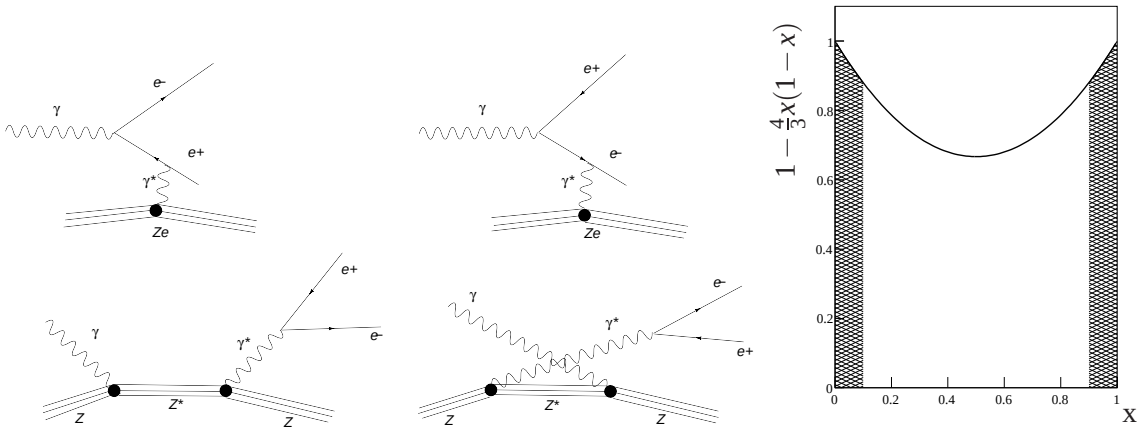

Figure 13.2.1: *Left: Leading-order Feynman diagrams for photon conversions following from interaction with a nucleus [ega08]. Right: Equation 13.2.3 (up till normalization factors). The dashed areas, corresponding to 24% of the total integral, illustrate the fraction of events where one of the electrons has* $p_T^e < 500$ *MeV for* $E_T^\gamma = 5$ *GeV.*

$$\sigma(\gamma \to e^+e^-) = \frac{7A}{9\lambda N_A}, \tag{13.2.1}$$

where A is the atomic mass measured in g/mol and λ is the radiation length of the matter traversed by the photon. Except for the very lightest gasses, the radiation length can be approximated by:

$$\lambda = \frac{716.4\ \text{gcm}^{-2}A}{Z(Z+1)\ln(287\sqrt{Z})}, \tag{13.2.2}$$

where Z is the atomic number. Although energy and momentum conservation is ensured due to the interaction with the material, the electrons need not to share the photon energy equally as can be inferred from the below differential cross-section with respect to the electron energy fraction $x = E_{e^-}/E_\gamma$ [ega08]:

$$\frac{d\sigma}{dx} = \frac{A}{\lambda N_A}\left(1 - \frac{4}{3}x(1-x)\right) \tag{13.2.3}$$

As expected, this expression is unchanged under charge conjugation - i.e. under interchange of x and $(1-x)$. Since the electron energy fraction in a given event can take any value between zero and one, either one of the electrons is likely to fall below the minimal requirement of transverse momentum $p_T^e \gtrsim 500$ MeV as defined by the tracking algorithms, even in cases of where the converting photon is considerably more energetic (see figure 13.2.1(right)). Thus the conversion reconstruction is not entirely trivial. However, reconstruction algorithms can take advantage of the facts, that the invariant mass of the decaying particle should be vanishing and the reconstructed tracks should be parallel at the vertex as required by momentum conservation (due to the zero invariant mass of the photon).

13.3 Motivations for studieng late conversions

As discussed below, finding conversions has multiple applications, but in addition to the actual usage of the conversion vertices for analysis, it should be emphasized that the pure fact of tagging hits as

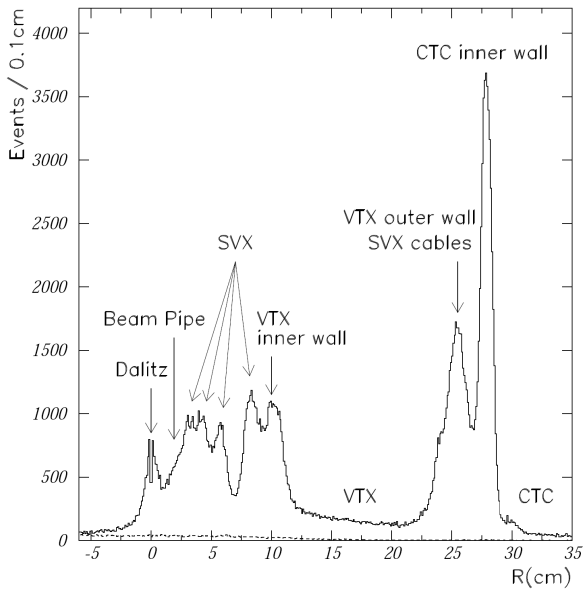

Figure 13.3.1: *Radial distribution of conversions at CDF. The various detector layers are easily distinguishable. Source [CDF01].*

originating from electrons due to a photon conversion reduces the uncertainty in the event and thus to some extent ease the remaining of the event reconstruction.

It is clear that many conversions will occur in the dense silicon layers of the Pixel and SCT as well as in service regions of these sub-detecotors. Due to the large amount of material in and around the TRT (despite all efforts to reduce it), a significant percentage will convert within this volume. An estimate of this is can be obtained from figure 9.1.8. This plot shows, that the TRT constitutes roughly $\frac{1}{2}$ radiation length, implying that $\sim \frac{1}{3}$ of the photons entering the TRT will convert within this volume.

Below it is studied to which extent one could gain knowledge of the position of e.g. the TRT barrel shells from reconstructing the conversion vertexes. That indeed this should be possible is illustrated by the CDF example in figure 13.3.1, where a radial resolution of reconstructed vertexes of about 4 mm is obtained. As opposed to the in situ calibration of the momentum scale using leptons from Z decays for the W mass measurement of ATLAS (cf. Part II), CDF use conversions (in essence figure 13.3.1) and J/ψ and Υ decays to correct the momemtum scale. The main reason for choosing this approach is (presumably) the highly reduced Z statistics with respect to the ATLAS expectations.

Figure 13.3.2 shows the conversion radius in the Inner Detector according MC truth as observed in a singe photon run with $E_T^\gamma = 5$ GeV, $\eta = 0$ and vertex located at $(x,y,z) = (0,0,550)$ mm (the displacement from $(0,0,0)$ mm is chosen to avoid the central non-active region of the innermost TRT barrel straw-layers). In this figure, the SCT layers and TRT barrel shells can clearly be identified. Note that the figure cannot be directly translated to a density map due to the dependence of the photon conversion cross-section on the atomic number of the interacting material as described by equations 13.2.1 and 13.2.2. For such translation to be possible, the material composition of the various parts as discriebed by the GeoModel most be taken into properly account.

In addition to the above use of reconstructed conversions to map the detector material, there are applications which are more directly related to physics. Most notably is the Higgs decay into two photons,

where atleast one of the high p_T photons converts. Regardless of whether the decay photon(s) convert or not, the corresponding electromagnetic cluster is reconstructed. However, in case the photon is tagged as such, this information in itself provides a useful handle to be used by the clustering algorithms.

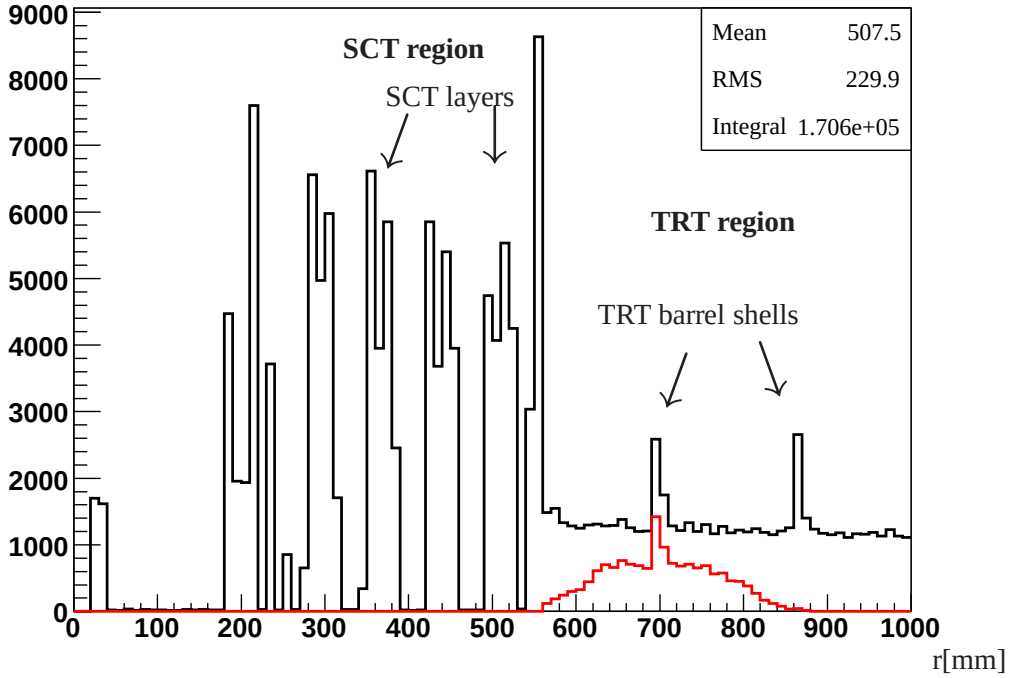

Figure 13.3.2: *Conversion radius of photons from a single-photon $E_T^\gamma = 5$ GeV run according to MC truth. The high density SCT layers and TRT barrel module shells are clearly visible (cf. figure 3.2.3), whereas this particular single photon run configuration totally avoids the Pixel layers. The red histogram refers to the selection discussed in section 13.4.3.*

13.4 Late conversions and the TRT Conversion Finder

Reconstructing conversions is by no means a new exercise within ATLAS software. Numerous efforts have been made, and for decay configurations with SCT and/or Pixel hits, existing software is able to fit the vertex with a satisfactory precision [ega08]. The late conversions, taking place after the silicon layers, constitute a special problem for standard fitters, since the information in z is limited in the TRT barrel and similarly is the precision of r in the end-caps. Figure 13.4.1 shows examples of radial residuals obtained using existing fitters for different photon conversion configurations: Both tracks have silicon hits, one of the tracks has silicon hits and the case where both tracks consist of TRT hits only. Clearly the latter two lies outside the scope of the standards fitters calling for an specialized TRT conversion fitter.
Below, the develupment of a fitter is described, and the resulting conversion finder tool is tested against the latter catagory of events where both conversion tracks consist of TRT only hits.

The developed method is based upon kinematic fitting [Ave00, Ave08], where the knowledge of the

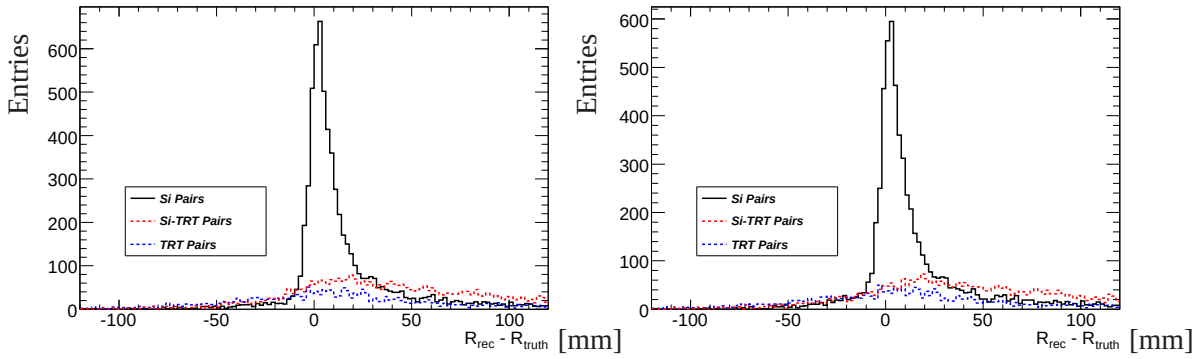

Figure 13.4.1: *Radial residuals for Kalman (left) and Chi2 (right) fitters for different inputs using single photons at $E^{\gamma} = 20$ GeV. Figures are provided by T. Koffas.*

physics governing the photon decay, is exploited to improve the actual measurements. The implications of the physical laws are expressed in terms of constraint equations, and the χ^2 minimization proceeds by the use of a Lagrange multiplier principle [lgs08]. The method of Lagrange multipliers has the advantage of being able to handle constraints (e.g. $M_{\gamma} = 0$), and in the case of vertex fitting, the correlation between the participating tracks can be correctly included.
The minimization thus attempts to satisfy the constraints defined by the physical principles under the limitations provided by the measurement precision - i.e. the covariance matrix is not to be violated by changing measurements more than their uncertainty can account for.

One complication encountered by choosing this approach is, that the constraints are most easily expressed in position / momentum space rather than the perigee representation usually used for tracking within ATLAS reconstruction software. In order to resolve, a transformation between the two coordinate spaces is required.

13.4.1 Coordinate transformations

The usual ATLAS perigee representation: $\beta^{track} = (\phi, \theta, d_0, z_0, \frac{q}{p})$ is substituted to the position/momentum representation: $\alpha^{track} = (p_x, p_y, p_z, E, x, y, x)$ via the following relations:

$$
\begin{aligned}
p_x &= \sin(\theta)\cos(\phi)/|\frac{q}{p}| \\
p_y &= \sin(\theta)\sin(\phi)/|\frac{q}{p}| \\
p_z &= \cos(\theta)/|\frac{q}{p}| \\
E &= \sqrt{\left(\frac{q}{p}\right)^{-2} + m_e^2} \\
x &= -d_0\sin(\phi) \\
y &= d_0\cos(\phi) \\
z &= z_0
\end{aligned}
\tag{13.4.1}
$$

where the reference point of the perigee representation is assumed to be $(0,0,0)$.

This set of variables is not mutually independent, but has the advantage that constraints can be expressed in a straightforward way.

Although principally trivial, the complexity of the algebra increases significantly when expressing the covariance matrix in the position/momentum representation. For each entry (i,j) the covariance matrix takes the form:

$$Cov(\alpha_i^{track},\alpha_j^{track}) = \sum_{k,l}(\partial\alpha_i^{track}/\partial\beta_k^{track})(\partial\alpha_j^{track}/\partial\beta_l^{track})Cov(\beta_k^{track},\beta_l^{track}) \tag{13.4.2}$$

13.4.2 Lagrange multipliers

The details of the fitting technique can be found in [Ave00, Ave08], for the present purposes it is sufficient to state the general results, adopted to cover the special case of conversion fitting.

The parameters describing the tracks combined in a single column vector, α, of length 2×7 :

$$\alpha^T = (p_{x,1},p_{y,1},p_{z,1,}E_1,x_1,y_1,z_1,p_{x,2},p_{y,2},p_{z,2},E_2,x_2,y_2,z_2) \tag{13.4.3}$$

There are two constraints:

- The invariant mass of the decaying particle is zero. Equivalently: At the vertex, the two tracks are parallel.
- At the points on the tracks, where the tracks are parallel, they should occupy the same point in space.

This gives 2×3 constraints, since both constraints give rise to an equation for each spatial(/momentum) dimension.

To apply the formalism, the constraints must be expressed in equations of the form: $\mathbf{H}(\alpha)=\mathbf{0}$. Expanding around an approximate solution, α_A, yields the linearized equations:

$$\mathbf{0} = [\partial\mathbf{H}(\alpha_\mathbf{A})/\partial\alpha](\alpha-\alpha_\mathbf{A})+\mathbf{H}(\alpha_\mathbf{A}) \equiv \mathbf{D}\delta\alpha+\mathbf{d} \tag{13.4.4}$$

where

$$D = \begin{bmatrix} \frac{\partial H_1}{\partial\alpha_1} & \frac{\partial H_1}{\partial\alpha_2} & \cdots & \frac{\partial H_1}{\partial\alpha_{14}} \\ \frac{\partial H_2}{\partial\alpha_1} & \frac{\partial H_2}{\partial\alpha_2} & \cdots & \frac{\partial H_2}{\partial\alpha_{14}} \\ \vdots & \vdots & \ddots & \vdots \\ \frac{\partial H_6}{\partial\alpha_1} & \frac{\partial H_6}{\partial\alpha_2} & \cdots & \frac{\partial H_6}{\partial\alpha_{14}} \end{bmatrix} \tag{13.4.5}$$

$$d = \begin{bmatrix} H_1(\alpha_A) \\ H_2(\alpha_A) \\ H_3(\alpha_A) \\ H_4(\alpha_A) \\ H_5(\alpha_A) \\ H_6(\alpha_A) \end{bmatrix} = \begin{bmatrix} \frac{p_{x,1}}{\sqrt{{p_{x,1}}^2+{p_{y,1}}^2+{p_{z,1}}^2}} - \frac{p_{x,2}}{\sqrt{{p_{x,2}}^2+{p_{y,2}}^2+{p_{z,2}}^2}} \\ \frac{p_{y,1}}{\sqrt{{p_{x,1}}^2+{p_{y,1}}^2+{p_{z,1}}^2}} - \frac{p_{y,2}}{\sqrt{{p_{x,2}}^2+{p_{y,2}}^2+{p_{z,2}}^2}} \\ \frac{p_{z,1}}{\sqrt{{p_{x,1}}^2+{p_{y,1}}^2+{p_{z,1}}^2}} - \frac{p_{z,2}}{\sqrt{{p_{x,2}}^2+{p_{y,2}}^2+{p_{z,2}}^2}} \\ x_1-x_2 \\ y_1-y_2 \\ z_1-z_2 \end{bmatrix} \tag{13.4.6}$$

$$\delta\alpha = \alpha - \alpha_A \tag{13.4.7}$$

By this, the equation to be minimized can be written:

$$\chi^2 = (\alpha - \alpha_0)^T V_{\alpha_0}^{-1}(\alpha - \alpha_0) + 2\lambda^T(D\delta\alpha + d), \tag{13.4.8}$$

where V_{α_0} is the (14×14) covariance matrix, with '0' representing the result of the previous iteration. At the minimum the following relations hold:

$$\begin{aligned} \alpha &= \alpha_0 - V_{\alpha_0} D^T \lambda \\ \lambda &= V_D(D\delta\alpha_0 + d) \\ V_D &= (DV_{\alpha_0}D^T)^{-1} \\ V_\alpha &= V_{\alpha_0} - V_{\alpha_0} D^T V_D D V_{\alpha_0} \\ \chi^2 &= \lambda^T V_D^{-1} \lambda \end{aligned} \tag{13.4.9}$$

13.4.3 Implementation and preselection

The kinematic fitter, which is named TRT Conversion Finder, is merged into the standard ATLAS conversion finding software, where it is used in case of TRT only track segments. Based on truth information, the following preselection is performed: Each photon is required to convert within the TRT, resulting in two reconstructed and oppositely charged tracks, each with $p_T^{e,truth} > 500$ MeV non of which are subject to a bremsstrahlung loss above 10% of the track momentum according to MC truth. The combined reconstruction and selection efficiency is illustrated in figure 13.3.2 as the ratio between the histograms. Ultimately, the use of truth information must be abondoned, but for the develupment of the algorithm, it provides a useful handle. Note in this respect that the particle identification efforts from notably HT probability studies as discussed on several occations in this thesis, provide a useful information in the track preselection.

After successful vertex fitting, the resulting tracks and corresponding covariance matricies are translated back into perigee space, so that the conversion vertex and the updated tracks can be returned to the standard ATLAS offline reconstruction framework. Note, that not only is the vertex found, but also, are the tracks updated using the constraints, so that in principle, more accurate track-parameters is a side-effect of the vertex fit. The extent to which the tracks are improved will be shown in the next section (figure 13.4.2(a,c)).
The TRT Conversion Finder is presently being implemented to be part of the standard conversion reconstruction software of ATLAS.

13.4.4 Results and preliminary optimization

As starting point (α_0) for the fitter is chosen the geometrical mean between the innermost hits on the two tracks and the corresponding track-parameters. Figure 13.4.2 shows the performance with respect to p_T and the opening angle, ψ, between the tracks at the vertex. As argued in section 13.2, this angle should be vanishing from a theoretical point of view, and it is one of the quantities which the fitter seeks to minimize, while subject to the constraints of not changing track-parameters more that allowed by the covariance matrix.

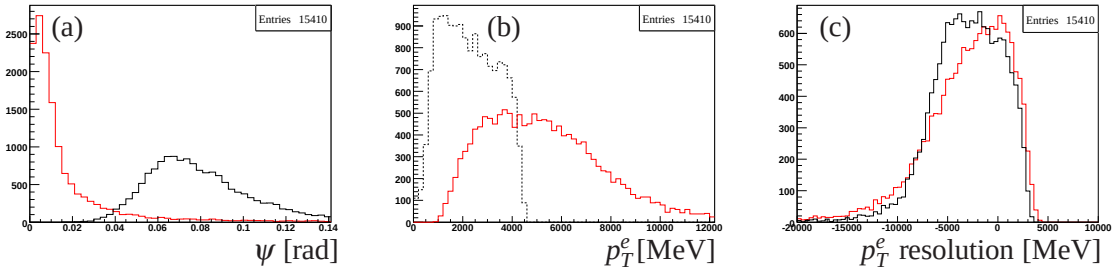

Figure 13.4.2: *Performance with respect to ψ(a) and p_T^e(b,c) for the $E_T^\gamma = 5$ GeV single photon run discussed in the text (section 13.3). Black full histograms represent the starting point and red histograms show the results after fitting, whereas the black dashed histogram in figure (b) represents MC truth.*

For algorithm optimization, the performance of the algorithm with respect to the radial resolution, r_{conv}, depending on the number of iterations is shown in figure 13.4.3. Practically no dependence is observed, and the default setting is for this reason set to 1 iteration only.
The energy dependence on the conversion finder performance is shown in figure 13.4.4 for $E_T^\gamma = 2$ GeV and $E_T^\gamma = 10$ GeV single photon runs. As would be expected from tracking performance considerations, the vertex resolution is significantly worse in the $E_T^\gamma = 2$ GeV run with respect to the $E_T^\gamma = 10$ GeV and $E_T^\gamma = 5$ GeV runs (cf. figure 13.4.3).

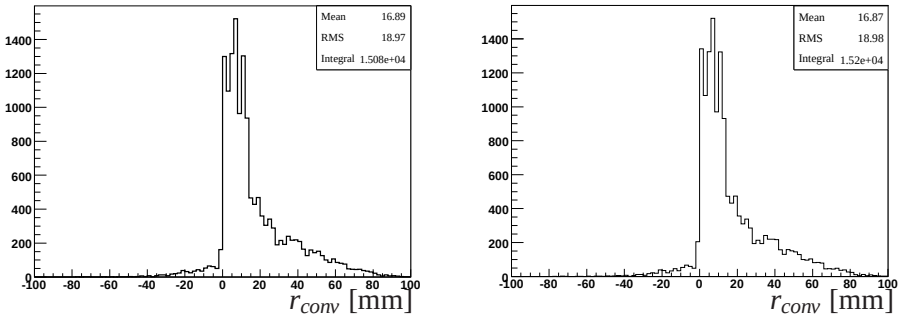

Figure 13.4.3: *r_{conv} resolution after 1 (left) and 10 (right) iteration(s). Based on the $E_T^\gamma = 5$ GeV single photon run discussed in the text.*

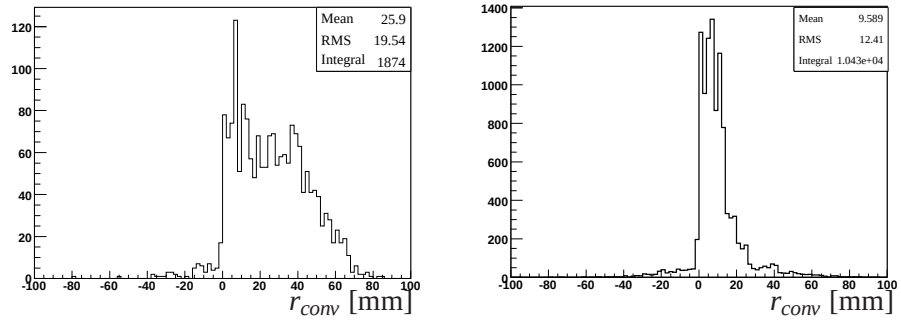

Figure 13.4.4: *r_{conv} resolution for a $E_T^\gamma = 2$ GeV run (left) and a $E_T^\gamma = 10$ GeV run (right). These runs differ from the $E_T^\gamma = 5$ GeV run discussed in section 13.3 only by the photon energy.*

13.4.5 Full ATLAS events

To assess the performance of the develuped conversion finder in more realistic event topologies, the fitter is tested on $t\bar{t}$ events which are some of the most complicated events expected during ATLAS operation. Figure 13.4.5 shows the corresponding performance of the TRT Conversion Finder. The result shows no obvious signs of degrading. Note, that the integrals of the two histograms are similar in the left-hand part of this figure, showing that the efficiency to reconstruct conversions is high. In the right-hand side, the efficiency falls off as expected, due to the low number of hits on the tracks, causing the tracking algorithms to fail the track reconstruction. It is emphasized that figure 13.4.5 is merely an example, and further studies are needed to validate the fitter with respect to performance in full ATLAS events.

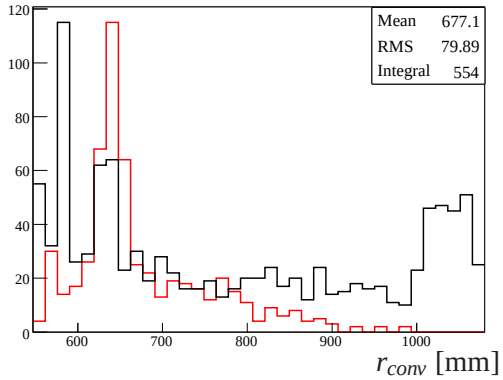

Figure 13.4.5: *Reconstructed (red) and true (black) conversions as a function of r_{conv} for $t\bar{t}$ events.*

13.5 Applications of the TRT Conversion Finder

13.5.1 Material mapping

In figure 13.5.1(left) is shown the results of a fit to about 15000 conversions of the $E_T^\gamma = 5$ GeV sample. The resolution obtained is about 4 mm. To make a sensible estimate of the expected precision achievable in real data, by using the expected photon statistics shown in figure 13.1.1, one would need to understand and remove the bias observed in figure 13.5.1(left). However, it is clear that once this is understood and removed, the location of high density volumes in the TRT, such as module shells, can be reconstructed to a high degree of accuracy.

By this, a number of ATLAS analyzes can indirecty benefit from the conversion finder, due to the improvements in the description of the detector material it facilitates. One example of this is the W mass analysis which depends on accurate detector description to minimize the systematic error inflicted by final state radiation. However, there are numerous other applications which depend on precise material maps; for example to account accurately for multible scattering, or to estimate photon background in various analyzes.

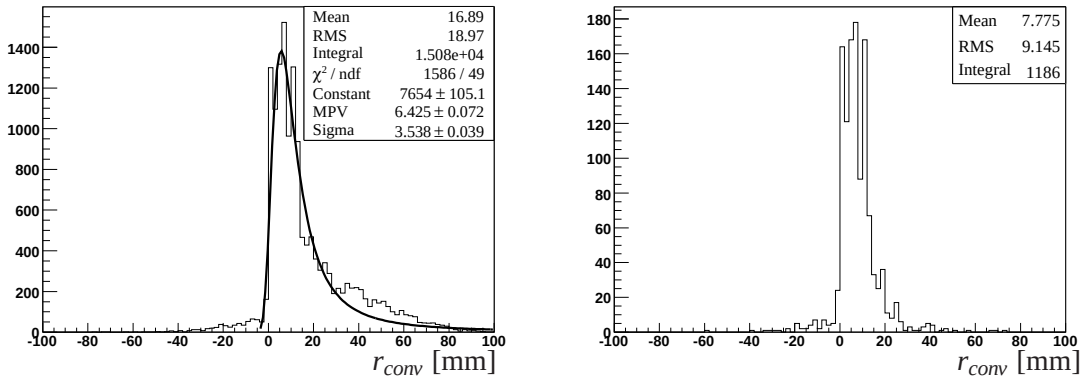

Figure 13.5.1: *Left: Fit to the radial conversion resolution of the $E_T^\gamma = 5$ GeV sample using a Landau function. Right: r_{conv} resolution for a $E_T^\gamma = 60$ GeV single photon run.*

13.5.2 Higgs search

In figure 13.5.1(right) the radial vertex resolution is shown for a 60 GeV single photon sample, generated using the same settings as the $E_T^\gamma = 5$ GeV run, except for the increased energy.

This energy is chosen in order to assess the performance of the algorithm in the energy range relevant for a Higgs search in the $H \rightarrow \gamma\gamma$ channel. From the results, it seems plausible that the present fitter will add to the mass resolution of Higgs signal in this decay channel, if for nothing else, then simply due to the fact that the electrons are identified as such, and this is valuable information when reconstructing the energy in the LAr calorimeter. However, it is emphasized that an in depth study is needed to quantify this issue in detail.

13.6 Conclusion

A method for fitting conversions taking place within the TRT has been established. Although not final in terms of understanding and correcting for the observed bias in the r_{conv} resolution, the results in terms of mapping of non-active material are promising. With respect to the possible usage for $H \rightarrow \gamma\gamma$ reconstruction, additional studies are needed to assess the impact of the conversion fitter on the mass resolution.

With respect to material mapping capabilities, the initial performance assessment presented is encouranging, suggesting that radial resolutions of about 4 mm of the conversion vertexes in the TRT barrel should be achievable. Furthermore, improvements are likely to arise from outside, in terms of improved tracking of low momenta electrons. As most photons are expected to be produced with low energy ($\pi^0 \rightarrow \gamma\gamma$), and since the precision in geometry determination will be dominated by the statistical error as determined by the number of photons and the track reconstruction efficiency, improving low p_T tracking would imply significant improvements in the geometry mapping capabilities of the TRT Conversion Finder.

I order for the fitter to be usefull, even in the case where one electron is lost due to the p_T requirement in the tracking algorithms, the fitter is being updated to allow for single track conversions.

Part IV

Towards data taking

Introduction to Part IV

On the verge of data taking, a number of issues emerge which need studying; some are mostly of practical character, while others are more closely related to physics. This last part of the thesis describes work which has been done to ensure that the detector and the software is well-understood and ready for LHC startup. Again, focus is put on the TRT sub-system which is where the author has contributed, but important results from other sub-systems will be summarized in chapter 18.

Commissioning of the TRT has been a continuous effort in several years. Without grasping too far back in history, one can argue that commissioning started at in 2001-2005 where the modules and wheels of the TRT barrel and end-caps arrived at CERN after production at US universities and Russia institutes respectively. Chapter 14 describes the initial tests and repairs performed at this stage, focusing on the barrel modules.
Later on, in the summer of 2004, a subset of the barrel modules were placed in a test-beam delivered by the SPS. The test-beam setup falls in two categories: The TRT stand-alone test-beam, from which results are presented in chapter 16 originate, and the Combined Test Beam on which chapter 11 is based. During the period: 2001-2005 the barrel and end-cap detectors were assembled (separately) in a building called SR-1 close to the entrance of the ATLAS pit. In parts of this period a fraction of the sub-detectors were equipped with read-out electronics, enabling them to record cosmic muons passing through the detector. A selection of results from this running period is presented in chapter 18. In 2007 the barrel and end-cap detectors were lowered to the ATLAS cavern and assembled into in the Inner Detector. Presently, increasing parts of the TRT and the other sub-detectors are equipped with read-out electronics and connected to data acquisition system. Data is collected in series of dedicated running periods called M-runs (i.e. M1, M2,...). Results from the M runs are reported, partly in chapter in chapter 17, but mainly in chapter 18 along with a description of the simulation setup developed to resemble interactions of cosmic muons.

Chapter 14

Acceptance testing of barrel modules

Once the TRT barrel modules and end-cap wheels arrive at CERN they are subject to a number of tests to ensure performance and detector safety[1]. Problems due to improper construction or shipment are repaired if possible or, if necessary, concealed, in order not to affect other detector parts or interfere with the running of the experiment.

14.1 TRT Barrel acceptance tests

Before a barrel module is approved for installation in ATLAS it must pass the following tests:

- *Dimension:* The geometry and weight of each module is measured and crosschecked against specifications.
- *Wire tension:* By the means of a tone generator each wire is set into oscillations, and the wire tension inferred from the resonance spectrum. Wires outside a specified wire tension range (in gram equivalents: [47-100] g) are removed and re-strung. See figure 14.1.1(left) for an example.
- *Gas Leak Test:* Gas is flushed through the modules, while the amount flowing in and out each module is closely monitored. Modules with abnormal leak ($> 0.1 \frac{\text{mbar}}{\text{bar}\cdot\text{min}}$) are examined in detail to locate and repair leaks.
- *Gain Mapping:* Using an X-ray probe, the gain of each wire is monitored along the wire length, see figure 14.1.1(right). In case of bend straws, the electric field in the wire is asymmetric and thus non-optimal for charge collection. Such straws, which have low gains, are repaired when possible.
- *High voltage tests:* High voltage is applied to each wire, to ensure electrical stability and that the current leakage is sufficiently low.

The high voltage tests are described in detail below, whereas more information on the other tests can be found in [TRT08b].

[1] For example: A module with an abnormal power consumption is potentially dangerous, since the module would heat up and thus risk damaging neighboring sub-systems which must be operated under cool conditions.

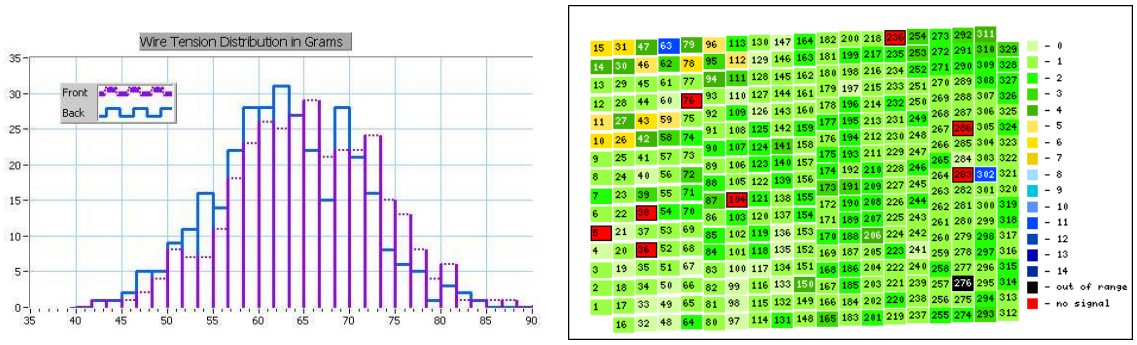

Figure 14.1.1: *Left: Wire tension in gram equivalents. Right: Gain map for front side (channels corresponding to one end of the straws) - summary of results from scans along the length of the individual straws. Both plots are based on tests of module 1.1. Source [Gag05].*

14.2 High voltage tests

The objective of the high voltage tests is to study any anomalous behavior of modules when subject to high voltage. Of particular relevance is to locate and repair current leaks. The reason for its importance, is that in case substantial leakage would build up while ATLAS is operating, the power consumption might exceed its specifications and the responsible sub-system must be shot down for detector safety reasons. In the TRT, this proceeds by burning the relevant fuse, but unfortunately fuses are installed only at an eight straw granularity, so in case a current leakage builds up during the operation of the experiment, one would have to take out eight neighboring straws, hereby creating a dead region in the detector.

In order to stress test the modules and to provoke problems to occur on a short timescale, the applied voltage between the anode wire and the straw is -1575 V which exceeds the expected nominal value of about -1480 V. While subject to high voltage, $ArCO_2$ is flushed through the straws (and CO_2 is flushed through the radiator) and the leakage current is monitored (see figure 14.2.1(left)). In case the leakage exceeds 2 μA the module is said to *trip* and an investigation is launched to find the exact location of the problem. Most trips are caused by electrically unstable anode wires, but occasionally a high voltage supply is the source (determined from the sign of the coherent voltage sack). Since the high voltage is supplied from a number of monitored connections, it is trivial to locate which high voltage connection, called high voltage pad (see figure 14.2.1(right)), a given trip occurred - except for ambiguities caused by the fact that the measurement equipment did not allow to monitor all pads individually, but only group-wise. In case of only one (or a few) tripping wire(s) the responsible pad(s) can be identified rather straightforwardly by redistributing the connections in the monitored groups and await the occurrence of another trip. Following this, probes are put on the individual wires to find which of the ≈ 8 [2] wires on the pad causes tripping. Once located, the module is sent the re-work, where the tripping wire(s) is repaired or removed and the high voltage test continues. For reasons unknown, some modules were dirty inside upon arriving at the test station. When subject to high voltage, the foreign objects caused electrical connections between the anode wire and the straw, resulting in frequent high voltage trips. It was found that a successful method for cleaning such modules is to apply the opposite voltage, causing electrons to move toward the straw tube and in the process burning electrical bridges between wires and straws, hereby drastically reducing the trip rate.

[2] Some pads have only 7 straws connected - see figure 14.2.1(right).

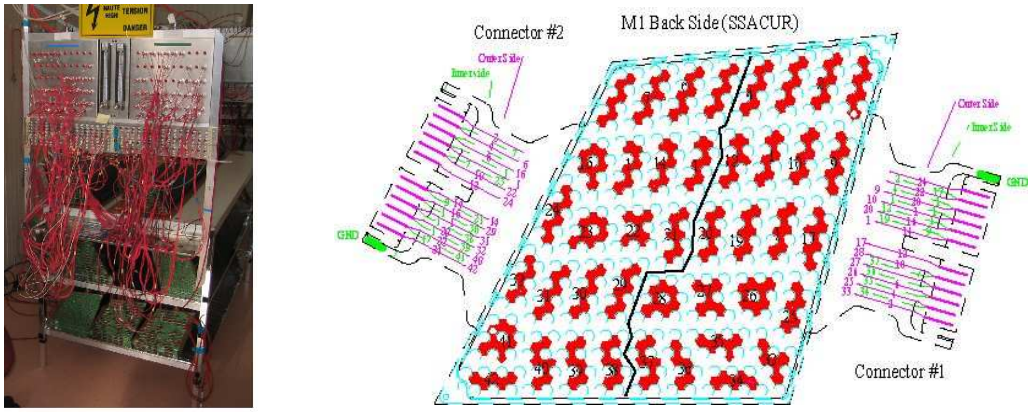

Figure 14.2.1: *Left: High voltage test station showing the monitored high voltage connections. Right: Layout of the high voltage connections of a type 1 barrel module. The individual pads connecting* ~ 8 *straws are shown in red. Also visible are the gas connections (lower left and upper right corner).*

Once the trip rate is sufficiently low, the modules are long term tested ($\sim$ 4 weeks) without monitoring individual pads. In case the trip rate exceeds specifications ($\sim$ 1 per day per module, where a trip corresponds to a current above 20 μA in at least 5 s), the module is returned to the high voltage test station and the above scenario is repeated.

Apart from locating current leaks and shortened wires, it is tested whether shell, high voltage plate or tension plate is shortened (cf. figure 3.2.4). On a number of occasions, such problems were found and repaired.

When a given module has successfully passed all the tests listed in section 14.1, it is reviewed. Problematic modules which have, e.g. many *dead* straws, non-constant high voltage behavior etc. can be marked “spare” and are to be used only in test-beam, or in case another module breaks down. Approved modules are moved to the assembly hall where they are mounted in the TRT support structure. Care is taking when distributing the modules in the TRT support rack, in order not place modules which have many dead straws in the same ϕ section.

A summary of the results in terms of dead channels can be found in table 14.2.1.

All test results are written to a database, where each module is given a “passport” in which all results, comments etc. for the specific module is stored for future reference [Gag05].

Problem	**Fraction** [%]
Dead at arrival	19.7
HV problems	28.6
Gain mapping	4.8
Bent straws	44.9
Broken sockets	1.8
Tension	0.3

Table 14.2.1: *Breakdown of the causes for dead straws. In total 1031 straws, corresponding to 2% of all barrel channels are listed as dead, whereas 1055 straws were successfully repaired.*

The end-cap wheels were subject to a similar series of tests [Cwe06]. Altogether 1354 end-cap straws are declared dead corresponding to less than 4‰.

Chapter 15

TRT Conditions and Calibration tools

In order to make optimal use of the TRT detector, it is important that the status of the individual channels is known at all times - i.e. which detector parts are functioning? (is a given channel dead?), and how are they functioning? (is a given channel noisy? What is its $r-t$ relationship? etc.). This chapter describes the development of software necessary to answer these and other questions, once the experiment goes into operation.

15.1 TRT Conditions

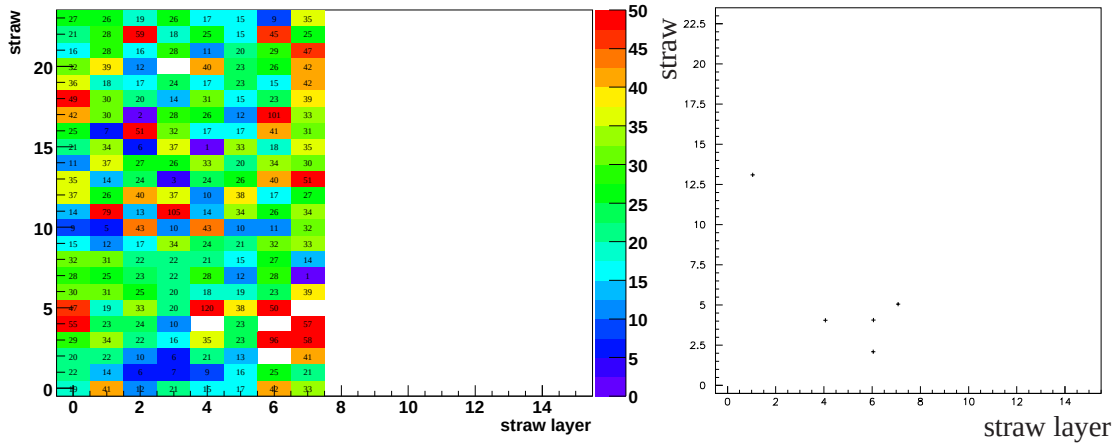

Figure 15.1.1: *Occupancy (left) and dead straws (right) of ϕ sector 10, negative end-cap wheel 13.*

Figure 15.1.1 shows an example of two maps of the same end-cap wheel in the same ϕ sector. The left-hand plot shows the occupancy in a M4 run, whereas the right-hand plot shows the channels which are declared dead (for example due to failing acceptance tests as described in the previous chapter). Clearly there is a correlation between the channels of zero occupancy and the dead channels, illustrating that the conversion from the hardware numbering scheme to the one used in the offline

software is correct. However, one channel which is declared dead has a nonzero noise level[1]. In fact, this is normal behavior of dead channels, and it occurs even when the wire is removed, which is standard procedure when a channel is declared dead. The explanation comes from the fact, that even in the case where the anode wire is removed, a voltage is applied to the straw tube and since the individual channel socket is not removed, a shortened or electrically unstable straw tube can give rise to a signal. In chapter 17 it is shown, that there is an enhanced probability that noise signals occur in the vicinity of a trajectory of a particle. For this reason, it is important to reject such noise signals in order not to introduce a bias to the passing track due to a fake measurement. To cope with this requirement, a tool (TRT StrawStatusSummaryTool), is written enabling to mask out dead channels in the offline reconstruction software. The tool can be used on a channel to channel basis, by means of the so called identifier - a unique label assigned to each straw. In data (i.e. cosmics so far) this tool can be invoked at the creation each of TRT measurement (called a TRT driftcircle[2]), so that measurements originating from dead straws are not created. Likewise, the tool is used in the simulation at the digitization stage in order for MC to resemble data with respect to the dead straw fraction and distribution. Needless to say, performance is of utmost importance for this tool, explaining why the choice of data container fell on the nested container of so called expanded identifiers (a $C++$ structure), in which the data can be retrieved by direct access, hereby avoiding a potentially time consuming search.

During ATLAS operation, the number of dead straws is expected to increase - if for nothing else, then simply due to the fact that the fuses have a limited lifetime[3]. Apart from an increasing dead straw fraction, it plausible that groups of straws are temporarily non-functioning due to for example high voltage or read-out problems. The latter underlines the fact, that the dead straw map is indeed a conditions quantity and therefore, the tool is initialized by a folder in the Conditions Database holding the information of dead straws, based on a review of the passports of the all modules and wheels as discussed in chapter 14. In case of temporary problems, the dead straw list in memory (i.e. the one based on the Conditions Database folder) is easily enlarged for a given run, based on user requirements.

An example of the usage of the tool, is from the M runs where increasing parts of the detector was connected to data stream. Simple calls to the tool allow in the simulation to switch off relevant parts of the detector in the software chain as shown in figure 15.1.2.

In order to take advantage of the software setup, the tool functionality is expanded to foresee additional usage. In particular, the fundamental data-word in which it is stored whether or not a given straw is dead, is enlarged in such a way that it is capable of holding information on:

- *LT occupancy level*. For low luminosity, this approximately equals the noise level of individual straws, but has the advantage that it can be set for each run from the on-line monitoring - i.e. before the track reconstruction, making it usable at that stage.
- *HT occupancy level*. In case of severe problems with a straw or read-out electronics, this could differ significantly from zero (discussed in section 16.2.2, in particular figure 16.2.5). As the LT occupancy, the HT occupancy is set in each run by the on-line monitoring.

[1] Also, there is a channel with zero occupancy which is not declared dead. This can be due either to an abnormal low noise level, simply that the channel is dead, but not (yet) declared so.

[2] In the initial processing, before the track reconstruction, it is not known at which side of a given straw a given track passed. What is known, is the time at which a signal occurred and from that a corresponding drift-radius is calculated. Therefore the objects are named driftcircles.

[3] An assessment by L. Rossi showed, that only one in 15000 fuses broke during one year [Ros06]. The rate at which fuses break down is expected to increase during detector operation.

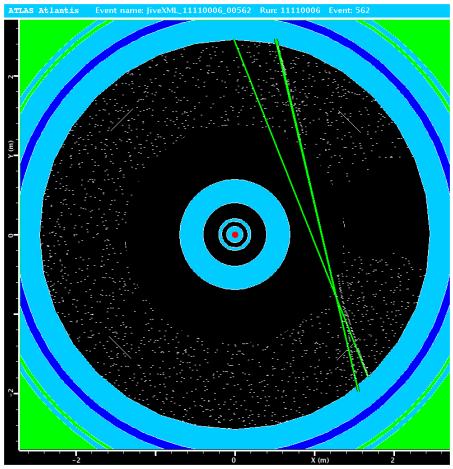

Figure 15.1.2: *Example of the usage of the TRT StrawStatusSummaryTool. Detector parts which are not read out (i.e. the dark noise-free area) is masked using the TRT StrawStatusSummaryTool in a simulated cosmic event.*

- *Particle identification flag*. Set by the reconstruction.
- *Tracking flag*. Set by the reconstruction.

In order to reduce memory usage, the information is encoded in the individual bits of a 16-bit data-word as shown in figure 15.1.3.

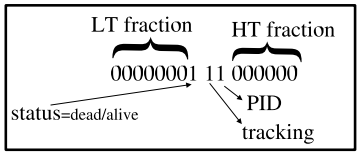

Figure 15.1.3: *Data-word used in the TRT StrawStatusSummaryTool.*

7 bits are used to store the LT occupancy, O_{LT}, and 6 bits are used for the HT occupancy, O_{HT}. Most straws are expected to have LT noise levels $\mathcal{O}(1\%)$ (cf. chapter 16). As an example of this, consider figure 15.1.1 which is based on 10092 events, the individual straw occupancy ranging $[0;1]\%$. For this reason it is advantagerous to use dynamical binning. The following binning is chosen:

- 6 equal size bins for $O_{LT} \in [0,5]\%$
- 1 bin for $O_{LT} \in [5,100]\%$
- 6 equal size bins for $O_{HT} \in [0,100]\%$

Since the occupancy information is to be filled already by the on-line monitoring, the information is available at the stage where the reconstruction algorithms enter the software chain, and thus noisy or problematic straws can here be rejected by a simple cut.

15.2 TRT Calibration

Related to the map of dead and noisy straws, is the mapping of the individual straw to its various hardware groupings. For a number of applications, it is useful to know to which high voltage connection or read-out electronics chip a given straw belongs. Equally important is the knowledge of which other straws belong to the same grouping. To facilitate this need, a tool (TRT StrawNeighbourTool) has been developed, which maps barrel and end-cap channels according to:

- DTMROC read-out chip, connecting 16 straws (some have only 15 straws).
- High voltage connection, connecting 8 straws (some have only 7 straws).
- Electronics board, connecting $\sim$ 16 straws (some have only 15 straws).

As the TRT StrawStatusSummaryTool, the TRT StrawNeighbourTool uses expanded identifier technology for direct access. Both tools are public available within the ATLAS software repository and are used throughout the community.

An example of the usage of the TRT StrawNeighbourTool is within the framework of the TRT calibration. Based on large track samples, the TRT calibration is responsible that t_0's and $r-t$'s relations are up to date and adequate for each straw at all times. During the running of the experiment, it can be required to calibrate the TRT more often than the track statistics allows. With the tool developed, one can take advantage of the fact that straws belonging to the same chip are expected to have roughly equal t_0, since a reasonable assumption would be, that the individual t_0 can differ only between chips, and if the length of the read-out wires differ (and they do). This implies, that straws belonging to the same chip, are expected to have approximately the same t_0, whereas there could be significant variations between chips. The same is not necessarily true for the $r-t$ relation, since for instance a bend straw is expected to have different $r-t$ relation than a straight straw. On the other hand: $r-t$ relations are presumably more stable than the t_0 offsets and therefore it is expected for the default $r-t$ calibration to use module-level granularity, supplemented by time independent channel to channel variations (taking into account e.g. bend straws). In order to test the validity of the assumption, figure 15.2.1 shows two examples of chip-wise t_0. The results are as expected: The variation between chips (i.e. the mean values of the histograms in figure 15.2.1) is much larger (up to 4 ns) than the variation within chips ($RMS < 1$ ns).

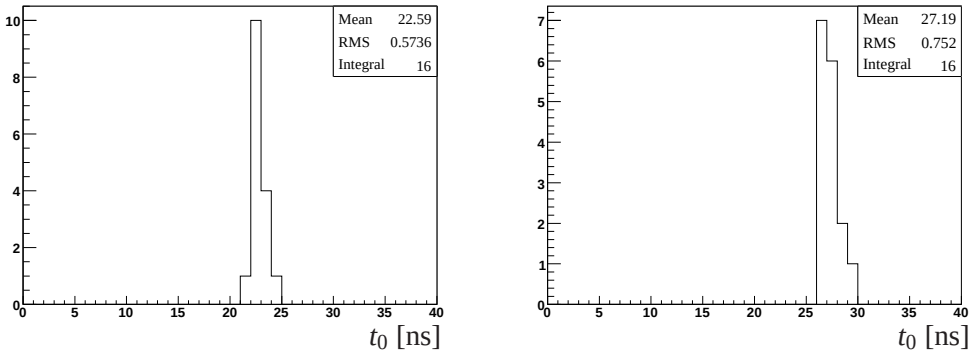

Figure 15.2.1: t_0 *distributions for straws belonging to two different chips.*

Calibrating t_0 per chip rather than per straw would, in the limit of infinite statistics, make the resolution worse by no more than maximum: $\sim 50\ \mu\text{m}\,(= RMS \cdot v_{drift} \approx 1\text{ ns} \cdot 50\ \mu\text{m/ns})$. Here it is assumed,

that the variations in t_0 seen in figure 15.2.1 are due to real physical differences - i.e. the individual straws are assumed to be perfectly calibrated which of course is an idealization. In the realistic case, t_0 is subject to uncertainty which could very well explain the spread observed in figure 15.2.1. In this case, the chip based method works equally well as the straw based calibration, even in the high statistics limit. In the converse case, where that statistics is limited, the gain in statistical uncertainty by using a chip-based approach is simply $\sqrt{N_{straws\,pr\,chip}} \approx 4$. Here it is assumed that variations in t_0 - i.e. the spread in figure 15.2.1 is due purely to statistical representations of *one* true t_0. In the converse case, where t_0 differs between straws belonging to the same chip, a systematic error of < 50 μm is introduced using the chip-wise t_0 determination.

The chip-wise calibration is implemented as one of the default calibration schemes of the TRT. In addition, a similar approach exist, based on the board grouping rather than chip grouping. Additional examples of the usage of the TRT StrawNeighbourTool are presented in chapter 17.

Chapter 16

A study of TRT noise in 2004 stand-alone Test Beam data

In this chapter noise in the TRT is analyzed using data from selected runs from the June 2004 TRT stand-alone test-beam. A procedure which reliably extracts noise hits is presented and the main features of those are examined. Finally, channel to channel correlations in noise levels are examined and the distribution of dead channels is compared results from the acceptance tests described in chapter 14. This chapter is based on [KK06] which is written in collaboration with T. Kittelmann.

16.1 Introduction

Even though the noise level in the TRT is known to be quite low, $\mathcal{O}(1\%)$, noise is still a relevant effect and as such ought to be both simulated along with the rest of the electronics response in the digitization phase as well as accounted for in reconstruction algorithms.

The purpose of the present study is to provide a basis for such an inclusion in the simulation algorithms by analyzing data from the 2004 TRT standalone test-beam [LR04]. It is demonstrated in section 16.2 how genuine noise hits are reliably extracted from the test-beam data and the general characteristics of those are shown. Finally in section 16.3 correlations between noise levels in different channels are investigated.

16.2 2004 Test Beam data

In July 2004 6 functional and tested TRT barrel modules, corresponding to 2 out of 32 phi sectors, were placed at CERN Prévessin at the end of a test-beam delivered by the SPS. Using various targets and magnet field selectors, beams of either pions, electrons or muons were delivered.

As explained in chapter 11, this was the first test-beam with the front-end electronics (including the ASDBLR chips) essentially of the final design, while the readout chain and data acquisition system were final prototypes, very similar to the ones that will be used in ATLAS.

In figure 16.2.1(a) the setup is shown, with the beam entering from the left. Before and after passing the TRT barrel the beam goes through various detectors with abilities to do high quality particle

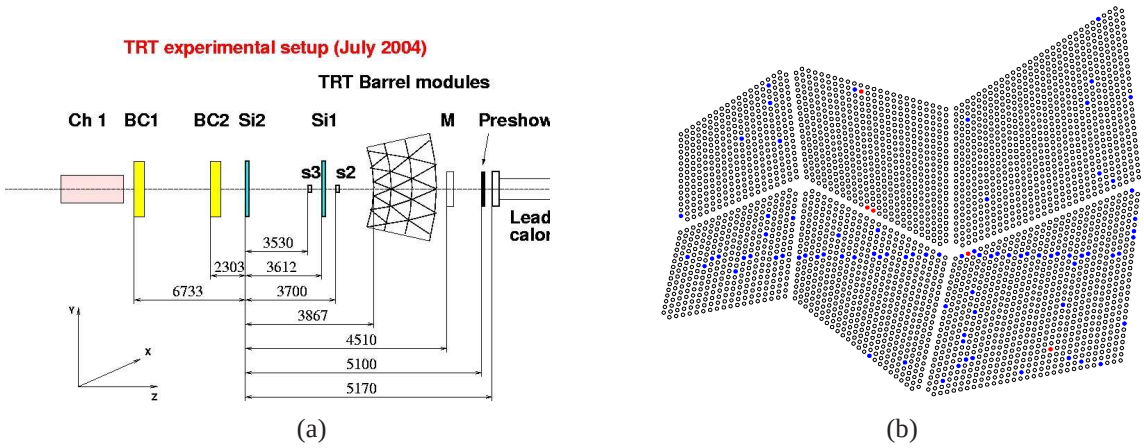

(a) (b)

Figure 16.2.1: *Basic setup of the 2004 TRT standalone test-beam (a), and example pion event from run 3183 (b). Hits with a high threshold bit set are shown in red.*

Run number	Beam Energy	Electrons	Number of events
3183	80 GeV	no	90K
3240	20 GeV	yes	60K
3241	20 GeV	yes	80K

Table 16.2.1: *Beam types and number of events for the three runs of data taking used in this section. All of the runs were taken using low threshold values of approximately 300 eV, high threshold values around 7 keV and with the beam passing at "position 9" – the meaning of which can be inferred from figure 16.2.1(b). Note that the beams were not pure electron or pion beams in the strict sense, but contaminated to some extent – see figure 16.2.2.*

identification, tracking and shower vetoing: A Čerenkov detector (Ch1), beam chambers (BC1-2) and silicon microstrip detectors (Si1-2). After the TRT the beam enters a multiplicity counter (M) and a lead-glass calorimeter. In the offline analysis, the multiplicity counter was used to reject events with multiple particles while the beam counter drift-chambers were used to seed the tracking algorithms – working dominantly on the high precision silicon measurements. The details of the setup and its performance are described in more details in e.g. [Tik04].

The setup thus provides events where the identity of the passing particle is well known and with good external knowledge of the parameters of the passing track, thus making them suitable for detailed studies of detector performance.

For the present noise studies the type of beam should in principle not matter, but for crosschecking purposes three runs with different beam compositions and energies are selected as summarized in table 16.2.1 and table 16.2.2.

16.2.1 Initial selection of noise hits

The goal of present study is to understand the rate and composition of the noise digits, i.e. the digits in figure 16.2.1(b) whose appearance are clearly not due to the passing track. Since the number of such noise digits over an entire run is rather high, quite safe cuts can be afforded.

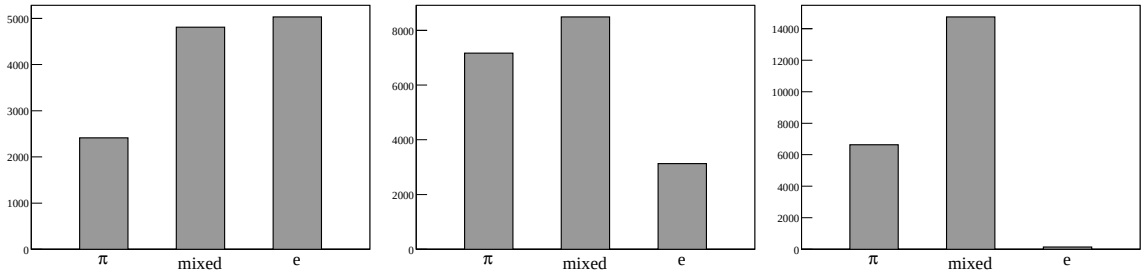

20 GeV e (run 3240) | 20 GeV π (run 3241) | 80 GeV π (run 3183)

Figure 16.2.2: *Beam compositions for the three investigated runs. The electron and pion identification was performed using external detectors and the remaining impurities are thought to be at a negligible level. The central column marked* mixed *simply refers to the events that were not identified as either electrons or pions under the given cuts.*

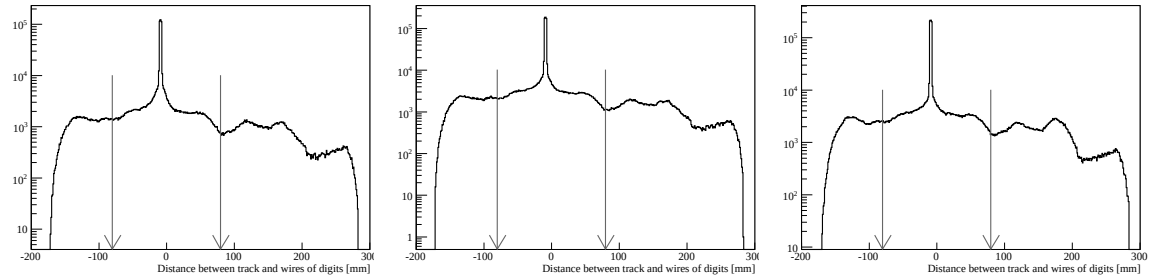

20 GeV e (run 3240) | 20 GeV π (run 3241) | 80 GeV π (run 3183)

Figure 16.2.3: *Illustration of the cut used to disregard digits from straws too close to the track.*

The first and primary cut is to only consider digits originating from straws with wires located at a certain minimum distance away from the passing track. In addition to removing hits on the reconstructed track this cut must also ensure a high rejection of digits caused by secondary particles and "crosstalk" – i.e. wire currents induced through conductive couplings to a genuine large current in a neighboring wire. Finally some events will have more than one beam particle, and since the typical vertical spread of the beam was around 3 cm, the cut must be much larger than this. The final value is found by looking at the actual distribution of the distance between the wires of the digits and the reconstructed track as shown in figure 16.2.3. A cut of 8 cm is chosen as the tails from the track peak at zero seems negligible after this distance.

Another way to ensure that the single track in the event is indeed single and well reconstructed, is to require the number of hits on the track not to be too deviant from the expected number. As indicated by the grayed out regions in figure 16.2.4 the reconstructed track is required to have at least 33 and a maximum of 43 hits on track. In particular the distribution in the 80 GeV pion run exhibits a small secondary peak around 48 which is probably due to multiple beam particles, and something the chosen cut avoids.

In addition one should note that some digits have already been disregarded by the requirement that it should be possible to identify at least one leading edge in the LT bit pattern. This simply means that bit patterns where the first LT bit is already on, e.g. `11111100000000000000000` are discarded as they do not allow one to identify the leading edge time since it could have occurred before the

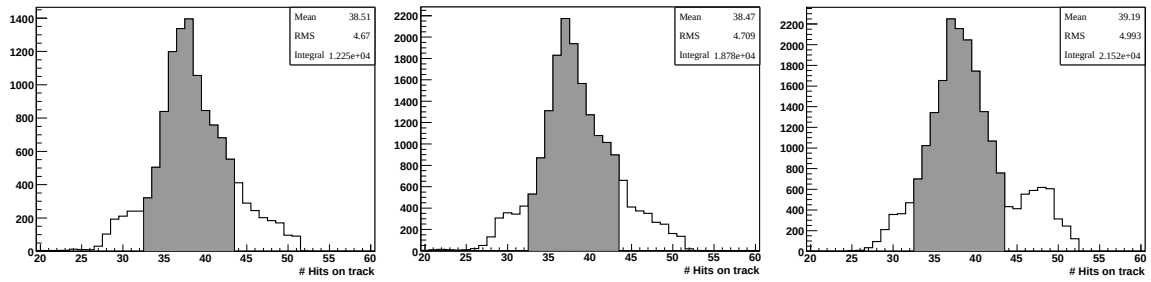

20 GeV e (run 3240) | 20 GeV π (run 3241) | 80 GeV π (run 3183)

Figure 16.2.4: *Distribution of number of hits that are classified as being "on track". The utilized cuts are indicated in gray.*

considered 75 ns interval. The exception to the rule is where a second leading edge is present like in `11110000000111111000000`.

Finally, straws with a noise level higher than 15% (corresponding to a noise frequency of $0.15/75$ ns $=$ 2 MHz) have been masked out. This is reasonable since such noisy channels will certainly be masked out in the final setup of the detector in ATLAS.

16.2.2 Removal of hits in abnormal straws

The vast majority of noise digits are thought somehow to originate from Gaussian fluctuations in thresholds and potentials in the various channels, occasionally exceeding the low threshold and producing said noise. However, looking at the data one notices a few noise digits that clearly have another origin. This could for instance be digits such as,

```
0 01111111 0 11111111 0 11111111 [a]
1 00000000 1 00000000 1 00000000 [b]
0 00000001 1 00000000 0 00000000 [c]
```

Here digit [a] is from a straw where the LT is almost always exceeded indicating a major problem in that particular straw or front-end electronics. Such a straw will probably be masked in any case in the long run. Digit [b] shows a similar structure but here the problem is in the high threshold. Finally digit [c] shows an otherwise innocent noise digit with a high threshold in the second 25 ns time-slice where somewhat mysteriously the low threshold was never exceeded. A possible explanation is that the noise digit was in reality `0 00000011 0 00000000 0 00000000`, but that the readout driver (ROD) was somehow off by one bit – a problem known to have occurred occasionally.

While these problems are real and present in the test-beam data, there is no reason to believe that they will be sufficiently similar to the ones encountered in the full ATLAS running to make a detailed study sensible. Furthermore they represent a relatively small fraction of the total number of noise hits. For these reasons the present studies will only try to understand and model the intrinsic noise of the apparatus and will not deal with these kinds of noise. Therefore an attempt will be done to exclude straws producing such "abnormal" digits.

In the following it will therefore be described how straws producing abnormal digits can be identified and removed based on a statistical analysis of the digits they produce. To be meaningful this of course

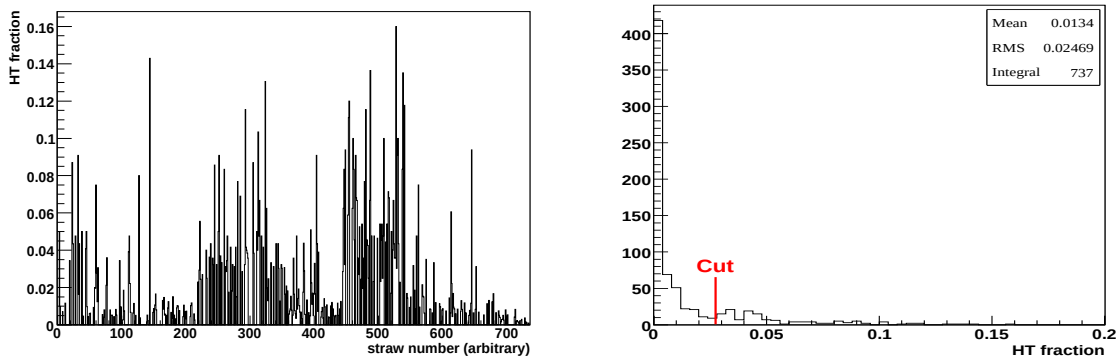

(a) (b)

Figure 16.2.5: *Average high threshold fractions straw by straw. Around 10 straws even had an observed HT fraction of exactly 1.0, but they are outside the scale.*

requires a minimum number of digits from each straw, and noise hits originating from straws from which there are accumulated less than a total of 20 hits are therefore a priori ignored. This of course systematically throws away noise hits from the least noisy straws, but the alternative is to keep a few straws around with e.g. quite abnormal electronics. Given the low number of hits from these straws, neither choice is likely to affect our conclusions, as long as the overall noise level is not taken too literally. For simplicity the plots shown in this section will all be based on the 20 GeV electron run, although all runs have of course been examined.

The first thing to do is to consider, on a straw-to-straw basis, the fraction of noise hits having at least one high threshold bit turned on. The high threshold is typically much higher than the low threshold (e.g. 7 keV versus 0.3 keV) and the frequency with which the low threshold is being exceeded by noise is low ($\mathcal{O}(1\%)$). This means, given the naïve expectation of noise being generated by Gaussian fluctuations in electronics voltages and thresholds, that it is very unlikely that high thresholds will appear in noise hits, apart from those really caused by abnormal electronics and possibly stray tracks.

In figure 16.2.5(a) the average high threshold fraction is shown for each of the remaining relevant straws. It is clear that not all straws give noise hits with negligible HT fractions, and that there is some structure caused by systematic differences between the straws and their electronics (although the straw numbering is somewhat arbitrary, it is still such that straws with numbers close to each other are usually placed close to each other in the detector). In figure 16.2.5(b) the distribution of those same fractions is shown. As expected there is a huge peak around zero with a tail toward higher values which could be due to secondaries. However at values around 0.4 there is again a peak, which is hard to interpret as anything else than straws with some sort of abnormal behavior. One might be tempted to put in an aggressive cut just around the peak at zero, on the other hand, one could fear that such a cut would simply remove a genuine "non-abnormal" effect ("throwing the baby out with the bathwater"). Consequently it is chosen to place the cut just before the peak, eliminating any straw with an average HT fraction above 0.028. Not surprisingly this gets rid of almost all of straws producing digits consisting almost entirely of 1's (which really is a sign of seriously flawed electronics).

Another indication that a straw is "abnormal" is if it often produces noise digits with a relatively large number of LT bits set. In figure 16.2.6(a) is shown the distribution of the average number of set LT bits in the selected noise digits for each straw. The gray regions show how the straws with a HT fraction higher than respectively 6% and 2.8% are distributed. It shows that there is clear correlation between

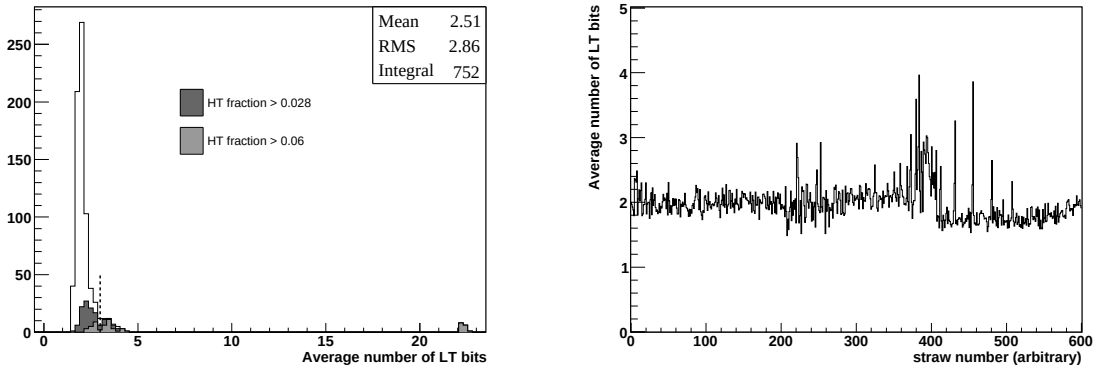

(a) (b)

Figure 16.2.6: *Average number of low threshold bits that are set for each straw. Note that 24 set LT bits is impossible due to the requirement of a leading edge as discussed in the text. In (a) the distributions of straws with a high HT content are also indicated. In (b), only the straws with HT fraction < 0.028 are shown.*

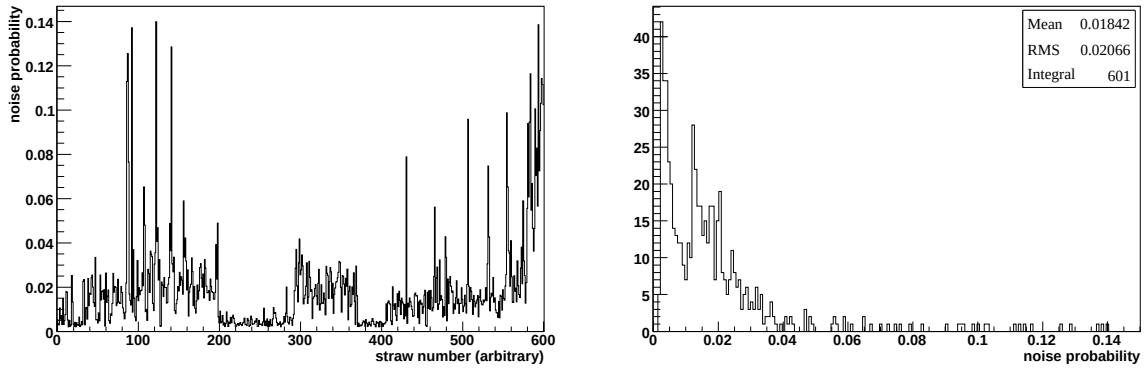

(a) (b)

Figure 16.2.7: *Observed noise levels versus straw number (a) and the distribution of those numbers (b).*

straws with a relatively large number of LT bits set and straws with a large HT fraction. This supports the claim that the source of noise in these straws is somehow “abnormal”, if not simply contamination due to remaining real passing particles. Based on this knowledge, straws with an average of more than 3.0 set LT bits are discarded.

Finally the distribution of noise levels of the individual remaining straws is shown in figure 16.2.7. Note that the removal of straws with less than 20 hits earlier has removed entries at the lowest values.

16.2.3 Noise digit features

Having thus selected a number of noise digits, and excluded contributions from “abnormal” sources, features of the noise can be extracted. Regardless of the considered feature, its distribution ought to be independent of beam type and run.

First one can gain an insight into the time structure of the noise by plotting the mean occupancy of the 24 LT bits in noise digits as is done in figure 16.2.8. If there were indeed no time structure to the

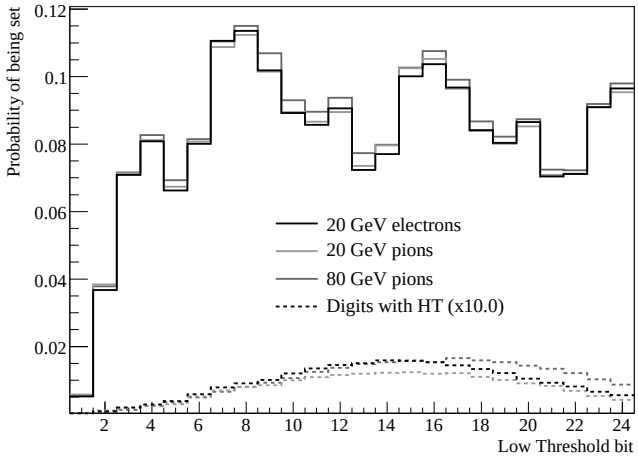

Figure 16.2.8: *Solid histograms show the observed mean low threshold bit occupancy in selected noise digits for the three different runs. The dashed histograms show the contribution from digits with a high threshold – scaled up by a factor of 10 for better visibility.*

noise one would expect a totally flat distribution, but this is obviously not what is seen. First of all there is a large dip in the early bins, but that is easily understood as an artificial effect caused by the requirement of a leading edge as discussed in section 16.2.1.

Apart from the dip, there does seem to be some sort of plateau around 8-10% with a 8 bit (25 ns) periodic structure on top of it. This should not be too surprising since the front-end electronics is influenced by an externally driven 25 ns clock cycle. Also shown in the figure is the contribution which is due to digits with a HT. First of all the very low number of HT digits means that their contribution is too small to be of significance. Secondly it is clear that they have a different and in-time shape, not too different (if a little broader) from that of beam particles. This could support the hypothesis that the noise digits with HT content are due somehow to stray beam particles or secondaries.

Perhaps the most striking feature of figure 16.2.8 is how robust the distributions seem to be across the three runs, which underlines the consistency of the entire procedure. Furthermore, it shows the stability of the detector conditions which means that e.g. reconstruction and digitization can in principle reliably use appropriate calibration data to improve performance.

Figure 16.2.9 shows another extracted quantity, namely the distribution of the number of set low threshold bits. Figure 16.2.9(a) shows that, in the selected noise digits, about 99% of the entries have 4 bits or less set, and the three runs agree completely regarding the distribution in those bins. Looking at the distribution for digits with a HT bit, it once more seems to agree with the hypothesis that there is a small and negligible contamination of stray particles and secondaries, thus explaining the present tail. If instead, for instance, the presence of set HT bits were caused by ROD off-by-one problems, one would expect the distribution of digits with HT to follow the overall distribution, apart from being shifted left by one.

The mean of the distribution corresponds to an average time above threshold around $1.96 \cdot 3.125$ ns $\approx$ 6 ns, which is quite low compared to the time over threshold due to pulses from traversing particles that are usually around 15-35 ns, as shown in figure 16.2.9(b). This is certainly a feature that could be used for reducing the impact of noise at just a small cost in tracking efficiency.

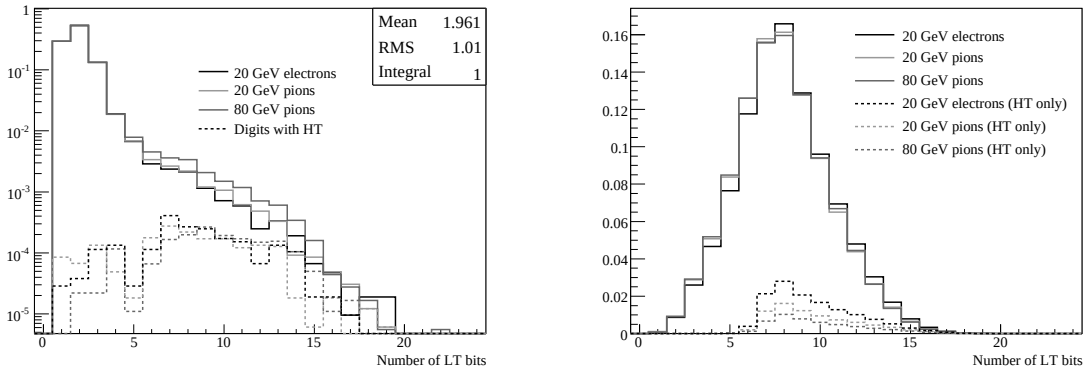

(a) (b)

Figure 16.2.9: *The solid histograms in (a) show the distribution of the number of low threshold bits set in the selected noise digits, with the hashed histograms showing the small contribution of digits with a HT. In (b) the same distribution is shown for on-track digits.*

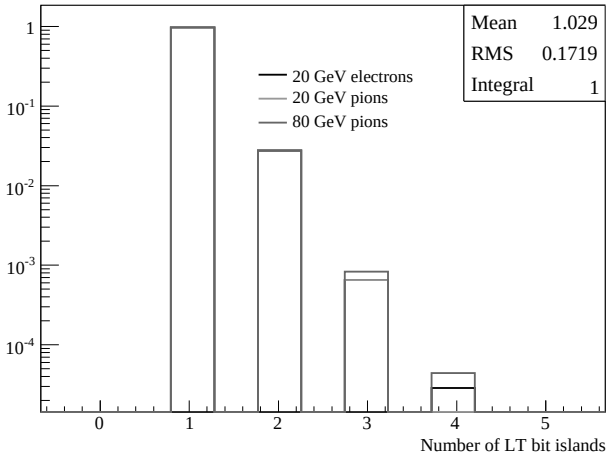

Figure 16.2.10: *Distributions of the number of LT bit "islands" (or "trains") in the selected noise digits.*

Finally, figure 16.2.10 shows the distribution of the relative fractions of number of LT bit "islands" (also known as "trains"). An island is simply a group of set LT bits surrounded by unset bits (00000001100010000000000 thus contains two islands while 00111000000000000000000 contains only one). One notices that the relative suppression of the fraction of 2-island digits compared to 1-island digits is roughly equal to the one between 3 vs. 2 islands and 4 vs. 3 islands respectively, and that the suppression is comparable to the overall noise level of around 2%. This shows that the appearance of noise at different times happens independently.

16.3 Channel to channel correlations in noise levels

The distributions studied in the previous sections have all been based on the entire pool of (usable) channels. For a more complete understanding it is also necessary to study the channel to channel correlations caused by their various mechanical and electrical groupings. Channels are connected to different high voltage supplies, belong to different chips and are connected to wires in different barrel modules. More detailed, the obvious relevant groupings are:

- Groups of eight neighboring wires are connected to the same ASDBLR chip, responsible for the analog treatment and digitization of the potential fluctuations in the wires. The threshold values can not be tuned independently for each channel, but only overall for each ASDBLR chip.
- Two ASDBLR chips are connected to a DTMROC, responsible for collecting and, given a level 1 trigger, reading out the digitized results from the ASDBLR chips to the ROD's as well as keeping the clock synchronized with the overall ATLAS clock through interaction with the TTC (Trigger Timing Control) boards.
- Groups of $\sim$8 wires share a single high voltage connection and are denoted as "HV pad's". Note that the high voltage is supplied to the straw tube which then supplies high voltage to the two channels within the given straw - i.e. each straw end.
- Several hundreds of straws and corresponding electronics are mechanically assembled into three types of barrel modules. Such barrel modules contain either 329, 520 or 793 straws and are accordingly denoted as type I, II or III (with type I modules closest to the beam axis)[1].

In the next sections (and in the next chapter), correlations and non-uniformities in the straw noise levels will be investigated at several levels. First the module to module differences will be discussed in section 16.3.1. Next, in section 16.3.2, it is investigated how the straw noise levels are correlated with their groupings into sets of $\sim$8 wires connected to the same HV pad. Finally the distribution of straw noise levels within each HV pad is examined in section 16.3.3, and in section 16.3.4 it is checked whether noise in one channel could give rise to noise in neighboring channels. A study of the noise correlations on the chip level will await the next chapter.

For the analysis here, several runs of test-beam data were used in addition to the three considered in section 16.2. This was done because the beam position (cf. figure 16.2.1(b)) was the same in all of the three runs considered so far, meaning that a large group of straws was excluded in every event

[1] While end-cap elements were not present in the test-beam it should be noted that the situation for those is not entirely the same, as each mechanical grouping of straws (into "wheels") contains a much larger number of straws and many more electronics boards.

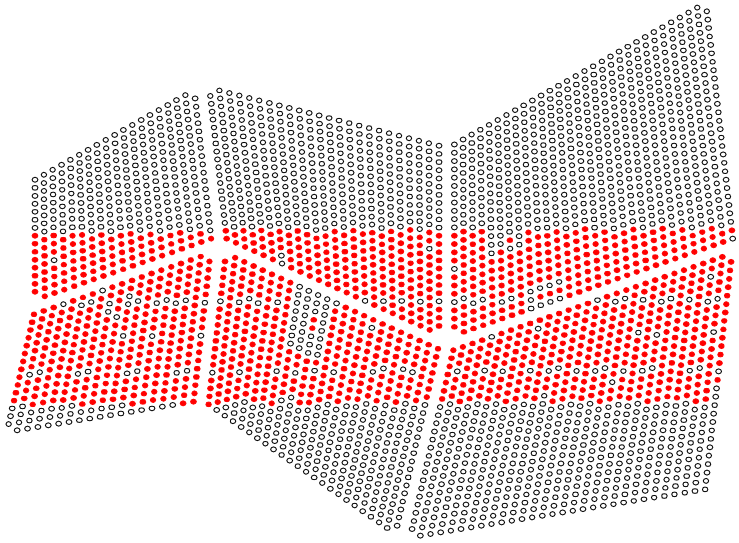

Figure 16.3.1: *Straws illuminated by the beam (i.e. containing on-track hits) in any of the runs considered for the channel to channel noise level variation studies.*

solely by the distance to track cut. The inclusion of other runs with different beam positions alleviates this problem and allows for a more detailed understanding of the noise, but of course care should be taken not to add samples which differ significantly in some way or another. A number of crosschecks showed no major deviations between the runs, and the addition of different runs is considered safe. The difference in beam positions for all of the considered runs is illustrated by the beam illumination map shown in figure 16.3.1. Finally the studies are complicated by the fact that some channels are excluded by the quality cuts discussed in section 16.2.2. This means in particular that not all HV pads will contain data from all its channels, but rather some subset instead. Care must therefore be taken to ensure that artifacts from this varying number of channels in each grouping are not mistaken from genuine statistical effects.

16.3.1 Module to module variations

In the full ATLAS setup there will be installed 96 barrel modules, whereas only 6 modules were present in the 2004 test-beam setup. Furthermore the modules used for the test-beam were, each in its own way, classified as “abnormal” based on the results from tests described in the chapter 14.

In table 16.3.1 is shown the mean of the individual channel noise levels in each of the six modules. It is clear that there are significant module to module differences which is perhaps not very surprising considering that the six modules for various reasons are labeled as *rejected* or *spare* based on results from the barrel test station. Also, one should note that the low thresholds in the test-beam setup were set to the same value across all ASDBLR chips, whereas the plan for the configuration in the final ATLAS setup is to adjust the threshold for each chip such that the noise level averaged over its eight channels will be fixed at e.g. 2.25%[2]. This future configuration scheme will obviously limit

[2]Corresponding to a noise frequency of 300 kHz.

	Module Type		
	I	II	III
Upper Sector	1.6%	0.5%	1.9%
Lower Sector	0.3%	0.3%	0.3%

Table 16.3.1: *Mean noise levels of the individual channels within each of the six modules.*

the module to module variations in noise levels considerably, but the variation will then instead occur in the effective channel to channel low threshold. Despite the module to module variations, the data from all of the six test-beam modules is still useful for studying other channel to channel variations as will be done in the following sections.

16.3.2 The HV pad level

In order to investigate whether straw noise levels are significantly correlated with their groupings into pads, the distribution of the normalized mean noise levels of the pads, i.e. the mean of the noise levels of the (usable) straws within each pad, is normalized to the mean straw noise level of the containing module, as shown in figure 16.3.2(a). As one of the straw quality cuts (explained in section 16.2) is a requirement of a minimum number of noise hits, one might worry that errors are introduced when perfectly well-functioning straws with extremely low noise levels are discarded. As a cross check, two different distributions are shown in figure 16.3.2(a): One where only the straws considered for the pad noise studies are used to calculate the mean value, and one where in addition all the remaining straws are used with an assumed noise level of 0%. Apart from an expected enhancement in the first bin, the two methods seem to give compatible results. One should also note that the mean values of the distributions in figure 16.3.2(a) are not equal to 1 as one might expect, since the straw noise levels have been normalized to the average straw noise levels of the containing modules. This is not so surprising however, as the different pads do not contain the same number of (usable) straws, so the individual straws will contribute to the mean with a different weight depending on which pad they belong to. Hypothesizing that straws with a high noise level will more often belong to pads where all straws are used than those with low noise level, one would indeed expect a mean value lower than 1.

It is difficult, however, to tell directly from the distributions in figure 16.3.2(a) whether they indicate a significant correlation between straw noise level and pad groupings. In order to test this further, a similar distribution is made in figure 16.3.2(b), but this time using randomized straw to pad groupings instead of the actual ones. It is indeed seen that the mean value of the distribution approaches one, while the root-mean-square of the distribution decreases, which is exactly what one would expect to happen when the pad groupings are randomized, effectively making the pads more similar on average. To test the significance of the results, the mean value and root-mean-square the distributions for a hundred different randomized pad groupings are shown in figure 16.3.3. They show with high significance that a random pad grouping could never reproduce the distributions in figure 16.3.2(a).

16.3.3 The straw level

In figure 16.3.4 is shown the distribution of noise in straws normalized to the average noise in the pad to which the straw belongs. The distribution is peaked around unity with most entries within $[0.4; 1.5]$, which shows that the noise level of most straws is approximately the noise level of their corresponding

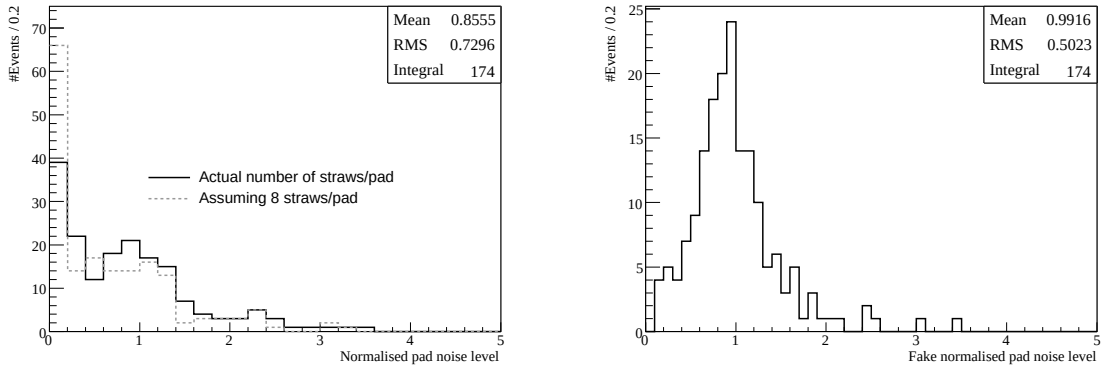

(a) (b)

Figure 16.3.2: *In (a) is shown the distribution of the mean straw noise level within each pad, normalized to the average noise level of the containing module. Both the actual average of the used straws within each pad as well as the average after assuming all unused straws to be straws with a noise level of* 0% *are plotted. Figure (b) shows the same distribution, but the straw to pad assignment has been randomized.*

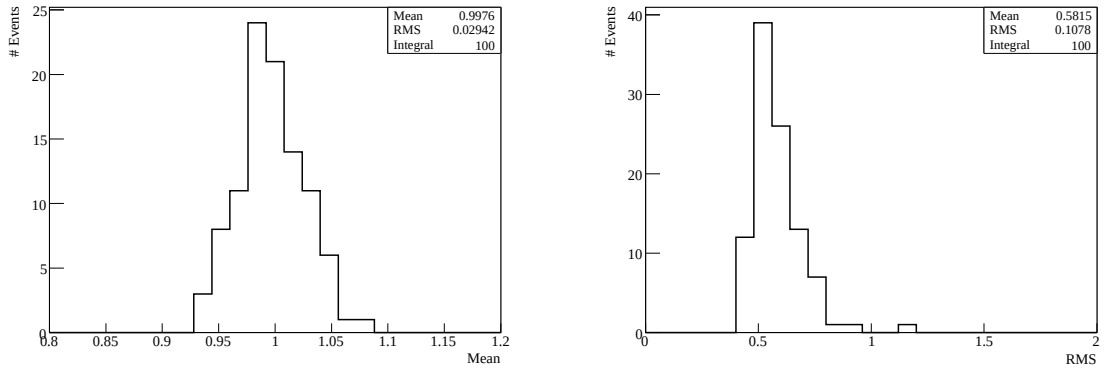

(a) (b)

Figure 16.3.3: *In (a) and (b) respectively are shown the distribution of the means and root-mean-squares of 100 randomized straw to pad mappings such as the example shown in figure 16.3.2.(b).*

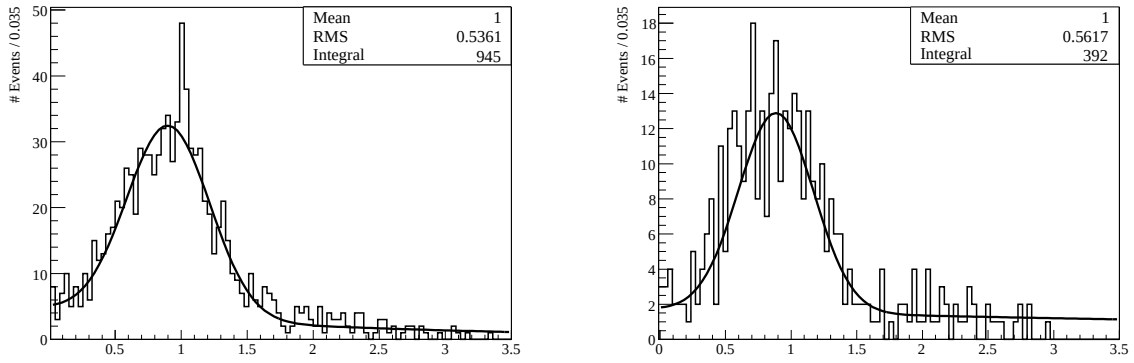

(a) (b)

Figure 16.3.4: *Distribution of noise level in straws normalized to the average level in the pad to which the straw belongs for all pads (left) and for pads where all eight straws contribute (right).*

pad, although of course the mean is guaranteed to be one by construction and the tail toward high values is not negligible. For use in the simulation it is noted that the distribution is well described when fitted by a Gaussian plus an exponential. To check that no significant biased introduced due to the fact that the number of considered straws within a given pad is not always 8 (since some pads contain only 7 straws and some straws are disregarded by cuts) the same distribution is also plotted solely for pads with 8 surviving straws. The distribution seems to be relatively unaffected by this requirement, with the most striking difference being the disappearance of the artificial peak at exactly 1.0 caused by pads for which only one channel were considered usable.

16.3.4 Noise induced channel to channel crosstalk

An effect one should be aware of is the possibility of crosstalk between straws, i.e.: The signal in one channel induces a signal in another. This is potentially dangerous for track reconstruction as a signal due to a passing particle could give rise to a fake signal in a nearby straw. These issues are investigated in [TRT04] and in chapter 17. Here it will instead be investigated whether a *noise* hit in one straw is likely to induce noise hits in nearby straws.

To estimate the magnitude of this effect from noise one can look at the number of noise hits within a given pad in a given event, of course using the fact that straws connected to a given pad are located neighboring each other. The distribution is shown in figure 16.3.5, but only for pads where all eight straws are deemed usable. Assuming no crosstalk the ratio, r_{10}, between the content of the $'1'$ and $'0'$ bins given the probability for a noise hit in a given straw, p_{nl}, and the number of channels per pad, $N_{\mathrm{ch}} = 8$, should follow from binomial distributions:

$$r_{10} = \frac{N_{\mathrm{ch}} p_{\mathrm{nl}} \left(1-p_{\mathrm{nl}}\right)^{N_{\mathrm{ch}}-1}}{\left(1-p_{\mathrm{nl}}\right)^{N_{\mathrm{ch}}}} = \frac{N_{\mathrm{ch}} p_{\mathrm{nl}}}{1-p_{\mathrm{nl}}} \quad \Rightarrow \quad p_{\mathrm{nl}} = \frac{r_{10}}{r_{10}+N_{\mathrm{ch}}} \tag{16.3.1}$$

Likewise the expected ratio of the $'2'$ and $'0'$ bins is found to be:

$$r_{20} = \binom{N_{\mathrm{ch}}}{2} \frac{p_{\mathrm{nl}}^2 \left(1-p_{\mathrm{nl}}\right)^{N_{\mathrm{ch}}-2}}{\left(1-p_{\mathrm{nl}}\right)^{N_{\mathrm{ch}}}} = \binom{N_{\mathrm{ch}}}{2} \frac{p_{\mathrm{nl}}^2}{\left(1-p_{\mathrm{nl}}\right)^2} \tag{16.3.2}$$

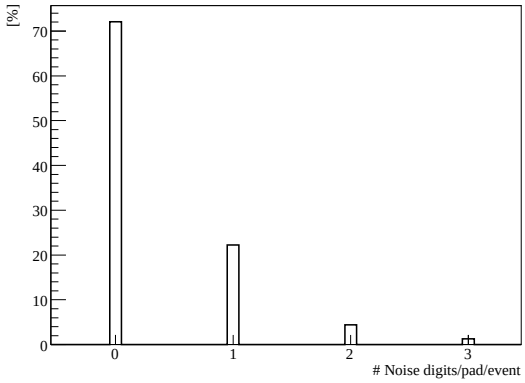

Figure 16.3.5: *Number of noise hits in a given pad in a given event.*

If the assumption of truly independent channel noise is valid a direct calculation of r_{20} from the bin content in figure 16.3.5 should give the same result as first calculating p_{nl} via equation 16.3.1 and inserting the result in equation 16.3.2. Inserting numbers the two methods turns out to result in $r_{20}^{\mathrm{obs}} = 6.1\%$ and $r_{20}^{\mathrm{indep}} = 4.2\%$ respectively. This thus reveals a slightly enhanced tendency to get two noise hits in the same pad which could to some extent be explained by noise induced channel to channel crosstalk. However it is still true that $r_{10}^{\mathrm{obs}} \gg r_{20}^{\mathrm{obs}}$, meaning both that the effect is relatively rare and it is difficult to conclude with any certainty that it is not simply caused by e.g. a small contamination of the noise hit samples from real particle induced hits. From a slightly different perspective, namely using hits close to tracks in cosmic events, this issue is studied further in the next chapter.

16.3.5 Dead channels

Another method of studying detector inhomogeneities is examination of the distribution of non-sensitive, or "dead", channels in the test-beam setup. One would expect two major sources of such channels. The first being problems with individual channels and the second being possible problems in a chip connecting 8 channels.

Already at the barrel test facility $\mathcal{O}(1\%)$ of all assembled straws were found to have serious and unrepairable problems, as discussed in chapter 14. The causes were numerous: Gas leaks, bend straws or abnormal wire tension, gain or high voltage behavior. Consequently their anode wires were (usually) removed to avoid e.g. voltage problems affecting other nearby channels. Investigating whether or not those straws can still give rise to noise hits in the test-beam can tell something about the nature of the noise as was already done in an example for the end-cap in chapter 15, see figure 15.1.1. In figure 16.3.6 the channels of the test-beam are shown and, in addition to pointing out the problematic channels known from the acceptance tests, color codes differentiate between the channels that are entirely without noise hits in the test-beam, those with a very low rate of noise and the rest. The larger collection of straws entirely without hits are indeed seen to correspond to non-functioning ASDBLR or DTMROC chips. There is a clear correlation between the channels disconnected at the test bench and the straws that hardly (if ever) produce noise hit. However, the main part of them *do* produce noise hits to some degree, meaning that part of the noise is produced in the front-end electronics itself. This fact underlines the usefulness of the TRT StrawStatusSummaryTool as discussed in the previous chapter.

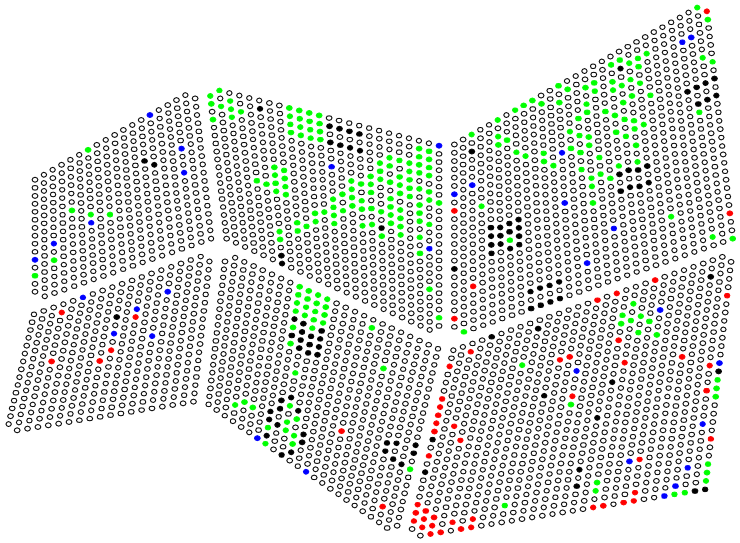

Figure 16.3.6: *End view of the straws in the test-beam setup. Black straws have no hits in the test-beam, green straws have a noise level below* 0.01%. *Blue straws correspond to those declared dead at the test bench, and which had a noise level below* 0.01% *in the considered test-beam runs, whereas red straws are the ones which were declared dead at the test bench, but which had a noise level above* 0.01%.

By using this tool in the offline reconstruction in both data and simulation, the problematic channels can be rejected altogether, hereby protecting the tracking algorithms of potential problems with fake hits (although, of course, such hits are relatively rare and thus can only influence the tracking to a limited extent).

16.4 Conclusions

Data from several runs of the summer 2004 TRT standalone test-beam has been analyzed. After having selected and removed a smaller number of channels with decidedly “abnormal” behavior, the appearance and composition of the noise hits in the remaining channels have been studied and can to a large degree be said to be understood. It is shown that the composition of noise digits is very stable across the different runs and the channel to channel correlations between noise levels have been investigated. To further understand the nature of the TRT noise, a different data sample is needed. To accommodate, a study presented in the next chapter is performed using cosmic events, but ultimately, of course, the issue must be addressed using real ATLAS collision data.

Chapter 17

TRT noise in cosmic events from the ATLAS pit

In the previous chapter the correlations of noise levels for straws belonging to the same high voltage pad was established in a pure noise environment - i.e. in the absence of close by tracks. This chapter focuses on possible crosstalk phenomena; where a signal in one channel induces a signal in a secondary channel. Potentially this effect can occur if the channels are not totally isolated from each other, and in this case one would expect the effect to be largest in case a large signal is produced in the primary channel. Since, in general, signals due to the passage of a particle through a straw are larger than the average noise signal, crosstalk, if any, is expected to be more pronounced in regions close to tracks. This region coincides with the region where tracking is potentially most sensitive to noise hits which, by mistake, could be assigned to a track. For this reason, the extent of the problem is important to assess.

The data used is from the M4 cosmic run, the setup of which will be briefly described in chapter 18. For the present study the details of the setup are of less importance. What matters is that the data is collected using 13 barrel ϕ-sectors. On side A 11 sectors were read out, whereas only 9 side C sectors were read out.

The data consists mainly of noise, with an occasional track - in general only one track per event, originating from a cosmic muon. The low track rate implies that it is unlikely that an additional track is missed by the reconstruction software (unless a cosmic muon causes a shower in the vicinity of the TRT). This setup is therefore well suited to expand the noise study of the previous chapter, since in the test-beam the high track rate and relatively low reconstruction efficiency required the noise study to be based on hits far a way from the beam to prevent the data sample to be contaminated by hits from unreconstructed tracks. Due to this, track induced noise, could not be studied reliably in the test-beam. The cosmics setup, however, offers a good testing ground for this kind of study.

In the following, it is studied whether possible correlations exist for noise hits belonging to the same grouping as a hit on a track. The groupings considered are:

- Channels on the same DTMROC chip as hit(s) on track.
- Channels on the same high voltage pad as hit(s) on track.
- Channels on the same high voltage pad as HT hit(s) on track.

- Channels situated at the opposite end of a straw which has a hit on track.

All hits which do not belong to a track are selected. The time-over-threshold distribution for hits on tracks is shown in figure 17.0.1(a). Since noise can be reliably characterized by their low time over threshold (as discussed chapter 16), one can estimate the contamination in the selected noise hits from hits on unreconstructed tracks by comparing with the time-over-threshold distribution for hits, selected from chips without track hits, shown in figure 17.0.1(b). Comparing the distribution shown in the insert to the corresponding for hits on tracks, it is clear that some contamination due to hits from unreconstructed tracks is present in the noise selection. However, the majority of the selected noise hits have low ToT as expected for noise - 8% hits has ToT$>$10 ns.

The noise occupancy in a number of configurations is summarized in table 17.0.1. Below, the various configurations are explained, and the results are discussed one by one.

Label	**Configuration**	**Noise-level** [%]
1	*Straw noise − level − average of all straws*	2.392 ± 0.002
2	*Chip noise − level − chips with track hit(s)*	29.771 ± 0.002
3	*Pad noise − level − pads with track hit(s)*	27.921 ± 0.002
4	*− pads with 1 track hit*	27.790 ± 0.002
5	*− pads with 2 track hits*	27.433 ± 0.003
6	*− pads with 3 track hits*	29.863 ± 0.008
7	*− pads with 4 track hits*	41.88 ± 0.02
8	*− pads with track HT hit(s)*	49.03 ± 0.02
9	*Straw noise − level − track hit at the other end*	3.976 ± 0.002

Table 17.0.1: *Noise levels in various configurations discussed in the text.*

The first line in table 17.0.1 (referred to from now on by 17.0.1(1)) shows the average noise for all selected channels - i.e. $\frac{number\ of\ hits\ not\ on\ track}{(number\ of\ read\text{-}out\ channels \times number\ of\ events)}$, regardless of grouping.

Although each DTMROC chip has 16 channels only averagely 15.8 correspond to an actual straw, due to the physical constraints induced by the odd module geometry. Therefore, the expected chip noise level is:

$$1-(1-0.02392)^{15.8-1.7} = (29 \pm 2)\%, \tag{17.0.1}$$

since the average number of track hits per chip is 1.7 (for chips with at least one track hit). This means, that in case the noise is truly random, one expects about 29% of chips crossed by a track would have one or more noise hits.

Table 17.0.1(2) shows the corresponding measurement. The result: 29.8% is in excellent agreement with the expectations. However a corresponding calculation for the high voltage pad grouping gives:

$$1-(1-0.02392)^{7.9-1.3} = (15 \pm 1)\%, \tag{17.0.2}$$

in stark contrast to the result shown table 17.0.1(3).

The corresponding individual channel noise level, for channels belonging to a high voltage pad crossed by a track, is found by inverting equation 17.0.2 to be $(4.84 \pm 0.03)\%$ or more than double the average channel noise level.

Table 17.0.1(4-7) shows the dependence of the pad noise level on the number of hits from a track a given pad has.

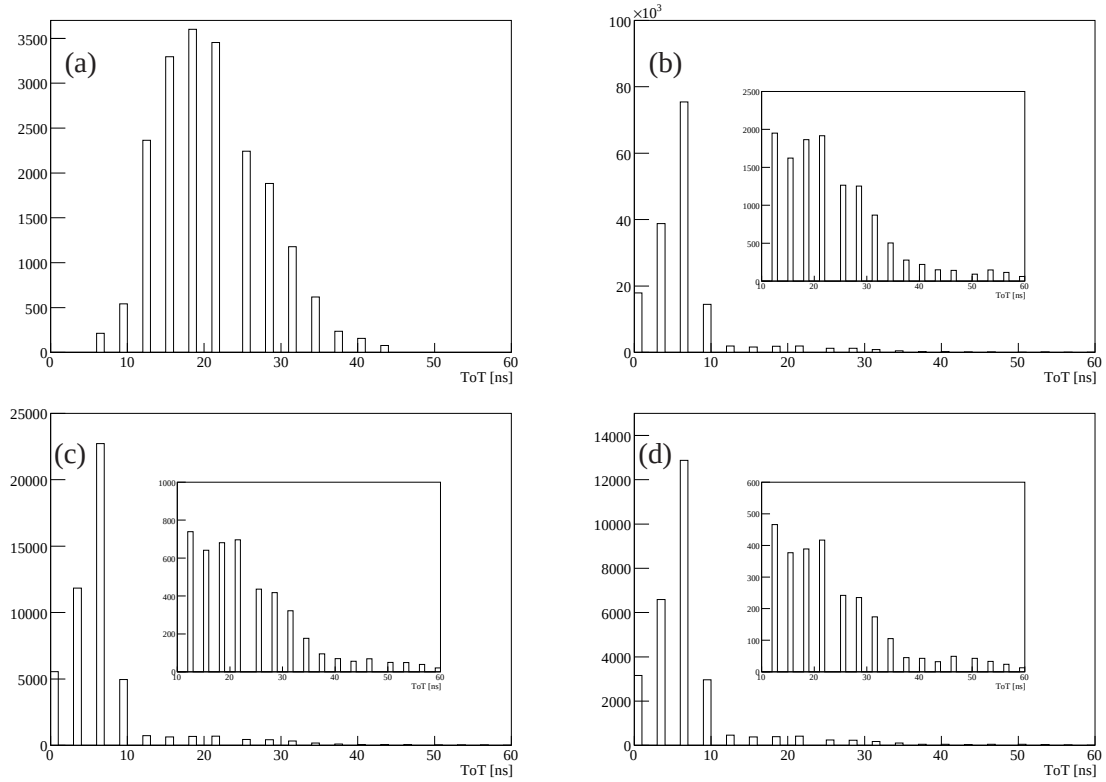

Figure 17.0.1: *Time-over-threshold distributions for various selection of hits. (a) Hits on track. (b) Noise from chips without track hits. (c) Noise from pads with track hits. (d) Noise from chips with track hits. Inserts show the same as the plot in which they reside, but for ToT>10 ns.*

In table 17.0.1(8), the noise level from straws belonging to pads which have one or more HT hits from a track is given. The result: 49% corresponds to a single straw noise probability of 9.8% which is a factor of 4 above the average noise level.

In case a track caused a signal in a given channel, it is plausible that the other end of the same channel could have an increased noise level. Note that there are two channels corresponding to each straw: One in each end of the straw and the anode wire is isolated centrally by a piece of glass. Since, however, the straw tube (cathode) does not have a corresponding isolation centrally, noise which is somehow related to the high voltage supply (i.e. which does not originate from the electronics) could be increased for channels at the other end of a channel crossed by a particle. Table 17.0.1(9) gives the noise level of these channels. Indeed the level is significantly increased with respect to the 2.4% (table 17.0.1(1)) expected in the absense of correlation.

As argued in the introduction to this chapter, noise in the vicinity of a track can potentially degrade the tracking performance. However, as shown in figure 17.0.1, the majority of the problematic hits can easily be rejected by a simple cut on the time-over-threshold distribution. In most of the track reconstruction software, a cut on time-over-threshold is applied, by which the majority of the potential problem is avoided. Nevertheless, such non-random noise should be simulated, and the framework for this has been developed. Its usage as default in the ATLAS software still awaits tuning from real data of which there is still too little and what exists is still not sufficiently reliable to achieve the desired

precision. One reason for the latter is, that the above study is based on 13 modules only, and the noise behavior could be different in other modules as was the case in the test-beam (see section 16.3.1). Moreover the nature of the noise might change once ATLAS is subject to collisions, where tracks will have a different energy distribution and rate than the cosmic muons on which the present study is based.

Note also, that the above analysis could be extended to study the effects of δ-rays. Since δ-rays are expected to give rise to hits in the vicinity of tracks, the relevant grouping for such study would be defined by the distance from a given straw to a track. Such study would aim at validating the model responsible for the simulation of δ-rays, and since this has little to do with noise or the noise model implementation in the TRT digitization software, the study is not performed in the present context.

Chapter 18

Inner Detector Commissioning

A practical approach to accelerate detector commissioning and hereby reduce the number of problems unavoidably faced at LHC start up, is by the use of cosmic rays. Cosmic rays at the surface consist mostly of low energy muons (average 2 GeV) produced in the atmosphere. Figure 18.0.1 illustrates the situation faced in the ATLAS cavern. Although in many aspects different collision data, the cosmic ray data is useful for locating a number potential problems, which would be otherwise be encountered at the first collisions. This chapter concerns the efforts of commissioning of the Inner Detector using cosmics ray muons at the various stages of the detector assembly and integration. Only a brief overview of the efforts is presented, based on the work of many people (most figures originate from people working with Inner Detector commissioning). Integral parts of the outline are based on proceedings written for the 10^{th} ICATPP conference [Kli07].

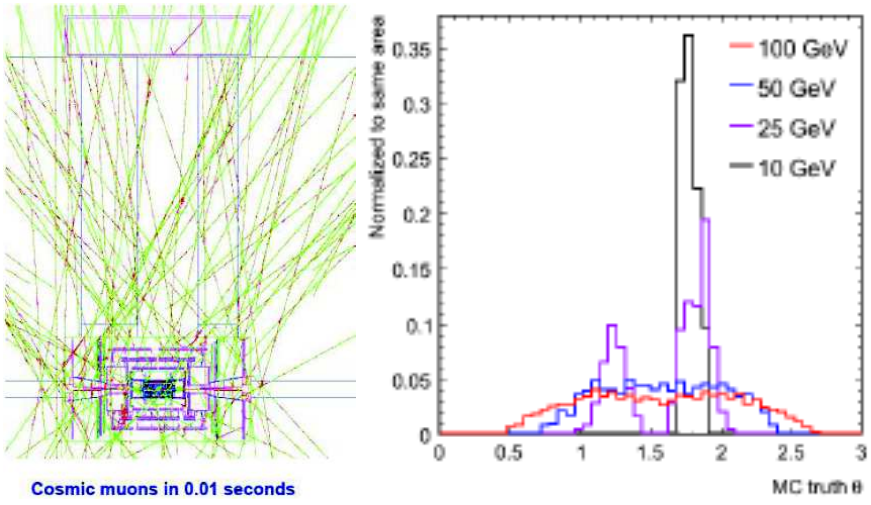

Figure 18.0.1: *Cosmic muon simulations. Left: Cosmic muons in the ATLAS pit in 0.01 s. Right: Angular distribution of cosmic muons in the ATLAS pit at different energies. At 10 GeV (and below) muons mainly reach the cavern through the shaft.*

Recently the Inner Detector has been installed at its final position. Various parts of the detector have been commissioned using cosmic rays both on the ground (building SR-1) and in the ATLAS pit. Different calibration, alignment and monitoring methods have been tested as well as the handling of the conditions data. Both real and simulated cosmics events are reconstructed using the full ATLAS

software chain, with modifications to account for the lack of magnetic field, the lack of timing of cosmics events as well as to remove any vertex requirements in the track fitters. Results show that the Inner Detector generally performs within expectations with respect to noise, hit efficiency and track resolution. However only parts of the detector have been read out, and the commissioning efforts will proceed until LHC startup.

18.1 Introduction

Integration of the SCT and TRT barrel took place at the surface, and was followed cosmic runs to test the individual sub-detectors as well as combined sub-detector performance. Presently the Inner Detector is installed in its final environment in the ATLAS pit. For practical reasons, the Inner Detector is installed in several steps beginning at the surface and continuing in the pit, allowing for series of tests with increasing parts of the Inner Detector connected to the data stream. Below, results from measurements at the surface as well as in the ATLAS cavern are presented, and the software setup to deal with cosmics is discussed. However, as in the previous chapters, focus will be put on issues related to the TRT, where the author has contributed. Main results from other sub-detector systems be shown, as well as recent results from setups where significant parts of the full ATLAS detector have been integrated into the data acquisition system.

18.2 SR-1 Cosmics: Data

The arrival time of cosmic muons is of course random, and the surface setup for the integrated SCT-TRT cosmics therefore included scintillator plates used for triggering. These plates were placed above and below the sub-detectors (see figure 18.2.1) in such a way that a coincidence would require a particle passing near the center of the detector and therefore, to some extent, resemble a particle produced in a beam collision - at least with respect to which detector parts are passed. With respect

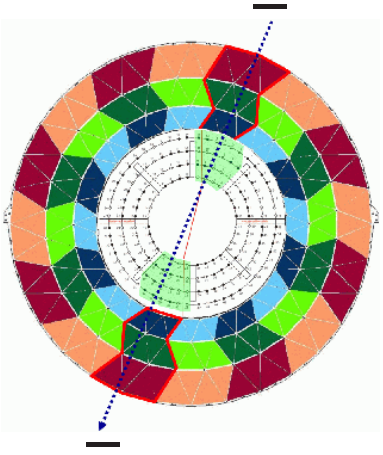

Figure 18.2.1: *Setup for cosmics data taking at the surface. Scintillator plates are placed above and below the detector. Only the shaded sectors are read out.*

to hit efficiencies, both sub-detectors proved well within expectations - see figure 18.2.2. Additional

tests using a random triggers to record noise levels were also successful - results for the SCT (barrel and end-caps) and the Pixel (end-caps) are shown in figure 18.2.3. After alignment and calibration the resolution of the SCT and TRT tracks are $\sigma = 59$ μm and $\sigma = 170$ μm respectively, which is within expectations for the cosmic setup (see figure 18.2.4). The reason that SCT uncertainty is larger than the ATLAS expectations (cf. section 3.2) is partly due to the low momenta of the cosmic rays, and partly that no magnetic field is applied, and therefore the particle momentum could not be measured and effects of multiple interactions could not be corrected for.

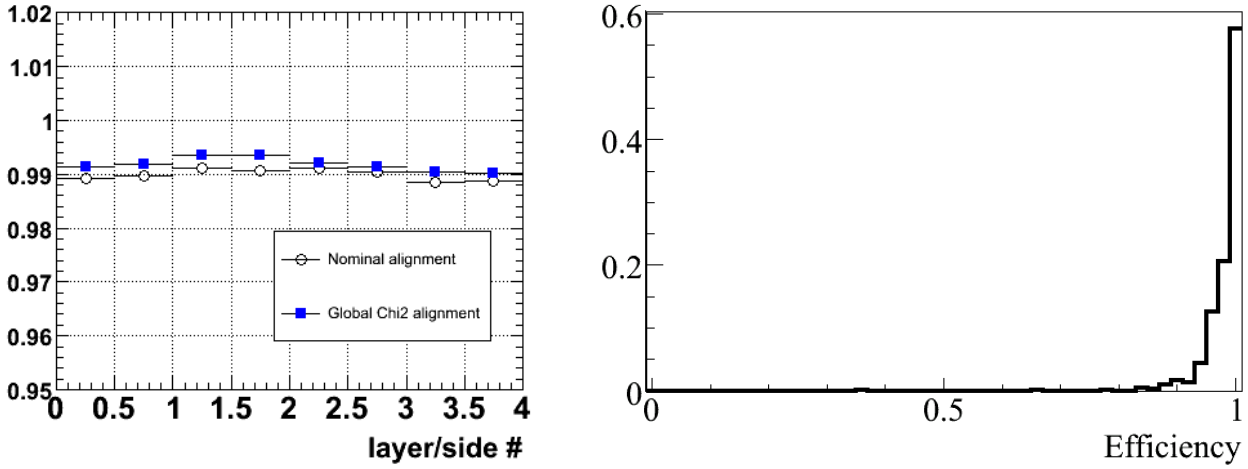

Figure 18.2.2: *Hit efficiencies of the SCT (left) and TRT (right) as measured doing tests on the surface.*

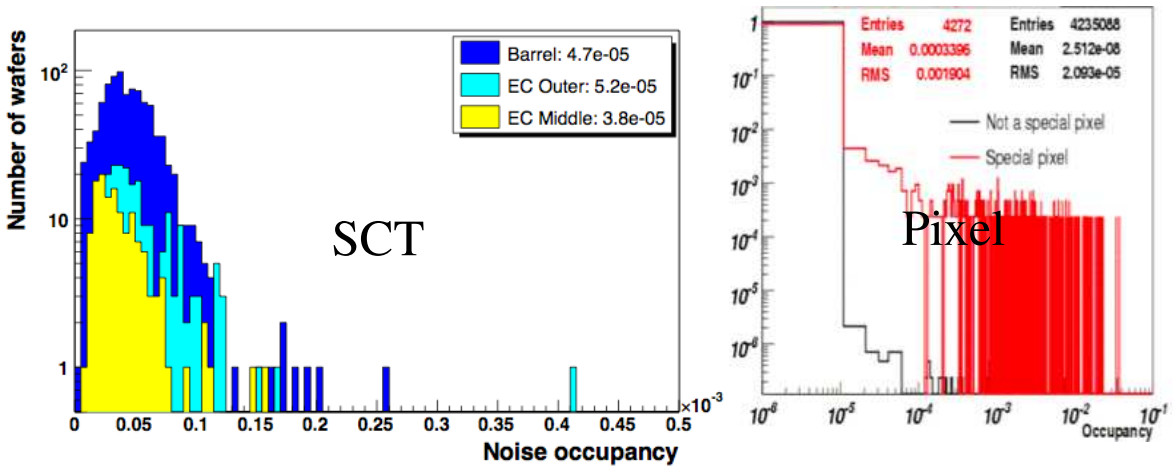

Figure 18.2.3: *Noise levels of the Pixel and SCT as measured doing tests on the surface.*

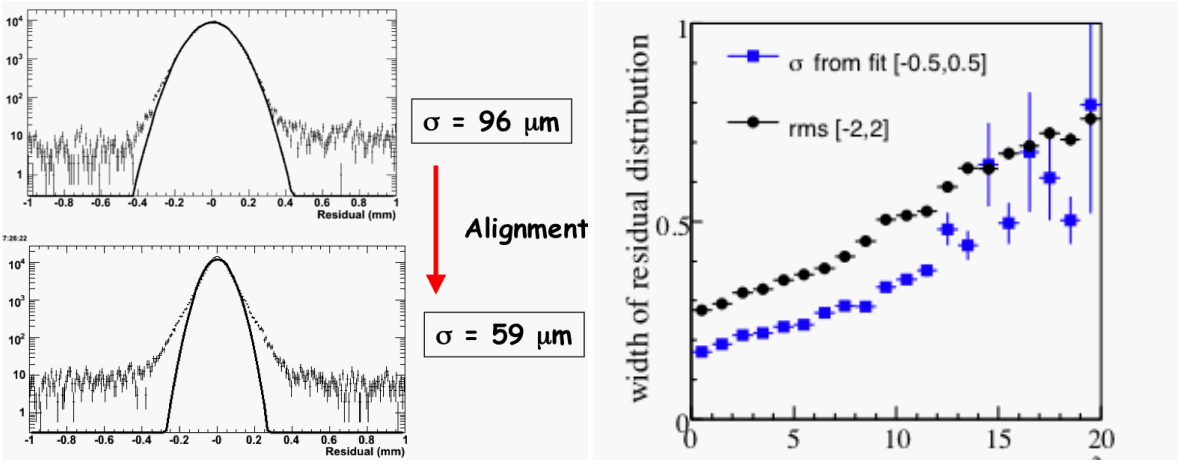

Figure 18.2.4: *Left: SCT track residuals before and after alignment. Right: σ of the residual distribution for the TRT as a function of the unbiased χ^2 for each given hit (i.e. the χ^2 of the track removing the contribution of the hit under evaluation). Both plots stems from tests performed at the surface.*

18.3 SR-1 cosmics: Simulation

Simulation of cosmics events for the surface setup proceeds by generating single muons on a plate high above the detector as shown in figure 18.3.1. The reason for this choice of origin, is to mimic the effects of the scintillator trigger plates used in the real data taking, without actually building a software counterpart. In order for the signals to arrive within the 75 ns read-out window of the TRT, the flight time of $\frac{100\text{ m}}{c}$ is subtracted from the global time for all hits. Following, the TRT digitization proceeds as described in chapter 10, except that a non-active gas is used, and that for straws above $y = 0$ the opposite than normal time correction is applied to account for the fact that cosmic muons originate from outside the detector.

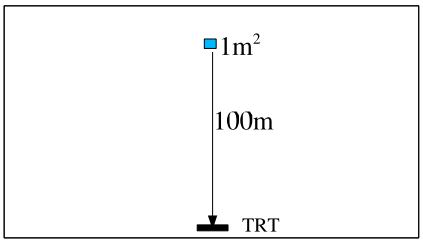

Figure 18.3.1: *Setup for surface cosmics. The generation plate is placed at a large distance from the Inner Detector to mimic the effects of the scintillators used for data taking.*

18.4 Pit Cosmic: Data

Recently the Inner Detector has been installed in the ATLAS pit and tests performed with parts of the SCT and TRT integrated into the ATLAS data acquisition. Figure 18.4.1(left) shows an event from the

test run. In the lack of the ATLAS clock and scintillators, the muon chambers and tile calorimeter are used as triggers and this has caused some difficulties: This usage of the tile calorimeter is not part of the design requirements and the timing of the different muon modules differs, complicating its usage as trigger. Simultaneously, a different approach is used in runs later in the commissioning phase (M6 and beyond), where scintillator plates are placed on top of the ATLAS detector as shown in figure 18.4.1(right). For practical reasons, the area covered with scintillators is limited, causing a low event rate from this cosmic trigger. The results of the M4 cosmic run in terms of TRT noise and resolution are shown in figure 18.4.2.

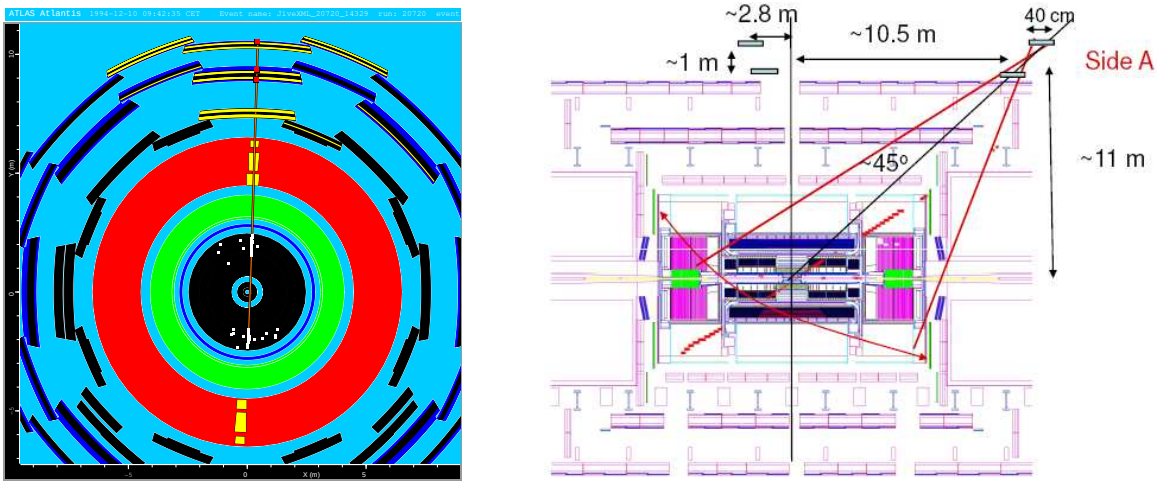

Figure 18.4.1: *Left: Event display showing an event from cosmics. Note how the track is formed based on the information of many sub-detectors. Right: Setup for the M6 run. Apart from the calorimeter and muon triggers used in the M4 run an additional scintillator trigger is added.*

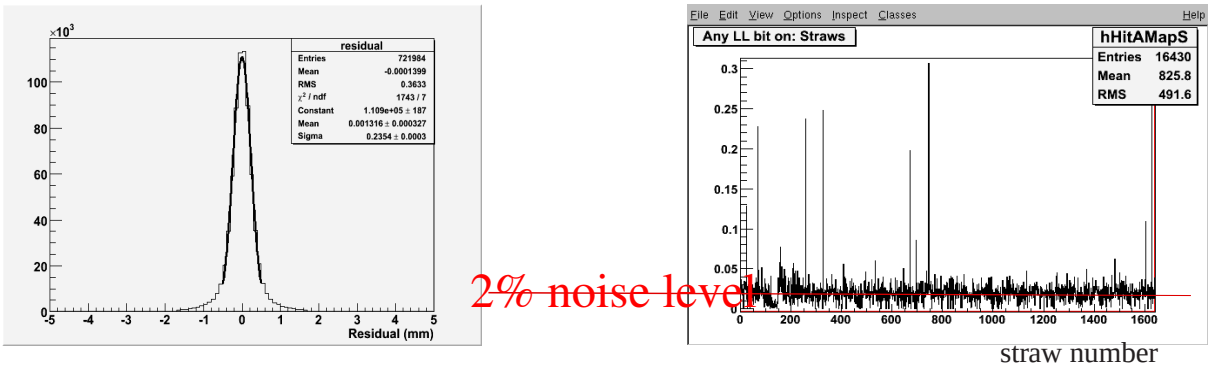

Figure 18.4.2: *Left: TRT track residuals. Right: Noise levels of the various straws in one TRT ϕ sector. The noise level is generally below the expected* 3%. *Both plots stems from test performed in the ATLAS cavern (M4).*

18.5 Pit cosmics: Simulation

The majority of the cosmic data is recorded using the calorimeters for triggering. Since the calorimeter enclose the Inner Detector, the origin of real data cosmics in unknown (cf. figure 18.0.1(left)). In order to resemble this with some degree of accuracy in the simulation, the generation plate used in SR-1 cosmics setup (figure 18.3.1) must be enlarged significantly as shown in figure 18.5.1. To reduce the required computational effort, a filtering algorithm selects only muons which enter a spherical volume of 20 m radius around the Inner Detector (see figure 18.5.1(right)). Only selected events are passed to the full simulation, which apart from simulating interactions with the ATLAS detector also simulates interaction with air in the ATLAS shaft as well as with the surrounding rock.
Digitization of simulated cosmics pit data constitutes a special problem due the lack of "cosmic bunch crossing" combined with the unknown source of the particles. One cannot, as in SR-1, assume that a given muon traveled a certain distance upon arriving in the TRT, since the time difference between muons can be as large as $(\sqrt{(600\text{ m})^2+(100\text{ m})^2}-100\text{ m})/c = 1120$ ns, which is much larger than the 75 ns TRT read-out window.

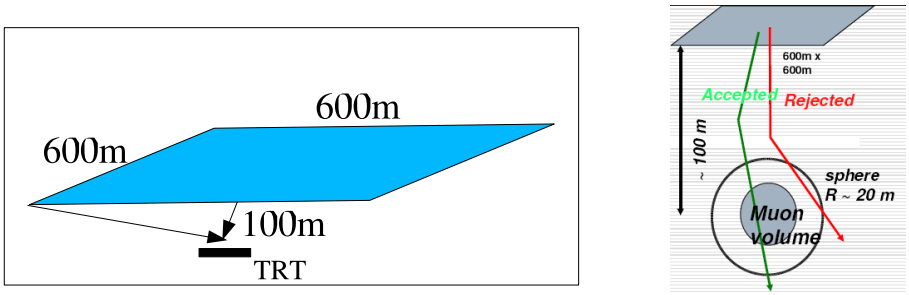

Figure 18.5.1: *Setup for simulating cosmics in the pit. The difference between the shortest and the longest path corresponds to more than 1 μs.*

To make the digitized data resemble real data, would require a MC simulation of the calorimeter trigger. Such trigger is not available, instead, the TRT digitization package is updated to cope with the setup. In the lack of triggering, one can choose between the following two digitization schemes:

- Switch off all time corrections by which all signals start in the first of the 24 time bins (unless an overall shift is applied).
- Try to steer the TRT digitization to perform slightly more realistic, by including, as much as possible, the various time corrections, without actually building a software trigger.

Obviously the first approach represents an idealization with respect to data in which the arriving signal have a wide time spread.

In the second approach the time at $y = 0$, $t_{y=0}$, is retrieved and used as a reference point, upon which time corrections are added. The read-out clock is started at:

$$t_{hit} - t_{y=0} + 12.5\text{ ns} \cdot rnd \tag{18.5.1}$$

where *rnd* is a flat random number $rnd \in [-1;1]$. The effect of the latter smearing is to simulate the lack of bunch-crossing clock. After the above operation, the standard TRT digitization proceeds as

described in chapter 10. By this approach, the average leading edge is randomly distributed, but the locations of the leadings edges in the hits of a given event are (somewhat) realistic.
An example of a successful digitization and track reconstruction of a simulated cosmic event is shown in figure 18.5.2.

The digitization of the Pixel and SCT sub-systems proceeds in a similar way.

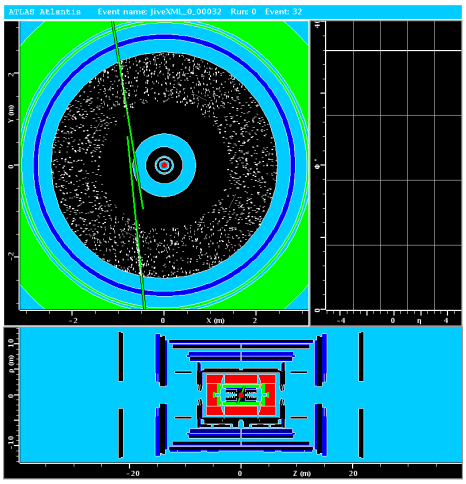

Figure 18.5.2: *Atlantis event view of a reconstructed cosmic event.*

18.6 Conclusions

The ATLAS Inner Detector is being commissioned with cosmic rays. The full data acquisition chain is in use, and cosmics data as well as simulation is reconstructed with standard ATLAS software. The results in terms of noise, hit efficiency and track resolution are well within expectations for the cosmic setup. However the integration of the remaining parts of the Inner Detector into the ATLAS data acquisition is ongoing and the detector commissioning proceeds until LHC startup. A simulation setup able to provide MC for cosmic events has been developed and successfully tested.

Chapter 19

Summery and outlook

During the summer of 2008 LHC should provide the first collisions, and in this thesis some of the preparation efforts are described. Mainly discussed is the Transition Radiation Tracker (TRT). Results from the hardware testing are presented, but focus is put on the simulation, in particular the software modeling of the detector response. Based on Garfield simulations and test-beam measurements, a number of updates compared to earlier simulations are presented. Independent tunes of the simulation with respect to; efficiency, time over threshold and track resolution yield compatible results in terms of simulation settings, and a detailed comparison with test-beam data shows, that the simulation accurately resembles data. In addition, a tune of the transition radiation model to test-beam data is presented, and it is shown that the simulation accurately describes data also in this aspect.
In order to be able assess the conditions and perform calibration of the TRT during LHC operation, tools have been written and successfully tested against cosmic data. Concerning the implementation of the detector description in the software, survey data from the completed TRT detector allowed for an update of the detector geometry and material, which has been implemented in the simulation. Also a conversion finder, able to locate photons conversions in the TRT is described, and it is argued how the fact, that the conversion cross-section depends on the local density will allow the dead material of the detector (support structures etc.) to be accurately mapped during the first year(s) of data taking. Many analyzes benefit from an accurate mapping of the detector material, among others the W mass analyzes as discussed below. Moreover, a considerable effort is invested in understanding the nature of the noise in the TRT, allowing for accurate modeling in the simulation.
Finally are the commissioning efforts of the Inner Detector described, including updates in the TRT simulation implemented to resemble the interactions of cosmic muons.
In general it is concluded, the simulation of the TRT matches data well, and it is ready to reproduce collision data coming from the experiment after LHC startup.
Also discussed are the prospects of an ATLAS measurement of the W mass. Due to Standard Model constraints, the W mass is linked to the Higgs mass, and measuring precisely M_W allows not only for a consistency check of the Standard Model, but also might help distinguishing between the various extensions of the Standard Model, which are characterized by posing different constraints on the W and Higgs masses.
Non-surprisingly the evaluation of the systematic errors affecting the M_W measurement are subject to some unknowns, which can only be answered after running the ATLAS experiment. For example is the knowledge of the parton density functions expected to improve with LHC data, and the corresponding error induced in the W mass measurement is consequently difficult to assess accurately

at the present time. Likewise is the systematic error due to the uncertainty of the QCD background estimated, basically using qualitative arguments. With respect to final state radiation, the fact that radiated photons in the electron channel tend to recombine with the electron cluster in the calorimeter, as opposed to the muon channel, requires that the traversed material must be accurately known (i.e. the detector description in the simulation must be accurate) in order not to introduce a significant systematic error to the W mass measurement.

Nevertheless, in the absent of unforeseen complications, it is argued that a competitive W mass measurement should be possible with the use of the ATLAS experiment. In an optimistic assessment, the W mass should be possible to measure to within $\sim 6-7$ MeV with 10 fb^{-1} of data. Note that the systematics are evaluated by the use of considerably smaller (simulated) datasets, which are scaled to 10 fb^{-1} assuming no unforeseen difficulties emerging with increased statistics. The superior precision with respect to earlier measurements is made possible mainly through the large Z sample expected, which, when combined with the precise knowledge of the Z properties from earlier experiments, provides a possibility for precise differential calibration of the energy scale of the experiment. Even in case the systematic errors turn out of considerably larger than estimated in this thesis, the M_W measurement could still be competitive and is thus likely to help resolving the problems of the generation of mass in the electroweak sector once and for all.

Acknowledgments

Needless to say, the work presented in this thesis would not have possible, had it not been for the help and support of a number of people. It would not be possible for me to mention all here, and for that I apologies.
First of all I would like to thank my supervisor Prof. Jørn Dines Hansen for always supporting me, and for sharing his impressive knowledge in numerous fruitful discussions.
It has been a true pleasure to work with the excellent people of the HEP group at NBI, where help is always granted to those who ask for it. This I have taking advantage of on a number of occasions. In particular I am grateful to Thomas Kittelmann; for his friendship and for always taking time to share his considerable knowledge of physics as well as software. Also, I am grateful to Troels Petersen, who considered it as a personal challenge to make a good physicist out of me.
Thanks also goes to my other office mates: Rasmus Mackeprang and Katrine Facius, as well as Jacob Groth and Sasha Mehlhase for making every day memorable - at the institute and not least while traveling.
Also, I am grateful to Peter Hansen, Jørgen Beck Hansen and Mogens Dam for the many interesting discussions on TRT software, as well as the many joyful social events. Thanks to Bjørn Nilsson and Anders Wäänänen for keeping the local computing infrastructure in good shape and to Daniel Kalici for ensuring that I always had the resources available necessary for large scale productions on the Steno cluster.
At CERN I have had the pleasure to work within the TRT software group, and enjoyed the weekly phone meetings with people like Christian Schmitt, Andrea Bocci and Sasa Fratina. Also, in my work I have enjoyed collaborating with Nathalie Besson and Maarten Boonekamp on the W mass analysis, and many others have helped me with TRT related topics, some of whom are:
Peter Cwetanski who provided the scripts for running the Garfield simulations.
Thomas Koffas who helped merging the conversion finder into the default conversion software.
Vladimir Tikhomirov who provided the test-beam data on which the noise study in chapter 16 is based.
Pauline Gagnon who supervised my work on the acceptance tests of the barrel modules.
Franck Martin who helped me extending the TRT StrawStatusSummeryTool to cover the end-caps.

Also, I am grateful to my family, my friends and my study mates; without your cheering and unconditioned support, I would not have made it this far. If I was able to express my gratitude towards my girlfriend Trine, this is where I would do it... Then again, in that case I would probably be a poet rather than a physicist and this thesis would never have existed. So that, I won't even try.
Thanks Trine, I think you know...

Konklusion på dansk

I sommeren 2008 foretages de første proton-proton kollisioner ved Large Hadron Collider (LHC) på CERN, ved en CM energi på 14 TeV. Denne afhandling beskriver nogle af de forberedelser foretaget på et af eksperimenterne ved LHC: ATLAS eksperimentet. Fokus ligger på Transition Radiation Tracker (TRT) - en gas-baseret sub-detektor der udover at fungere som sporfindingsdetektor ved hjælp af opsamling af ionisation, også er i stand til at identificere elektroner via deres forøgede stråling som følge 'transition radiation'.
Resultater fra tests af færdigbyggede sub-detektor moduler præsenteres, men fokus ligger på simulation af detektorens virkemåde. Baseret på Garfield simulationer og resultater fra 'test beam', præsenteres en række opdateringer i simuleringen af TRT'en. Resultater sammenlignes med resultater fra test beam, hvormed man i detaljer kan forstå den observerede effektivitet og sporresolution.
Ydermere er støjen i TRT'en undersøgt ved hjælp af test beam studier, og simuleringen er opdateret således at den forventede støj i den rigtige detektor reproduceres i simuleringen.
I afhandlingen diskuteres endvidere muligheden for en kompetitativ måling af W massen. I Standard Modellen er det muligt ud fra målinger af W og top-kvark masserne at forudsige Higgs massen. En præcis måling af W massen gør det derfor muligt at teste Standard Modellen til en meget høj grad af præcision, samt eventuelt at skelne imellem forskellige udvidelser til Standard Modellen, som kendetegnes ved at give forskellige forudsigelser af sammenhængen imellem W, top-kvark og Higgs massen. Ikke overraskende er der en del ubekendte størrelser i forbindelse med at estimere med hvilken præcision W massen kan forventes målt ved ATLAS eksperimentet. For eksempel antages det at protons strukturfunktioner bliver bedre kendte efterhånden som dataindsamlingen finder sted, og den systematiske fejl som skyldes usikkerheden i kendskabet til strukturfunktionerne er derfor vanskelig at estimere præcist på nuværende tidspunkt. Tilsvarende er den systematiske fejl som følge af usikkerheden i bestemmelsen af QCD baggrunden estimeret baseret på kvalitative argumenter.
Ikke desto mindre argumenteres det i denne afhandling, at såfremt der ikke opstår uforudsete komplikationer, kan W'ens masse bestemmes ved ATLAS eksperimentet med en hidtil uovertruffen præcision på $\sim 6-7$ MeV for 10 fb^{-1} data. Bemærk at de systematiske fejl er evalueret med betragteligt mindre (simulerede) datasæt, og skaleret til 10 fb^{-1} under antagelse af at ingen uforudsete problemer bliver målbare som følge af den øgede statistik. Den forventede forbedring i forhold til tidligere målinger skyldes især den store Z produktion, samt det faktum at Z'ens egenskaber er præcist målt ved tidligere eksperimenter. Dette muliggør en meget præcis kalibrering af eksperimentets energiskala ved brug af leptoner fra Z henfald.
Selv i det tilfælde hvor den systematiske fejl viser sig at være betragteligt større end estimeret i denne afhandling, er en konkurrencedygtig måling mulig, og det betragtes derfor som sandsynligt at målingen af W massen kan bidrage til at forstå massebegrebet en gang for alle og herved hjælpe med at løse et af Standard Modellens allerstørste problemer.

Bibliography

[A+01] C. Alexander et al., *Progress in the development of the DTMROC time measurement chip for the ATLAS transition Radiation Tracker (TRT)*, IEEE Trans. Nucl. Sci. **48**, 514–519 (2001).

[A+07] N. Ali et al., *LHC Magnet Tests: Operational Techniques and Empowerment for Successful Completion*, (2007), Particle Accelerator Conference PAC07 25-29 Jun 2007, Albuquerque, New Mexico.

[AC80] W. W. M. Allison and J. H. Cobb, *Relativistic Charged Particle Identification by Energy Loss*, Ann. Rev. Nucl. Part. Sci. **30**, 253–298 (1980).

[ACD01] T. Appelquist, H.-C. Cheng and B. A. Dobrescu, *Bounds on universal extra dimensions*, Phys. Rev. **D64**, 035002 (2001), hep-ph/0012100.

[ACF06] M. Awramik, M. Czakon and A. Freitas, JHEP **11**, 48 (2006).

[ACFW04] M. Awramik, M. Czakon, A. Freitas and G. Weiglein, Phys. Rev. **D69**, 053006 (2004).

[ADL+06] ALEPH, DELPHI, L3, OPAL and S. Collaborations, Phys. Rept. **427**, 257 (2006).

[AFGS+07] A. Ahmad, D. Froidevaux, S. González-Sevilla, G. Gorfine and H. Sandaker, *Inner Detector as-built detector description validation for CSC. ATL-INDET-INT-2007-002; ATL-COM-INDET-2007-012; CERN-ATL-COM-INDET-2007-012*, (2007).

[AHDD99] N. Arkani-Hamed, S. Dimopoulos and G. R. Dvali, *Phenomenology, astrophysics and cosmology of theories with sub-millimeter dimensions and TeV scale quantum gravity*, Phys. Rev. **D59**, 086004 (1999), hep-ph/9807344.

[AL95] A. Collaboration (ALICE Collaboration), *ALICE: Technical proposal for a large ion collider experiment at the CERN LHC*, (1995), CERN-LHCC-95-71.

[And07] X. Anduaga, Triggering Photons in 3 decades of pT, Talk given at ATLAS Trigger & Physics Week, November 5-9, 2007.

[ATL96a] ATLAS calorimeter performance, Dec 1996, CERN-LHCC-96-40.

[ATL96b] *ATLAS liquid argon calorimeter: Technical design report*, (1996), CERN-LHCC-96-41.

[ATL97a] *ATLAS Inner Detector: Technical Design Report. Vol. 1*, (Apr 1997), CERN-LHCC-97-16.

[ATL97b] *ATLAS Inner Detector: Technical Design Report. Vol. 2*, (Apr 1997), CERN-LHCC-97-17.

[ATL99] ATLAS Detector and Physics Performance: Technical Design Report. Vol. 2, May 1999, CERN-LHCC-99-15.

[ATL07] T. Cornelissen and W. Liebig (ATLAS Collaboration), *ATLAS Inner Detector results from the 2004 combined test beam data*, Nucl. Phys. Proc. Suppl. **172**, 292–295 (2007).

[ATL08a] G. Aad et al. (ATLAS Collaboration), *The ATLAS Experiment at the CERN Large Hadron Collidor*, JINST To be published (2008).

[ATL08b] N. Besson et al. (ATLAS Collaboration), *Re-evaluation of the LHC potential for the measurement of Mw*, ATL-COM-PHYS-2007-047, To be published (2008).

[ATL08c] N. Besson et al. (ATLAS Collaboration), *W mass CSC note. Measurement of W mass at ATLAS with early data, To be published*, (2008).

[ATL08d] G. A. Cavalli, D. (ATLAS Collaboration), *J13+J14+J15 Etmiss CSC performance note. To be published*, (2008).

[ATL08e] A. Collaboration (ATLAS Collaboration), *EGamma CSC performance note. To be published*, (2008).

[Ave00] P. Avery, *Kinematic fitting algorithms and lessons learned from KWFIT*, (2000), Prepared for International Conference on Computing in High- Energy Physics and Nuclear Physics (CHEP 2000), Padova, Italy, 7-11 Feb 2000.

[Ave08] P. Avery, Kinematic Fitting, 2008, Available on http://www.phys.ufl.edu/∼avery/.

[Aym08] R. Aymar, A word from the DG: The home straight, http://cdsweb.cern.ch/journal/article?issue=4/2008&name=CERNBulletin&category=News%20Articles&number=2&ln=en, 2008.

[B+07a] V. Buge et al., J. Phys. **G34**, N193–N220 (2007).

[B+07b] V. Buge et al., *Prospects for the precision measurement of the W mass with the CMS detector at the LHC*, J. Phys. **G34**, N193–N220 (2007).

[BB06] N. Besson and M. Boonekamp, (2006), ATL-PHYS-PUB-2006-007.

[BH07] A. Bocci and W. Hulsbergen, *TRT alignment for SR1 cosmics and beyond*, (2007), ATL-INDET-PUB-2007-009.

[BHO99] O. Bruning, W. Herr and R. Ostojic, *A beam separation and collision scheme for IP1 and IP5 at the LHC for optics version 6.1*, (1999), CERN-LHC-PROJECT-REPORT-315.

[BNOY05] S. Berge, P. Nadolsky, F. Olness and C. P. Yuan, Phys. Rev. **D72**, 033015 (2005).

[BNVBW96] B. Bevensee, F. M. Newcomer, R. Van Berg and H. H. Williams, *An amplifier shaper discriminator with baseline restoration for the ATLAS transition radiation tracker*, IEEE Trans. Nucl. Sci. **43**, 1725–1731 (1996).

[Boc08] A. Bocci, *Private communications*, (2008).

[Bou03] J. Boudreau, Geometry Kernel Classes, `http://atlas.web.cern.ch/Atlas/GROUPS/DATABASE/detector_description/`, 2003.

[BT04] J. Boudreau and V. Tsulaia, The GeoModel Toolkit for Detector Description, in *Proceedings of the Conference on Computing in High Energy and Nuclear Physics (CHEP 2004), Interlaken, Switzerland*, Sep 2004.

[Bus07] V. Buscher, *Search for Higgs bosons and supersymmetry at the Tevatron*, AIP Conf. Proc. **957**, 13–20 (2007).

[BW94] E. Barberio and Z. Was, *PHOTOS: A Universal Monte Carlo for QED radiative corrections. Version 2.0*, Comput. Phys. Commun. **79**, 291–308 (1994).

[BY97] C. Balazs and C. P. Yuan, Phys. Rev. **D56**, 5558–5583 (1997).

[C$^+$02] G. Corcella et al., *HERWIG 6.5 release note*, (2002), hep-ph/0210213.

[CDF94] F. Abe et al. (CDF Collaboration), *Evidence for top quark production in $\bar{p}p$ collisions at $\sqrt{s} = 1.8$ TeV*, Phys. Rev. Lett. **73**, 225–231 (1994), hep-ex/9405005.

[CDF01] A. A. Affolder et al. (CDF Collaboration), *Measurement of the W boson mass with the Collider Detector at Fermilab*, Phys. Rev. **D64**, 052001 (2001), hep-ex/0007044.

[CDF07a] T. Aaltonen et al. (CDF Collaboration), *First Measurement of the W Boson Mass in Run II of the Tevatron*, Phys. Rev. Lett. **99**, 151801 (2007), arXiv:0707.0085 [hep-ex].

[CDF07b] T. Aaltonen et al. (CDF Collaboration), *First Run II Measurement of the W Boson Mass*, (2007), arXiv:0708.3642 [hep-ex].

[CER08] CERN, CERN Accelerators, 2008, `http://user.web.cern.ch/user/AcceleratorServices/Machines/Machines.html`.

[CMNT04] C. M. C. Calame, G. Montagna, O. Nicrosini and M. Treccani, Phys. Rev. **D69**, 037301 (2004).

[CMS06] G. L. Bayatian et al. (CMS Collaboration), *CMS physics: Technical design report*, (2006), CERN-LHCC-2006-001.

[Cow] G. Cowan, *Statistical data analysis*, Oxford, UK: Clarendon (1998) 197 p.

[CSC08a] *Muon CSC performance note. To be published*, (2008).

[CSC08b] *W/Z cross section CSC note. To be published*, (2008).

[CSS85] J. C. Collins, D. E. Soper and G. Sterman, Nucl. Phys. **B250**, 199 (1985).

[Cwe06] P. Cwetanski, *Straw performance studies and quality assurance for the ATLAS transition radiation tracker*, (2006), CERN-THESIS-2006-025.

[Cwe07] P. Cwetanski, *Private communications*, (2007).

[Dam04] M. Dam, Simulation of ATLAS Transition Radiation, Talk given at TRT Collaboration Meeting, CERN, February 16-23, 2004.

[Daw06] S. Dawson, Electroweak Theory, Lecture series given at the 1st Hadron Collider Physics Summer School, Fermilab, August 9-18, 2006.

[dBS04] W. de Boer and C. Sander, *Global electroweak fits and gauge coupling unification*, Phys. Lett. **B585**, 276–286 (2004), hep-ph/0307049.

[DGDG+05] B. Di Girolamo, A. Dotti, V. Giangiobbe, P. Johansson, L. Pribyl and M. Volpi, *Beam-line instrumentation in the 2004 combined ATLAS testbeam*, (2005), ATL-TECH-PUB-2005-001, ATL-COM-TECH-2005-001, Geneva, CERN.

[Dol86] B. Dolgoshein, *Transition Radiation Detectors and Particle Identification*, Nucl. Instrum. Meth. **A252**, 137–144 (1986).

[DØ96] S. Abachi et al. (DØ Collaboration), *Measurement of the W Boson Mass*, Phys. Rev. Lett. **77**(16), 3309–3314 (Oct 1996).

[DØ98] B. Abbott et al. (DØ Collaboration), *A Measurement of the W Boson Mass at the Fermilab $p\bar{p}$ Collider*, Phys. Rev. Lett. **80**(14), 3008 (1998).

[DØ00a] B. Abbott et al. (DØ Collaboration), *Measurement of the inclusive differential cross section for Z bosons as a function of transverse momentum in $p\bar{p}$ collisions at $s = 1.8$ TeV*, Phys. Rev. D **61**(3), 032004 (2000).

[DØ00b] B. Abbott et al. (DØ Collaboration), *Measurement of the W Boson Mass Using Electrons at Large Rapidities*, Phys. Rev. Lett. **84**(2), 222–227 (Jan 2000).

[ega08] *EG-4 Photon conversions. To be published*, (2008).

[Ege98] U. Egede, *The search for a Standard Model Higgs at the LHC and electron identification using transition radiation in the ATLAS tracker*, (1998), CERN-THESIS-98-001.

[G403] S. Agostinelli et al. (GEANT4 Collaboration), *GEANT4: A simulation toolkit*, Nucl. Instrum. Meth. **A506**, 250–303 (2003).

[Gag05] P. Gagnon, ATLAS TRT Barrel module passports, Web interface can be found at `http://trt-wts.web.cern.ch/trt-wts/passp/bmenu.html`, 2005.

[Gai82] J. Gaiser, *Charmonium Spectroskopy from Radiative Decays of the J/psi and psi-prime*, (1982), SLAC-0255.

[GHKD89] J. F. Gunion, H. E. Haber, G. L. Kane and S. Dawson, *The Higgs Hunters's Guide*, (1989), SCIPP-89/13.

[Gor98] A. S. Gordon, *Measurement of the W boson mass with the Collider Detector at Fermilab*, (1998), FERMILAB-THESIS-1998-10.

[Gor07] G. Gorfine, Inner Detector Material, `https://twiki.cern.ch/twiki/bin/view/Atlas/InDetMaterial/`, 2007.

[Gor08] G. Gorfine, Inner Detector GeoModel, `https://twiki.cern.ch/twiki/bin/view/Atlas/InDetGeoModel`, 2008.

[Gou06] M. Goulette, *Update on the TRT material weight*, (2006), ATL-INDET-PUB-2006-008; ATL-COM-INDET-2006-006. Geneva, CERN.

[Gou07] M. Goulette, *Update on the TRT end-cap material weight*, (2007), ATL-INDET-PUB-2007-002; ATL-COM-INDET-2007-001; CERN-ATL-COM-INDET-2007-001. Geneva, CERN.

[GW06] P. Golonka and Z. Was, *PHOTOS Monte Carlo: A precision tool for QED corrections in Z and W decays*, Eur. Phys. J. **C45**, 97–107 (2006), hep-ph/0506026.

[H$^+$03] S. Haywood et al., (2003), hep-ph/0003275.

[H$^+$04] C. D. Hoyle et al., *Sub-millimeter tests of the gravitational inverse-square law*, Phys. Rev. **D70**, 042004 (2004), hep-ph/0405262.

[Han08] P. Hansen, *Private communications*, (2008).

[HHW06] S. Heinemeyer, W. Hollik and G. Weiglein, *Electroweak precision observables in the minimal supersymmetric standard model*, Phys. Rept. **425**, 265–368 (2006), hep-ph/0412214.

[hig08] High Energy Physics Group, Imperial College London, CMS: Higgs Physics, 2008, http://www.hep.ph.ic.ac.uk/cms/physics/higgs.html.

[HLS75] R. Haag, J. T. Lopuszanski and M. Sohnius, *All Possible Generators of Supersymmetries of the s Matrix*, Nucl. Phys. **B88**, 257 (1975).

[JWDK93] S. Jadach, Z. Was, R. Decker and J. H. Kuhn, *The tau decay library TAUOLA: Version 2.4*, Comput. Phys. Commun. **76**, 361–380 (1993).

[K$^+$08] T. Kittelmann et al., Virtual Point One (VP1), http://atlas-vp1.web.cern.ch/atlas-vp1/, 2008.

[Kit07] T. H. Kittelmann, *Slepton spin determination and simulation of the Transition Radiation Tracker at the ATLAS experiment*, (2007).

[KK06] T. H. Kittelmann and E. B. Klinkby, A Study of TRT Noise in 2004 Test Beam Data, ATL-COM-INDET-2006-015, Nov 2006.

[Kli07] E. Klinkby, *On behalf of the ATLAS Collabaration. Commissioning of the ATLAS Inner Detector with cosmic rays*, (2007), Conference proceedings prepared for the 10th ICATPP Conference on Astroparticle, Particle, Space Physics, Detectors and Medical Physics Applications, Villa Erba, Como, Italy, 8-12 Oct 2007. To be published.

[Kli08] E. Klinkby, The EventBoost Algorithm, `http://alxr.usatlas.bnl.gov/lxr/source/atlas/Generators/GenAnalysisTools/`, 2008.

[KM07] K. Kong and K. T. Matchev, *Phenomenology of universal extra dimensions*, AIP Conf. Proc. **903**, 451–454 (2007), hep-ph/0610057.

[KT90] E. W. Kolb and M. S. Turner, *The Early universe*, Front. Phys. **69**, 1–547 (1990).

[Lb03] L. Collaboration (LHCb Collaboration), *LHCb technical design report: Reoptimized detector design and performance*, (2003), CERN-LHCC-2003-030.

[Leo87] W. R. Leo, *Techniques for Nuclear and Particle Physics Experiments: A How To Approach*, (1987), Berlin, Germany: Springer (1987) 368 p.

[LEP07] J. Alcaraz et al. (LEP Collaboration), *Precision Electroweak Measurements and Constraints on the Standard Model*, (2007), 0712.0929.

[lgs08] Lagrange multipliers, `http://en.wikipedia.org/wiki/Lagrange_multipliers`, 2008.

[LHC06] G. Weiglein et al. (LHC/LC Study Group Collaboration), *Physics interplay of the LHC and the ILC*, Phys. Rept. **426**, 47–358 (2006), hep-ph/0410364.

[LR04] F. Luehring and A. Romaniouk, ATLAS TRT Barrel in Test Beam, Atlas eNews, Sep 2004, `http://aenews.cern.ch/aenews.php?issueno=200409`.

[M+05a] A. Moraes et al., (2005), ATL-PHYS-PUB-2005-007.

[M+05b] A. Moraes et al., (2005), ATL-PHYS-PUB-2005-015.

[Mar97] S. P. Martin, *A supersymmetry primer*, (1997), hep-ph/9709356.

[MO94] E. Mirkes and J. Ohnemus, Phys. Rev. **D50**, 5692–5703 (1994).

[MP07] S. Mehlhase and T. C. Petersen, *A probability based approach to PID in the TRT detector of ATLAS. ATL-COM-INDET-2006-017*, (2007).

[MS99] G. Miu and T. Sjostrand, Phys. Lett. **B449**, 313 (1999).

[NA5194] A. Baldit et al. (NA51 Collaboration), *Study of the isospin symmetry breaking the in the light quark sea of the nucleon from the Drell-Yan process*, Phys. Lett. **B332**, 244–250 (1994).

[Nad05] P. M. Nadolsky, AIP Conf. Proc. **753**, 158 (2005).

[NS01] R. S. Towell et al. (FNAL E866/NuSea Collaboration), *Improved measurement of the anti-d/anti-u asymmetry in the nucleon sea*, Phys. Rev. **D64**, 052002 (2001), hep-ex/0103030.

[NW06] G. Nanava and Z. Was, (2006), hep-ph/0607019.

[OAC+06] E. Obreshkov, S. Albrand, J. Collot, J. Fulachier, F. Lambert, C. Adam-Bourdarios, C. Arnault, V. Garonne, D. Rousseau, A. Schaffer et al., *Organization and Management of ATLAS Offline Software Releases*, (2006), ATL-SOFT-PUB-2006-008, CERN-ATL-SOFT-PUB-2006-008, ATL-COM-SOFT-2006-013, Geneva, CERN.

[P+95] W. Press et al., *Numerical Recipes in C*, Cambridge University Press, Reading, MA, U.S.A., 2^{nd} edition, 1995.

[P+02] J. Pumplin et al., JHEP **07**, 012 (2002).

[PDG06] W. M. Yao et al. (Particle Data Group Collaboration), *Review of particle physics*, J. Phys. **G33**, 1–1232 (2006).

[Pet07] T. Petersen, Particle ID, Talk given at ATLAS Inner Detector Week, CERN, October 1-5, 2007.

[PS95] M. E. Peskin and D. V. Schroeder, *An Introduction to quantum field theory*, (1995), Reading, USA: Addison-Wesley (1995) 842 p.

[Ric08] D. Richter, *Energy Loss Measurements with the ATLAS Transition Radiation Tracker Using Test Beam Data*, (2008).

[Ros06] L. Rossi, Inner Detector, Talk given at ATLAS Overview Week, Stockholm, Sweden, July 9-14, 2006.

[S+06] A. Salzburger et al., *The New Fast ATLAS Track Simulation Engine (Fatras)*, (2006), Prepared for International Conference on Computing in High- Energy Physics and Nuclear Physics (CHEP 2006), Mumbai, India, 13-17 Feb 2006.

[S+08] R. Seuster et al., HepVis, https://particle.phys.uvic.ca/twiki/bin/view/AtlasUVic/HepVis, 2008.

[Shp00] D. L. Shpakov, *A W boson mass measurement using the ratio of transverse masses of the W and Z bosons in $p\bar{p}$ collisions at 1.8 TeV with the DØ detector*, PhD thesis, State University of New York at Stony Brook, 2000.

[SLMS03] T. Sjostrand, L. Lonnblad, S. Mrenna and P. Skands, *PYTHIA 6.3 physics and manual*, (2003), hep-ph/0308153.

[SMS06] T. Sjostrand, S. Mrenna and P. Skands, *PYTHIA 6.4 physics and manual*, JHEP **05**, 026 (2006), hep-ph/0603175.

[The05] The ALEPH, DELPHI, L3, OPAL, SLD Collaborations, the LEP Electroweak Working Group, the SLD Electroweak and Heavy Flavour Groups, *Precision Electroweak Measurements on the Z Resonance*, page 302 (2005), hep-ex/0509008.

[Tik04] V. Tikhomirov, Barrel TRT performance and electron/pion rejection, Talk given at ATLAS TRT Meeting, CERN, August 30, 2004.

[TRT04] T. Akesson et al. (ATLAS TRT Collaboration), *ATLAS Transition Radiation Tracker test-beam results*, Nucl. Instrum. Meth. **A522**, 50–55 (2004).

[TRT08a] E. Abat et al. (ATLAS TRT Collaboration), *The ATLAS Transition Radiation Tracker (TRT) proportional drift tube: Design and performance*, JINST **3**, P02013 (2008).

[TRT08b] E. Abat et al. (ATLAS TRT Collaboration), *The ATLAS TRT barrel detector*, JINST **3**, P02014 (2008).

[Tul02] C. Tully, *LEP Higgs Search Results*, (2002), Slides presented at 18th International Workshop on Weak Interactions and neutrinos (WIN02), 21-26 Jan 2002, Christchurch, New Zealand.

[UA183a] G. Arnison et al. (UA1 Collaboration), *Experimental observation of isolated large transverse energy electrons with associated missing energy at s**(1/2) = 540-GeV*, Phys. Lett. **B122**, 103–116 (1983).

[UA183b] G. Arnison et al. (UA1 Collaboration), *Experimental observation of lepton pairs of invariant mass around 95-GeV/c**2 at the CERN SPS collider*, Phys. Lett. **B126**, 398–410 (1983).

[UA283a] P. Bagnaia et al. (UA2 Collaboration), *Evidence for Z0 –> e+ e- at the CERN anti-p p collider*, Phys. Lett. **B129**, 130–140 (1983).

[UA283b] M. Banner et al. (UA2 Collaboration), *Observation of single isolated electrons of high transverse momentum in events with missing transverse energy at the CERN anti-p p collider*, Phys. Lett. **B122**, 476–485 (1983).

[UT08] M. Bona et al. (UTfit Collaboration), *First Evidence of New Physics in b <–> s Transitions*, (2008), 0803.0659.

[Vee93] R. Veenhof, *Garfield, a drift chamber simulation program*, (1993), Prepared for International Conference on Programming and Mathematical Methods for Solving Physical Problems, Dubna, Russia, 14-19 Jun 1993.

[YFS61] D. R. Yennie, S. C. Frautschi and H. Suura, Ann. Phys. **13**, 379 (1961).

Appendix

Appendix A

W mass analysis

A.1 Validation of the template method : η and p_T^l bins

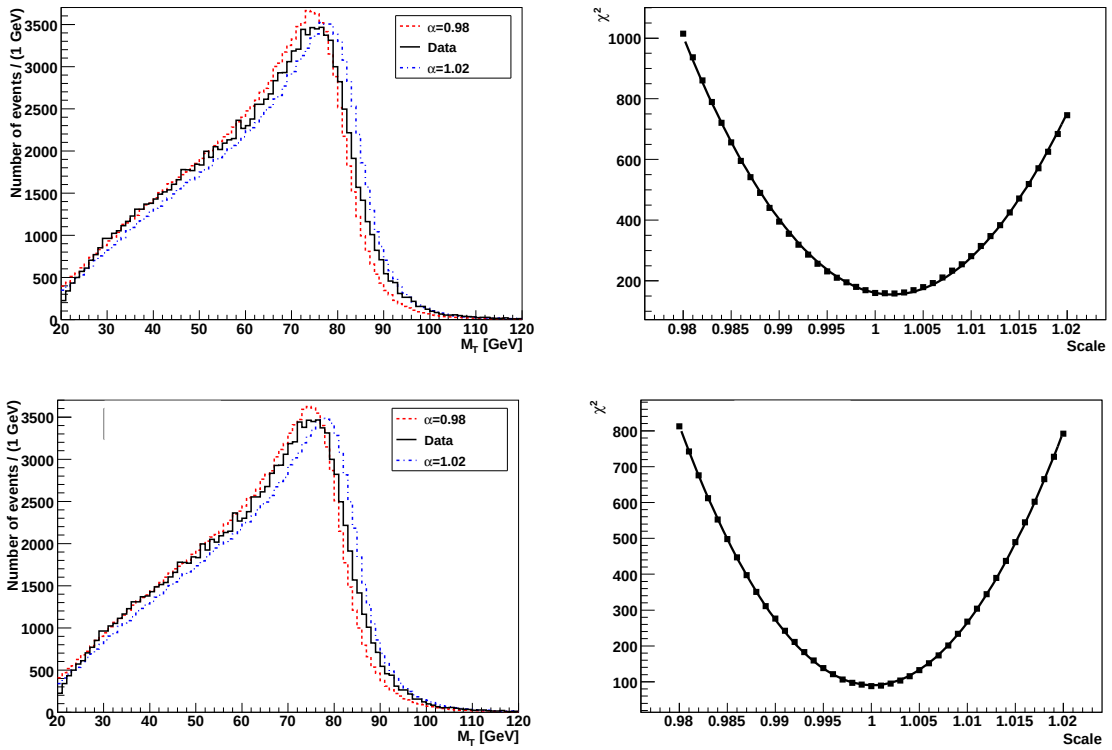

Figure A.1.1: *Top: Fit to the transverse W mass in the* $W \to \mu\nu$ *channel using bins 7* η *bins* $[0;2.5]$ *and 10* p_T^l *bins* $[10;60]$ *GeV(plus an overflow bin). Bottom: The same for* $Z \to \mu\mu$

A.2 Validation of the template method: Fits of smearing distributions

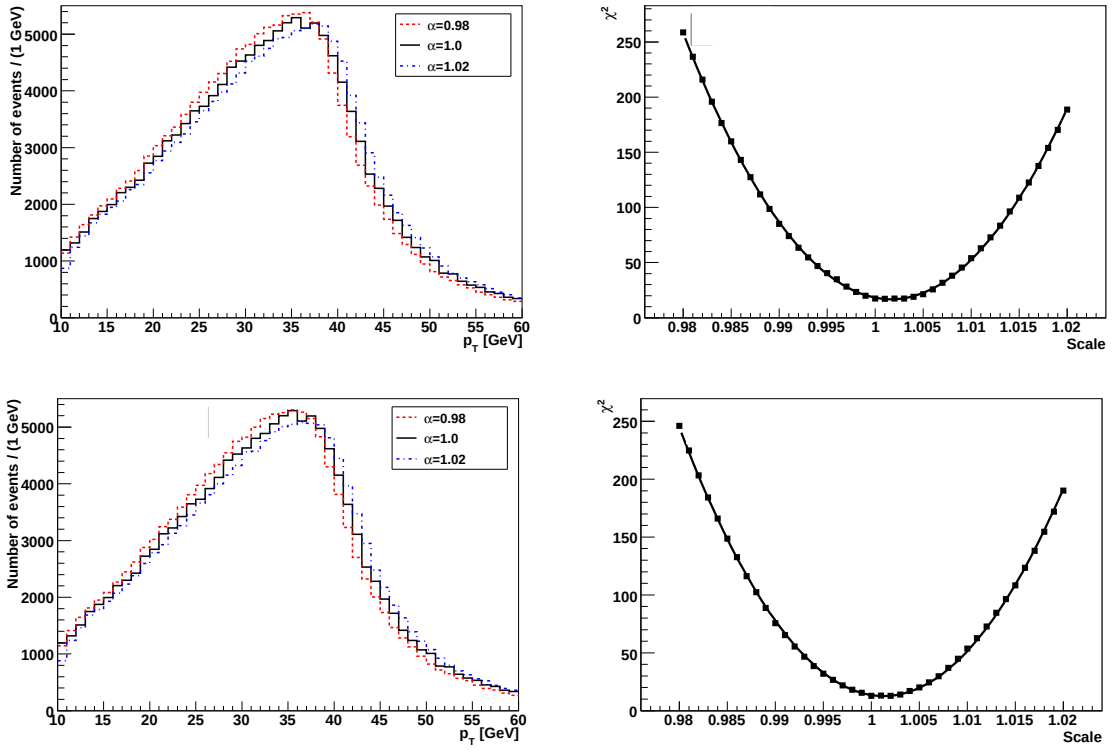

Figure A.1.2: *Top: Fit to p_T^l in the $W \to \mu\nu$ channel using bins 7 η bins $[0;2.5]$ and 10 p_T^l bins $[10;60]$ GeV(plus an overflow bin). Bottom: The same for $Z \to \mu\mu$*

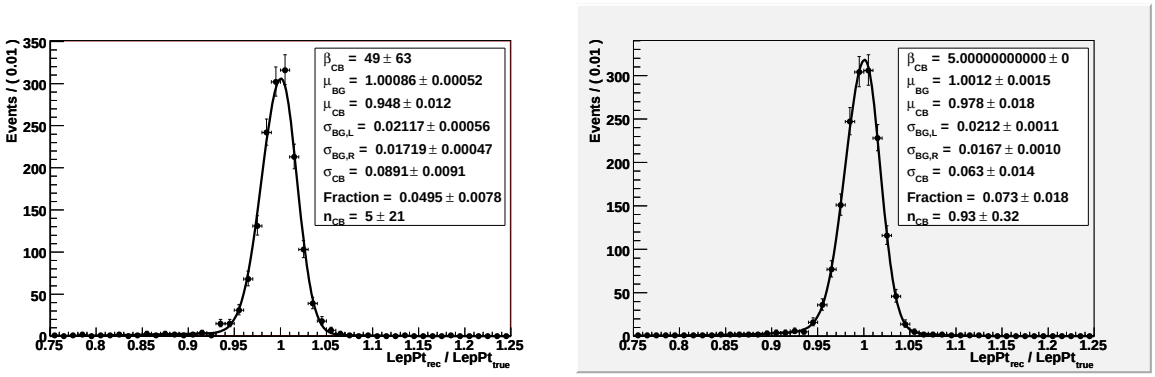

Figure A.2.1: *Example of the comparison between a fit smearing distribution (left) and a fit to the numbers actually used (right) - i.e. originating from a distribution described by the fit-parameters on the left-hand plot. p_T bin: $[10;20]$ GeV, η bin $[0;0.36]$.*

A.3 $\not\!\!E_T$ resolution

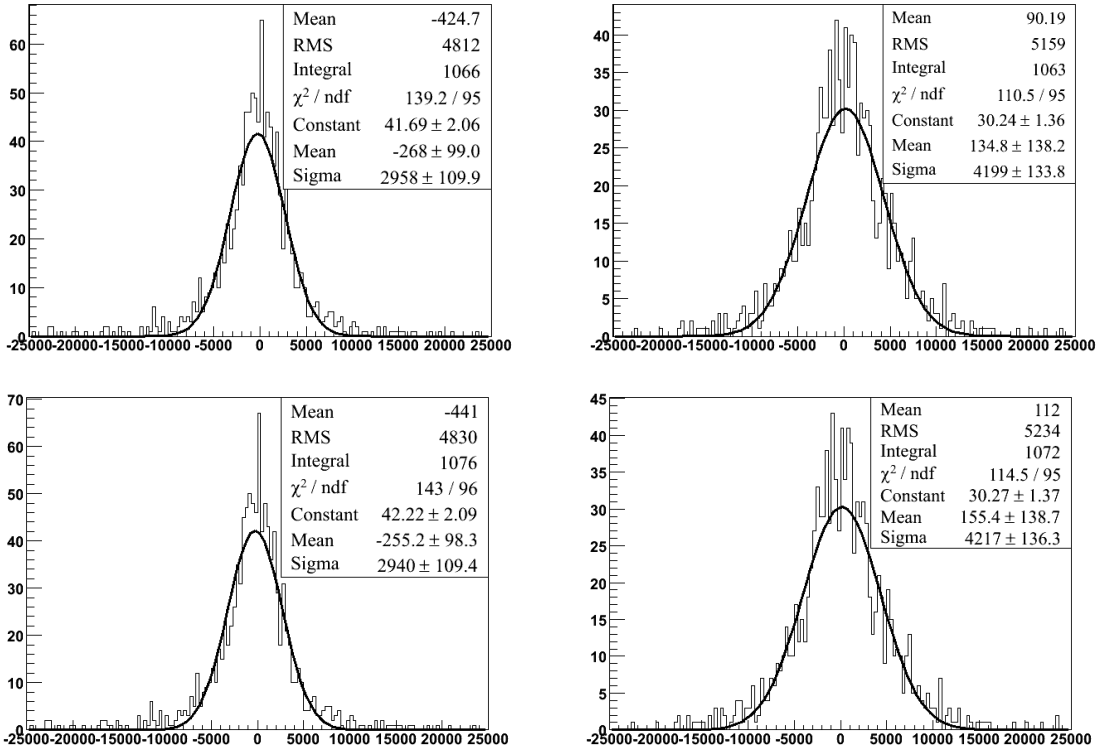

Figure A.3.1: *$\not\!\!E_T$ residual for parallel (left) and perpendicular (right) when replacing 1 neighbor (top) and 3 neighbors (bottom). As noise, the measurements from cells of the same type but located 90 degrees from the cluster is chosen.*

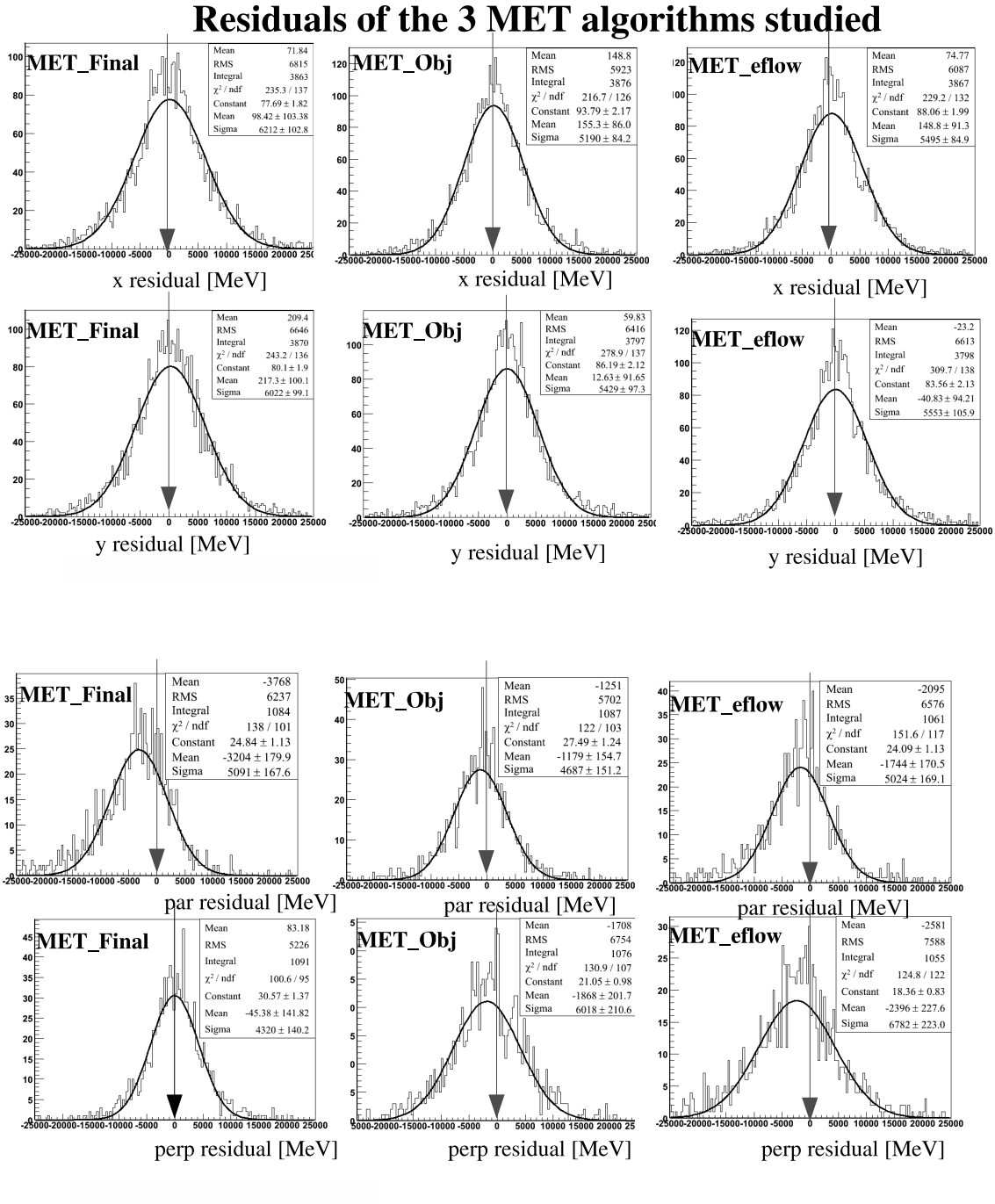

Figure A.3.2: *$\not\!\!E_T$ residual for various $\not\!\!E_T$ algorithms using (x,y) coordinate (top) and (par,perp) below.*

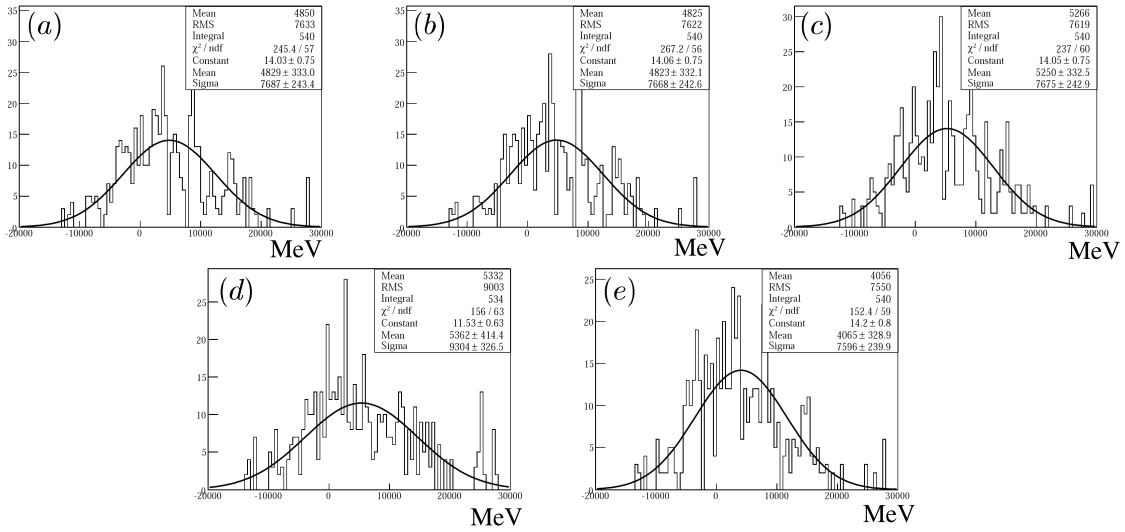

(a) Zero
(b) Gaussian (width determined from simulation)
(c) Random cells from same layer
(d) Modifying also Neighbours-neighbours
(e) Random cell – cell-list expanded to include cells neighbouring the cluster

Figure A.3.3: *Dependence of the $\not\!\!E_T$ resolution on the choice of noise algorithm.*

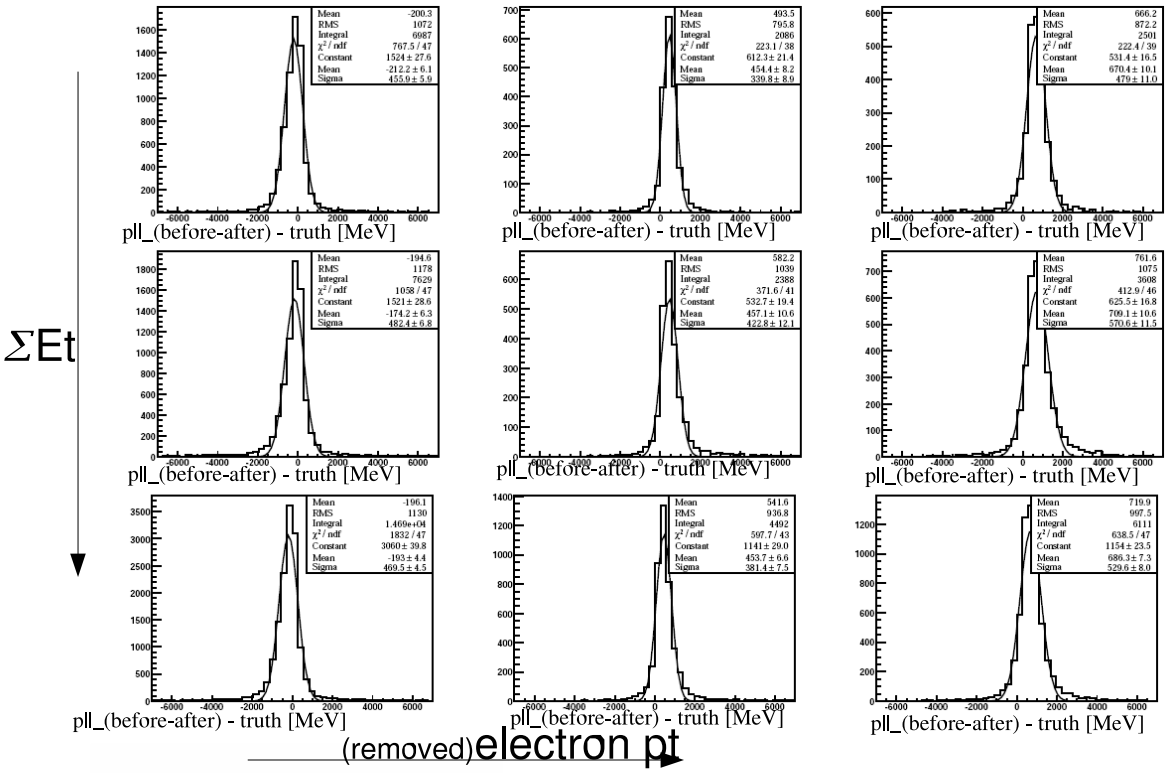

Figure A.3.4: *Dependence of the $\not\!\!E_T$ residual on the ΣE_T and transverse lepton momentum.*

Appendix B

TRT Digitization

B.1 Garfield distributions

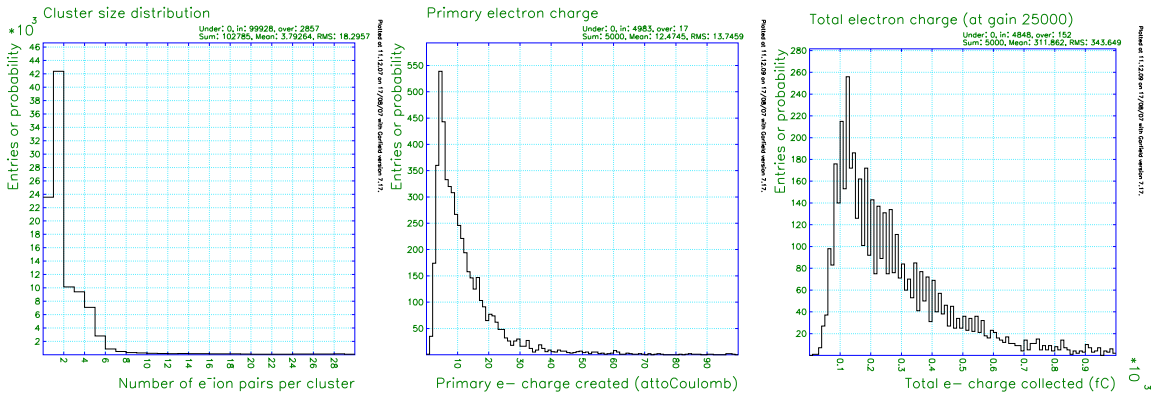

Figure B.1.1: *Left: Number of electron/ion pairs per cluster according to Garfield simulations. Middle: Distribution of initially produced charge in a cluster. Right: Distribution of total collected charge per cluster.*

B.2 Comparison of TRT digitization to Combined Test Beam results

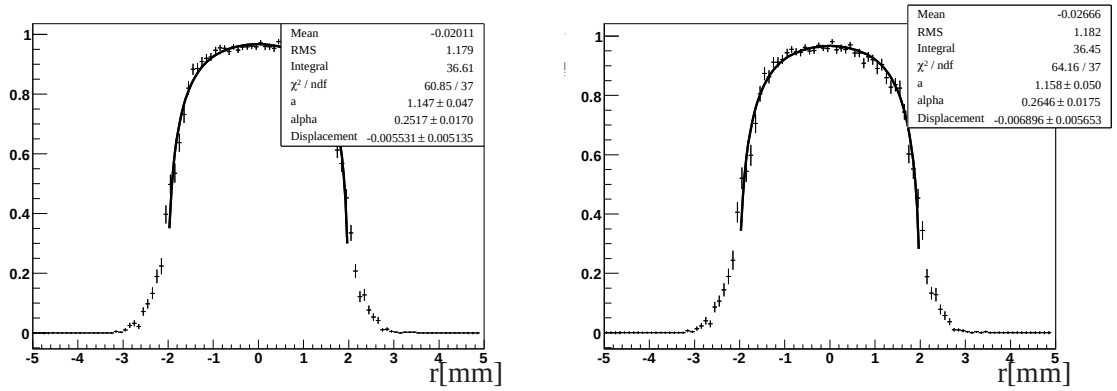

Figure B.2.1: *Efficiency as a function of r for run 2106 (left) and 2118 (right) without requirement on particle type.*

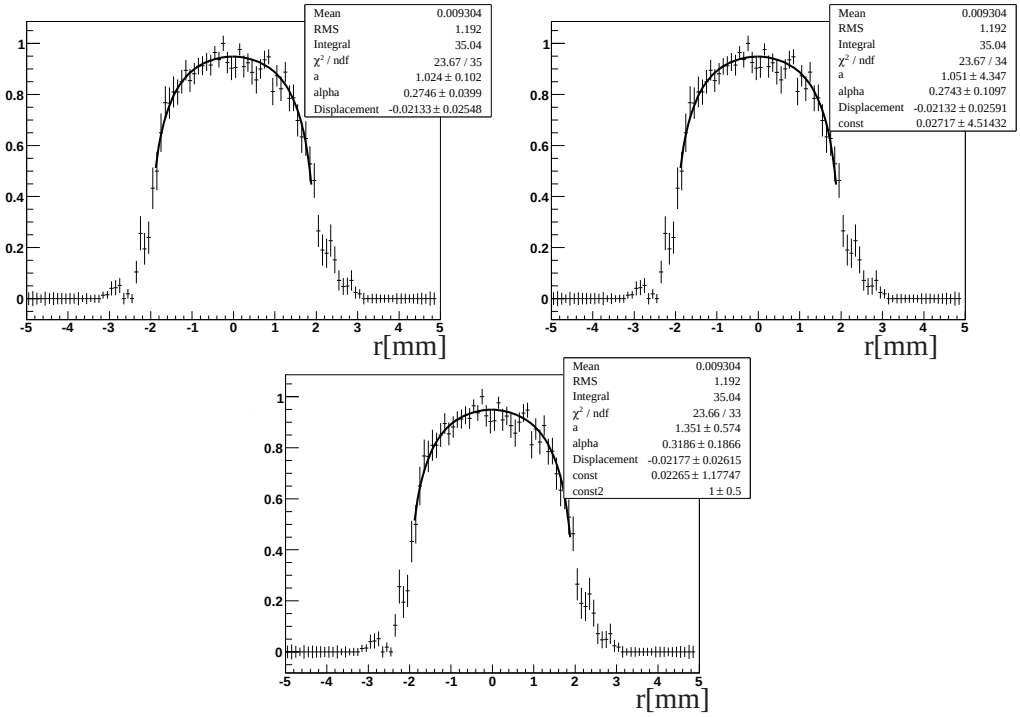

Figure B.2.2: *Efficiency for different orders (0,1,2) of the Poisson expansion described in section 11.3. Run 2118.*

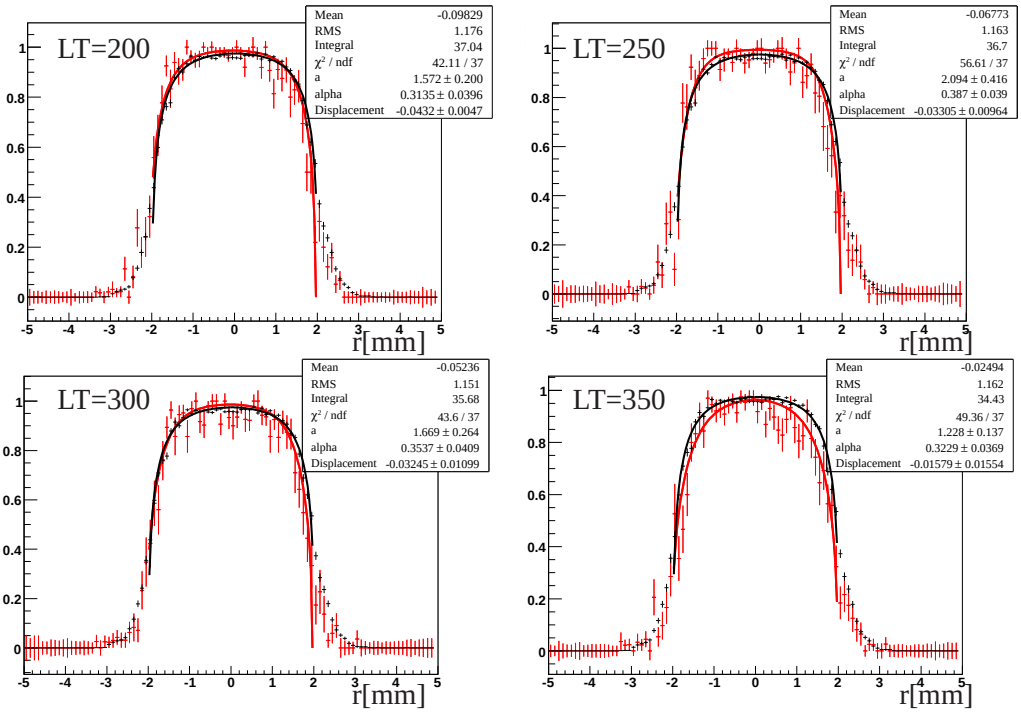

Figure B.2.3: *Efficiency as a function of r for run 2106 in data and MC for various LT settings.*

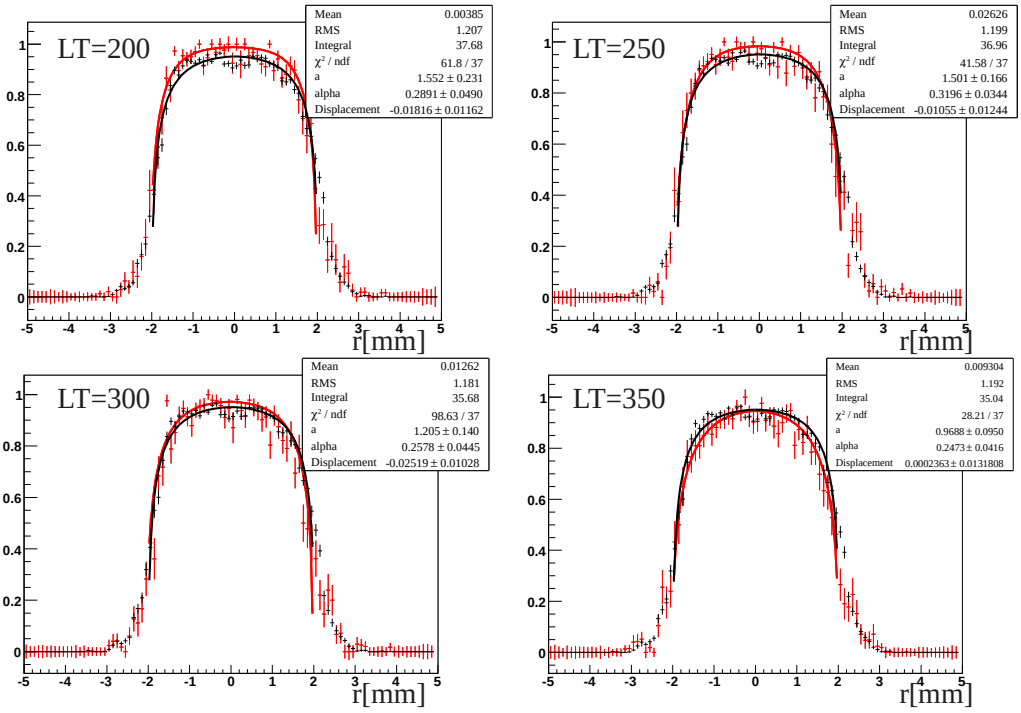

Figure B.2.4: *Efficiency as a function of r for run 2107 in data and MC for various LT settings.*

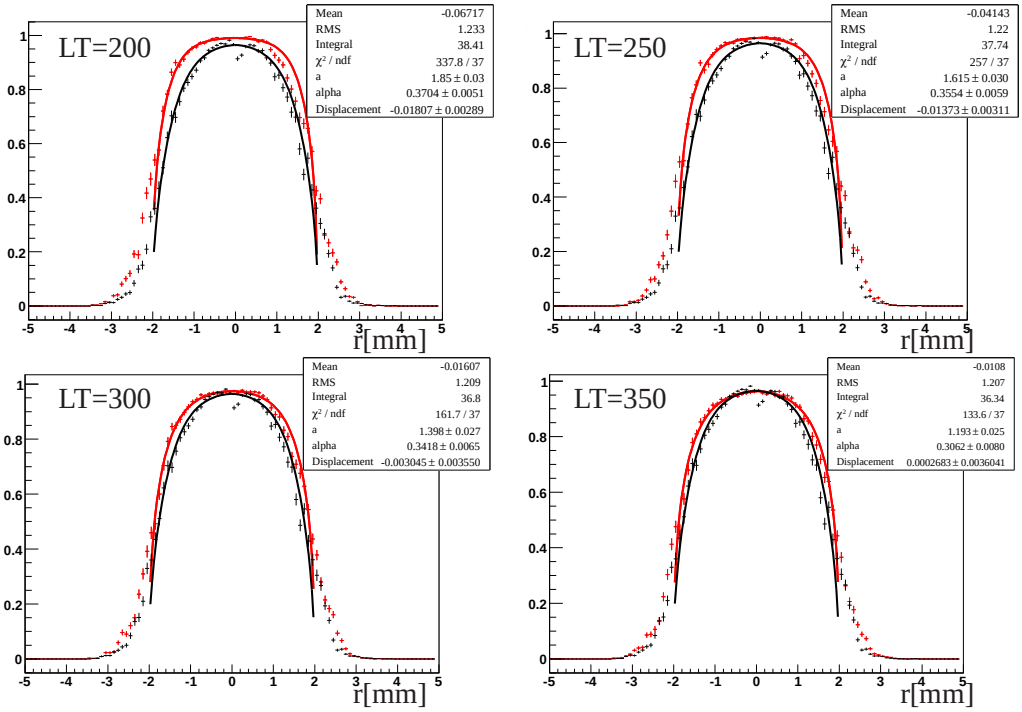

Figure B.2.5: *Efficiency as a function of r for run 2399 (100 GeV pion/electron) in data and MC for various LT settings.*

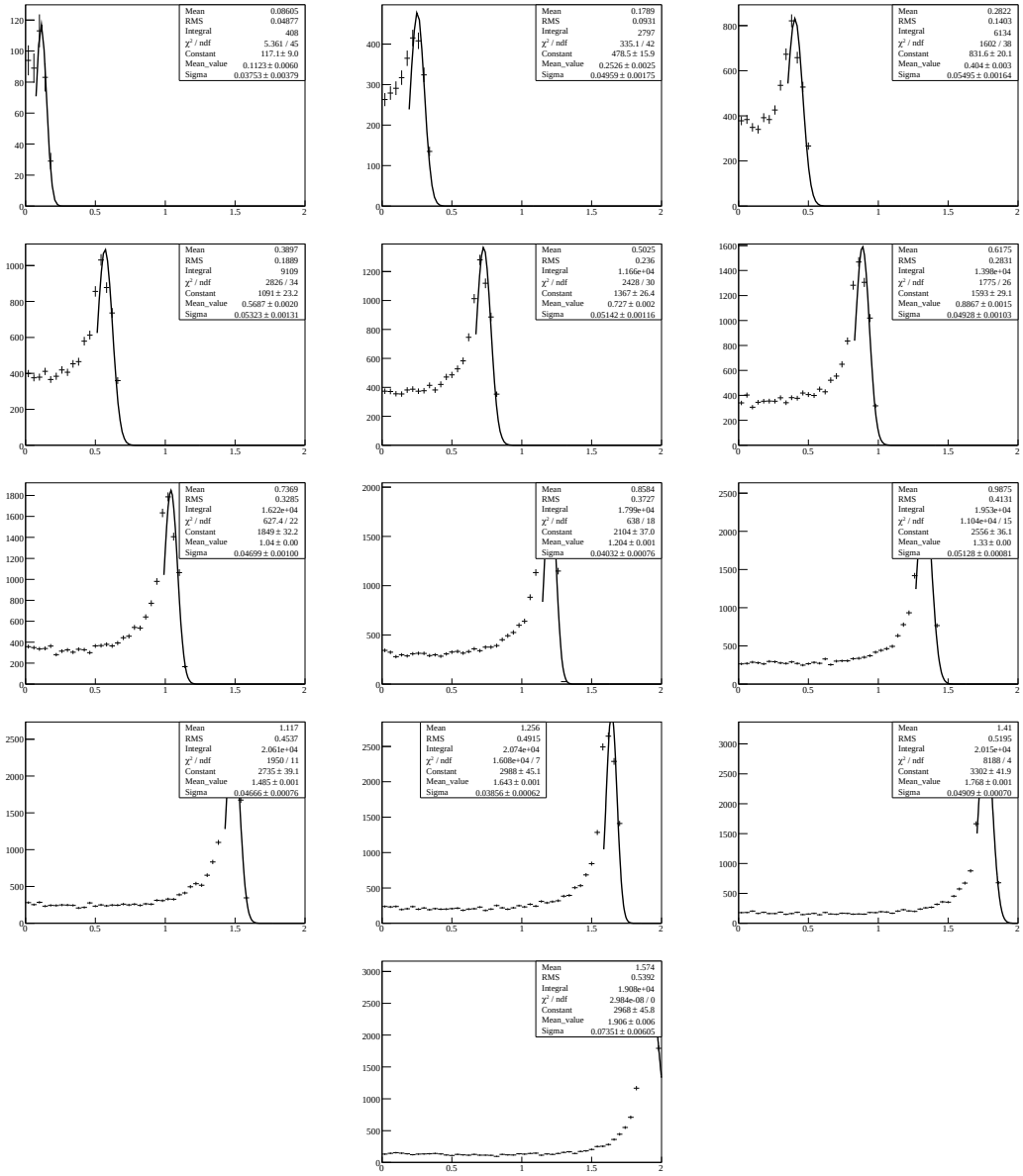

Figure B.2.6: *r in bins of t from toy MC study.*

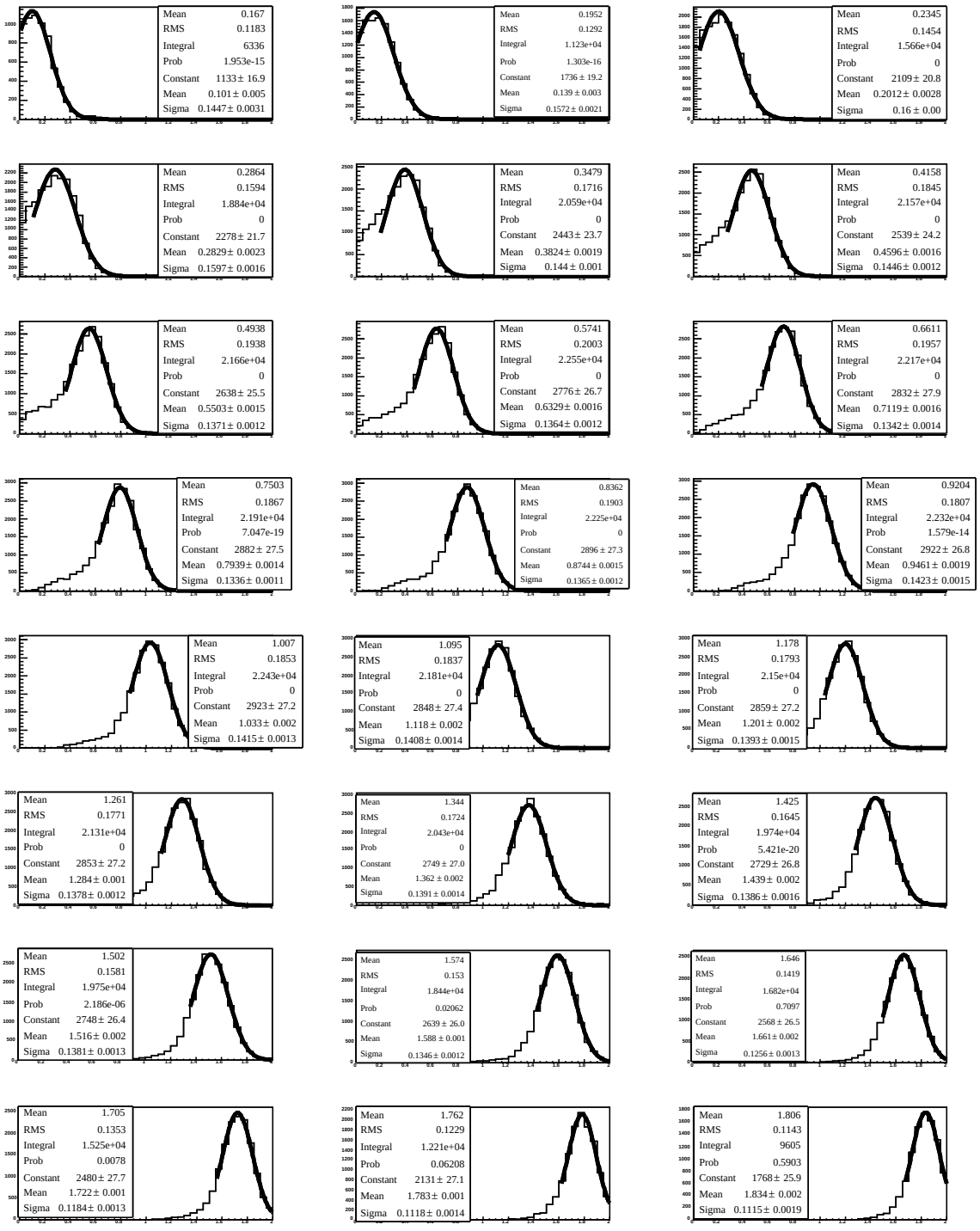

Figure B.2.7: *r in bins of t from default ATLAS calibration.*

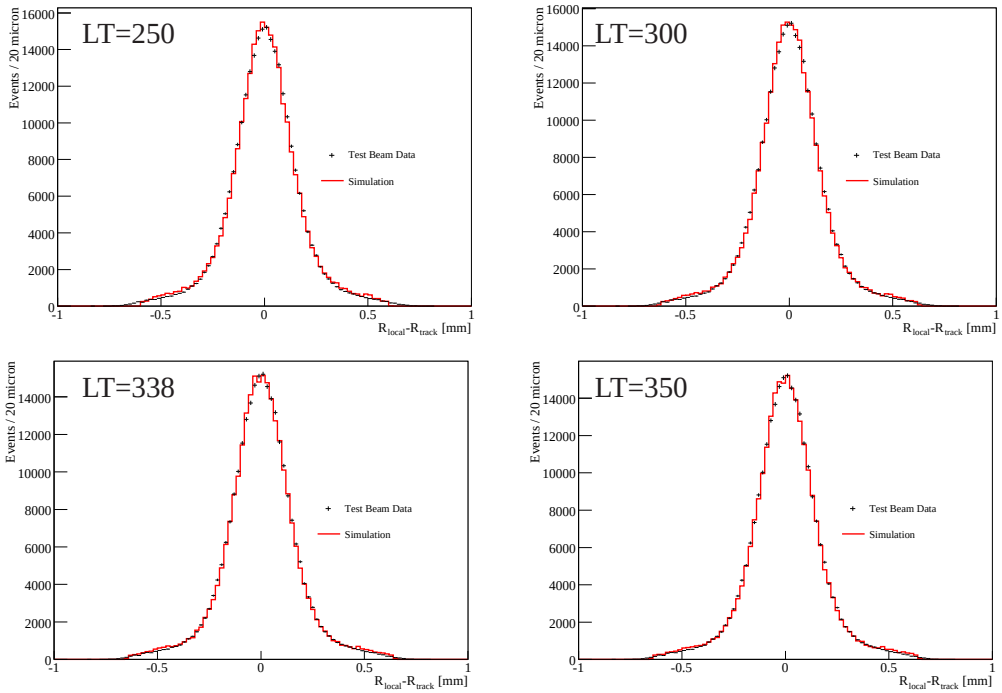

Figure B.2.8: *Track resolution for various LT settings.*

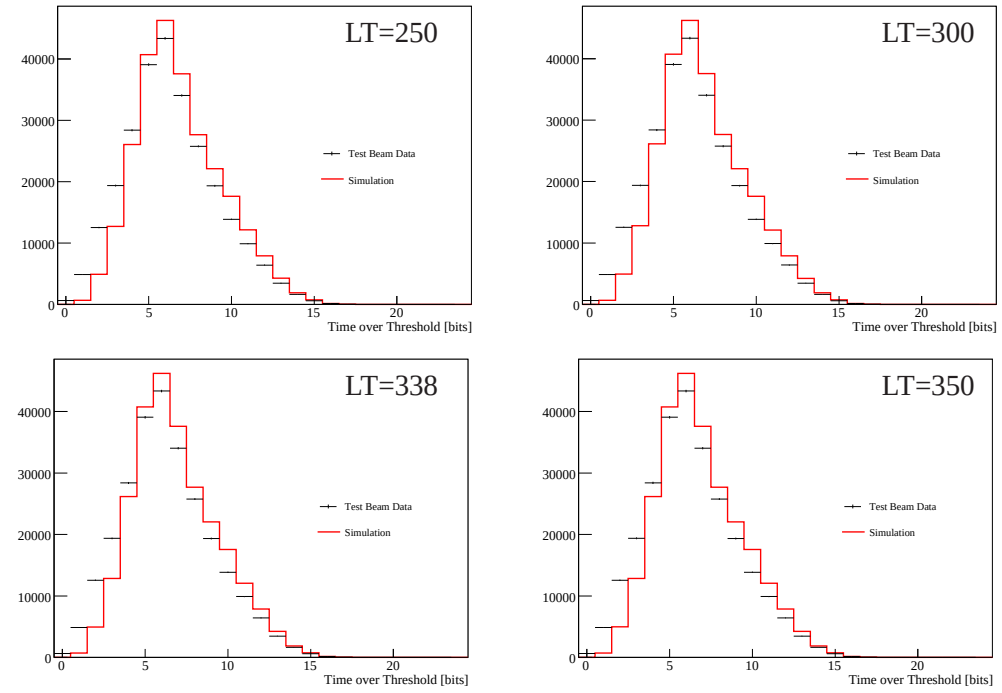

Figure B.2.9: *Time-over-threshold distributions for various LT settings.*